Free-Space Optical Communication Systems with a Partially Coherent Gaussian Beam and Media Diversity

It Ee Lee

A thesis submitted in partial fulfilment of the requirements of the University of Northumbria at Newcastle for the degree of Doctor of Philosophy

Research undertaken in
the Faculty of Engineering and Environment

January 2014

Abstract

Terrestrial free-space optical (FSO) communications is an emerging low-cost, license-free and high-bandwidth access solution, albeit hampered by the combined effects from atmospheric loss, turbulence and pointing errors (PEs). Partially coherent beams (PCBs) are capable of mitigating the turbulence-induced signal fading and PEs, while causing reduction in the mean received signal intensity. This implies the necessity of PCB optimization technique, such that the trade-off between the reduction in the scintillation index and the decrease in the mean received irradiance can be achieved conveniently.

This thesis investigates the performance of partially coherent FSO communication links from the information theory perspective. The important link design criteria are considered, and the Gaussian-Schell beam model is adopted to characterize the optical beam propagation through random turbulent medium. Numerical results show that beam width optimization presents a feasible approach in promoting capacity enhancement for long-distance terrestrial FSO systems, since the optimum beam width is susceptible to the deterring effects of atmospheric turbulence and PEs. Next, joint investigation of the effects of a PCB and aperture averaging is presented, which confirms the distinctive advantages of introducing an enlarged receiver aperture and the interest of optimizing the beam width to maximize the FSO channel capacity. A theoretical beam width optimization model is proposed to determine the optimum beam width. Subsequent investigation studies on the characteristics of PCB propagating through the turbulent channel reveal the relationship between the beam width and spatial coherence length to optimize the PCB. Therefore, a joint beam width and spatial coherence length optimization technique is proposed to maximize the average capacity in partially coherent FSO links. An optimization metric is developed to enable a feasible translation of the joint optimal transmitter beam parameters into an analogous level of divergence of the received optical beam. It is demonstrated that the PCBs are desirable in the weak-to-moderate turbulence regimes, whereas coherent laser beams with high transmit power exhibit greater resilience to strong turbulences.

An experimental study is carried out to demonstrate the effects of aperture averaging and beam width on the FSO link under laboratory-controlled atmospheric turbulence

conditions. The aperture-averaging effect is characterized through the signal density distributions, showing good agreement with the theoretical models. It is demonstrated that the relationship between the aperture averaging factor and point-received scintillation index can be described by a first-order linear regression model, whereby the coefficients of the model are provided and compared. Measurements of the Q-factor for an aperture-averaged optical receiver and its corresponding finite point receiver reveals that manifold gain in the link performance can be achieved with increasing scaled aperture size, thus concluding that the introduction of an enlarged receiver aperture enhances the effective collection of the optical signal and potentially mitigates the scintillation effect.

Atmospheric loss resulting from visibility-limiting weather conditions significantly attenuates the intensity of a propagating laser beam, which imposes degrading impacts on the link range and availability. Hybrid FSO and radio frequency (RF) systems present the most prominent alternative to enable these technologies in complementing one another's weaknesses, since fog and rain drastically affect the FSO and RF links, respectively, but only insignificantly vice versa. The viability of deploying the media diversity technique in the FSO system is investigated through a case study, in which a new hybrid-base transceiver station (H-BTS) system architecture is proposed for the green Metrozones. The hybrid FSO/RF system is integrated at the macro-cellular tier, to enable high-capacity, power-efficient wireless backhauling. A resource prioritization mechanism is designed, to maintain good control and optimal on-demand resource allocation, and to establish sustainable backhaul link availability. Next, a basic access signalling (BAS) scheme is introduced, to necessitate the discovery, registration and monitoring of active metro access points (M-APs). The proposed BAS scheme enables the sleep-wake-on-demand (SWoD) mechanism and the cooperative inter-cell support. Findings from this work suggest that adaptation and optimization at the link- and system-level are vital for Metrozones deployment, due to the occurrence of numerous time-varying factors in real networks.

Acknowledgements

The journey through my PhD studies, which bears enlightening life and research experiences, fruitful technical achievements and timely completion of this thesis, is impossible without the wonderful people who have walked with me and uplifted me through numerous good and difficult moments.

First of all, I would like to express my heartfelt gratitude to my supervisors – Prof. Zabih Ghassemlooy and Dr. Wai Pang Ng for giving their most sincere and thoughtful advice, guidance and support, particularly in justifying proper research direction of the project and ensuring that the research aims and objectives are fulfilled. In addition, I would like to thank Dr. Sujan Rajbhandari, Dr. Mohammad-Ali Khalighi and Dr. Moh Lim Sim for the insightful discussions, which have helped me to solve the technical problems and improve my research work. In particular, I felt indebted and thankful to Dr. Sujan Rajbhandari for the time-sacrificial training, guidance and support, which have enabled me to acquire the fundamental knowledge and important practical skills to carry out the experimental work in the laboratory, thereby generating some interesting results and notable findings. Moreover, I would like to express my utmost appreciation to my employer – Multimedia University for securing an academic position with the University and providing the much needed financial support during my leave of study. Furthermore, I am deeply grateful to Northumbria University for the financial contribution through the Northumbria Research Studentship programme.

Next, I would like to convey my sincere acknowledgement to my parents and siblings and their spouses for their understanding and moral support, especially during the most challenging moments of my research; and not forgetting my adorable nieces and nephews who have never failed to cheer me up in every moment of my life. In addition, I am deeply thankful to my beloved fiancé who has persistently accompanied me in completing this journey, sharing my tears and cries and showering upon me with love, joy and laughter. I would like to express my heartfelt gratitude to my best friends, colleagues and acquaintances for sharing their experiences and opinions, which have inspired me with more feasible ideas and solutions to overcome the roadblocks encountered in my research

studies. Last but not least, I thank God for upholding me with perseverance, wisdom and strength throughout this journey, and allowing everything to happen miraculously such that I could learn, grow and show appreciation in every aspect of my life. His blessings have brought me success and smooth accomplishment to this research project.

Declaration

I declare that the work contained in this thesis has not been submitted for any other award and that it is all my own work. I also confirm that this work fully acknowledges opinions, ideas and contributions from the work of others.

Name: It Ee Lee

Signature:

Date:

Table of Contents

Glossary of Acronyms

3G	Third generation
4G	Fourth generation
AMC	Adaptive modulation and coding
AP	Access point
APD	Avalanche photodiode
Ar	Argon
AWGN	Additive white Gaussian noise
BAS	Basic access signalling
BER	Bit-error rate
BTS	Base transceiver station
BWA	Broadband wireless access
CCD	Charge-coupled device
CDF	Cumulative distribution function
CO_2	Carbon dioxide
CO_2e	Carbon dioxide equivalent
CRC	Cyclic redundancy check
CSI	Channel state information
DD	Direct detection
DF	Degrees of freedom
DFB	Distributed feedback
DWDM	Dense wavelength-division multiplexing
FEC	Forward error correction
FOV	Field-of-view
FPGA	Field-programmable gate array
FSO	Free-space optical
GaAs	Gallium arsenide
GaAsSb	Gallium arsenide antimonide
Gbps	Gigabits per second
Ge	Germanium

GeSI	Global eSustainability Initiative
GigE	Gigabit Ethernet
GOF	Goodness-of-fit
Gt	Billion tonnes
GW	Gateway
H_2O	Water
H-BTS	Hybrid-base transceiver station
HDTV	High-definition television
ICT	Information and communications technology
IEC	International Electrotechnical Commission
IM	Intensity modulation
InGaAs	Indium gallium arsenide
InGaAsP	Indium gallium arsenide phosphide
IP	Internet protocol
ISDB-T	Integrated services digital broadcasting-terrestrial
LAN	Local area network
Laser	Light amplification by stimulated emission of radiation
LD	Laser diode
LDPC	Low-density parity-check
LED	Light-emitting diode
LOS	Line-of-sight
M-AP	Metro access points
MAN	Metropolitan area network
MD	Multiple description
MIMO	Multiple-input multiple-output
MISO	Multiple-input single-output
MMW	Millimetre wave
MUT	Mobile user terminal
Mt	Million tonnes
N_2	Nitrogen
NRZ	Non-return-to-zero
O_2	Oxygen
O_3	Ozone
OOK	On-off keying

OPEX	Operational expenditure
pa	Per annum
PCB	Partially coherent beam
PDF	Probability density function
PE	Pointing error
p-i-n	Positive-intrinsic-negative
PMT	Photomultiplier tube
PSD	Power spectral density
QAM	Quadrature amplitude modulation
QoS	Quality of service
RAI	Radio access interface
RAN	Radio access network
RF	Radio frequency
RLC	Redundant link controller
rms	Root mean square
RoFSO	Radio-on-FSO
RRM	Radio resource management
SD	Single description
Si	Silicon
SIMO	Single-input multiple-output
SINR	Signal-to-interference-and-noise ratio
SISO	Single-input single-output
SNR	Signal-to-noise ratio
SON	Self-organizing network
SWoD	Sleep-wake-on-demand
Tbps	Terabits per second
TE	Traffic estimator
TEM_{00}	Lowest-order transverse electromagnetic
VoIP	Voice over internet protocol
WAN	Wide area network
WiMAX	Worldwide Interoperability for Microwave Access
WMN	Wireless mesh network

Glossary of Symbols

α	Effective number of large-scale turbulent eddies
α_0	Complex parameter related to the transmitter beam width and phase front radius of curvature
α_m	Dimensionless size parameter of the Mie theory
α_t	Level of significance of the student t-test
β	Effective number of small-scale turbulent eddies
γ	Detector responsivity
γ_{APD}	Responsivity of an APD
$\Gamma(\cdot)$	Gamma function
$\Gamma_I(\cdot)$	Mutual coherence function of a Gaussian-beam wave propagating in the turbulent medium
δ	Variable defined for the aperture-averaged scintillation index in (2.79)
ε	Average energy dissipation rate
η	Quantum efficiency
$\eta_{(i)}$	Total access traffic demand at the i^{th} H-BTS
η_K	Kolmogorov microscale
$\eta_{RA,low}$	Lower threshold of the radio access traffic
$\eta_{RA,high}$	Upper threshold of the radio access traffic
Θ_n	Curvature parameter at the input plane
Θ_L	Curvature parameter at the output plane
$\overline{\Theta}_L$	Parameter related to the curvature parameter at the output plane
σ	Attenuation coefficient
σ_0, σ_1	Standard deviation for the average received optical signals resembling the data bits ‘0’ and ‘1’
σ_{pe}	PE-induced jitter standard deviation
σ_B^2	Approximated Rytov variance for a Gaussian-beam wave
σ_g^2	Variance of the Gaussian describing the ensemble average of the random phases

σ_I^2	Scintillation index
$\sigma_I^2(0)$	Point-received scintillation index
$\sigma_{I,\,\mathrm{pl}}^2(0)$	Point-received scintillation index for the plane-wave model
$\sigma_{I,\,\mathrm{sp}}^2(0)$	Point-received scintillation index for the spherical-wave model
$\sigma_I^2(D)$	Aperture-averaged scintillation index
$\sigma_{I,\,\mathrm{pl}}^2(D)$	Aperture-averaged scintillation index for the plane-wave model
$\sigma_{I,\,\mathrm{sp}}^2(D)$	Aperture-averaged scintillation index for the spherical-wave model
$\sigma_{\ln X}^2$	Large-scale log variance of the irradiance
$\sigma_{\ln Y}^2$	Small-scale log variance of the irradiance
σ_n^2	Noise variance of the FSO system
$\sigma_{n,\,\mathrm{RF}}^2$	Noise variance of the RF system
σ_R^2	Rytov variance
υ_p	Parameter defining the ratio between the receiver aperture diameter and beam width
ϕ	Parameter related to the phase front radius of curvature for a PCB at the receiver
$\lambda_T(t)$	Instantaneous normalized traffic of a BTS
λ	Laser wavelength
λ_2	Wavelength of the RF system
Λ_n	Fresnel ratio at the input plane
Λ_L	Fresnel ratio at the output plane
$\mu(\cdot)$	Complex degree of spatial coherence
ν	Photon frequency
ν_K	Kinematic viscosity
ν_0	Centre frequency of the quasi-monochromatic Gaussian laser beam
ξ	Ratio between the equivalent beam radius at the receiver and the PE displacement (jitter) standard deviation at the receiver
$\xi_{FSO,Th}$	SINR threshold of the FSO link
$\xi_{FSO}^{(i,k)}$	SINR of the FSO link
$\xi_{RF,Th}$	SINR threshold of the RF link
$\xi_{RF}^{(i,k)}$	SINR of the RF link

$\boldsymbol{\rho}$	Observation point in the receiver plane
$\rho_T(t)$	Poisson distributed random process modelling the random fluctuations of the traffic
ρ_0	Coherence length of a spherical wave
ζ	Global coherence parameter
ζ_s	Source coherence parameter
φ	Uniform random variable with interval [0, 2π] determining the traffic pattern among the BTSs
ϕ	Parameter related to the phase front radius of curvature at the output plane
$\chi_{BH,low}$	Lower threshold of the backhaul traffic
$\chi_{BH,high}$	Upper threshold of the backhaul traffic
ψ	Parameter determining the abruptness of the traffic profile
$\Psi(\cdot)$	Random part of the complex phase of a spherical wave propagating in the turbulent medium
Ω	Received signal power
Ω_L	Non-dimensional parameter characterizing the spot radius of the collecting lens
a_1, a_2	Chanel state of the parallel fluctuating channels
a_{oxy}	Attenuation due to oxygen
a_{rain}	Attenuation due to rain
A_0	Error function of v_p
A_g	Aperture-averaging factor
A_ζ^{opt}	Optimization metric
$b_I(\cdot)$	Normalized covariance function
B	Bandwidth of the RF system
$B_I(\cdot)$	Irradiance covariance function
$\langle BER \rangle$	Average BER
$\mathbf{c_1}, \mathbf{c_2}$	Codeword
$\hat{\mathbf{c}}_\mathbf{1}, \hat{\mathbf{c}}_\mathbf{2}$	Demodulated codeword
$C(\cdot)$	Channel capacity
$\langle C \rangle$	Average channel capacity
C_0, C_1	Coefficients of the linear regression model

C_r	Scaling constant
C_n^2	Refractive index structure parameter
C_T^2	Temperature structure constant
C_V^2	Velocity structure constant
d	Scaled aperture size
D	Receiver aperture diameter
D_H	Diffusivity of heat in air
$D_n(R_p)$	Structure function of turbulence
$D_{RR}(R_p)$	Structure function of wind velocity
$D_T(R_p)$	Structure function of temperature
$E(\cdot)$	Optical frequency electric field
$E^*(\cdot)$	Complex conjugate of the electric field
E_1, E_2	Ground- and excited-state energies of the electron
E_g	Bandgap energy of the material
E_{photon}	Photon energy
f_c	Carrier frequency of the RF system
$f_h(h)$	PDF of the optical channel
$f_{h_p}(h_p)$	PDF of misalignment
$f_{h_s}(h_s)$	PDF of atmospheric turbulence
F_0	Phase front radius of curvature at the input plane
F_L	Phase front radius of curvature at the output plane
g_{RF}	Average power gain of the RF system
$G(\cdot)$	Green's function
G_{Rx}	Receive antenna gain
G_{Tx}	Transmit antenna gain
$\hbar$	Planck's constant
h	Channel state of the FSO system
h_2	RF fading gain
h_l	Atmospheric loss
h_p	PE loss

h_s	Attenuation due to scintillation
$\mathcal{H}_{(i)}$	H-BTS
I	Intensity of the optical beam wave
$\bar{I}_0, \bar{I}_1$	Average received optical signals of the data bits '0' and '1'
I_p	Average photocurrent generated by the photodetector
k	Optical wave number
K	Rician factor
$K_{\alpha-\beta}$	Modified Bessel function of the second kind of order $(\alpha - \beta)$
l_0	Inner scale of turbulence
l_c	Spatial coherence length
L	Link distance
L_0	Outer scale of turbulence
$\mathbf{m_1}, \mathbf{m_2}$	Original source of the parallel fluctuating channels
$\hat{\mathbf{m}}_1, \hat{\mathbf{m}}_2$	Estimate of the source
m_κ	Message signal
$\mathcal{M}_{(i,j)}$	M-AP
M	Photocurrent gain
MBE	Mean bias error
n	Atmospheric index of refraction
n_o	Signal-independent AWGN of the FSO system
$n_{o,\,\mathrm{RF}}$	Complex AWGN of the RF system
N	Total number of observations
N_0	Noise power spectral density of the RF system
N_F	Receiver noise figure of the RF system
$p(I)$	Unconditional irradiance distribution
$p_X(X)$	Gamma distribution of the large-scale irradiance fluctuations
$p_Y(Y)$	Gamma distribution of the small-scale irradiance fluctuations
P	Pressure
P_0	Steady-state average optical power incident on the photodetector
P_e	BER

P_{FSO}	Average transmitted optical power
P_{out}	Probability of outage
P_R	Received optical power
P_{RF}	RF transmit power
$P_X(\cdot)$	Probability of the bit
q	Electronic charge
q_s	Parameter related to the particle size distribution and visibility
Q	Q-factor
$Q(\cdot)$	Gaussian-Q function
r	Transversal distance from the Gaussian-beam centre line
$\mathbf{r}$	Observation point in the transmitter plane
$\langle r_c^2 \rangle$	Beam wander variance of a Gaussian-beam wave
r_0	Fried's parameter
r_p	Radius of the atmospheric particle
R	Correlation coefficient
R_0	Transmission rate
$\mathbf{R_P}$	Vector displacement between two observation points
R-square	Coefficient of determination
$RMSE$	Root mean square error
$\mathbf{s}$	Source sequence
$\hat{\mathbf{s}}$	Estimate of the source
SNR	Received SNR
$\langle SNR \rangle$	Average electrical SNR
SNR_{RF}	Received SNR of the RF link
t_{c}	Critical value of the student t-test
t_{idle}	Time interval of an M-AP remaining inactive
t_{s}	t-statistic
T	Temperature
T_1, T_2	Temperature at two points separated by distance R_p
T_{Tot}	Sum of contributions resulting from small-scale beam spread and large-scale beam wander

T_{LS}	Large-scale contribution due to beam wander
T_{SS}	Small-scale contribution due to beam spread
$U(\cdot)$	Free-space electric field of the optical beam wave
$U^{*}(\cdot)$	Complex conjugate of the free-space electric field
$\widetilde{U}(\cdot)$	Resultant field of the optical wave emerging from a phase diffuser
V	Visibility
V_1, V_2	Velocity components at two points separated by distance R_p
w_0	Transmitter beam width
w_0^{opt}	Optimum beam width
w_L	Beam width at the output plane
w_{LT}	Long-term beam radius
w_{ST}	Short-term beam radius
$w_{z_{eq}}$	Equivalent beam radius at the receiver
$w_{z_{eq}}^{\mathrm{nom}}$	Equivalent beam radius for the nominal coherent beam
$w_{z_{eq}}^{\mathrm{opt}}$	Equivalent beam radius for the optimum beam
$W(\cdot)$	Cross-spectral density function of a Gaussian-beam wave propagating in the turbulent medium
x	Observed value
$\bar{x}$	Mean of the observed values
$\mathbf{x_1}, \mathbf{x_2}$	Modulated codeword
x_2	Modulated RF signal
x_κ	Optical intensity of the transmitted signal
X	Large-scale irradiance fluctuations
y	Predicted value from the functional representation
$\bar{y}$	Mean of the predicted values
y_2	Received RF signal
y_κ	Received optical signal
Y	Small-scale irradiance fluctuations
z	Axial distance of the Gaussian-beam wave

List of Figures

Chapter 3: Investigation of the Effects of Aperture Averaging and Beam Width

Chapter 5: Experimental Demonstration of the Effects of Aperture Averaging and Beam Width under Controlled Turbulence Condition

List of Tables

CHAPTER 1

Introduction

1.1. Overview

The evolution of the wireless communications standards into the fourth generation (4G) has witnessed recent rapid progress in information and communication technologies, which in turn revealed a multitude of mobile broadband facilities, such as ultra-broadband internet access, internet protocol (IP) telephony, gaming services, streamed multimedia applications, and high-definition television (HDTV) broadcasting services [1, 2]. The exponential surge in the commercial demand to pursue unlimited high-speed and ubiquitous broadband wireless access, to accommodate the ever-increasing utilization of internet and multimedia services among individual mobile users and residential and enterprise clusters, has spurred prodigious growth in internet traffic demand in the recent decade, scaling much faster than the prediction of Moore's law [3, 4]. As a result, data

transmission rates have been rising at approximately a factor of ten every five years, which corresponds to a tremendous growth in the overall traffic volume by several hundred-fold within the next decade [5], in order to be able to transport an exponentially increasing amount of (available) data to end users within an acceptable amount of time, inadvertently resulting in severe congestion of the radio frequency (RF) spectrum and wireless traffic bottleneck [6]. Complementing the existing wireless RF solutions, free-space optical (FSO) communications is poised to become a promising broadband wireless access (BWA) candidate to resolve the existing "last mile" access network problems [7-9]. This is mainly due to the vastly attractive features of such technology option, which include: (i) no licensing requirements or tariffs for its utilization; (ii) virtually unlimited bandwidth for providing near-optimal capacity and supporting high-speed applications; (iii) extensive link range in excess of 5 km; (iv) high energy efficiency due to low power consumption, reduced interference and fading immunity; (v) high scalability and reconfigurability; (vi) secure and reliable data transmission medium; (vii) minimal cost of deployment; and (viii) reduced time-to-market [10].

Terrestrial FSO communication is a line-of-sight (LOS) technology based upon the transmission of optical laser beam waves operating at typical wavelengths of 850 nm and 1550 nm through the atmosphere, in order to establish wireless communication for providing larger bandwidths and high-data-rate transfer of information [7, 11]. The deployment of FSO communication systems is particularly advantageous in metropolitan areas, geographically challenging terrains and underserved rural areas lacking broadband network connectivity [12, 13]; whereby the installation of optical-fibre links is least feasible or impossible, as evident from the numerous case studies brought forward by LightPointe^{TM} [14]. With the emergence of powerful and efficient optoelectronic components and advanced communication techniques, current state-of-the-art FSO

prototypes have demonstrated data transmission through the atmospheric channel at ultra high speed up to terabits per second (Tbps) [15-20]. In [21], Arimoto presented the design and demonstration of a novel FSO communication terminal, featuring fast and accurate fine tracking system and transparent connectivity to single-mode fibre lines; which represents a significant breakthrough in the stability, reliability and capacity of terrestrial FSO communications. This state-of-the-art compact FSO terminal has demonstrated an aggregated 320 (8 × 40) gigabits per second (Gbps) transmission at a link distance of 212 m in [17], and then successfully upgraded to an astounding 1.28 Tbps (32 × 40 Gbps) in [18], which is by far the highest achievable capacity reported for terrestrial FSO communication systems. Furthermore, the transmission of multiple RF signals carrying various broadband wireless services including the integrated services digital broadcasting-terrestrial (ISDB-T) signals over a 1 km turbulent FSO link based on the advanced dense wavelength-division multiplexing (DWDM) technique have been demonstrated in [22]. The proposed work unfolds new insight on the system design, operation and performance characteristics relevant in implementing economical and reliable alternative broadband wireless technology for complementing optical-fibre networks, especially in environments where the deployment of optical-fibre links are not feasible.

1.2. Problem Statement

1.2.1. Challenges of the FSO Communication Channel

FSO communications remains as one of the least commercially deployed broadband technologies, albeit its tremendous potential in resolving the “last mile” issues. The widespread deployment of such BWA solution is hampered by the combined effects from numerous factors, which include: the atmospheric channel which is highly variable,

unpredictable and vulnerable to different weather conditions, such as scattering, absorption and turbulence [6, 11, 23]; and the presence of pointing errors (PEs) [13, 24, 25]. Aerosol scattering and absorption due to rain, snow and fog result in significant optical power attenuation, beam spreading and link distance reduction, severely impairing the system performance with an increase in the link error probability; thus causing the FSO system to fall short of the desired carrier-grade availability of 99.999% under heavy, visibility-limiting weather conditions [26]. In particular, Kim and Korevaar reported in [27] that the atmospheric attenuation of laser beam is a random function of the weather, which can vary from 0.2 dB/km in exceptionally clear weather to 350 dB/km in very dense fog.

Laser beams propagating through the atmospheric turbulent channel are highly susceptible to the adverse effects of scintillation and beam wander, which are natural phenomena commonly observed in terrestrial FSO communication systems, due to the refractive index variations along the transmission paths caused by inhomogeneities in both temperature and pressure of the atmosphere [11]. Correspondingly, this produces random fluctuations in both temporal and spatial domains of the received irradiance, known as channel fading, whereby the FSO links may suffer temporary signal degradation or complete system annihilation under the influence of deep signal fades [28, 29]. Modelling of the fading effects in an atmospheric turbulent channel using the extended Huygens-Fresnel principle [11] shows that large transient dips in the optical signals typically last approximately 1-100 milliseconds, which may result in the loss of potentially up to 10^9 consecutive bits at a transmission rate of 10 Gbps [28].

Misalignment-induced fading is another non-negligible effect in FSO systems, as optical terminals typically installed on high-rise buildings are susceptible to building sway, while continuous precise pointing is required to establish link connectivity for successful

data transmission with minimum error probability, particularly when narrow beam divergence angle and receiver field-of-view (FOV) are employed [13]. Under the influence of wind loads, thermal expansions and weak earthquakes, building sway causes vibrations in both the transmitter and receiver, in which the stochastic process deviates the optical wave propagation path from the common LOS, thus resulting in decrease of the average received signal [13, 30, 31]. In addition, PEs can arise due to mechanical misalignment, errors in tracking systems, or presence of mechanical vibrations within the system [25].

Through an in-depth survey of the relevant literatures, it is evident that a substantial number of analytical and simulation studies [32-35] have isolated the contributing effects of different atmospheric channel conditions resulting from atmospheric loss, turbulence-induced fading and PE loss for the sake of analytical simplicity. These channel impairments must be collectively taken into account using a combined channel fading model, in order to describe the optical channel characteristics with better accuracy. In addition, the limiting cases of unbounded plane- or spherical-wave approximations are insufficient to characterize the propagation properties of the optical beam wave through random turbulent medium, particularly for the case of spatially partially coherent Gaussian laser beam, whereby the spatial coherence and beam divergence of the optical laser source are concerned. Moreover, the conventional Rytov-based scintillation model associated with the above-mentioned approximations may not accurately reflect the irradiance fluctuations, mainly because the beam wander effect contributing to a widening of the long-term beam profile and PEs is not considered in the limiting Rytov theory. In this research work, the above concerns are appropriately addressed and taken into account through the joint adoption of a combined optical slow-fading channel model and Gaussian-Schell beam model; which in turn substantiate the development of a comprehensive design benchmark encompassing important link design criteria in Chapter 3, thereby creating a holistic

perspective for optimal planning and design of terrestrial FSO communication links. Through reliable theoretical analysis and simulation studies, feasible mitigation techniques and/or optimization methods can be proposed and examined with better accuracy, in order to promote effective mitigation of the adverse atmospheric channel effects.

1.2.2. Mitigation Techniques to Overcome the Atmospheric Channel Effects

The feasibility and physical deployment of the FSO technology relies upon extensive research efforts to address numerous challenges and issues involving all aspects of the system design, and then introduce mitigation and enhancement approaches to overcome the limitations and optimize the system performance, respectively. Various techniques have been investigated and proposed to combat the deterioration of signal quality due to the adverse atmospheric conditions and link misalignment, which include: adaptive optics [36, 37], spatial [28, 29, 38-48], temporal [49, 50], wavelength [51] and media/channel [27, 52-57] diversity schemes, modulation and signalling formats [58-62], forward error correction (FEC) [35, 63-70], aperture averaging [40, 71], beam optimization methods [72-76], and signal processing techniques [77].

The adaptive optics techniques were originally developed to improve the quality of stellar telescopes in optical astronomy, whereby deformable mirrors or phase conjugation methods are used to pre-distort the wavefront of a transmitted laser beam, such that the distorted wavefront is restored to its original unperturbed form upon propagating through the turbulent atmosphere, thereby arriving at the receiver as an undistorted wave. While these techniques have demonstrated limited success in FSO systems, the adaptive optics approach in compensating the effects of atmospheric turbulence along a propagation path remains ineffective when the link distance exceeds the sum of the transmitter and receiver Rayleigh ranges, or when the transmitter and receiver are not moving fast laterally with

respect to each other [78]. In addition, bulky, high-complexity and computation-intensive systems are required to achieve wavefront correction fast enough to counteract the adverse effects of turbulence, whereas full reciprocal adaptive optics can only be made possible under the condition of a sufficiently short link range; thus deterring its widespread adoption for long-distance terrestrial FSO communication.

In principle, diversity techniques take advantage of multiple identical transmissions with distinct uncorrelated paths between the transmitters and receivers, such that the effective level of scintillation and probability of fade can be reduced, and hence increasing the likelihood of signal detection with minimum bit error. The more rigorously investigated and commonly adopted diversity approach in FSO communication systems is the spatial diversity technique [79, 80], in which multiple transmitters and/or receivers appearing in single-input multiple-output (SIMO), multiple-input single-output (MISO) or multiple-input multiple-output (MIMO) configurations are spaced further apart than the lateral correlation distance on the link. Temporal diversity is an alternative approach which relies upon multiple replicated signal transmissions separated by a time delay (typically longer than the expected fade duration), whereas wavelength diversity requires the transmission of data on at least two distinct optical wavelengths. Nevertheless, these diversity techniques require a significant electronic and processing overhead, in order to accommodate the synchronization, buffering and retiming processes and logical combining of the replicated transmissions [81].

FEC is another widely considered fade mitigation technique, in which redundant check bits are intentionally inserted in the encoded packets prior to transmission, in order to ensure that the transmitted bits can be automatically corrected and recovered if some are lost due to fading, while inadvertently contributing to additional power, bandwidth and

processing overhead on the system. Even though error control coding can provide an additional layer of information security, this method may not effectively negate the effects of atmospheric turbulence albeit using the best available FEC codes, mainly because the transmission time of a codeword (typically a few μs) in a high-speed FSO system is even much shorter than the shortest fade duration [81]. Correspondingly, interleaving is introduced in conjunction with coding to provide temporal diversity by spacing coded symbols with time offsets that are longer than the expected fade durations, such that a fade can only affect a single symbol per codeword and the length of the required codeword can be drastically reduced. The major drawback of FEC-interleaving schemes is increased latency and processing time, since the data must be buffered at the transmitter and receiver for at least the duration of the used coding constraint length. In general, the overall transmission delay can be expected to exceed 100 ms, thus making such implementation unrealistic for delay-critical data transmissions.

While majority of these mitigation techniques have been proposed at the expense of increased circuit complexity and massive signal processing requirements, low-overhead methods may be introduced into the system under study without incurring additional power, bandwidth, size, weight, cost and/or processing overhead to the overall design. This research work investigates and proposes a more simplistic approach based upon a joint consideration of partially coherent Gaussian laser beam and aperture averaging, which is capable of mitigating the turbulence-induced beam wander and scintillation effects and jitter-induced PE loss. Similar to all other communication systems, terrestrial FSO communication systems must be carefully designed and system parameters must be appropriately adjusted in accordance to the varying channel conditions, such that the best achievable FSO channel capacities can be obtained under most scenarios. Taking advantage of a simple mathematical solution, a theoretical beam width optimization model

is developed in Chapter 4, in order to determine the optimum beam width for maximizing the average channel capacity. In addition, this thesis demonstrates the necessity of a joint beam width and spatial coherence length optimization technique to maximize the average capacity in FSO links employing partially coherent beam (PCB), under the combined effects of turbulence and PEs, while taking into account the aperture-averaging effect.

On the other hand, media/channel diversity (commonly termed as hybrid FSO/RF) takes advantage of the symbiotic relationship between the FSO and RF sub-systems in complementing each technology option's limitations to different atmospheric phenomena, in order to enhance the reliability of the wireless communication links [82]. By operating the FSO link in conjunction with an RF link, the latter technology option may be used to facilitate a variety of purposes, which include: link establishment, control and operation, backup link support in the event of a failure, data splitting for parallel data transmission, and codeword partitioning for FEC enhancement. At present, rigorous investigation and extensive research studies are carried out to integrate FSO/RF links in wireless macro-cellular networks, broadband access networks [83] and multihop networks [84, 85] for providing high-rate data connectivity with low end-to-end delay; thereby unveiling numerous open research problems, particularly in the aspects of feasibility analysis of hybrid FSO/RF communication networks, topology discovery, dissemination, link restoration, optimal FSO/RF configurations and routing. In this research work, the media diversity technique is introduced in the terrestrial FSO communication systems, and applied to a case study for next generation Metrozones in wireless macro-cellular networks in Chapter 6.

1.3. Research Aims and Objectives

The primary aim of this research project is to carry out extensive theoretical investigation and simulation studies and experimental demonstration pertaining to the system design, performance analysis and optimization of FSO communications for terrestrial applications. The main objectives of this research work are defined as follows:

- To carry out thorough literature survey and preliminary studies, in order to acquire in-depth knowledge and understanding pertaining to the key areas as follows:
  (1) Transmitter, channel and receiver characteristics of the FSO communication system;
  (2) Technical advantages and challenges of the system under study; and
  (3) Mitigation and enhancement techniques.

- To perform theoretical analysis and simulation studies on the FSO system with the key aspects outlined below:
  (1) To examine the effects of numerous important link design criteria on the proposed system, which include the transmitter beam width, spatial coherence length, receiver aperture dimension and its resulting aperture-averaging effect, and knowledge of channel state information (CSI);
  (2) To investigate the influence of different operating conditions on the proposed system, which comprises the weather effects as signified by the visibility and turbulence strength, the PE loss as indicated by the jitter variance, and the propagation distance;

(3) To evaluate the system performance through the important performance metrics encompassing the bit-error rate (BER), probability of outage and average channel capacity; and

(4) To propose new optimization techniques based upon the numerical method, in order to optimize the beam width and spatial coherence length of the partially coherent Gaussian laser beam wave, and the receiver aperture dimension.

- To conduct analytical and simulation studies on the hybrid FSO/RF system with the key aspects highlighted as follows:

  (1) To evaluate the system performance through the analysis of the outage probability for both FSO and RF links; and

  (2) To investigate the feasibility of the proposed hybrid/channel diversity system in the specific application of next generation Metrozones for wireless macro-cellular networks.

- To carry out experiment demonstration of the system under study, and perform measurements in laboratory-controlled atmospheric environment.

- To validate the feasibility of the proposed system through detailed comparison between the experimental results and theoretical models.

1.4. Original Contributions of Research

During the course of this research, the original contributions pertaining to the design, analysis and optimization of terrestrial FSO communication links have been achieved, which are clearly depicted in the research road map in Figure 1.1 and highlighted here.

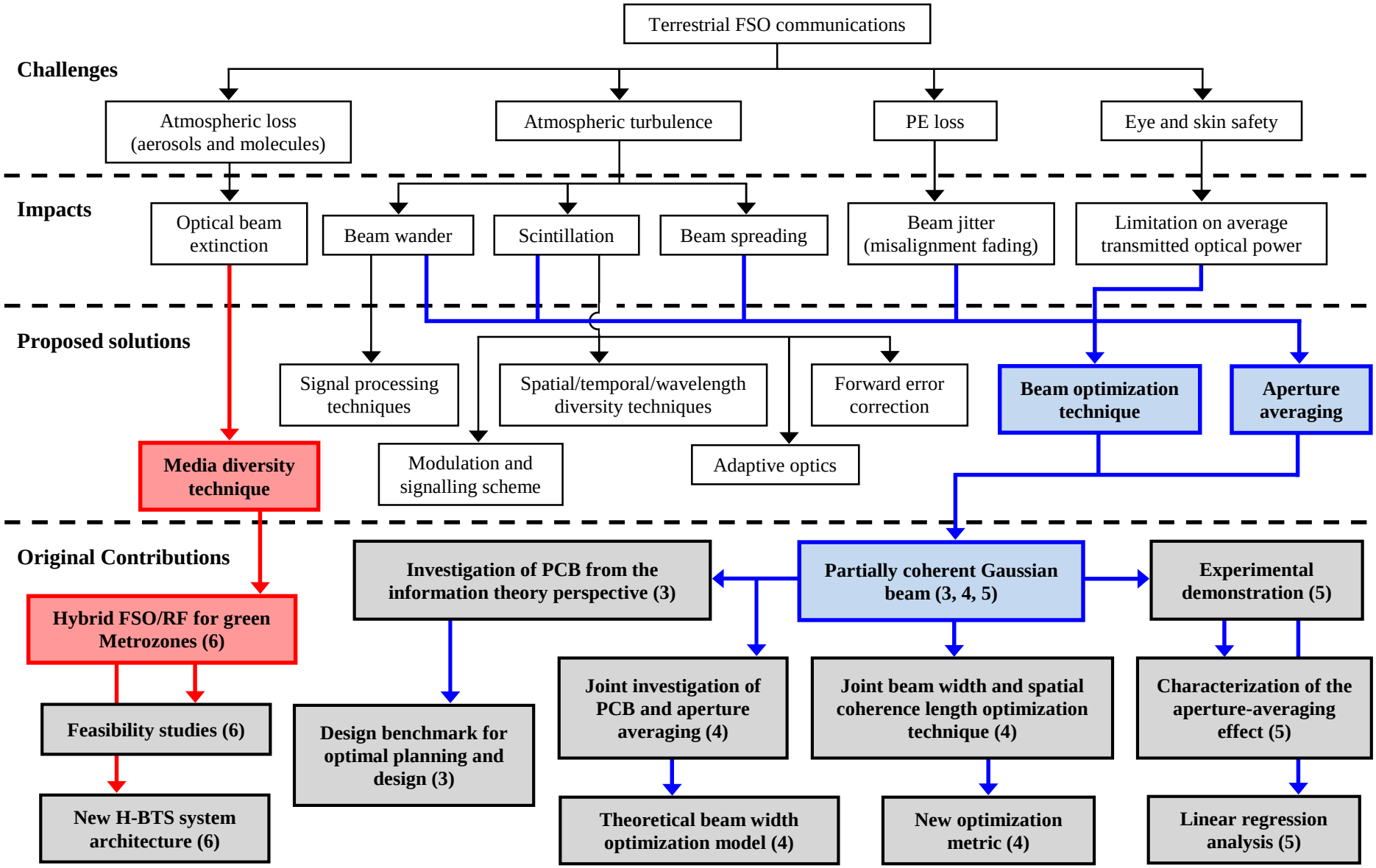

Figure 1.1: Research road map depicting the key challenges, degrading impacts, existing and proposed solutions for horizontal-path terrestrial FSO communication systems. The original contributions of this thesis are summarized here, with the contributing chapters provided in brackets.

The performance of FSO communication links with a spatially partially coherent Gaussian laser beam is investigated from the information theory perspective in Chapter 3, taking into account various adverse effects of the atmospheric channel and numerous important link design criteria. In particular, a combined optical slow-fading channel model is used to describe the influences of atmospheric loss, turbulence and PEs within the atmospheric channel, for evaluating the important performance metrics of the FSO link encompassing the BER, average channel capacity and outage probability. While theoretical treatments based upon the classical unbounded plane- or spherical-wave approximations are insufficient to characterize the propagation properties of the optical beam wave through random turbulent medium, the Gaussian-Schell beam model is introduced in the theoretical and simulation studies; which considers the diverging and focusing characteristics of the PCB, and the scintillation and beam wander effects arising from the turbulent eddies. These turbulence-induced effects result in the aggravation of optical irradiance fluctuations and random signal losses at the receiver side; in which such stochastic behaviour can be appropriately modelled by the log-normal and gamma-gamma distributions, valid in the weak-to-moderate and moderate-to-strong scenarios, respectively. Hence, this study presents a holistic perspective for optimal planning and design of horizontal FSO communication links employing spatially partially coherent Gaussian laser beams. The corresponding results and findings are reported in [J3], [C3] and [C4].

Joint investigation of the effects of a partially coherent Gaussian laser beam and aperture averaging is presented in Chapter 4, in order to examine the resulting impact of the PCB parameters and receiver aperture diameter on the average channel capacity of the FSO link, in the presence of turbulence-induced beam wander and scintillation effects and PEs. This in turn substantiates the development of a theoretical beam width optimization model, which takes advantage of a simple mathematical solution to determine the optimum

beam width. Based on the proposed theoretical model, several appealing observations are obtained and reported for the first time in [J2].

Through subsequent studies on the propagation properties and performance of PCB through random turbulent media, a joint beam width and spatial coherence length optimization technique is proposed in Chapter 4, while taking into account the aperture-averaging effect; in order to enable the effective mitigation of the scintillation effects and PE loss, thus maximizing the average channel capacity in partially coherent FSO links. In particular, an optimization metric, known as the beam spreading gain is developed to examine the changing behaviour of the optimum beam divergence, by providing a feasible translation of the joint optimal transmitter beam parameters into an analogous level of divergence of the received optical beam. The proposed technique and important results derived from this work are reported in [J1] and [C5].

Joint investigation and practical demonstration of the effects of aperture averaging and beam width on the FSO link are presented in Chapter 5, based on a carefully designed experiment setup to reproduce the turbulence-induced scintillation effects typically encountered in the FSO communication channel on outdoor environment. The proposed experimental study reports here for the first time the characterization of the combined effects of aperture averaging and beam width for a Gaussian laser beam under laboratory-controlled atmospheric turbulence conditions. In particular, the probability density distributions of the received optical signal are estimated from the experimental data, in order to examine the extent of signal fluctuations resulting from the diminishing effects of aperture averaging and increase in scintillations; and then compared with the theoretical lognormal and gamma-gamma turbulence models through a series of goodness-of-fit (GOF) tests. The experimental results and findings are presented in [J4] and [C6].Taking into

account numerous transmitter beam radius, turbulent channel conditions and receiver aperture dimensions in the experiment, it is demonstrated in Chapter 5 that the aperture-averaging factor exhibits a linear characteristics with respect to the changes in the point-received scintillation index, which can be represented by a first-order linear regression model. Regression analysis is introduced and applied in the proposed experimental study to determine the coefficients of the model; and the accuracy of the linear regression model in describing this empirical-based relationship is validated through the GOF tests. Furthermore, a comparison study on the performance of an aperture-averaged optical receiver and its corresponding finite point receiver is carried out, in order to evaluate the achievable performance enhancement with aperture averaging. The proposed experimental work is presented in [J5].

The media diversity technique is introduced in the terrestrial FSO communication systems, which takes advantage of the symbiotic relationship between the FSO and RF technologies, in order to overcome the link outage challenge resulting from severe atmospheric loss under adverse weather effects, such as fog and haze. In particular, the concept of hybrid FSO/RF is applied to a case study for next generation Metrozones in wireless macro-cellular networks in Chapter 6. Feasibility studies are performed in the proposed study to examine the time-varying characteristics of the base transceiver station (BTS) daily traffic profile, and to evaluate the outage performance of the proposed hybrid FSO/RF systems under different weather conditions.

New hybrid-BTS (H-BTS) system architecture for the green Metrozones is proposed in Chapter 6, in which a radio resource management (RRM) module encompassing a resource prioritization mechanism is designed and introduced into the system hub of the proposed architecture. In addition, a basic access signalling (BAS) scheme is considered,

which necessitates the discovery, registration and monitoring of active metro access points (M-APs), in order to enable the sleep-wake-on-demand (SWoD) mechanism and cooperative inter-cell support. The proposed approach and results based on the hybrid FSO/RF systems for green Metrozones are collectively reported in [B1], [C1] and [C2].

1.5. Research Outcome

Book Chapter

[B1] I. E. Lee, Z. Ghassemlooy, W. P. Ng, and M. A. Khalighi, "Green-Inspired Hybrid Base Transceiver Station Architecture with Joint FSO/RF Wireless Backhauling and Basic Access Signalling for Next Generation Metrozones", in *Green Networking and Communications: ICT for Sustainability*, Boca Raton, FL: Taylor & Francis Group, 2014.

Journals

[J1] I. E. Lee, Z. Ghassemlooy, W. P. Ng, and M. A. Khalighi, "Joint optimization of a partially coherent Gaussian beam for free-space optical communication over turbulent channels with pointing errors", *Opt. Lett.*, vol. 38, no. 3, pp. 350-352, Feb. 2013.

[J2] I. E. Lee, Z. Ghassemlooy, W. P. Ng, and M. A. Khalighi, "Reducing pointing errors in free space optical links with a partially coherent Gaussian beam", *IEEE Photon. Technol. Lett.*, under review.

[J3] I. E. Lee, Z. Ghassemlooy, W. P. Ng, M. A. Khalighi, and S. K. Liaw, "Effects of aperture averaging and beam width on a partially coherent Gaussian beam over free space optical links with pointing errors", *J. Lightw. Technol.*, under review.

[J4] I. E. Lee, Z. Ghassemlooy, and W. P. Ng, "Characterization of the aperture-averaging effect for Gaussian beam waves in free space optical links under controlled turbulence condition", *J. Lightw. Technol.*, to be submitted.

[J5] I. E. Lee, Z. Ghassemlooy, and W. P. Ng, "Experimental demonstration of the effects of aperture-averaging and beam width on a Gaussian laser beam over free space optical links under controlled turbulence conditions", *Opt. Lett.*, to be submitted.

Conferences

[C1] I. E. Lee, Z. Ghassemlooy, W. P. Ng, and S. Rajbhandari, "Fundamental analysis of hybrid free space optical and radio frequency communication systems", in *Proc. 12th Annual Post Graduate Symposium on the Convergence of Telecommunications, Networking and Broadcasting (PGNet 2011)*, pp. 281-285, Jun. 2011.

[C2] I. E. Lee, Z. Ghassemlooy, W. P. Ng, and M. A. Khalighi, "Green-inspired hybrid FSO/RF wireless backhauling and basic access signalling for next generation Metrozones", in *Proc. 2nd International Symposium on Environment-Friendly Energies and Applications (EFEA 2012)*, pp. 230-236, Jun. 2012.

[C3] I. E. Lee, Z. Ghassemlooy, and W. P. Ng, "Effects of aperture averaging and beam width on Gaussian free space optical links in the presence of atmospheric

turbulence and pointing error", in *Proc. 14th International Conference on Transparent Optical Networks (ICTON 2012)*, pp. 1-4, Jul. 2012.

[C4] I. E. Lee, Z. Ghassemlooy, W. P. Ng, and M. Uysal, "Performance analysis of free space optical links over turbulence and misalignment induced fading channels", in *Proc. 8th International Symposium on Communication Systems, Networks and Digital Signal Processing (CSNDSP 2012)*, pp. 1-6, Jul. 2012.

[C5] I. E. Lee, Z. Ghassemlooy, W. P. Ng, M. A. Khalighi, and M. Uysal, "Capacity analysis of free space optical links for a partially coherent Gaussian beam over a turbulent channel with pointing errors", in *Proc. 18th European Conference on Networks and Optical Communications (NOC 2013)*, pp. 281-286, Jul. 2013.

[C6] I. E. Lee, Z. Ghassemlooy, and W. P. Ng, "Experimental demonstration of the effects of aperture averaging under controlled turbulence condition", presented at *the 5th EU COST Action IC1101 Management Committee meeting co-located with the 2nd International Workshop on Optical Wireless Communications (IWOW 2013)*, Newcastle Upon Tyne, United Kingdom, Oct. 23, 2013.

1.6. Organization of the Thesis

This thesis mainly focuses on the performance analysis and optimization of horizontal-path FSO communications for long-distance terrestrial applications (in excess of 5 km); in which the relevant background information, key contributions and results, and in-depth discussions on the notable findings derived from the proposed work are presented and organized as follows:

The present chapter introduces the terrestrial FSO communications as a viable technology option, particularly in complementing the existing wireless RF solutions; in which the technical advantages and major limitations of the FSO systems are highlighted accordingly here. Taking into account the main challenges and open research issues pertaining to the system under study addressed in Section 1.2, the aims and objectives of the proposed research study are outlined in Section 1.3. Correspondingly, the original contributions and outcomes of this research project are presented in Section 1.4 and Section 1.5, respectively.

In Chapter 2, a comprehensive review and discussion pertaining to the key aspects of FSO technology are presented, which include: (1) the link built-up and operating principles of the proposed system model based upon the single-input single-output (SISO) horizontal-path FSO communication links for long-distance terrestrial applications; (2) the relevant components encompassing the optical transmitter and receiver; and (3) the important characteristics and modelling of the atmospheric channel. In particular, the widely adopted optical sources are extensively reviewed and compared. The Gaussian-Schell beam model is introduced and applied in the optical wave propagation analysis of a spatially partially coherent Gaussian laser beam, in order to characterize the propagation properties of the optical laser beam, under the influence of optical turbulence in the atmosphere. Moreover, the FSO communication channel comprising the atmospheric loss, optical turbulence-induced beam wander and scintillation effects and misalignment-induced PEs are explained in detail, with particular emphasis on the occurrence, characteristics, resulting impacts and modelling of the respective phenomena. These channel components are collectively described by the combined channel fading model, which is thoroughly examined and taken into account in the theoretical analysis and simulation studies of this research project. Furthermore, the common types of photodetectors used almost

exclusively for FSO applications are reviewed and compared, and the total noise contributions to the receiver front-end are discussed here. The effects of the aperture-averaging phenomenon in mitigating the random temporal fluctuations in the optical intensity of the laser beam through the intentional utilization of enlarged receiver apertures in direct detection systems are explicitly described here.

Next, Chapter 3 investigates the performance of partially coherent FSO communication links from the information theory perspective; in which the relevant performance metrics comprising the BER, the probability of outage, and the average capacity for both cases of known and unknown CSI at the receiver are extensively reviewed. Taking into account the influence of different operating conditions and important link design criteria, the outage analysis is performed and notable findings are depicted here; demonstrating the necessity of optimization methods to minimize the FSO link outages under changing atmospheric channel effects. The effects of aperture-averaging on the average channel capacity of FSO links employing spatially partially coherent Gaussian laser beams are reported for the first time; showing that an improvement in the FSO channel capacity can be achieved with the introduction of an enlarged receiver aperture, albeit without knowledge of the channel state conditions. Further simulation studies are carried out to examine the impacts of numerous link design criteria on the alteration of the PCB characteristics, which in turn reveal that beam width optimization is a feasible approach in promoting capacity enhancement for long-distance horizontal FSO communication links.

In Chapter 4, joint investigation of the effects of a spatially partially coherent Gaussian beam and aperture averaging is presented from the information theory perspective; demonstrating the distinctive advantages of introducing an enlarged receiver

aperture, and the interest of optimizing the beam width to maximize the average capacity. A theoretical beam width optimization model is proposed, which takes advantage of a simple mathematical solution to determine the optimum beam width; and hence, several new and appealing observations are discovered and reported here. Furthermore, a joint beam width and spatial coherence length optimization technique is proposed to maximize the average channel capacity in partially coherent FSO communication links, while taking into account the aperture-averaging effect. In particular, an optimization metric is developed to examine the characteristics of the optimum beam divergence, whereby it is shown that both the beam width and spatial coherence length of the Gaussian laser beam must be adjusted accordingly to optimize the beam divergence by a factor of the beam spreading gain.

Then, Chapter 5 presents the joint investigation and experimental demonstration of the effects of aperture averaging and beam width on the FSO link, under laboratory-controlled atmospheric turbulence conditions; in which the experiment setup, data acquisition and post-analysis processes are explained in detail here. Taking into account a variety of transmitter beam radius, turbulent channel conditions and receiver aperture dimensions, the aperture-averaging effect is examined and characterized through the probability density distributions of the received optical signal; which are then compared with respect to the theoretical lognormal and gamma-gamma turbulence models through a series of GOF tests. Subsequent analysis are performed to study the relationship between the aperture-averaging factor and point-received scintillation index, which can be resembled by a first-order linear regression model with good accuracy, as validated through the GOF tests; and the coefficients of the model are determined through curve fitting technique. A comparison study of the measured Q-factor between an aperture-averaged optical receiver and its corresponding finite point receiver is carried out,

demonstrating that performance enhancement of manifold gain can be achieved with increasing scaled aperture size.

In Chapter 6, a point-to-point hybrid FSO/RF communication system is conceptually described and modeled as a system architecture having a pair of independent, non-ergodic channels with random states, in which the information signal is transmitted through the parallel fluctuating channels. The viability of deploying the media diversity technique is investigated through a case study for next generation Metrozones in wireless macro-cellular networks, in which a new H-BTS system architecture is proposed for the green Metrozones. The hybrid FSO/RF system is integrated at the macro-cellular tier, to enable high-capacity, power-efficient wireless backhauling. A resource prioritization mechanism is designed, to maintain good control and optimal on-demand resource allocation, and to establish sustainable backhaul link availability via essential switching between the FSO and RF sub-systems. Next, a BAS scheme is introduced, to necessitate the discovery, registration and monitoring of active M-APs. The proposed BAS scheme enables the SWoD mechanism and the cooperative inter-cell support. Furthermore, feasibility studies are performed to examine the time-varying characteristics of the BTS daily traffic profile, and to evaluate the outage performance of the proposed hybrid FSO/RF systems under different weather conditions; thus revealing the importance of adaptation and optimization at the link- and system-level for Metrozones deployment, due to the occurrence of numerous time-varying factors in real networks.

Finally, Chapter 7 presents the key concluding remarks and recommendations and directions for future research.

CHAPTER 2

An Overview of Free-Space Optical Communications

2.1. Introduction

The introduction of the first working *L*ight *A*mplification by *S*timulated *E*mission of *R*adiation device (widely known for its acronym *LASER*) in 1960, has spurred a plethora of research efforts to discover new and more advanced applications involving this light-emitting device. In particular, it was suggested that lasers be used to extend RF atmospheric communications and radar techniques to the optical-frequency band, which in turn marked the humble beginnings of terrestrial FSO communications, as evident by the initial flurry of activities and FSO demonstrations in the early 1960s [86]. With the rapid development and maturity of optoelectronic devices, the FSO technology is now capable of delivering up to 2.5 Gbps of data, voice and video communications through the air, and enabling optical connectivity without the need of fibre-optic cable [11, 87]. Driven by the

ever-increasing demand for high-data-rate connectivity in face of new and emerging applications requiring more sophisticated services, network operators are steered towards deploying fibre-optic backbone in local area networks (LANs), metropolitan area networks (MANs) and wide area networks (WANs). While classical RF bandwidth has approached its limitation and cannot fully utilize the high bandwidth offered by the fibre-optic backbone, FSO communications presents a viable line-of-sight (LOS), high-speed and secure wireless technology that can facilitate the realization of next-generation carrier-grade high-reliability backbone and last-mile network access, thus overcoming the capacity challenges in an inexpensive and timely manner [83].

To substantiate the design, analysis and optimization of FSO communication systems for long-distance terrestrial applications, this chapter presents an extensive review and discussion on the key aspects of the FSO technology, which include:

(1) The link built-up based upon the SISO horizontal-path FSO communication links (in Section 2.2);

(2) The widely adopted optical sources (in Section 2.3.1) and their implications on eye safety (in Section 2.3.2), and the Gaussian-beam wave model (in Section 2.3.3) in characterizing the propagation properties of the optical laser beam in free-space;

(3) The important characteristics and modelling of the atmospheric propagation channel effects encompassing the atmospheric loss (in Section 2.4.1), optical turbulence-induced beam wander and scintillation (in Section 2.4.2), and misalignment-induced PEs (in Section 2.4.3), which are collectively described by the combined channel fading model (in Section 2.4.4); and

(4) The common types of photodetectors (in Section 2.5.1) and their respective noise contributions to the optical receiver front-end (in Section 2.5.2), and the relevant analytical model in describing the aperture-averaging phenomenon (in Section 2.5.3).

2.2. System Model

Figure 2.1 illustrates the block diagram of a SISO horizontal FSO communication link, employing intensity modulation with direct detection (IM/DD) and the non-return-to-zero on-off keying (NRZ-OOK) technique. In principle, the information-bearing electrical signals are modulated onto the instantaneous intensity of a collimated Gaussian-beam wave operating in the lowest-order transverse electromagnetic (TEM_{00}) mode [88, 89], and then goes through a phase diffuser [90, 91]. The latter alters the divergence of the optical beam while retaining its beamlike (i.e., highly directional) properties [11, 92]. Next, the PCB propagates along a horizontal path through a turbulent channel with additive white Gaussian noise (AWGN), in the presence of beam extinction and PEs, in which the turbulence is assumed to be uniform across the link [6]. At the receiving-end, the optical signals are collected by a finite Gaussian lens [11, 24] before being focused onto a photodetector, which in turn converts the received optical intensities into a resulting photocurrent.

The received signal y_κ can be described by the conventional channel model [29, 34]:

$$y_\kappa = h\gamma x_\kappa + n_o \; ; \tag{2.1}$$

where h is the channel state, γ is the detector responsivity (in A/W), $x_\kappa \in \{0, 2P_{\mathrm{FSO}}\}$ is the optical power of the transmitted signal which corresponds to the message signal m_κ taking values 0 or 1, P_{FSO} is the average transmitted optical power, and n_o is signal-independent AWGN with zero mean and variance σ_n^2. The noise n_o arises from various sources, such as

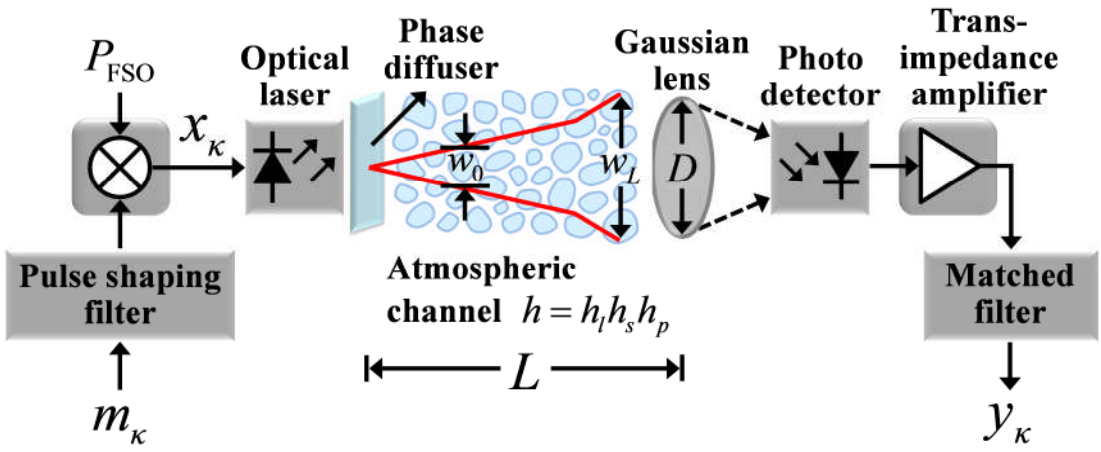

Figure 2.1: Block diagram of a single-input single-output horizontal FSO communication link.

shot noise caused by the signal itself and/or ambient light, dark current noise, and electrical thermal noise [6]. For a slow-fading channel with OOK signalling, the received electrical signal-to-noise ratio (SNR) is defined as [24, 93]:

$$SNR(h) = \frac{2P_{\mathrm{FSO}}^2 \gamma^2 h^2}{\sigma_n^2} \; ; \tag{2.2}$$

and is a fluctuating term (i.e., an instantaneous value) due to the influence of h, which is chosen from the random ensemble according to the distribution $f_h(h)$.

The channel state h models the optical intensity fluctuations resulting from atmospheric loss, and turbulence- and misalignment-induced channel fading, which can be described as [24, 94]:

$$h = h_l h_s h_p \; ; \tag{2.3}$$

where h_l, h_s and h_p denote the attenuation due to beam extinction arising from both scattering and absorption, scintillation effects, and geometric spread and PEs, respectively. The attenuation h_l is a deterministic component which exhibits no randomness in its behaviour, thus acting as a fixed scaling factor for a long period of time (i.e., on the order

of hours) that stands in contrast to the bit intervals in ranges of nanoseconds or less [29]. On the other hand, both h_s and h_p are time-variant factors, exhibiting variations in the fading channel on the order of milliseconds, in which their stochastic behaviour are described by their respective distributions [25, 65, 95].

2.3. Transmitter

2.3.1. Optical Sources

Semiconductor light-emitting diodes (LEDs) and laser diodes (LDs) are widely employed as the optical sources for wireless optical communications, in order to convert an electrical input signal into the corresponding optical signal. The main advantages of these semiconductor optical sources include: (1) compact size; (2) high efficiency; (3) good reliability; (4) desirable wavelength and linewidth; (5) low forward voltage and drive current; (6) high modulation bandwidth, implying the possibility of direct modulation at relatively high frequencies; and (7) excellent brightness in the visible wavelengths, with the option of emission at a single wavelength or range of wavelengths [23, 96].

In principle, solid-state light-emitting devices are p-n junction diodes operating under the forward-biased condition, which produce an optical intensity approximately linearly related to the drive current through the recombination of a large proportion of the injected minority carriers by giving up their energy as emitted photons. Direct bandgap semiconductor materials (typically of compound group III and group V elements) are commonly used in the construction of light-emitting devices, whereby the extrema of the conduction and valence bands coincide at the same wave vector value, as depicted in Figure 2.2(a) [97]. The electrons with the lowest allowed energy in the conduction band

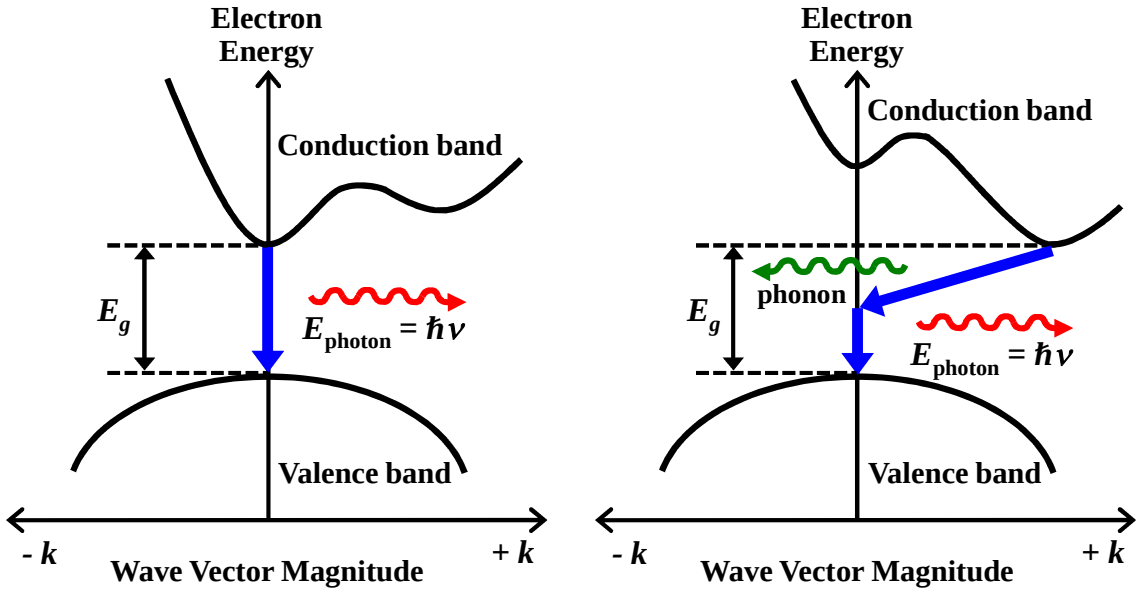

Figure 2.2: One dimensional variation of band edges as a function of wave number k, which illustrates (a) electron recombination and the associated photon emission for direct bandgap semiconductor materials; and (b) electron recombination for indirect bandgap semiconductor materials involving the transfer of phonon particles [98, 105].

have very similar crystal momentum (resembled by the wave vector) as the electrons at the highest energy level of the valence band; thereby allowing a high probability of direct band-to-band recombination events to take place, resulting in photon emission with relatively high internal quantum efficiency (i.e., the ratio of the number of photons generated to the number of carriers crossing the junction) [98]. Majority of the photons emitted through the recombination process have energy $E_{photon} = E_g = \hbar\nu$, which can be expressed in terms of the wavelength of the emitted photon λ (in nm) through the relation:

$$\lambda = \frac{1240}{E_g} \; ; \tag{2.4}$$

where E_g is the bandgap energy of the material (in eV), $\hbar$ is Planck's constant, and ν is the photon frequency (in Hz).

For indirect bandgap semiconductor materials (such as silicon (Si) and germanium (Ge)), the extrema of the conduction and valence bands do not coincide at the same wave vector value (see Figure 2.2(b)), implying that the electrons at the lowest energy level of the conduction band has a rather different momentum compared to the electrons with the highest energy in the valence band. As a result, the occurrence of recombination events would rely upon crystalline lattice interaction (modelled as the transfer of phonon particles) to absorb the surplus momentum, which in turn enables the carriers to cross the band gap. When recombination does take place, a significant portion of the energy generated from the recombination process is dissipated as heat due to lattice vibrations, leaving the remaining transition energy for photon emission. Therefore, indirect bandgap semiconductor materials produce highly inefficient light-emitting devices with poor quantum efficiency [98].

2.3.1.1. Light-Emitting Diodes

As compound III-V semiconductor materials are desirable due to their higher quantum efficiency, the construction of LEDs invariably takes the form of a five-layer double heterostructure, which is shown schematically in Figure 2.3(a). The two outermost layers are essentially contact layers, with one being the substrate on which the other layers are grown epitaxially; and the middle three layers are collectively known as double heterostructure, which is formed by depositing two wide bandgap materials (confinement layers) on either side of a lower bandgap material (active layer) and doping the materials appropriately to give diode action [97]. Under forward-biased conditions, the band diagram forms a potential well in the low bandgap material (see Figure 2.3(b)), whereby carriers are injected and confined within this active region for recombination events to take place; thus resulting in spontaneous emission, a phenomenon referred to as electroluminescence [96].

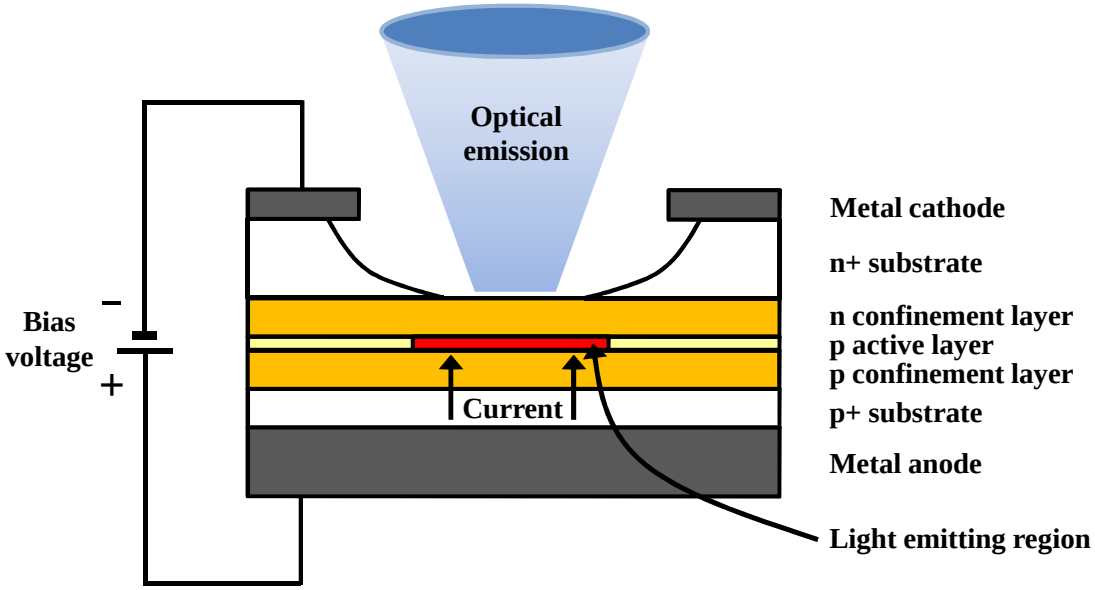

(a)

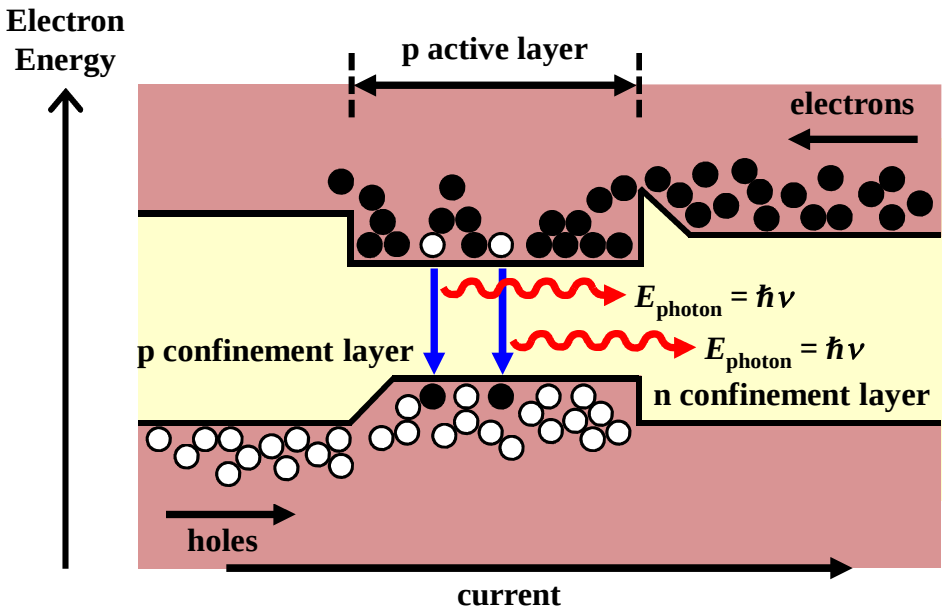

(b)

Figure 2.3: (a) Schematic representation of an etched-well, surface-emitting, five-layer double heterostructure light-emitting device; and (b) energy-band diagram showing the active region, and the electron and hole barriers which confine the charge carriers within the active region under forward-biased condition [98, 104, 105].

In this process, the recombination of injected carriers occurs in a random manner, causing the photons to be generated incoherently (i.e., the phase relationship between emitted photons is random in time). The advantages of using a double heterostructure stem from

the fact that electrons and holes are well-defined to the active layer, producing a higher and more uniform concentration of carriers, such that a much higher recombination rate can be established within the active layer for a given injection current density, thereby improving the frequency response of the device. In addition, the losses due to absorption of radiation can be minimized in the active layer, since the adjoining regions have a larger bandgap than the active region, thus making the adjacent layers more transparent.

The thickness of the active layer is a critical parameter in the design and construction of LEDs, due to the inherent trade-off between the source linearity and frequency response of the device. The increase in thickness results in a wider range of input currents over which the behaviour is linear, while reducing the confinement of carriers and hence limiting the frequency response of the device. Furthermore, device self-heating remains as another key concern affecting the performance of LEDs, whereby the drive current flowing through the device produces heat, mainly due to the resistance of the ohmic contacts and inefficiency of the device. The increase in temperature causes a large majority of injected carriers to gain sufficient energy for surmounting the barrier. Correspondingly, this reduces the confinement of carriers in the active region, and degrades the internal quantum efficiency of the device, as evident from the non-linear drop in the output intensity with respect to higher input drive current in Figure 2.4. Prolonged operation under high temperature environments reduces the output optical intensity at a given current, eventually leading to device failure [99, 100]. The impact of self-heating on linearity can be improved through the introduction of pulsed operation and compensation circuitry [101].

2.3.1.2. Laser Diodes

Semiconductor LDs are more recent technology that evolved from the underlying LED fabrication techniques, which can be created by placing an LED in an optically

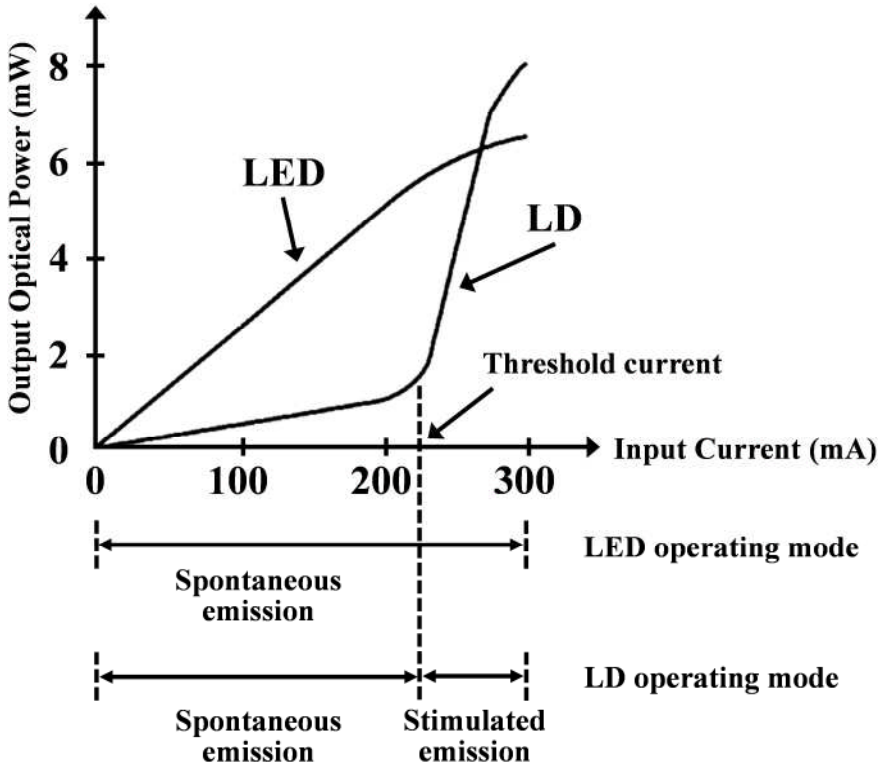

Figure 2.4: Relationship between the optical output power and input drive current for LEDs and LDs. It is shown that the LDs produce spontaneous LED-type emissions, when operated well below the lasing threshold [100].

resonant cavity. These laser devices still depend on the transition of carriers over the bandgap to produce radiant photons, but with modifications to the device structure, in order to enable the efficient production of coherent light over a narrow optical bandwidth. Coherent output light is produced when the emitted photons have the same energy, frequency and phase as the incident photons [102, 103]. In addition to the aforementioned spontaneous emission, the LDs must undergo a second form of photon generation process known as stimulated emission, whereby a large threshold (forward) current is required for population inversion to take place. In this process, an excess of electrons is maintained in the active region through the confinement of carriers and carrier pumping of the forward biased junction, such that the product of the number of electrons in the conduction band and number of holes in the valence band is larger than the product of the number of

electrons in the valence band and the number of holes (empty states) in the conduction band. For LDs operating well below the threshold level of the input drive current, the radiation of photons is typically dominated by spontaneous emission, thus causing the device to behave essentially as a low intensity LED (see Figure 2.4). Upon surpassing the threshold current, the LDs exhibit an approximately linear variation of output optical intensity in terms of input drive current and a high optical efficiency, as indicated by a sharp increase in the slope within the stimulated emission region of the characteristics curve in Figure 2.4. Therefore, laser action encompasses three key transition processes, which include photon absorption, spontaneous emission and stimulated emission, as illustrated in Figure 2.5 [97, 104].

To achieve a sustainable lasing process, the double heterostructure of semiconductor lasers are modified to provide optical feedback, which occurs essentially by placing a reflective surface to send generated photons back through the active region to re-initiate

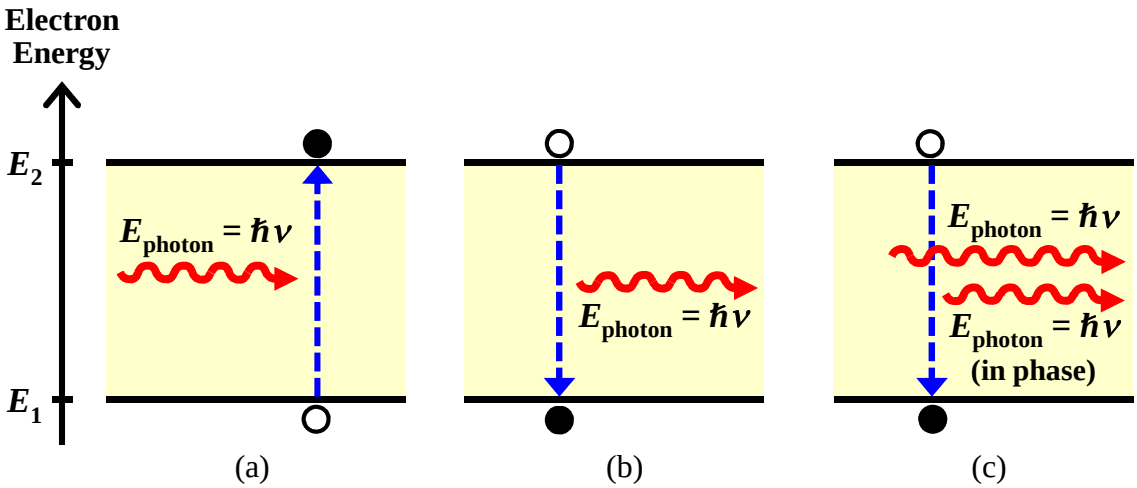

Figure 2.5: Two-energy-level diagrams depicting the three key transition processes involved in laser action, which include: (a) absorption, (b) spontaneous emission, and (c) stimulated emission; where E_1 and E_2 denote the ground- and excited-state energies, respectively. The open circle represents the initial state of the electron, and the filled circle indicates the final state. The incident photons are shown on the left of each diagram, whereas the emitted photons are presented on the right [98, 105].

the recombination process, thereby converting an amplifier into an oscillator. The optical feedback operation is analogous to microwave resonators, which confine electromagnetic energy by high conductivity metal; and can be made possible using various techniques, in which the more common approaches include the Fabry-Perot and distributed feedback (DFB) methods.

2.3.1.3. Comparison between Optical Sources

The main advantage of LDs over LEDs is in the speed of operation, which is a key criterion affecting the maximum achievable bit rate of wireless optical systems. In the event of stimulated emission, the recombination time constant is approximately one to two orders of magnitude shorter compared to spontaneous recombination [105]; thus allowing the LDs to operate at pulse rates up to tens of gigahertz, while the modulation bandwidth of LEDs are limited to a few hundred megahertz. Therefore, the LDs present a more viable alternative for high data rate applications, due to the inherently higher modulation bandwidth of such optical sources for supporting high communication speeds. In addition, the LDs have higher electrical-to-optical conversion efficiency, typically ranging between 30 % and 70 %; whereas the efficiencies of LEDs are limited between 10 % and 20 % [106]. The necessity of rendering laser output eye safe presents an important design limitation for wireless optical applications involving the use of LDs, due to the coherency and high intensity of the emitted radiation. Correspondingly, the output light must be diffused appropriately through the use of filters, in order to reduce the power of the laser device, while inadvertently increasing the system cost. Table 2.1 summarizes and compares the technical properties and features of semiconductor LDs and LEDs for wireless optical applications [23, 103].

Table 2.1: Comparison of the technical properties and features between an LED and a semiconductor LD [23, 104].

Characteristics	LED	LD
Optical output power	Low power	High power
Optical spectral width	25 – 100 nm	0.01 – 5 nm
Modulation bandwidth	Tens of kHz to hundreds of MHz	Tens of kHz to tens of GHz
Electrical-to-optical conversion efficiency	10 – 20 %	30 – 70 %
Directionality	Beam is broader and spreading	Beam is directional and highly collimated
Coherence	Non-coherent	Coherent
Eye safety	Considered eye safe	Must be rendered eye safe
Reliability	High	Moderate
Drive and control circuitry	Simple to use and control	Threshold and temperature compensation circuitry
Temperature dependence	Low	High
Cost	Low	Moderate to high
Harmonic distortions	High	Low
Receiving optical filter	Wide (higher noise floor)	Narrow (lower noise floor)

The design of terrestrial FSO communication systems must take into account the atmospheric propagation effects, due to various meteorological conditions (such as rain, fog and snow) and high levels of atmospheric turbulence across the horizontal path, which affect the system performance in different degrees. In addition, the transmission of optical signal in free-space over longer link distances under direct sun's contribution would require careful selection of optical source. The superior characteristics of the LDs encompassing high modulation bandwidth (for achieving higher data rate), efficient electrical-to-optical conversion, extremely narrow spectral width and high optical launch power capability, make these devices desirable for long-distance outdoor directed-LOS FSO links. The choice of optical wavelength for the LDs is dependent on a variety of

factors, which include: atmospheric conditions and the resulting channel characteristics, optical background noise, laser technology, photodetectors, and optical filters [23].

2.3.2. Eye Safety

From a theoretical perspective, deliberately increasing the launch power of an optical source can overcome some of the data transmission limitations suffered by the optical wireless technology, such as compensating for the high attenuation of the transmitted optical signal when propagating through air, increasing the link range of the system, and improving the SNR and maximum achievable bit rate [10, 107]. While high optical launch power is desirable to approach the promised bit rates, direct exposure of such intense optical radiation can impose hazardous impact on human safety, potentially causing harm to the eye and skin. The peril level of the optical emitter is determined by various factors, which include: source type, signal wavelength, radiation power, flux density (i.e., the power per unit area), and exposure time (i.e., the length of time that the eye is exposed to the source).

The International Electrotechnical Commission (IEC) standard has been widely adopted in classifying the use of lasers based upon their respective main exposure limits into different hazards categories, as listed and succinctly described in Table 2.2. Table 2.3 presents the allowable limits for the average transmitted optical power for the different IEC safety classes (listed in Table 2.2) at four different wavelengths [108]; which is computed based on the assumption of a point source, with optical radiation emitting from a small aperture and diverging slowly as is the case in LDs. With reference to the observed trend for Class 1 operation, it is apparent that the allowable average optical power increases with respect to larger optical wavelength (i.e., a 1550-nm laser source can produce at least 20 times more optical power than a 880-nm emitter); thereby suggesting that the far-infrared

wavelengths are best suited to wireless optical links, due to their considerably higher optical power budget for Class 1 operation.

Class 1 laser products are inherently safe and most desirable for wireless optical application, since optical emissions from these sources are safe under all circumstances; and hence, no warning labels or special safety precautions are required. Class 1M (an extension to Class 1) laser devices refer to sources that are safe under normal operation,

Table 2.2: Interpretation of IEC safety classification for optical sources [23, 104].

Class	Interpretation
Class 1	Low-power devices emitting radiation at a wavelength in the band 302.5 – 4000 nm. The optical sources are intrinsically safe under all reasonably foreseeable conditions of operation, including the use of optical instruments (such as monocular, binoculars, microscope, etc.).
Class 1M	An extension of Class 1 with the possibility of danger when viewed with optical instruments (such as binoculars, telescope, etc.). Class 1M sources produce large-diameter (i.e., divergent) optical beams.
Class 2	This safety class is applicable to low-power visible light sources only, with wavelengths ranging between 400 nm and 700 nm. Eye protection is afforded by aversion responses including blink reflex, which provides effective protection under all reasonably foreseeable usage conditions, including the use of optical instruments (such as monocular, binoculars, microscope, etc.).
Class 2M	An extension of Class 2 with the possibility of danger when viewed with optical instruments (such as binoculars, telescope, etc.)
Class 3A	Average-power devices emitting radiation at a wavelength in the band 302.5 – 4000 nm. The optical sources are safe for viewing with unaided eye. Direct intra-beam viewing with optical aids may be hazardous.
Class 3B	Low-power devices emitting radiation at a wavelength in the band 302.5 – 4000 nm. Direct intra-beam viewing is always hazardous. Viewing diffuse reflections is normally safe.
Class 4	Laser emissions with high optical power levels, which may impose hazardous impact on the eye and skin and possibility of fire risk. The laser devices must be equipped with a key switch and safety interlock. Medical checks and specific training are required prior to the installation or maintenance of laser equipments.

Table 2.3: Safety classification of point sources in accordance to the allowable average optical power output for a variety of optical wavelengths [104].

Safety Class	**650 nm visible**	**880 nm infrared**	**1310 nm infrared**	**1550 nm infrared**
Class 1	< 0.2 mW	< 0.5 mW	< 8.8 mW	< 10 mW
Class 2	0.2 – 1 mW	Not applicable	Not applicable	Not applicable
Class 3A	1 – 5 mW	0.5 – 2.5 mW	8.8 – 45 mW	10 – 50 mW
Class 3B	5 – 500 mW	2.5 – 500 mW	45 – 500 mW	50 – 500 Mw

but may inflict eye hazards when viewed with optical instruments [109]. Class 2 applies to optical radiation spanning the visible spectrum between 400 nm and 700 nm, and can be operated safely with eye protection supported by blink or aversion responses (i.e., the natural ability of the eye to protect itself by blinking, with typical response time of approximately 250 ms). This safety classification is only valid for visible-light sources, mainly because the blink response of the eye does not operate with energy in the near-infrared region of the electromagnetic spectrum [110]. Class 2M is a new category included in the new version of the standard, which refers to lasers sources that are safe under the operation of blink or aversion response and without the use of optical instruments. Class 3 (further classified into Class 3A and Class 3B) laser products can operate at a much higher power level, typically ranging between 1 mW and 0.5 W; thereby potentially causing damage to the human eye even when viewing the specular reflections of optical emissions. For applications involving the use of Class 3 lasers, it is important to wear the appropriate protective eyewear, as a measure to prevent eye hazards in the case of accidentally coming into contact with the (direct and/or reflected) beam paths. Outdoor point-to-point FSO systems generally use high-power lasers operating in the Class 3B band,

in order to achieve a good power budget for delivering high data rate transmission over moderate-to-long link distances; whereby safety can be maintained by locating optical terminals on rooftops, towers or high walls to prevent inadvertent human interruption [108]. When appropriate optics are employed to spread the laser radiation over a wider beam divergence angle, FSO systems operating in Class 3B mode can be reduced to a safer Class 1M. While divergent beams are advantageous in addressing eye safety issues, the author demonstrates (in Chapter 3 and Chapter 4) that laser sources with larger receiver beam size are capable of mitigating the turbulence-induced scintillations and PEs in terrestrial FSO systems.

2.3.3. Gaussian-Beam Wave

The propagation of optical beams in free-space can be described by the plane wave, spherical wave and Gaussian-beam wave models, in which the latter is most often preferred and introduced in optical wave propagation analysis. This is mainly because the simplified field models based upon the unbounded plane and spherical wave approximations are insufficient to characterize the propagation properties of the optical beam waves, particularly when focusing and diverging characteristics are important. The free-space propagation of a lowest-order Gaussian-beam wave (i.e., TEM_{00} wave) is considered, with properties defined as follow:

(1) The exit aperture of the transmitter is located in the plane $z = 0$;

(2) The intensity distribution of the optical laser beam in the z-plane is Gaussian with an effective beam radius (spot size) w_0 (in m), which represents the beam width at which the field amplitude falls to 1/e of its peak on the beam axis, as depicted in Figure 2.6; and

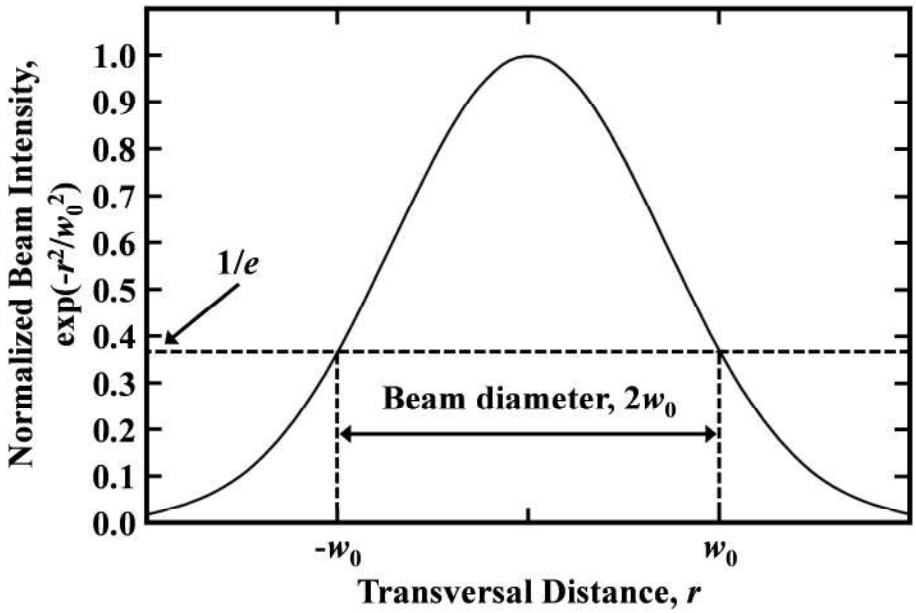

Figure 2.6: Optical intensity profile of a lowest-order Gaussian-beam wave showing the beam width (i.e., spot size) w_0 at which the field amplitude falls to 1/e of its peak on the beam axis [11, 115].

(3) The phase front radius of curvature F_0 (in m) is taken to be parabolic, in which the three possible scenarios of $F_0 = \infty$, $F_0 > 0$ and $F_0 < 0$ correspond to collimated, convergent and divergent beam forms, respectively (see Figure 2.7) [11].

At $z = 0$, the free-space electric field of the optical beam wave having unit amplitude and propagating predominantly along the *z*-axis is given by [89, 111]:

$$z = 0: \qquad U(r, 0) = \exp\left[-\left(\frac{1}{w_0^2} + \frac{jk}{2F_0}\right)r^2\right] = \exp\left(-\frac{1}{2}\alpha_0 k r^2\right); \qquad (2.5)$$

where $r = |\mathbf{r}|$ is the magnitude of the transversal distance from the beam centre line, $k = 2\pi/\lambda$ is the optical wave number with λ being the laser wavelength, $j = \sqrt{-1}$, and α_0 (in m^{-1}) is a complex parameter related to the transmitter beam width and phase front radius of curvature according to the relation:

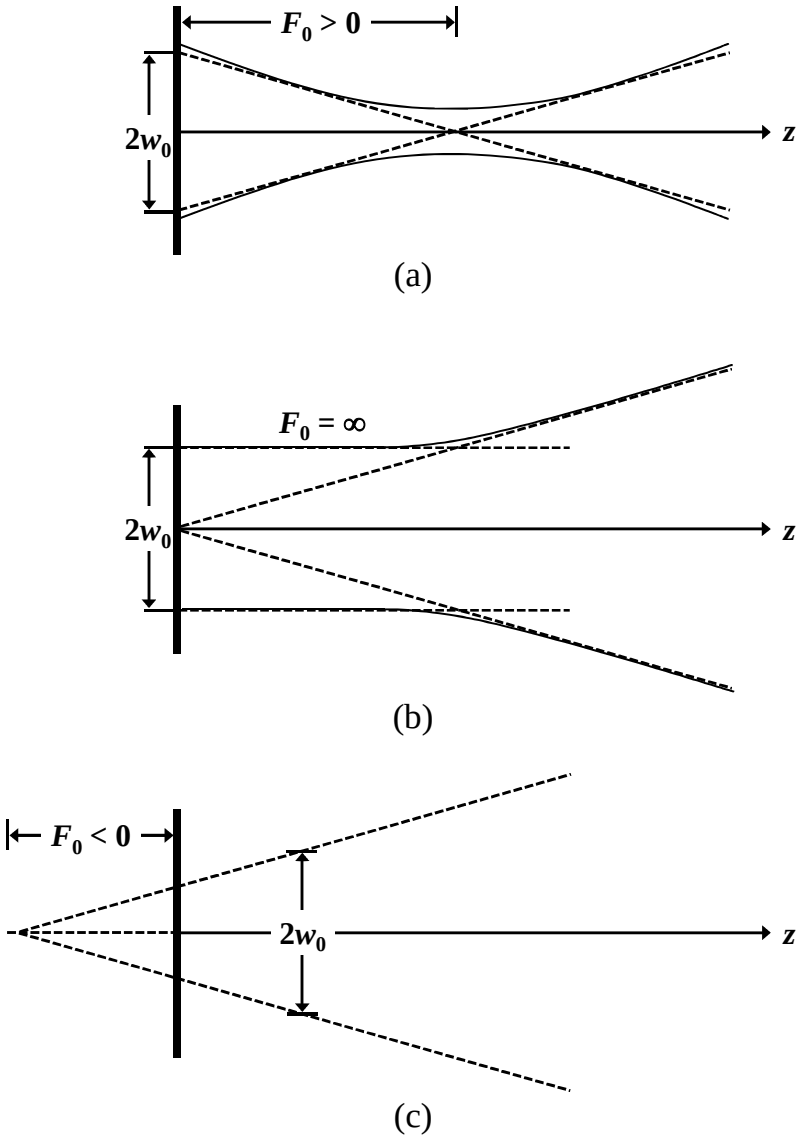

Figure 2.7: Lowest-order Gaussian-beam wave with an effective beam radius w_0 and phase front radius of curvature F_0 under three possible scenarios of (a) collimated ($F_0 = \infty$); (b) convergent ($F_0 > 0$); and (c) divergent ($F_0 < 0$) beams [11].

$$\alpha_0 = \frac{2}{kw_0^2} + j\frac{1}{F_0} \ . \tag{2.6}$$

After propagating through a distance L from the transmitter, the free-space optical field in the receiver plane at $z = L$ becomes [112]:

$$z = L: \qquad U(\rho, L) = \frac{\exp(jkL)}{\Theta_n + j\Lambda_n} \exp\left[-\left(\frac{1}{w_L^2} + \frac{jk}{2F_L}\right)\rho^2\right], \tag{2.7}$$

where the non-dimensional input (transmitter) beam parameters are given by [112, 113]:

$$\Theta_n = 1 - \frac{L}{F_0} \quad \text{and} \quad \Lambda_n = \frac{2L}{kw_0^2}\ . \tag{2.8}$$

The curvature parameter Θ_n characterizes the refractive (focusing) properties in terms of deviation of the wave-front curvature from the optimal focusing condition $F_0 = L$, whereas the Fresnel ratio Λ_n depicts the diffractive changes in the on-axis amplitude of the Gaussian beam. The beam width w_L and phase front radius of curvature F_L at the output (receiver) plane are expressed in terms of the normalized components (in (2.8)) as:

$$w_L = w_0\sqrt{\Theta_n^2 + \Lambda_n^2}\ , \text{ and} \tag{2.9}$$

$$F_L = \frac{L\left(\Theta_n^2 + \Lambda_n^2\right)}{\Theta_n(1 - \Theta_n) - \Lambda_n^2}\ , \text{ respectively.} \tag{2.10}$$

In the case of a collimated beam, the parameters w_L and F_L can be described as a function of L through the well-known expressions below [114]:

$$w_L = w_0\sqrt{1 + \frac{\lambda L}{\pi w_0^2}}\ , \text{ and} \tag{2.11}$$

$$F_L = L\sqrt{1 + \frac{\pi w_0^2}{\lambda L}}\ . \tag{2.12}$$

The irradiance or intensity of the optical wave is a function of the axial z and radial r distances, and can be found by taking the squared magnitude of the field. Correspondingly, the average intensity at the receiver is given by [11, 114]:

$$I(r, L) = |U(r, L)|^2 = I(0, L)\exp\left[\frac{-2r^2}{w_L^2}\right]; \quad (2.13)$$

where $I(0, L)$ resembles the on-axis irradiance with relation as follow:

$$I(0, L) = \frac{w_0^2}{w_L^2} = \frac{1}{\Theta_n^2 + \Lambda_n^2}\ . \quad (2.14)$$

2.4. The Free-Space Optical Communication Channel

2.4.1. Atmospheric Loss

Attenuation (or extinction) of the optical beam wave limits the intensity of a propagating optical laser beam, mainly due to the presence of a vast variety of particulate composition within the earth's atmosphere, which include: nitrogen (N_2), oxygen (O_2), argon (Ar), ozone (O_3), water (H_2O), carbon dioxide (CO_2), and other small particles generated by combustion, dust, debris and soil [107, 115, 116]. These atmospheric particles result in the adverse effects of light absorption by gaseous molecules, and Rayleigh and Mie scattering contributed by gaseous molecules or aerosol particles suspended in the air.

In particular, the absorption process involves the capturing of electromagnetic radiation by a particle, and conversion of the photon energy into the kinetic energy of the particle's molecules, thus implying that absorption is a mechanism occurring from the heating of the atmosphere. Atmospheric absorption is a strong function of wavelength, in which the absorption by O_2 and O_3 essentially eliminates propagation of radiation at wavelengths below 0.2 mm, whereas very little absorption is observed at the visible wavelength window (i.e., 400 nm to 700 nm).

The Rayleigh and Mie scattering phenomena significantly deteriorate electromagnetic waves in the visible and infrared wavelength bands, when the optical radiation propagates through air molecules, aerosols and particulate matters, such as fog, haze, smoke and dust. The occurrence of Rayleigh scattering (also known as molecular scattering) is mainly contributed by air molecules and haze particles, which are smaller in comparison to the wavelength λ of electromagnetic radiation (see Figure 2.8(a)); and hence, this scattering effect is negligible at wavelengths greater than ~3 μm, since the scattering coefficient varies in accordance to λ^{-4} (a relation known as the Rayleigh law). On the other hand, Mie scattering (or aerosol scattering) is caused by particles comparable in size to or greater than the radiation wavelength; in which this scattering effect is concentrated in the forward direction (as depicted in Figure 2.8(b)), and the losses decrease rapidly with increasing wavelength, eventually approaching the Rayleigh scattering case. Since the operating wavelengths of terrestrial FSO links (i.e., 785 nm, 850 nm and 1550 nm) are chosen to fall within the transmission windows of the atmospheric absorption spectra, the light absorption process does not have much contribution to the atmospheric loss [26, 109]. The scattering effects typically dominate the total attenuation coefficient, in which the type of scattering (i.e., Rayleigh/molecular or Mie/aerosol) is determined by the size of the atmospheric particulate with respect to the laser wavelength of operation, as described by the dimensionless size parameter α_m of the Mie theory [117]:

$$\alpha_m = \frac{2\pi r_p}{\lambda} , \tag{2.15}$$

where r_p denotes the radius of the particle.

The atmospheric loss (or transmittance) is considered as a fixed scaling factor over multiple fading states of the FSO channel; and results from the combined deterministic

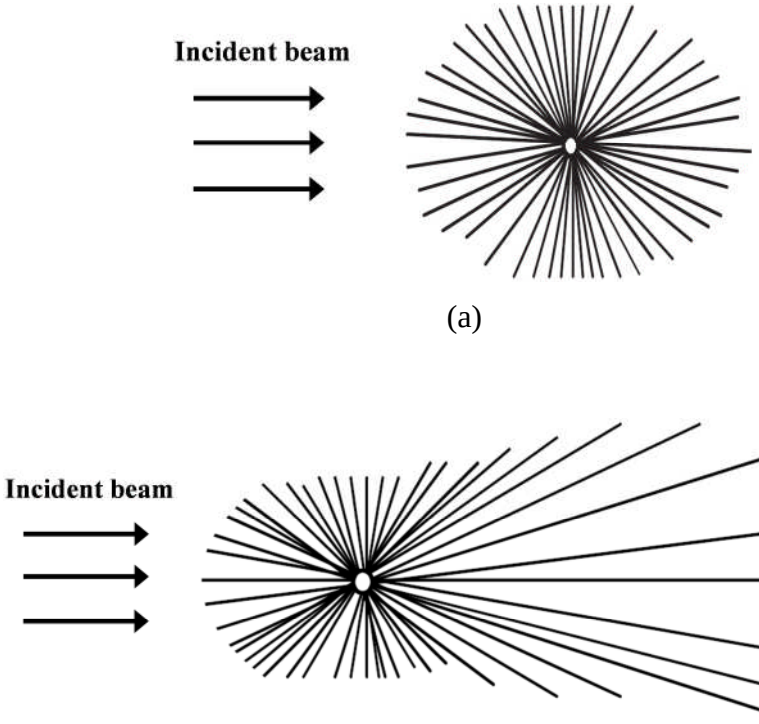

Figure 2.8: Distribution of the electromagnetic radiation resulting from (a) Rayleigh or molecular scattering; and (b) Mie or aerosol scattering [11, 118].

effects of absorption and scattering, which can be modelled by the exponential Beers-Lambert law [118]:

$$h_l = e^{-\sigma L}\,, \tag{2.16}$$

where σ denotes a wavelength- and weather-dependent attenuation coefficient, with typical values as follows: clear air = 0.1 (0.43 dB/km); haze = 1 (4.3 dB/km); and fog = 10 (43 dB/km). For clear and foggy weather conditions, the attenuation coefficient can be determined from the visibility data through Kim's model [26]:

$$\sigma = \frac{3.91}{V}\left(\frac{\lambda}{550}\right)^{-q_s}\,, \tag{2.17}$$

where V is the visibility (in km), λ is the laser wavelength (in nm), and q_s is a parameter related to the particle size distribution and visibility defined by:

$$q_s = \begin{cases} 1.6\,, & V > 50 \text{ km} & \text{(high visibility)} \\ 1.3\,, & 6 \text{ km} < V < 50 \text{ km} & \text{(average visibility)} \\ 0.16V + 0.34\,, & 1 \text{ km} < V < 6 \text{ km} & \text{(haze visibility)} \\ V - 0.5\,, & 0.5 \text{ km} < V < 1 \text{ km} & \text{(mist visibility)} \\ 0.585V^{1/3}\,, & V < 0.5 \text{ km} & \text{(fog visibility)}\,. \end{cases} \tag{2.18}$$

2.4.2. Optical Turbulence in the Atmosphere

Through multiple decades of extensive theoretical investigations [119-124], it is apparent that optical turbulence (i.e., random variations in the index of refraction) resulting from inhomogeneities in the temperature and pressure of the atmosphere contributes to the occurrence of various adverse channel effects, which include: (1) spreading of the optical laser beam beyond that due to pure diffraction (which reduces the spatial power density incident on the receiver); (2) random motion of the instantaneous beam centroid about the receiver (known as beam wander); (3) random fluctuations in the irradiance of the signal-carrying laser beam (termed as scintillations); (4) phase fluctuations; and (5) loss of spatial coherence. In principle, beam wander is primarily caused by turbulent eddies with scales sizes larger than the diameter of the optical beam, typically occurring near the transmitter; whereas the scintillation effect arises when the turbulence scale sizes are on the order of the first Fresnel zone. These turbulence-induced effects work in tandem to create random signal losses at the optical receiver; thereby degrading the error performance due to signal fading, and resulting in complete system annihilation under more severe channel conditions. The theoretical background, characteristics and analytical approach pertaining to the above-mentioned effects are introduced and discussed in detail here.

2.4.2.1. Beam Wander

In the presence of atmospheric turbulence, a finite optical laser beam is susceptible to random deflections when propagating through free-space, which aggravates the spreading of the optical beam due to large random inhomogeneities of the atmosphere with scale sizes bounded above by the outer scale L_0, thus causing the resultant beam to become highly skewed from Gaussian (see Figure 2.9(a)). This phenomenon is known as beam wander, which can be explained by the random displacement of the instantaneous beam centroid (i.e., point of maximum irradiance termed as hot spot) off the boresight, observed over short time periods in the receiver plane [125-129]. From a statistical point-of-view, the beam wander effect can be characterized by the variance of the hot spot displacement along an axis, or equivalently by the variance of the magnitude of the hot spot displacement.

Earlier studies [130] have shown that the principle of reciprocity can be applied to the performance of a telescope as measured by its effective coherence size in atmospheric turbulence, whether it is functioning as part of a transmitter or as part of a receiver. By invoking the reciprocity principle, beam wander at the receiver plane can be modelled as if it arises from a random tilt angle at the transmitter plane, in which the random movement of the short-term beam (i.e., instantaneous hot spot) depicted by the shaded circular regions in Figure 2.9(b) leads to the large outer circle over a long time period. The resultant beam width (observed at the receiver plane) is termed as the long-term spot size w_{LT}, which forms the basis for the variance of beam wander fluctuations, the square of which yields:

$$w_{\mathrm{LT}}^2 = w_L^2(1 + T_{\mathrm{Tot}}) = w_L^2\left(1 + 1.33\sigma_R^2\Lambda_L^{5/6}\right); \tag{2.19}$$

where Λ_L denotes the Fresnel ratio at the output plane, as defined by (2.46).

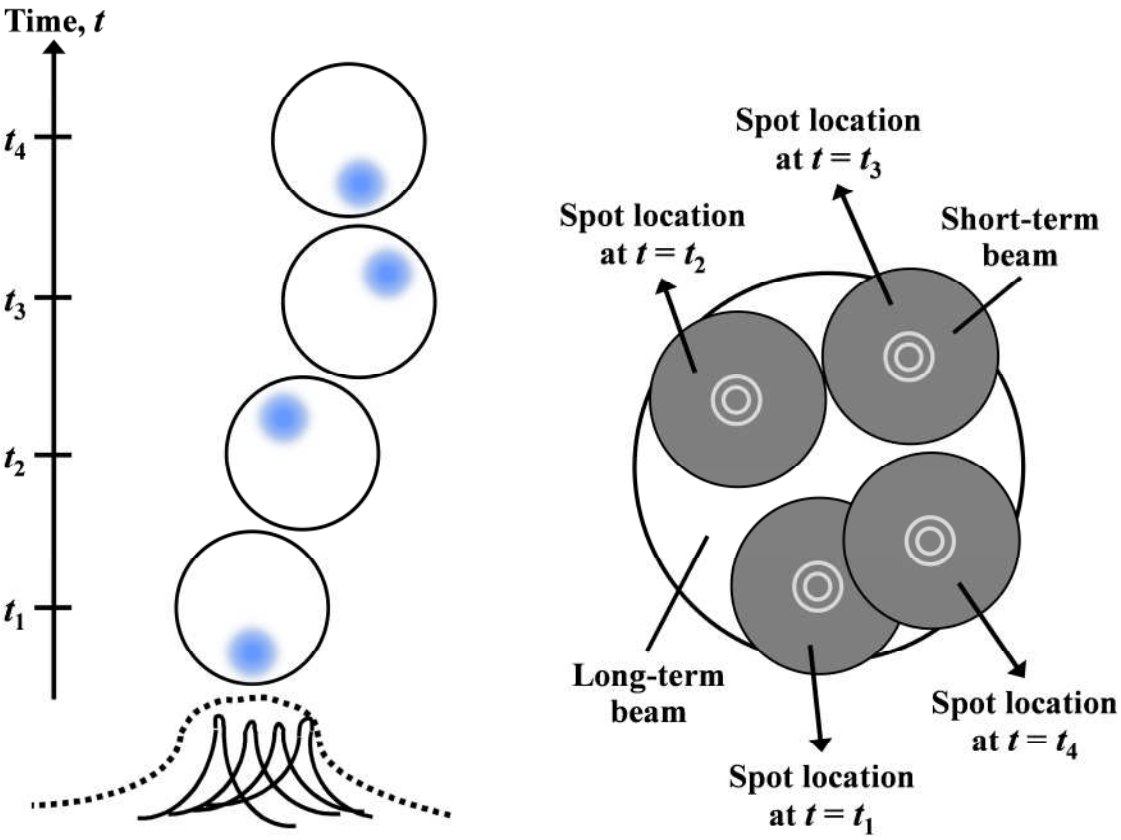

(a) (b)

Figure 2.9: (a) Random deflections of the optical laser beam due to the beam wander effect are observed by the movement of hot spot (i.e., instantaneous centre of maximum irradiance) within the beam, causing the resultant beam to become highly skewed from Gaussian; and (b) illustration of the long-term beam spot size resulting from the random motion of the short-term beam in the receiver plane with respect to time, as indicated by the shaded circles [11].

Based upon the concept of short- and long-term spot size, w_{LT}^2 can be expressed in the form:

$$w_{\mathrm{LT}}^2 = w_L^2 + w_L^2 T_{\mathrm{SS}} + w_L^2 T_{\mathrm{LS}} \; ; \tag{2.20}$$

where the term $T_{\mathrm{Tot}} = T_{\mathrm{SS}} + T_{\mathrm{LS}}$ can be partitioned into a sum of small-scale (T_{SS}) and large-scale (T_{LS}) contributions. It is apparent that the long-term spot size w_{LT} arises from the effects of pure diffraction spreading (as described by the first term w_L^2), and turbulent cells (or known as eddies) of all scale sizes due to random inhomogeneities of the atmosphere. Turbulent eddies with scale sizes smaller than the beam diameter produce

small-scale beam diffraction, as interpreted by the second term $w_L^2 T_{\mathrm{SS}}$; in which the combined diffractive effects of $w_L^2(1 + T_{\mathrm{SS}})$ (i.e., sum of the first and second term) is defined as "beam breathing". On the other hand, turbulent scale sizes larger than the beam diameter lead to refractive effects known as beam wander, which causes random displacement of the instantaneous centre of the incident optical beam in the receiver plane, as denoted by the final term $w_L^2 T_{\mathrm{LS}}$.

In accordance to Fante's [123] relation between the long-term beam radius w_{LT}, short-term beam radius w_{ST}, and beam wander variance $\langle r_c^2 \rangle$ of a Gaussian-beam wave, the above analytic expression is given by:

$$w_{\mathrm{LT}}^2 = w_{\mathrm{ST}}^2 + \langle r_c^2 \rangle \, . \tag{2.21}$$

Relating (2.21) to (2.20), the short-term beam radius w_{ST} can be identified by the relation:

$$w_{\mathrm{ST}} = w_L \sqrt{1 + T_{\mathrm{SS}}} \, . \tag{2.22}$$

In the case of an infinite outer scale, the expressions for w_{ST} and $\langle r_c^2 \rangle$ for a collimated and focused beam is given by:

$$w_{\mathrm{ST}} = \begin{cases} w_L \sqrt{1 + 1.33\sigma_R^2 \Lambda_L^{5/6} \left[1 - 0.66 \left(\dfrac{\Lambda_n^2}{1 + \Lambda_n^2}\right)^{1/6}\right]} & \text{(collimated beam)} \\ w_L \sqrt{1 + 0.35\sigma_R^2 \Lambda_L^{5/6}} & \text{(focused beam)} \, . \end{cases} \tag{2.23}$$

$$\langle r_c^2 \rangle = \begin{cases} 2.42 C_n^2 L^3 w_0^{-1/3} & \text{(collimated beam)} \\ 2.72 C_n^2 L^3 w_0^{-1/3} & \text{(focused beam)} \, . \end{cases} \tag{2.24}$$

To substantiate the interpretation of jitter-induced PEs, the root mean square (rms) beam wander displacement of a collimated beam is presented in the form:

$$\sqrt{\langle r_c^2 \rangle} = 0.69L\left(\frac{\lambda}{2w_0}\right)\left(\frac{2w_0}{r_0}\right)^{5/6} \quad ; \tag{2.25}$$

where $(\lambda/2w_0)$ is termed as the diffraction angle of the transmitted optical beam, and $r_0 = (0.16C_n^2k^2L)^{-3/5}$ denotes the Fried's parameters, or the atmospheric coherence width of a reciprocal propagating point source from the receiver at distance L. It should be noted that only the constant is different for a focused beam; and the beam wander effect arises from random tilt phase fluctuations averaged over the transmitter aperture on the order of $(2w_0/r_0)^{5/3}$.

Beam jitter is defined as the whole movement of the short-term optical beam around its unperturbed position in the receiver plane, due to random inhomogeneities of the atmosphere bounded above by r_0 ($r_0 \ll L_0$); thereby acting like an effective wavefront tilt at the transmitter, which can be significantly smaller than the wavefront tilt associated with the random fluctuations of hot spot displacement. The net result of total beam wander is a widening of the long-term beam profile near the boresight, which in turn leads to a slightly "flattened" beam as shown in Figure 2.10(a), in comparison to the conventional Gaussian-beam profile (dashed curve) as suggested by Rytov theory. The implication of the resultant flattened beam profile is an "effective PE" σ_{pe} corresponding to the "beam centre" (i.e., area within the circumference of the lightly-shaded circle) as depicted by Figure 2.10(b), which creates an increase in the longitudinal scintillation index that has not been considered in the first-order Rytov theory. In the case of a Gaussian-beam wave obeying the condition $2w_0 < r_0$, the scintillation effect resulting from the jitter-induced PEs can be explained by the presence of turbulent cells near the transmitter, with scale sizes on the

order of the beam diameter ($2w_0$) and larger up to the atmospheric coherence width r_0. When $2w_0 \geq r_0$, the coherence width r_0 diminishes.

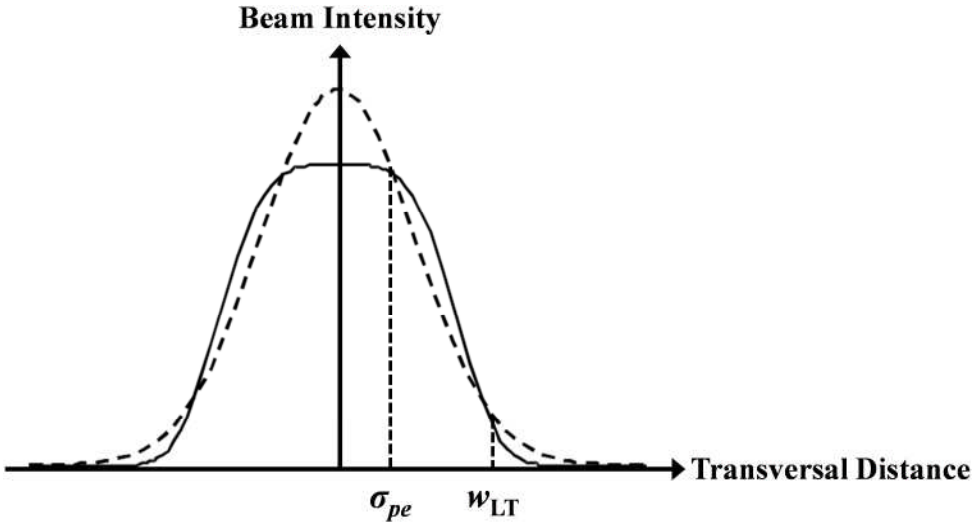

(a)

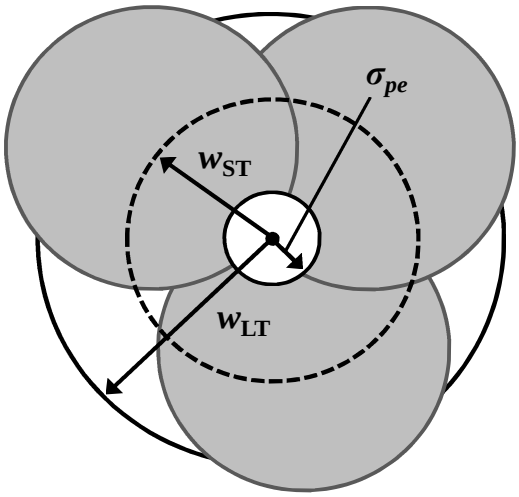

(b)

Figure 2.10: (a) The resultant flattened beam profile (solid line) as a function of the radial distance due to the widening of the long-term beam near the boresight, in comparison to the conventional Gaussian-beam profile (dashed line) as suggested by Rytov theory. (b) The net result is an effective rms PE σ_{pe} of the optical laser beam, as depicted by the small circle in the centre. The long-term beam (i.e., the larger hidden circle) is perceived as the superimposition of short-term beam over a long time period (as indicated by the shaded circles) [11].

In the case of a collimated beam ($\Theta_0 = 1$), the jitter-induced PE variance σ_{pe}^2 is given by:

$$\sigma_{pe}^2 = 0.48\left(\frac{\lambda L}{2w_0}\right)^2\left(\frac{2w_0}{r_0}\right)^{5/3}\left[1-\left(\frac{C_r^2 w_0^2/r_0^2}{1+C_r^2 w_0^2/r_0^2}\right)^{1/6}\right]; \tag{2.26}$$

and for a focused beam ($\Theta_0 = 0$), the comparable expression is:

$$\sigma_{pe}^2 \cong 0.54\left(\frac{\lambda L}{2w_0}\right)^2\left(\frac{2w_0}{r_0}\right)^{5/3}\left[1-\frac{8}{9}\left(\frac{C_r^2 w_0^2/r_0^2}{1+0.5C_r^2 w_0^2/r_0^2}\right)^{1/6}\right], \tag{2.27}$$

where the parameter C_r is a scaling constant typically on the order $C_r \sim 2\pi$.

Depending on the value of the ratio $(2w_0/r_0)$, the asymptotic behaviour can be deduced to give:

$$\sigma_{pe}^2 \sim \begin{cases} \left(\frac{\lambda L}{2w_0}\right)^2\left(\frac{2w_0}{r_0}\right)^{5/3}, & 2w_0/r_0 \ll 1 \\ \left(\frac{\lambda L}{2w_0}\right)^2\left(\frac{r_0}{2w_0}\right)^{1/3}, & 2w_0/r_0 \gg 1\,. \end{cases} \tag{2.28}$$

which is applicable to both collimated and focused beams. As a consequence, even though there can be significant beam wander in some cases (i.e., with smaller optical beams), the related PE variance in both asymptotic cases will tend to zero.

2.4.2.2. Scintillation

The inter-mixing of turbulent winds within the atmosphere with the always-present vertical moisture and temperature gradients due to the Sun's heating of the Earth's surface creates optical turbulences in the atmospheric channel. The resultant irregularities in the space-time redistribution of the refractive index of the atmosphere (appearing in the form

of eddies or cells, termed as optical turbules) are responsible for random fluctuations in the intensity of the optical laser beam, a phenomenon commonly known as scintillations. Theoretical treatments pertaining to the temporal irradiance fluctuations are largely based upon the classical Kolmogorov theory of turbulence [11], which relies on the dimensional analysis of isotropic velocity fields and inertial-subrange predictions of velocity spectra and velocity structure functions. Through this statistical approach, it was discovered that a subclass of optical turbules within the inertial subrange, defined as the range of turbulent cell sizes bounded above by the outer scale L_0 and below by the inner scale l_0, share a degree of statistical consistency; thus allowing further mathematical simplifications and approximations.

Since optical turbulence is fundamentally a nonlinear process, the energy cascade theory of turbulence (depicted in Figure 2.11) can be conveniently adopted to describe the structure of atmospheric turbulence. In the presence of turbulent winds with increasing velocities, local unstable air masses (conceptualized as “eddies”) are created in the atmosphere, with characteristic dimensions slightly smaller than, and independent of, the parent flow. Under the influence of inertial forces originating from wind shear or convection, the turbulent eddies of larger scale size break up into smaller turbulent eddies, in order to form a continuum of eddy size for the transfer of energy from a macroscale L_0 (i.e., outer scale of turbulence) to a microscale l_0 (i.e., inner scale of turbulence). The family of turbulent eddies bounded above by the outer scale L_0 and below by the inner scale l_0 constitutes the inertial subrange, as derived from the Kolmogorov theory; and exhibits the important characteristics of statistical homogeneity and isotropy. This implies that the mean value of the stochastic field is constant; and the point-to-point correlations between random fluctuations in the field are independent of the chosen observation points, while showing dependency only upon the magnitude of their vector separation.

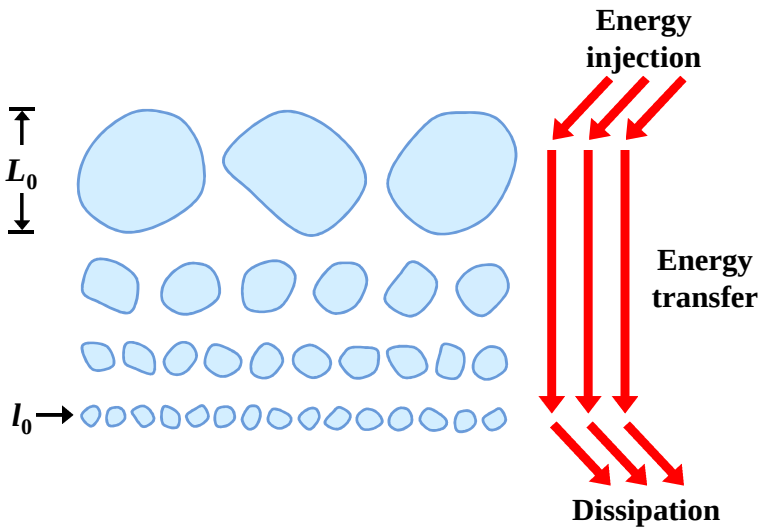

Figure 2.11: Conceptual illustration of the Kolmogorov energy cascade theory of turbulence. Within the inertial subrange, the family of turbulent eddies bounded above by the outer scale L_0 and below by the inner scale l_0 exhibits statistical homogeneity and isotropy [11].

The longitudinal structure function of wind velocity (parallel to the vector $\mathbf{R_P}$ connecting two observation points) is given by:

$$D_{RR}(R_p) = \langle (V_1 - V_2)^2 \rangle = \begin{cases} C_V^2 l_0^{-4/3} R_p^2 , & 0 \ll R_p \ll l_0 \\ C_V^2 R_p^{2/3} , & l_0 \ll R_p \ll L_0 ; \end{cases} \tag{2.29}$$

where V_1 and V_2 represent the velocity components at two points separated by distance R_p, and C_V^2 denotes the velocity structure constant (in units of $m^{4/3}s^{-2}$). Within the boundaries of the inertial subrange ($l_0 \ll R_p \ll L_0$), the longitudinal structure function is characterized by the universal 2/3 power law; whereas a quadratic behaviour is noted at small-scale sizes of turbulent cells ($R_p \ll l_0$). The velocity structure constant C_V^2 is a measure of the total amount of energy in the turbulence, and is related to the average energy dissipation rate ε (in units of m^2/s^3) through the relation:

$$C_V^2 = 2\varepsilon^{2/3} . \tag{2.30}$$

l_0 (in m) is typically on the order of the Kolmogorov microscale η_K:

$$l_0 \sim \eta_K = \left(\frac{\nu_K^3}{\varepsilon}\right)^{1/4} , \tag{2.31}$$

where ν_K resembles the kinematic viscosity. The inverse relationship between l_0 and ε reveals that the strong turbulence has smaller inner scales, whereas the weak turbulence has larger inner scales. On the other hand, L_0 is a function of $\varepsilon^{1/2}$; hence, varies in direct proportion to the strength of turbulence. In the case of statistically homogeneous and isotropic temperature fluctuations, the Kolmogorov theory is extended these conservative passive scalars (which do not involve the exchange of energy with the velocity turbulence) to define the associated structure functions as follows:

$$D_T(R_p) = \langle (T_1 - T_2)^2 \rangle = \begin{cases} C_T^2 l_0^{-4/3} R_p^2 , & 0 \ll R_p \ll l_0 \\ C_T^2 R_p^{2/3} , & l_0 \ll R_p \ll L_0 ; \end{cases} \tag{2.32}$$

where T_1 and T_2 are the temperature at two points separated by distance R_p, and C_T^2 is the temperature structure constant (in units of $\text{deg}^2\text{m}^{-2/3}$). l_0 of the small-scale temperature fluctuations, which forms the lower boundary of inertial-convective range ($l_0 \ll R_p \ll L_0$) has the same order of magnitude as the inner scale for velocity fluctuations, with expression given by [131]:

$$l_0 = 5.8 \left(\frac{{D_H}^3}{\varepsilon}\right)^{1/4} , \tag{2.33}$$

where D_H is the diffusivity of heat in air (in units of m^2s^{-1}).

The combined effects of small-scale temperature fluctuations and turbulent eddies induce a random behaviour in the atmospheric index of refraction n, which can be described by the expression:

$$n(\mathbf{R_p}, t) = n_0 + n_1(\mathbf{R_p}, t) . \tag{2.34}$$

At a point $\mathbf{R_p}$ in space and time t, $n_0 = \langle n(\mathbf{R_p}, t)\rangle \cong 1$ indicates the mean value of the refractive index; and $n_1(\mathbf{R_p}, t)$ represents the random deviation of $n(\mathbf{R_p}, t)$ from the corresponding mean, thus giving $\langle n_1(\mathbf{R_p}, t)\rangle = 0$. Since time variations in the atmospheric index of refraction can be suppressed in the treatment of optical wave propagation (i.e., the optical beam wave maintains a single frequency as it propagates), (2.34) can be written in the form:

$$n(\mathbf{R_p}) = n_0 + n_1(\mathbf{R_p}) , \tag{2.35}$$

in which $n(\mathbf{R_p})$ has been normalized by its mean value n_0.

For visible and infrared wavelengths, the atmospheric index of refraction are related to the temperature and pressure fluctuations according to [132]:

$$\begin{aligned} n(\mathbf{R_p}) &= 1 + 77.6 \times 10^{-6}(1 + 7.52 \times 10^{-3}\lambda^{-2})\frac{P(\mathbf{R_p})}{T(\mathbf{R_p})} \\ &\cong 1 + 79 \times 10^{-6}\frac{P(\mathbf{R_p})}{T(\mathbf{R_p})} ; \end{aligned} \tag{2.36}$$

where P is the pressure (in millibars), and T is the temperature (in Kelvin). The above approximation is based upon the assumption that $\lambda \sim 0.5\,\mu\text{m}$, since wavelength dependence is considerably small for optical frequencies; and the variations in the optical signal resulting from absorption or scattering by molecules or aerosols are not considered here. Furthermore, pressure fluctuations are typically assumed negligible, thus implying that index-of-refraction disturbances associated with the visible and near-infrared region of the spectrum are predominantly due to random temperature fluctuations.

For statistically homogeneous and isotropic turbulence, the related structure function exhibits the asymptotic behaviour as follows:

$$D_n(R_p) = \begin{cases} C_n^2 l_0^{-4/3} R_p^2 , & 0 \ll R_p \ll l_0 \\ C_n^2 R_p^{2/3} , & l_0 \ll R_p \ll L_0 . \end{cases} \tag{2.37}$$

The refractive index structure parameter C_n^2 (in unit of $m^{-2/3}$) is physically interpreted as a measure of the strength of the fluctuations in the index of refraction, and is expressed through the relation (as inferred directly from (2.36)):

$$C_n^2 = \left(79 \times 10^{-6} \frac{P}{T^2}\right)^2 C_T^2 ; \tag{2.38}$$

where C_T^2 denotes the temperature structure constant, which can be determined from (2.32). The C_n^2 values typically range from 10^{-17} $m^{-2/3}$ for weak turbulence scenarios and up to 10^{-13} $m^{-2/3}$ in the case of strong turbulences; and are essentially taken to be constant over short time intervals at a fixed propagation distance and height above ground level. For vertical or slant propagation paths, the refractive index structure parameter varies as a function of height above ground, which can be determined from the Hufnagel-Valley model [133]. This case does not fall within the present scope of discussion, since this research work is based upon long-distance horizontal (terrestrial) FSO communication links. The scintillation index [6, 126] presents a viable statistical quantitative measure of the magnitude of atmospheric turbulence-induced irradiance fluctuations (i.e., the level of scintillations) given by:

$$\sigma_I^2 = \frac{\langle I^2 \rangle - \langle I \rangle^2}{\langle I \rangle^2} = \frac{\langle I^2 \rangle}{\langle I \rangle^2} - 1 ; \tag{2.39}$$

where I is the irradiance of the optical laser beam, and $\langle \cdot \rangle$ denotes ensemble averaging, equivalent to long-time averaging with the assumption of an ergodic process. The classification of atmospheric turbulence-induced scintillations (i.e., weak, moderate and strong turbulences) is commonly distinguished through the values of the Rytov variance:

$$\sigma_R^2 = 1.23 C_n^2 k^{7/6} L^{11/6} \; ; \tag{2.40}$$

where C_n^2 is the strength of turbulence, as defined by (2.38). Weak irradiance fluctuation conditions are typically associated with $\sigma_R^2 < 1$, in which the scintillation index is proportional to the Rytov variance, physically representing the random disturbances in the optical intensity of an unbounded plane wave. On the other hand, moderate fluctuation scenarios are described by $\sigma_R^2 \sim 1$, whereas strong fluctuations are associated with $\sigma_R^2 \gg 1$; and the so-called saturation regime corresponds to the asymptotic limit of $\sigma_R^2 \to \infty$.

2.4.2.3. Atmospheric Turbulence Effects on Partially Coherent Gaussian Beam

Recall the characteristics of a lowest-order Gaussian-beam wave (i.e., TEM_{00} wave) travelling through free-space, as discussed in Section 2.3.3. To examine the propagation effects of a partially coherent Gaussian laser beam in the presence of atmospheric turbulence, a Gaussian Schell beam model [11, 91, 92] is considered, having a Gaussian amplitude distribution with effective beam radius (spot size) w_0 at the exit aperture of the optical transmitter. After travelling through the atmospheric turbulent channel over a link distance L, the receiving beam size is given by:

$$w_L = w_0 \sqrt{\Theta_n^2 + \zeta \Lambda_n^2} \; , \tag{2.41}$$

in which the normalized components (i.e., Θ_n and Λ_n) are defined by (2.8). The global coherence parameter is a measure of the global degree of coherence of light across each transversal plane along the propagation path, and is defined by:

$$\zeta = \zeta_s + \frac{2w_0^2}{\rho_0^2} \; . \tag{2.42}$$

It is related to the source coherence parameter:

$$\zeta_s = 1 + \frac{2w_0^2}{l_c^2} \ , \tag{2.43}$$

and the coherence length of a spherical wave:

$$\rho_0 = [0.55C_n^2 k^2 L]^{-3/5} \ ; \tag{2.44}$$

where l_c is the spatial coherence length. Parameter ζ_s describes the degree of partial (spatial) coherence of the source laser beam at the transmitter, in which $\zeta_s = 1$ for a coherent laser beam and $\zeta_s > 1$ for a partially coherent beam [6].

The point-receiver scintillation index can be conveniently expressed as a sum of radial and longitudinal components to give [11, 92]:

$$\sigma_I^2(0) \cong 4.42\sigma_R^2 \Lambda_L^{5/6} \frac{\sigma_{pe}^2}{w_L^2} + 3.86\sigma_R^2 \{0.40[(1+2\Theta_L)^2 + 4\Lambda_L^2]^{5/12}$$

$$\times \cos\left[\frac{5}{6}\tan^{-1}\left(\frac{1+2\Theta_L}{2\Lambda_L}\right)\right] - \frac{11}{16}\Lambda_L^{5/6}\Big\} \ ; \tag{2.45}$$

where σ_{pe}^2 is the jitter-induced PE variance (see (2.26) to (2.28)), and σ_R^2 is the Rytov variance for a plane wave as defined by (2.40). The receiver beam parameters are:

$$\Theta_L = 1 + \frac{L}{F_L} \quad \text{and} \quad \Lambda_L = \frac{2L}{kw_L^2} \ ; \tag{2.46}$$

where the phase front radius of curvature for a PCB at the receiver is defined by [90]:

$$F_L = \frac{L\left(\Theta_n^2 + \zeta\Lambda_n^2\right)}{\phi\Lambda_n - \zeta\Lambda_n^2 - \Theta_n^2} \ , \quad \text{with } \phi \equiv \frac{\Theta_n}{\Lambda_n} - \frac{\Lambda_n w_0^2}{\rho_0^2} \ . \tag{2.47}$$

In the limiting cases of a plane wave ($\Theta_L = 1$, $\Lambda_L = 0$) and a spherical wave ($\Theta_L = \Lambda_L = 0$), the radial term vanishes and the longitudinal term reduces, respectively, to the well-known results [124]:

$$\sigma_{I,\,\mathrm{pl}}^2(0) = \sigma_R^2 = 1.23 C_n^2 k^{7/6} L^{11/6} \qquad \text{(plane wave)}\,, \tag{2.48}$$

$$\sigma_{I,\,\mathrm{sp}}^2(0) = 0.4\sigma_R^2 = 0.5 C_n^2 k^{7/6} L^{11/6} \qquad \text{(spherical wave)}\,. \tag{2.49}$$

The aperture-averaging effect (to be discussed in further detail in Section 2.5.3) of a non-point receiver aperture is taken into account through the aperture-averaged scintillation index given by:

$$\sigma_I^2(D) = A_g \sigma_I^2(0)\,; \tag{2.50}$$

where A_g denotes the aperture-averaging factor as defined by (2.95), and D is the receiver aperture diameter. The aperture-averaged scintillation index for the limiting plane-wave and spherical-wave models take on the forms:

Plane wave:

$$\sigma_{I,\,\mathrm{pl}}^2(D) = \exp\left[\frac{0.49\sigma_R^2}{\left(1 + 0.65d^2 + 1.11\sigma_R^{12/5}\right)^{7/6}} + \frac{0.51\sigma_R^2\left(1 + 0.69\sigma_R^{12/5}\right)^{-5/6}}{1 + 0.90d^2 + 0.62d^2\sigma_R^{12/5}}\right] - 1\,, \tag{2.51}$$

Spherical wave:

$$\sigma_{I,\,\mathrm{sp}}^2(D) = \exp\left[\frac{0.49\sigma_{I,\,\mathrm{sp}}^2(0)}{\left(1 + 0.18d^2 + 0.56\sigma_{I,\,\mathrm{sp}}^{12/5}(0)\right)^{7/6}} + \frac{0.51\sigma_{I,\,\mathrm{sp}}^2(0)\left(1 + 0.69\sigma_{I,\,\mathrm{sp}}^{12/5}(0)\right)^{-5/6}}{1 + 0.90d^2 + 0.62d^2\sigma_{I,\,\mathrm{sp}}^{12/5}(0)}\right] - 1\,, \tag{2.52}$$

where $d = \sqrt{kD^2/4L}$ denotes the scaled aperture size.

2.4.2.4. Distribution Models for the Irradiance

Turbulence-induced scintillation effect resulting from beam propagation through the atmosphere causes significant power losses at the optical receiver and fading of the detected signal below a detectable threshold, thereby imposing severe diminishing effects on the performance of FSO communication systems. Myriads of theoretical and experimental studies have been carried out within the research community, in order to develop tractable and reliable mathematical models for the irradiance probability density function (PDF), capable of predicting the stochastic nature of the optical intensity fluctuations and deducing the reliability of the system under most possible atmospheric conditions. While numerous irradiance models have been proposed with varying degrees of success in predicting the observed phenomena, the log-normal distribution is the most widely adopted model for the PDF of the randomly fading irradiance signal under weak-to-moderate turbulence conditions due to its simplicity, albeit underestimating the peak irradiance of the PDF and the behaviour in the distribution tails, particularly with increasing turbulence strength [11]. The PDF of the irradiance intensity in the turbulent medium is given by:

$$f_{h_s}(h_s) = \frac{1}{h_s \sigma_I(D)\sqrt{2\pi}} \exp\left\{ -\frac{\left[ln(h_s) + \frac{1}{2}\sigma_I^2(D) \right]^2}{2\sigma_I^2(D)} \right\}; \tag{2.53}$$

where $\sigma_I^2(D)$ is obtained accordingly by using (2.50) for a spatially partially coherent Gaussian laser beam, taking into account the aperture-averaging effect. Alternatively, (2.51) and (2.52) can be employed for the limiting plane-wave and spherical-wave models, respectively.

Figure 2.12 presents the variation in the log-normal distribution for different values of Rytov variance σ_R^2 and aperture-averaged scintillation index $\sigma_I^2(D)$ in the weak turbulence regime, in which the corresponding parameters are common measures for the strength of the atmospheric turbulence-induced irradiance fluctuations. The C_n^2 values ranging from 10^{-15} to 10^{-13} $m^{-2/3}$ are considered here, with the assumption of $D = 200$ mm. It is evident that the distribution becomes more skewed with longer tails towards the infinity direction for greater values of σ_R^2 and $\sigma_I^2(D)$, which denotes the extent of fluctuation of the irradiance as the channel inhomogeneity increases [134].

To address the strong fluctuations or multiple scattering regimes, the statistical PDF models (of the optical field amplitude or irradiance) based upon heuristic arguments and observed experimental data, which relate the discrete scattering regions in the turbulent medium to the individual phase front inhomogeneities in the optical beam wave, are found

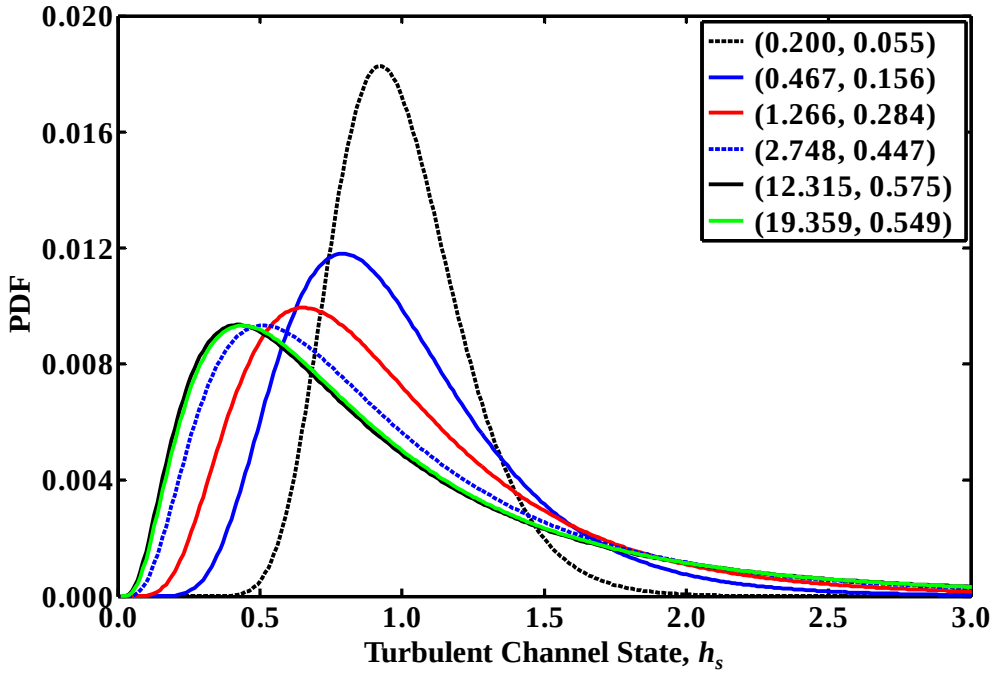

Figure 2.12: Variations of the log-normal PDF for different values of (Rytov variance σ_R^2, scintillation index $\sigma_I^2(D)$) (see figure legend) based on the spherical-wave model, with $D = 200$ mm and C_n^2 values ranging from 10^{-15} to 10^{-13} $m^{-2/3}$ [134].

to be more reliable by showing good agreement with actual field measurements. In the far saturation regime with sufficiently large number of discrete scattering regions, the radiation field of the wave is approximately zero-mean Gaussian; and thus, the irradiance statistics are governed by the negative exponential distribution. The gamma-gamma distribution is a more recent fading model which has evolved from an assumed modulation process, whereby the (normalized) irradiance $I = XY$ can be partitioned into factors arising from the large-scale (X) and small-scale (Y) scintillations under moderate-to-strong turbulence scenarios. Consider the large-scale and small-scale irradiance fluctuations are governed by gamma distributions (due to their excellent approximation in propagation problems involving intensity or amplitude) [135]:

$$p_X(X) = \frac{\alpha(\alpha X)^{\alpha-1}}{\Gamma(\alpha)} \exp(-\alpha X) , \quad \alpha > 0 , \; X > 0 ; \quad \text{and} \tag{2.54}$$

$$p_Y(Y) = \frac{\beta(\beta Y)^{\beta-1}}{\Gamma(\beta)} \exp(-\beta Y) , \quad \beta > 0 , \; Y > 0 ; \tag{2.55}$$

where $\Gamma(\cdot)$ denotes the gamma function [136]. The conditional PDF $p_Y(I|X)$ can be obtained by fixing X and representing $Y = I/X$, to give:

$$p_Y(I|X) = \frac{\beta(\beta I/X)^{\beta-1}}{X\Gamma(\beta)} \exp(-\beta I/X) , \quad I > 0 ; \tag{2.56}$$

in which X is the (conditional) mean value of I. Correspondingly, by forming the average of (2.56) over the distribution in (2.54), the unconditional irradiance distribution $p(I)$ can be defined by:

$$\begin{aligned} p(I) &= \int_0^\infty p_Y(I|X) p_X(X) dX \\ &= \frac{2(\alpha\beta)^{(\alpha+\beta)/2}}{\Gamma(\alpha)\Gamma(\beta)} I^{(\alpha+\beta)/2-1} K_{\alpha-\beta}\left(2\sqrt{\alpha\beta I}\right) , \quad I > 0 ; \end{aligned} \tag{2.57}$$

where $K_{\alpha-\beta}$ resembles the modified Bessel function of the second kind of order $(\alpha-\beta)$ [136]. Relating the normalized intensity I of the optical laser beam to the instantaneous turbulent channel state h_s, the gamma-gamma distribution is given by:

$$f_{h_s}(h_s) = \frac{2(\alpha\beta)^{(\alpha+\beta)/2}}{\Gamma(\alpha)\Gamma(\beta)} h_s^{(\alpha+\beta)/2-1} K_{\alpha-\beta}\left(2\sqrt{\alpha\beta h_s}\right). \tag{2.58}$$

Parameters α and β correspond to the effective number of large- and small-scale turbulent eddies, respectively; relating to the scattering effects of the atmospheric turbulent environment, and are valid with the relationship [11]:

$$\sigma_I^2(D) = \frac{1}{\alpha} + \frac{1}{\beta} + \frac{1}{\alpha\beta}\ ; \tag{2.59}$$

in which

$$\alpha = \frac{1}{\sigma_X^2} = \frac{1}{\exp(\sigma_{\ln X}^2) - 1}\ , \text{and} \tag{2.60}$$

$$\beta = \frac{1}{\sigma_Y^2} = \frac{1}{\exp(\sigma_{\ln Y}^2) - 1}\ . \tag{2.61}$$

For the Gaussian-beam wave model with aperture-averaging, in the presence of beam wander effects, the limiting case of the large-scale and small-scale log variances with $l_0 = 0$ and $L_0 = 0$ take the forms [11]:

$$\sigma_{\ln X}^2(D) = 4.42\sigma_R^2 \Lambda_L^{5/6} \frac{\sigma_{pe}^2}{w_L^2} + \frac{0.49\left(\frac{\Omega_L - \Lambda_L}{\Omega_L + \Lambda_L}\right)^2 \sigma_B^2}{\left[1 + \frac{0.4(2-\bar{\Theta}_L)(\sigma_B/\sigma_R)^{12/7}}{(\Omega_L + \Lambda_L)\left(\frac{1}{3} - \frac{1}{2}\bar{\Theta}_L + \frac{1}{5}\bar{\Theta}_L^2\right)^{6/7}} + 0.56(1+\Theta_L)\sigma_B^{12/5}\right]^{7/6}}\ , \text{and} \tag{2.62}$$

$$\sigma_{\ln Y}^2(D) = \frac{(0.51\sigma_B^2)/\left(1 + 0.69\sigma_B^{12/5}\right)^{5/6}}{1 + \left[1.20(\sigma_R/\sigma_B)^{12/5} + 0.83\sigma_R^{12/5}\right]/(\Omega_L + \Lambda_L)} \; ; \tag{2.63}$$

where $\overline{\Theta}_L = 1 - \Theta_L$, σ_R^2 is defined previously in (2.40), and the non-dimensional parameter characterizing the spot radius of the collecting lens is:

$$\Omega_L = \frac{16L}{kD^2} \; . \tag{2.64}$$

The approximated Rytov variance for collimated and divergent Gaussian beams is:

$$\sigma_B^2 \cong 3.86\sigma_R^2 \left\{0.40\left[(1 + 2\Theta_L)^2 + 4\Lambda_L^2\right]^{5/12} \cos\left[\frac{5}{6}\tan^{-1}\left(\frac{1 + 2\Theta_L}{2\Lambda_L}\right)\right] - \frac{11}{16}\Lambda_L^{5/6}\right\} \; . \tag{2.65}$$

2.4.3. Pointing Errors

A statistical misalignment-induced fading model developed in [24], based on an earlier work in [30], provides a tractable pdf for describing the stochastic behaviour of the PEs. The model assumes a circular detection aperture of diameter D, and a Gaussian spatial intensity profile of beam waist radius w_L on the receiver plane. In addition, both the elevation and horizontal displacement (sway) are considered independent and identically Gaussian distributed with variance σ_s^2. Correspondingly, the pdf of h_p is given by:

$$f_{h_p}(h_p) = \frac{\xi^2}{A_0^{\xi^2}} h_p^{\xi^2 - 1} \; , \qquad 0 \le h_p \le A_0 \tag{2.66}$$

where

$$\xi = \frac{w_{z_{eq}}}{2\sigma_{pe}} \; , \tag{2.67}$$

is the ratio between the equivalent beam radius at the receiver and the PE displacement (jitter) standard deviation at the receiver; and the remaining parameters are defined by [24]:

$$A_0 = \left[\text{erf}\left(\upsilon_p\right)\right]^2 , \tag{2.68}$$

$$w_{z_{eq}} = w_L \sqrt{\frac{\sqrt{\pi}\text{erf}\left(\upsilon_p\right)}{2\upsilon\exp\left(-\upsilon_p^2\right)}} \text{ , and} \tag{2.69}$$

$$\upsilon_p = \frac{\sqrt{\pi}D}{2\sqrt{2}w_L} . \tag{2.70}$$

2.4.4. Combined Channel Fading Model

The combined channel fading model of $h = h_l h_s h_p$ can be expressed as [24, 95]:

$$f_h(h) = \int f_{h|h_s}(h|h_s) f_{h_s}(h_s) dh_s , \tag{2.71}$$

where $f_{h|h_s}(h|h_s)$ is the conditional probability given a turbulence state h_s. Since h_l is deterministic and acts as a scaling factor, the resulting conditional distribution can be expressed as:

$$f_{h|h_s}(h|h_s) = \frac{1}{h_s h_l} f_{h_p}\left(\frac{h}{h_s h_l}\right)$$

$$= \frac{\xi^2}{A_0^{\xi^2} h_s h_l}\left(\frac{h}{h_s h_l}\right)^{\xi^2-1} , \qquad 0 \le h \le A_0 h_s h_l . \tag{2.72}$$

Substituting (2.72) into (2.71) yields:

$$f_h(h) = \frac{\xi^2}{(A_0 h_l)^{\xi^2}} h^{\xi^2-1} \int_{h/A_0 h_l}^{\infty} h_s^{-\xi^2} f_{h_s}(h_s) dh_s . \tag{2.73}$$

By substituting the proper atmospheric turbulence models $f_{h_s}(h_s)$ (as defined by (2.53) and (2.58)) into (2.73) and re-arranging the resultant expressions, the channel state distributions of $h = h_l h_s h_p$ for both the weak and strong turbulence regimes are given by (2.74) and (2.75), respectively. For the weak atmospheric turbulence conditions:

$$f_h(h) = \frac{\xi^2}{(A_0 h_l)^{\xi^2}} h^{\xi^2 - 1} \times \int_{h/A_0 h_l}^{\infty} \frac{1}{h_s^{\xi^2+1} \sigma_I(D)\sqrt{2\pi}} \exp\left[- \frac{\left[ln(h_s) + \frac{1}{2}\sigma_I^2(D) \right]^2}{2\sigma_I^2(D)} \right] dh_s \ . \quad (2.74)$$

In the strong turbulence regime:

$$f_h(h) = \frac{2\xi^2 (\alpha\beta)^{(\alpha+\beta)/2}}{(A_0 h_l)^{\xi^2} \Gamma(\alpha)\Gamma(\beta)} h^{\xi^2 - 1} \times \int_{h/A_0 h_l}^{\infty} h_s^{(\alpha+\beta)/2 - 1 - \xi^2} K_{\alpha-\beta}\left(2\sqrt{\alpha\beta h_s}\right) dh_s \ . \quad (2.75)$$

2.5. Receiver

2.5.1. Photodetector

Photodetectors are important solid-state devices of wireless optical systems, which operate essentially as reverse-biased diodes (hence, also referred to as photodiodes) to perform the inverse operation of optical sources (see Section 2.3.1), by sensing the luminescent power of the incident radiant light and converting the variation of the received optical power into a correspondingly varying electric current. Upon travelling through the communication channel, the optical signal is significantly attenuated (as a result of the absorption and scattering phenomena) and becomes weakened and distorted, thus implying the necessity of photodetectors to meet very high performance requirements, which include: (1) high response or sensitivity in the emission wavelength range of the laser source in use; (2) sufficient bandwidth or fast response speed to support the desired bit rate (extending from hundreds of megahertz to tens of gigahertz); (3) low addition of noise to the system;

(4) minimal contribution from dark current, leakage current, and parasitic induction and capacitance; (5) low sensitivity to temperature fluctuations; and (6) long-term stability [98, 104]. While conforming to the above-mentioned requirements, semiconductor-based photodiodes are used almost exclusively for FSO applications, primarily due to the wide availability of these small-size and inexpensive detectors in the wavelength bands of interest (i.e., 850 nm and 1550 nm). For instance, Si photodiodes are highly sensitive to optical wavelengths ranging between 800 nm and 900 nm, whereas Ge and indium gallium arsenide phosphide (InGaAsP) photodiodes are satisfactory for longer wavelengths in the range of 1.3 μm to 1.6 μm [98]. The two common types of photodiode include the positive-intrinsic-negative (*p*-*i*-*n*) photodiode and avalanche photodiode (APD) [137].

The quantum efficiency η and responsivity γ are two important parameters that are widely adopted to describe the characteristics of a photodiode; in which these parameters are dependent on various factors, such as the operating wavelength, material bandgap, doping and thickness of the *p*, *i* and *n* regions, and dimensions of the device [98, 104]. The quantum efficiency denotes the average number of primary electron-hole carrier pairs generated per incident photon (of energy $\hbar\nu$) impinging upon the diode [104]:

$$\eta = \frac{\text{number of electron-hole pairs generated}}{\text{number of incident photons}} = \frac{I_p/q}{P_0/\hbar\nu}\ , \tag{2.76}$$

where I_p represents the average photocurrent generated by a steady-state average optical power P_0 incident on the photodetector, and q is the electronic charge. To achieve higher quantum efficiency, the depletion layer of the photodiode can be made thicker to enable a larger fraction of the incident light to be absorbed, while inadvertently resulting in a longer time for the free carriers to drift across the reverse-biased junction, thereby affecting the response speed of the device. Correspondingly, a compromise has to be made between response speed and quantum efficiency.

The detector responsivity a useful parameter which specifies the average photocurrent generated per unit of incident optical power, and is related to the quantum efficiency through the relation [98, 103, 104]:

$$\gamma = \frac{I_p}{P_0} = \frac{\eta q}{\hbar \nu} \ . \tag{2.77}$$

Figure 2.13 presents the typical responsivities of different *p*-*i*-*n* photodiodes as a function of wavelength, whereby the corresponding peak representative values are 0.65 A/W for silicon at 900 nm, 0.45 A/W for germanium at 1.3 μm, and 1.0 A/W for InGaAs at 1.55 μm [104]. In most cases, the quantum efficiency is independent of the average received optical power of the photodiode (at a given photon energy), thus implying the responsivity is a linear function of the optical power, such that this parameter is constant at a given wavelength. On the other hand, the quantum efficiency is not constant at all wavelengths but varies according to the photon energy; and hence, the detector responsivity is a function of the wavelength and material bandgap. For a given material, as the wavelength of the incident photon becomes longer, the photon energy becomes less than that required to excite an electron from the valence band to the conduction band, thereby causing the responsivity to deteriorate rapidly beyond the cutoff wavelength, as evident in Figure 2.13.

2.5.1.1. Positive-Intrinsic-Negative Photodiodes

The *p*-*i*-*n* photodiodes are typically constructed by placing a relatively wide intrinsic semiconductor layer (i.e., a very lightly doped *n*-layer) between the *p*+ and *n*+ doped regions, as shown in Figure 2.14 [138]. Under the reverse-biased condition, the intrinsic region is free of charge carriers and becomes highly resistive, with majority of diode voltage appearing across the region, thereby creating a high electric field which extends throughout the intrinsic region. Upon approaching an anti-reflective coating (which

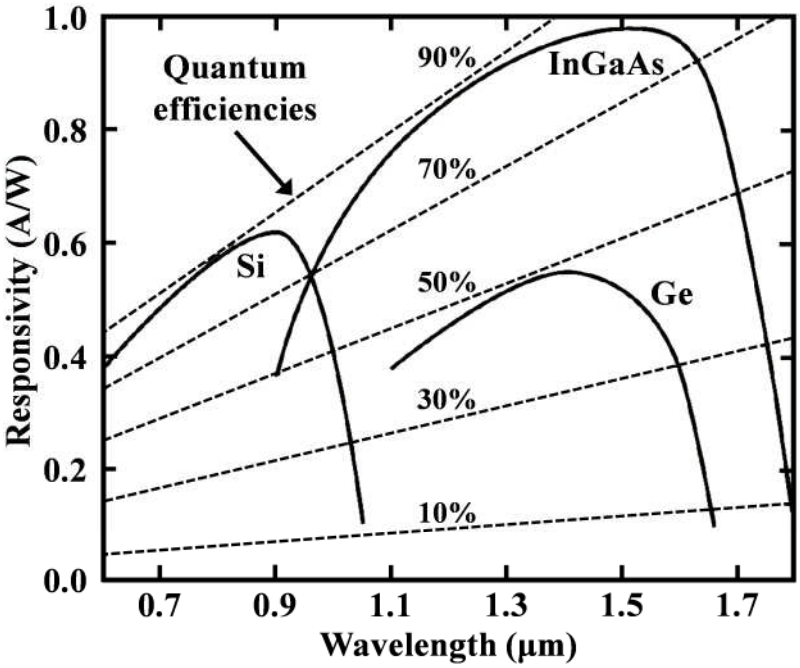

Figure 2.13: Comparison of the typical responsivity and quantum efficiency as a function of wavelength for silicon, germanium and InGaAs p-i-n photodiodes [105].

improves the coupling of energy from the environment into the device), the incident photons (of energy $\hbar\nu \geq E_g$) enter the p^+ layer of the photodiode. In general, the thickness of the p^+ layer is made much thinner than the absorption depth of the material, such that a large proportion of the incident photons are concentrated and absorbed within the intrinsic region, thus resulting in efficient generation of free electron-hole pairs. In the presence of strong electrical forces, the free charge carriers (residing in the intrinsic region) are swept up, and collected across the junction at a saturation velocity on the order of 10^5 m/s, in which the transport of these photon-generated carriers (by drift or diffusion) is the origin of the photocurrent flowing through the external circuit.

In wireless optical applications, the *p-i-n* photodiodes must have large active detection area, such that the radiant optical power can be collected as much as possible, while inadvertently resulting in a relatively larger junction depletion capacitance (and

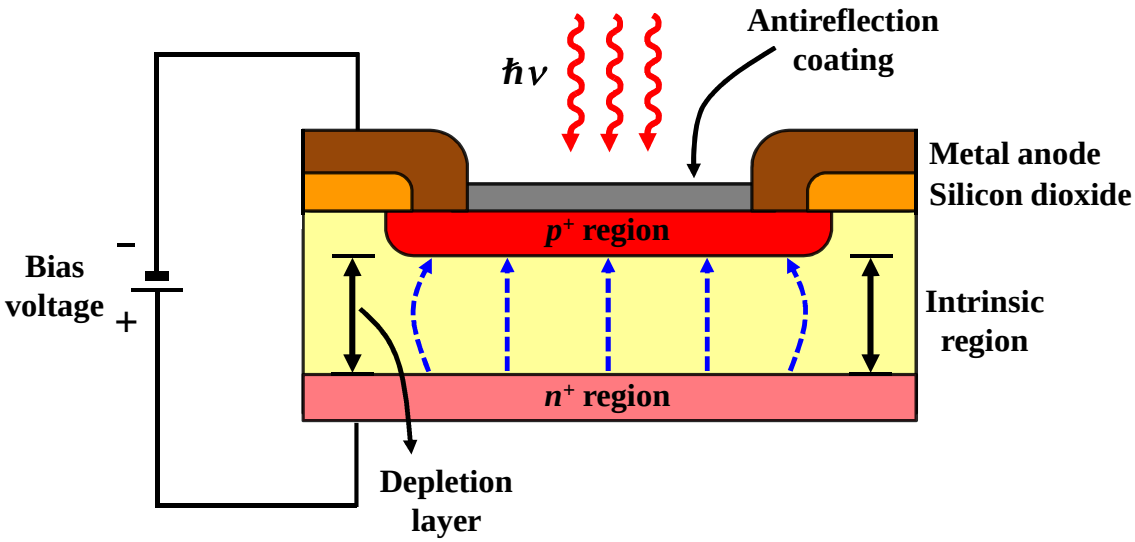

Figure 2.14: The structure of a *p-i-n* silicon photodiode, which is typically constructed by placing a relatively wide intrinsic semiconductor layer between the p^+ and n^+ doped regions [139].

hence, a larger circuit rise time), thereby limiting the frequency response of the photodiodes. While causing an increase in the carrier transit time, reverse bias voltages of lower magnitude also affect the junction capacitance of photodiodes, in which the typical values range from 2 pF (for expensive devices intended for high-speed applications) to 20 pF (for very low-speed and low-cost devices) at a reverse bias of 3.3 V [139]. Since the speed of response is limited by the carrier transit time or circuit rise time (whichever is larger), careful design of receiver structures is necessary, in order to prevent unduly reduction of system bandwidth or increase in noise [103, 140].

The resultant photocurrent I_p of *p-i-n* photodiodes exhibits a linear relationship with respect to the incident optical power P_0 over six to eight decades of input level [141]. However, second order effects are prevalent at higher operating frequencies of the devices (in excess of 5 GHz), mainly due to the variations in transport of carriers through the high-field region; and do not limit the linearity of links at lower frequencies of operation [142]. Since the frequency of operation is limited by the junction depletion capacitance, the *p-i-n*

photodiodes are typically not susceptible to the non-linearities resulting from charge transport, thereby behaving in an approximately linear fashion over a wide range of input optical intensities.

2.5.1.2. Avalanche Photodiodes

The APD is very much similar to the *p-i-n* photodiode with the exception of an internal gain, which multiplies the primary signal photocurrent (i.e., for every photon absorbed in the intrinsic layer, more than one electron-hole pair may be generated) to give a current gain greater than unity prior to entering the input circuitry of a cascading amplifier, thereby increasing the receiver sensitivity. In the event of avalanche multiplication, the photon-generated carriers must traverse across the depletion region of high intensity electric field (created by large reverse biases); whereby these free charge carriers acquire sufficient kinetic energy through strong accelerating forces, and ionize bound electrons in the valence band upon colliding with neutral atoms of the lattice. Correspondingly, the newly generated carriers are also accelerated by the electric field, and in turn gained enough energy to repeat the impact generation of carriers, thus causing further impact ionization to give the avalanche effect. Below the diode breakdown voltage, a finite total number of photon-generated carriers are created, resulting in photocurrent gain typically of the order 10^2 to 10^4 [138, 141]; whereas above the breakdown voltage, a phenomenal amount of charger carriers are produced.

The electron and hole ionization rates denote the average number of electron-hole pairs created by a carrier per unit distance travelled; and exhibit variations in their values for different semiconductor materials, as evident in Figure 2.15 [143]. The ratio of hole to electron ionization rates is a common measure to examine the performance of APDs, based upon the rationale that single type of carrier dominating the impact ionization typically

results in low noise and large gain-bandwidth products. From Figure 2.15, it is noted that silicon is the only semiconductor material which has a significant difference between the electron and hole ionization rates [144-149].

The photocurrent gain (or multiplication) M for all carriers generated in the APD is defined by:

$$M = \frac{I_M}{I_p} \; ; \tag{2.78}$$

where I_M is the average value of the total multiplied output current, and I_p is the primary unmultiplied photocurrent. In practice, the measured value of M is expressed as an average quantity, since not every carrier pair generated in the photodiode experiences the same multiplication, implying that the avalanche mechanism is a statistical process. Analogous to the *p-i-n* photodiode, the responsivity of an APD γ_{APD} is given by:

$$\gamma_{\text{APD}} = \frac{\eta q}{h\nu} M = \gamma M \; . \tag{2.79}$$

2.5.1.3. Comparison between Photodetectors

The APDs are capable of providing manifold gain in the resultant photocurrent through the carrier multiplication process, whereas *p-i-n* photodiodes can generate at most one electron-hole pair per photon absorbed (i.e., unity gain). In the case of long-distance outdoor FSO systems operating under intense ambient light and various atmospheric channel conditions, such gain feature of the APDs may introduce excessive shot noise in the optical receivers, potentially resulting in the adverse reduction of SNR [106]. In general, the *p-i-n* photodiodes are much preferred in optical receivers due to their distinctive advantages, which include: (1) vast availability at relatively low cost and at a

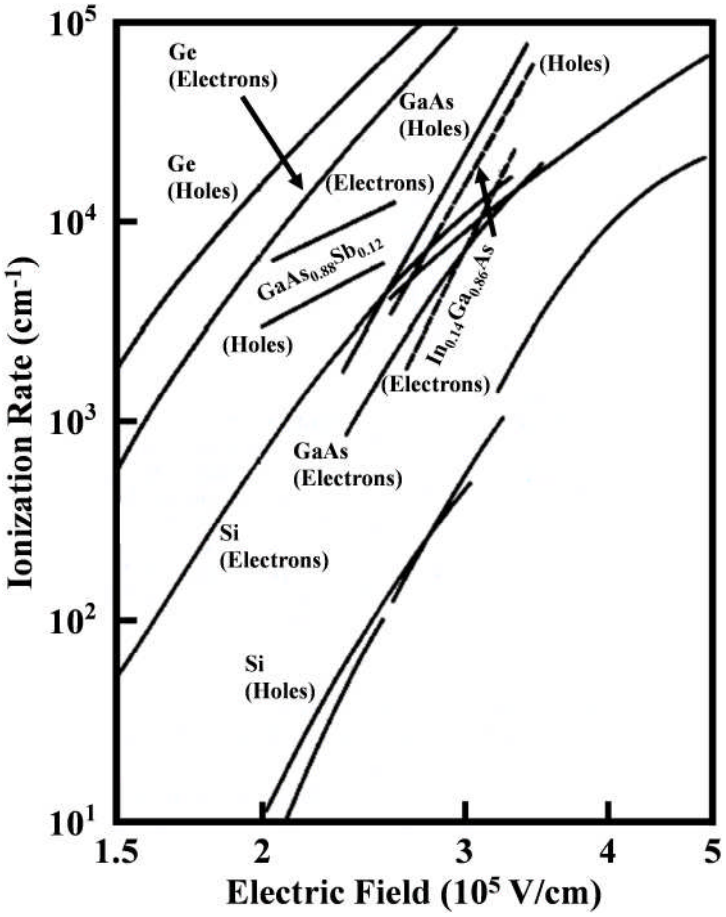

Figure 2.15: Electron and hole ionization rates obtained from experiment for different semiconductor materials, which include silicon, germanium, GaAs, GaAsSb and InGaAs [105].

variety of wavelengths; (2) good linearity of output current as a function of incident light; and (3) lower biasing supplies with the penalty of increasing junction capacitance. Table 2.4 summarizes and compares the characteristics of *p-i-n* photodiodes and APDs for wireless optical communication links [100, 141].

Optical lasers operating at longer wavelengths (i.e., 1310 nm and 1510 nm windows) are desirable for terrestrial FSO applications, in order to enable high-speed data transmission at higher transmitted optical power level while conforming to the eye-safety limits, thereby extending the link range with relatively large SNR. Correspondingly, InGaAs-based photodiodes are commonly employed in long-distance wireless optical links,

Table 2.4: Comparison of the characteristics between *p-i-n* photodiodes and APDs for wireless optical communication [101, 142].

Characteristics	***p-i-n* Photodiode**	**APD**
Modulation bandwidth (ignoring circuit)	Tens of MHz to tens of GHz	Hundreds of MHz to tens of GHz
Photocurrent gain	1	10^2 to 10^4
Requirement of additional circuitry	None	High bias voltages and temperature compensation circuitry
Linearity	High	Low – suited to digital applications
Cost	Low	Moderate to high
Sensitivity	Low	High

whereas silicon devices operating in the 850 nm band present a rather inexpensive alternative for short-distance applications. Therefore, care must be taken in the selection of photodetectors to ensure that cost, performance and safety requirements are satisfied.

A photomultiplier tube (PMT) is another type of practical photodetector, which consists of a photocathode and multiple plates (known as dynodes) for producing secondary emissions, which enables the multiplication of the current flow to give the internal gain mechanism [116]. The high gain (ranging between 10^3 and 10^5) and high sensitivity features of the PMT are particularly advantageous in detecting low levels of optical radiation and in overcoming noise originating from thermal sources, respectively; thereby increasing the signal level without significantly reducing the ratio of signal power to noise power [104, 116, 140]. In addition, the PMTs are very fast with some phototube devices having rise times of a few tenths of a nanosecond [140]. Nonetheless, the PMTs are least popular and scarcely considered for outdoor wireless optical communication mainly due to their inherent disadvantages, which include: high cost, relatively large size

and weight, and substantial voltage requirements (in excess of several hundred volts) for biasing [104, 140].

2.5.2. Noise Sources

In wireless optical systems, the photodiodes and pre-amplifiers typically constitute the receiver front-end (see Figure 2.16), in order to enable the detection of the weakest possible optical signals, while subjected to interferences and distortions arising from various fundamental noise sources, which include: quantum or shot noise, bulk dark current noise, surface leakage current noise, and thermal noise associated with the

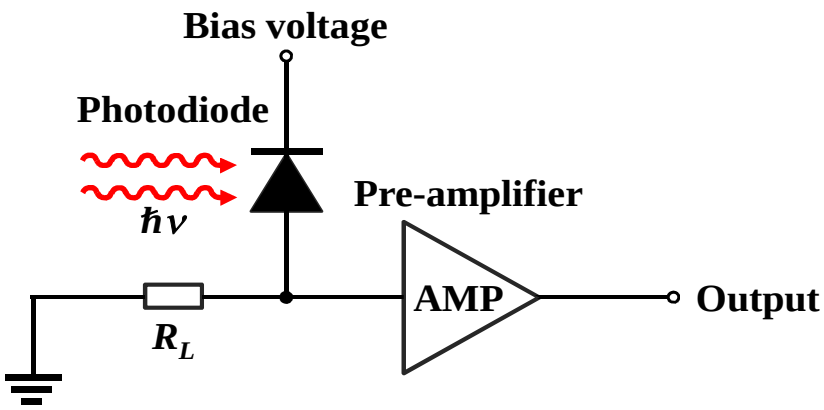

Figure 2.16: Schematic representation of an optical receiver front-end encompassing a photodetector and amplifier circuit.

amplifier circuitry. It is apparent that the noise currents are critical factors which determine the minimum detectable optical power of the incoming signals (i.e., the sensitivity of the photodiode), and hence, the following conditions should be met to achieve a high SNR: (1) the photodetector must have a high quantum efficiency (close to its maximum possible value) to generate a large signal power; and (2) the photodetector and amplifier noises should be minimized. Correspondingly, the design, performance evaluation and optimization of terrestrial FSO links would require in-depth understanding pertaining to

the occurrence, characteristics and inter-relationships of various noise sources present in the optical receivers.

At the receiving-end, thermal noise (also known as the Johnson noise) occurs mainly in the resistive elements of the pre-amplifier, due to the thermal fluctuations of electrons within the amplifier circuitry; whereby random motion of carriers causes frequent collisions with the atoms or molecules of the substance. While using a low resistance in the front end is capable of improving the frequency response, an excessive amount of thermal noise is generated by the pre-amplifier independent of the resultant photocurrent. Transimpedance pre-amplifier is a viable alternative for providing low impedance front-end through negative feedback, and presents a compromise between these constraints [139]. Thermal noise obeys the Gaussian distribution with zero mean and unit variance; and is regarded as a 'white' noise, mainly because the power spectral density (PSD) of this noise source is independent of frequency.

Photon-generated quantum or shot noise arises from the statistical nature of the production and collection of free charge carriers when an optical signal is incident upon a photodetector; whereby electron-hole pairs are generated randomly in the space charge region due to photon absorptions, and traverse the potential barrier in a stochastic manner depending on their kinetic energy. Correspondingly, the probabilistic generation and transport of free charge carriers due to the quantum effects in photodiodes produces shot noise in the photocurrent, in which these statistics have been demonstrated in [150] and modelled as having Poisson distribution with a white PSD [139, 151].

2.5.3. Aperture Averaging

The receiver aperture in an optical communication system behaves essentially like a "point aperture", when its aperture dimension is smaller than the correlation width of the irradiance fluctuations. When the aperture size increases beyond the irradiance correlation width, the receiver detects several correlation patches and the scintillation level measured in the image plane begins to decrease, thereby resulting in higher mean SNR. This phenomenon is known as the aperture-averaging effect, whereby enlarged receiver apertures are intentionally utilized in direct detection systems, in order to enhance the system performance through the reduction of scintillations. Measurements from early astronomical studies by Mikesell *et al.* [152, 153] revealed that aperture averaging potentially causes a shift in the relative frequency content of the irradiance power spectrum towards lower frequencies; in essence, averaging out the fastest fluctuations and thus mitigating the adverse effects of scintillation.

In principle, the reduction of scintillation level resulting from the aperture-averaging effect can be deduced from the ratio of received optical power fluctuations by a finite-size collecting aperture to that obtained by a very small (i.e., point) aperture [11]. Correspondingly, the normalized variance of the power fluctuations in the receiver plane is the same as the flux variance of irradiance fluctuations defined by:

$$\sigma_I^2(D) = \frac{\langle {P_R}^2 \rangle - \langle P_R \rangle^2}{\langle P_R \rangle^2}$$

$$= \frac{16}{\pi D^2} \int_0^D \rho B_I(xD, L) \left[\cos^{-1}\left(\frac{\rho}{D}\right) - \frac{\rho}{D}\sqrt{1 - \frac{\rho^2}{D^2}} \right] d\rho \; ; \qquad (2.80)$$

where P_R is the received optical power, D is the circular aperture diameter, $B_I(\rho, L)$ denotes the irradiance covariance function in the pupil plane, and the terms in brackets

arise from the modulation transfer function of the circular aperture. By defining the variable $\delta = \rho/D$, (2.80) can be simplified to give the expression as follows:

$$\sigma_I^2(D) = \frac{16}{\pi}\int_0^1 \delta B_I(\delta D, L)\left[\cos^{-1}\delta - \delta\sqrt{1-\delta^2}\right]d\delta\,. \tag{2.81}$$

For a circular aperture of diameter D, the aperture-averaging factor (or coefficient) is defined by:

$$A_g = \frac{\sigma_I^2(D)}{\sigma_I^2(0)} = \frac{16}{\pi}\int_0^1 \delta b_I(\delta D, L)\left[\cos^{-1}\delta - \delta\sqrt{1-\delta^2}\right]d\delta\,, \tag{2.82}$$

which typically ranges between 0 and 1, with A_g values approaching these extreme values implying complete aperture-averaging and no aperture-averaging, respectively; $\sigma_I^2(0) = B_I(0, L)$ is the scintillation index for a point aperture ($D = 0$), and the normalized covariance function is obtained through the relation:

$$b_I(\rho, L) = \frac{B_I(\rho, L)}{B_I(0, L)}\,. \tag{2.83}$$

2.5.3.1. Extended Huygens-Fresnel Principle

After propagating a distance L through a random medium, the complex field of the optical wave can be represented, using the Huygens-Kirchhoff principle, as:

$$U(\boldsymbol{\rho}, L) = \int\int \mathrm{d}^2\mathbf{r}\, G(\mathbf{r}, \boldsymbol{\rho}, L)U(\mathbf{r}, 0) \tag{2.84}$$

where $U(\mathbf{r}, 0)$ is the field at the transmitter plane $z = 0$, defined by (2.5). The paraxial (parabolic) wave equation derived from the Helmholtz equation has the Green's function solution:

$$G(\mathbf{r}, \boldsymbol{\rho}, L) = \frac{-jk}{2\pi L} \exp\left[jkL + \frac{jk}{2L}|\boldsymbol{\rho} - \mathbf{r}|^2 + \Psi(\mathbf{r}, \boldsymbol{\rho})\right], \tag{2.85}$$

where $\Psi(\mathbf{r}, \boldsymbol{\rho})$ resembles the random part of the complex phase of a spherical wave propagating in the turbulent medium from the point $(\mathbf{r}, 0)$ to the point $(\boldsymbol{\rho}, L)$. Using this Green's-function solution, (2.84) can be expressed in terms of the Huygens-Fresnel integral [120]:

$$U(\boldsymbol{\rho}, L) = \frac{-jk}{2\pi L} \exp(jkL) \int\int \mathrm{d}^2\mathbf{r} U(\mathbf{r}, 0) \exp\left[\frac{jk}{2L}|\boldsymbol{\rho} - \mathbf{r}|^2 + \Psi(\mathbf{r}, \boldsymbol{\rho})\right]. \tag{2.86}$$

The Huygens-Fresnel principle [114] states that each point on a wave front generates a spherical wave; in which the envelope of these secondary waves constitutes a new wave front, and their superposition produces the wave in another plane. The expression in (2.86) is commonly known as the extended Huygens-Fresnel principle, and is applicable to both the weak and strong turbulence fluctuation regimes.

2.5.3.2. Spatial Covariance of Irradiance Fluctuations

Classical studies have characterized wave propagation through atmospheric turbulence in terms of the complex mutual coherence function:

$$\Gamma_I(\boldsymbol{\rho}_1, \boldsymbol{\rho}_2; \tau) = \langle E(\boldsymbol{\rho}_1; \tau) E^*(\boldsymbol{\rho}_2; t + \tau) \rangle ; \tag{2.87}$$

where $\boldsymbol{\rho}_1$ and $\boldsymbol{\rho}_2$ are the observation points in the receiver plane with a time delay τ, $\langle \cdot \rangle$ denotes ensemble averaging, E is the optical frequency electric field, and E^* resembles the complex conjugate field. On the contrary, recent theoretical treatments [90, 92, 154, 155] pertaining to the propagation of partially coherent Gaussian laser beam in the presence of atmospheric turbulence, have placed much emphasis on the analysis of cross-spectral density function:

$$W(\boldsymbol{\rho}_1, \boldsymbol{\rho}_2; \nu) = \langle U(\boldsymbol{\rho}_1; \nu) U^*(\boldsymbol{\rho}_2; \nu) \rangle \,, \tag{2.88}$$

which is the temporal Fourier transform of $\Gamma_I(\boldsymbol{\rho}_1, \boldsymbol{\rho}_2; \tau)$. The cross-spectral density function, which obeys the Helmholtz equation, is a measure of the correlation between the fluctuations of two field components at the same frequency ν of a partially coherent laser beam. If the field is strictly monochromatic (i.e., having sufficiently narrow band), such that the condition below is satisfied:

$$\frac{|\boldsymbol{\rho}_2 - \boldsymbol{\rho}_1|}{c} \ll \frac{1}{\Delta\nu} \,, \tag{2.89}$$

then both characterizations give identical results; in which the typical values of $|\boldsymbol{\rho}_2 - \boldsymbol{\rho}_1|$ are on the order of 10 cm, requiring that $\Delta\nu < 1$ GHz.

At the input plane, a phase diffuser is placed over the exit aperture of a quasi-monochromatic Gaussian laser transmitter, such that the resultant field of the optical wave emerging from the diffuser can be modelled as:

$$\widetilde{U}(\mathbf{r}, 0) = U(\mathbf{r}, 0) \exp[j\varphi_d(\mathbf{r})] \,; \tag{2.90}$$

where $U(\mathbf{r}, 0)$ denotes the deterministic field entering the diffuser defined by (2.5), and $\exp[j\varphi_d(\mathbf{r})]$ resembles the small random perturbation introduced by the phase diffuser. Based on the assumption that the ensemble average of the spatially dependent random phases introduced by the diffuser is Gaussian and depends only on the separation distance and not on the actual location on the diffuser, the cross-spectral density at the transmitter can be expressed in the form of a Gaussian Schell-model beam:

$$W(\mathbf{r}_1, \mathbf{r}_2, 0) = \langle \widetilde{U}(\mathbf{r}_1, 0)\widetilde{U}^*(\mathbf{r}_2, 0)\rangle$$
$$= U(\mathbf{r}_1, 0)U^*(\mathbf{r}_2, 0)\langle \exp[j\varphi_{d1}(\mathbf{r}_1)]\exp[-j\varphi_{d2}(\mathbf{r}_2)]\rangle$$
$$= U(\mathbf{r}_1, 0)U^*(\mathbf{r}_2, 0)\exp\left[\frac{-(\mathbf{r}_1 - \mathbf{r}_2)^2}{2\sigma_g^2}\right] ; \quad (2.91)$$

where σ_g^2 is the variance of the Gaussian describing the ensemble average of the random phases (i.e., the partial coherence properties of the effective transmitted source), as determined by the characteristics of the diffuser. This variance can be interpreted to represent the number of "speckle cells" (i.e., statistically independent patches) at the diffuser, whereby each speckle cell essentially behaves like an independent source term. Weak diffusers ($\sigma_g^2 \gg w_0^2$) typically have only one speckle cell (implying a coherent wave), whereas many speckle cells will normally exist for the case of a strong diffuser.

Consider the behaviour of $W(\boldsymbol{\rho}_1, \boldsymbol{\rho}_2; \nu = \nu_0)$, where ν_0 is the centre frequency of the quasi-monochromatic Gaussian laser beam. The cross-spectral density at the receiver can be represented as:

$$W(\boldsymbol{\rho}_1, \boldsymbol{\rho}_2, L) = \langle U(\boldsymbol{\rho}_1, L)U^*(\boldsymbol{\rho}_2, L)\rangle$$
$$= \frac{1}{(\lambda L)^2}\int\int\int\int \mathrm{d}^2\mathbf{r}_1\mathrm{d}^2\mathbf{r}_2 W(\mathbf{r}_1, \mathbf{r}_2, 0)$$
$$\times \langle \exp[\Psi(\mathbf{r}_1, \boldsymbol{\rho}_1) + \Psi^*(\mathbf{r}_2, \boldsymbol{\rho}_2)]\rangle \quad (2.92)$$
$$\times \exp\left\{\frac{jk}{2L}[(\boldsymbol{\rho}_1 - \mathbf{r}_1)^2 - (\boldsymbol{\rho}_2 - \mathbf{r}_2)^2]\right\} .$$

The spatial covariance of irradiance fluctuations can be estimated through the relation:

$$B_I(\boldsymbol{\rho}_1, \boldsymbol{\rho}_2, L) = |\Gamma(\boldsymbol{\rho}_1, \boldsymbol{\rho}_2, L)|^2 ; \quad (2.93)$$

in which the mutual coherence function $\Gamma_I(\boldsymbol{\rho}_1, \boldsymbol{\rho}_2, L)$ can be approximated by the cross-spectral density function, i.e., $\Gamma_I(\boldsymbol{\rho}_1, \boldsymbol{\rho}_2, L) \cong W(\boldsymbol{\rho}_1, \boldsymbol{\rho}_2, L)$. By normalizing the spatial covariance of irradiance fluctuations $B_I(\boldsymbol{\rho}_1, \boldsymbol{\rho}_2, L)$ yields:

$$b_I(\rho, L) = \frac{B_I(\rho, L)}{B_I(0, L)}$$
$$= \exp\left\{-\frac{\rho^2}{\rho_0^2}\left[2 + \frac{\rho_0^2}{w_0^2\Lambda_n^2} - \frac{\rho_0^2\phi^2}{w_L^2}\right]\right\} = \mu(2\rho, L)\ ; \tag{2.94}$$

where $\mu(\rho, L)$ denotes the complex degree of spatial coherence, and $\rho = |\boldsymbol{\rho}_1 - \boldsymbol{\rho}_2|$. It is noted that the normalized spatial covariance of irradiance fluctuations has an analytic solution in terms of the complex degree of coherence $\mu(\rho, L)$ evaluated at twice the radial separation distance.

Substituting (2.94) into (2.82) results in an easily evaluated expression for the aperture-averaging factor [92]:

$$A_g = \frac{16}{\pi}\int_0^1 \delta d\delta \exp\left\{\frac{-D^2\delta^2}{\rho_0^2}\left[2 + \frac{\rho_0^2}{w_0^2\Lambda_n^2} - \frac{\rho_0^2\phi^2}{w_L^2}\right]\right\}$$
$$\times\left[\cos^{-1}(\delta) - \delta\sqrt{1-\delta^2}\right]\ . \tag{2.95}$$

2.6. Summary

This chapter has presented in-depth discussion pertaining to the FSO technology, which include: (1) the proposed system model based upon the SISO horizontal-path FSO communication links; (2) the relevant components of the optical transmitter and receiver; and (3) the important characteristics and modelling of the atmospheric channel. The two widely adopted optical sources encompassing the LEDs and semiconductor lasers have

been thoroughly reviewed and compared, revealing that the high-efficiency, high-power LDs are desirable for long-distance outdoor directed-LOS FSO links. In addition, the Gaussian-beam wave model have been introduced and applied in the optical wave propagation analysis of a partially coherent Gaussian laser beam, under the combined influences of beam wander and scintillation effects resulting from optical turbulence. While highly divergent optical laser beams are particularly advantageous in addressing eye safety issues, the author demonstrates (in Chapter 3 and Chapter 4) that partially coherent laser sources of larger receiving beam spot size are capable of mitigating the turbulence-induced scintillations and PEs in terrestrial FSO communication systems.

In the review of the FSO communication channel, detailed discussion on the occurrence, characteristics, resulting impacts and modelling of the respective phenomena have been presented here. The atmospheric loss due to the combined deterministic effects of light absorption and Rayleigh and Mie scattering is considered as a fixed scaling factor over multiple fading states of the FSO channel, and can be modelled by the Beers-Lambert law. While deliberately increasing the optical launch power presents a desirable approach for compensating the high attenuation of the transmitted optical signal when propagating through air, direct exposure of such intense optical radiation can impose hazardous impact on human safety, potentially causing harm to the eye and skin. The author investigates the hybrid FSO/RF communication system (in Chapter 6), which takes advantage of the media diversity technique with enhanced duality feature to switch between the two technology options, in order to overcome the deterioration of signal quality and link outages under different adverse weather conditions. Furthermore, the theoretical background, characteristics and analytical approach pertaining to the occurrence of optical turbulence-induced beam wander and scintillation have been introduced and discussed in detail here; in which it has been shown that these channel effects work in tandem to create random

signal losses at the optical receiver, potentially degrading the system performance due to signal fading. Considering the respective behaviour and effects of each channel component in describing the atmospheric propagation channel, the combined channel fading model have been thoroughly examined and taken into account in the theoretical analysis and simulation studies.

For the optical receivers, the two common types of photodetectors consisting of the *p-i-n* photodiodes and APDs that are used almost exclusively for FSO applications, have been examined and compared. While the APDs are capable of providing manifold gain in the resultant photocurrent through the carrier multiplication process, such gain feature of the APDs may produce excessive shot noise in the receiver front-end, particularly in the case of long-distance outdoor FSO systems operating under intense ambient light and various atmospheric channel conditions; thus making the *p-i-n* photodiodes a much preferred option over APDs in optical receivers. Finally, the effects of the aperture-averaging phenomenon in mitigating the random temporal fluctuations in the optical intensity of the laser beam through the intentional utilization of enlarged receiver apertures in direct detection systems are explicitly described here. The author demonstrates the effects of aperture averaging and beam width on the FSO link (in Chapter 5) via an extensive experimental study under laboratory-controlled atmospheric turbulence conditions; in which it is evident that manifold gain in the link performance can be achieved with increasing scaled aperture size of an aperture-averaged optical receiver.

CHAPTER 3

Investigation of the Effects of Aperture Averaging and Beam Width

3.1. Introduction

Terrestrial FSO communication presents an attractive alternative to deliver low-cost, license-free and high-bandwidth access solution for a variety of applications, such as last-mile connectivity, optical-fibre backup and enterprise connectivity [13, 51]. This is mainly due to the superior FSO characteristics, which include: no licensing requirements or tariffs for its utilization, virtually unlimited bandwidth for achieving very high aggregate capacity, reduced interference, high security, cost-effectiveness, and simplicity of system design and setup [10]. Nevertheless, the widespread deployment of such technology option is hampered by the atmospheric channel which is highly variable, unpredictable and vulnerable to different weather conditions, such as scattering, absorption and turbulence [6, 11]; and the presence of PEs [24, 25, 30, 31, 65].

The propagation properties and performance of spatially partially coherent Gaussian laser beams through random turbulent media have been substantially explored thus far [90-92], which revealed the benefits of mitigating the turbulence-induced scintillations and PEs. A partially coherent laser beam can be generated by passing an initially spatially coherent laser transmitter through a phase diffuser, which partially destroys the spatial coherence of the information-bearing laser beam, thereby increasing the receiver beam size while still retaining its beamlike (i.e., highly directional) properties [90]. This approach inadvertently results in the reduction of the average received power, thus implying the need for careful investigation and optimization of the PCB through free-space, such that the inevitable trade-off between the reduction in the scintillations and PEs, and the reduction in the mean received irradiance can be achieved conveniently.

A thorough review of the relevant literatures pertaining to the investigation studies and performance analysis of spatially partially coherent Gaussian laser beams in FSO communication systems is presented in Section 3.2, and the main contributions of the proposed research work are highlighted in Section 3.3. Next, Section 3.4 reviews the relevant performance metrics considered in the corresponding numerical analysis, which include the BER in Section 3.4.1, the probability of outage in Section 3.4.2, and the average capacity for both cases of known and unknown CSI at the receiver in Section 3.4.3. Based upon the aforementioned system and channel models in Section 2.2 and Section 2.4, respectively, notable findings from the outage analysis are depicted and discussed in Section 3.5.1; demonstrating the necessity of optimization methods to minimize FSO link outages under different atmospheric channel conditions, which is best performed through proper selection of receiver aperture size and beam width for a known laser wavelength and/or increasing the transmit power of the optical laser source. Then, joint investigation of the effects of PCB and aperture averaging are presented in Section 3.6, showing that an

improvement in the average channel capacity can be achieved with the introduction of an enlarged receiver aperture, albeit without knowledge of the channel state conditions. In Section 3.7, several appealing observations pertaining to the alteration of the PCB characteristics are made, which in turn reveal that beam width optimization is a feasible approach in promoting capacity enhancement for long-distance horizontal FSO communication links. Finally, concluding remarks are highlighted in Section 3.8.

3.2. Background and Motivation

The adverse effects of atmospheric loss, turbulence-induced channel fading and PEs on the performance and design of FSO links have been extensively investigated from the information theory perspective in a large body of literature. In these relevant studies, a variety of channel fading models have been considered in the evaluation of the error performance and channel capacities of the system under study. In particular, Farid and Hranilovic [24] presented a statistical model for the optical intensity fluctuation at the receiver due to the combined influences of turbulence and PEs, which include the effects of beam width, detector size and jitter variance. It was shown that beam width optimization provides large gains in the FSO channel capacity subject to outage. In [93], Sandalidis proposed several optimization models to limit the PE loss, taking into account various metrics such as the beam width, mean electrical SNR, normalized jitter, outage probability and BER. Similar approach to [24] was also noted in [65, 94, 95], whereby the authors evaluated the error performance by taking into account both misalignment- and turbulence-induced fluctuations. However, the link design criteria were not emphasized in the analytical studies, thus lacking a holistic perspective for optimal planning and design of FSO links. The above theoretical treatments are based upon the classical unbounded plane- or spherical-wave approximations (the latter often taken as a point source), which are the

limiting forms of the lowest-order Gaussian-beam wave model [11]. These simplified field models are insufficient to characterize the propagation properties of the optical wave through random turbulent medium, particularly for the case of spatially partially coherent Gaussian beam, whereby focusing and diverging characteristics are important [90]. In addition, the conventional Rytov-based scintillation model associated with these approximations may not accurately reflect the irradiance fluctuations, particularly in applications involving long-distance horizontal transmissions and strong atmospheric turbulence [156]. This is mainly because the influence of beam wander attributed to the presence of large-scale turbulent eddies, which contributes to a widening of the long-term beam profile and PEs, is not considered in the limiting Rytov theory [11, 156].

Furthermore, the effects of aperture averaging on PCB in mitigating the scintillations and PEs for achieving higher mean SNR have not been thoroughly examined [25, 74]. In [25], Borah and Voelz demonstrated the effect of PEs on the capacities of FSO links affected by the atmospheric turbulence, taking into account a Gaussian-beam wave model and wave-optics-based simulation approach; but the effects of larger apertures and optimization method were not considered here. In [156], Ren *et al.* investigated the impact of beam wander on the average and outage capacities of the FSO link, through the direct inclusion of this effect in the traditional scintillation theory; and showed that an optimum transmitter beam radius can be selected for best achievable channel capacities. Nevertheless, the effects of PEs and aperture averaging were not considered in their work. Therefore, it is vital to investigate the combined effects of PCB and aperture averaging in horizontal (terrestrial) FSO links, in the presence of turbulence and PEs; which then substantiates the study of beam width optimization.

3.3. Main Contributions of Research

The performance of partially coherent FSO communication links is investigated from the information theory perspective, taking into account the impairments resulting from atmospheric loss, turbulence and PEs. In particular, a spatially partially coherent Gaussian-beam wave and important link design criteria are jointly considered, in which the latter consists of the receiver aperture dimension and its resulting aperture averaging effect, transmitter beam width, link range, knowledge of CSI, and weather conditions. The optical channel characteristics is analytically described using a combined optical slow-fading channel model, for evaluating the important performance metrics of the FSO link – the BER, average channel capacity and outage probability. These performance indicators resemble the error performance, practically achievable data rate averaged over all fading states, and probability of the system being in an outage for achieving a specified rate of transmission, respectively. The log-normal and gamma-gamma distributions are utilized in modelling the stochastic behaviour of optical irradiance under weak-to-moderate and moderate-to-strong atmospheric turbulence conditions, respectively. The lowest-order Gaussian-beam wave model characterizes the propagation properties of the optical signal through random turbulent medium; taking into account the beam spreading (i.e., diverging) and focusing of the PCB, and the scintillation and beam wander effects arising from the turbulent eddies. Correspondingly, this study presents a holistic perspective for optimal planning and design of horizontal FSO links employing spatially partially coherent laser beams.

From the outage analysis, it is evident that a lower outage probability can be achieved with the introduction of a larger receiver aperture due to the aperture-averaging effect, which effectively mitigates the PE loss and scintillation-induced optical intensity

fluctuations. In addition, outage capacity optimization is best performed through proper selection of the transmitter beam width and the receiver aperture size for a known laser wavelength and/or increasing the transmit power. Under the light fog condition, complete system outage occurs at link distances exceeding 1.5 km, and is non-recoverable albeit optimizing the system parameters. Furthermore, it is demonstrated that the average channel capacity can be significantly improved due to the aperture-averaging effect, albeit without knowledge of the channel state conditions; and the PCB experiences substantial alteration in its characteristics when propagating through free-space. Several interesting observations are made here, showing that the optimum beam width can be made smaller to maximize the average capacity, albeit in the presence of turbulence-induced scintillations and PEs, given the condition that either one or both of these adversities are least dominant. In the strong turbulence regime, the beam width must be increased accordingly with respect to the PE loss, where such incremental trend changes from a linear to an exponential behaviour. Hence, beam width optimization presents a feasible approach in promoting capacity enhancement for long-distance horizontal FSO links; since the optimum beam width of the laser transmitter is susceptible to the combined effects of turbulence and PEs, and must be adjusted accordingly to obtain optimality.

3.4. Performance Metrics

The BER, probability of outage and average channel capacity are the three key application-specific performance indicators identified and employed throughout the proposed studies, in order to present a comprehensive performance evaluation of the partially coherent FSO links, which are commercially deployed to complement and/or serve numerous wireless communication purposes [157]. In a binary-encoded IM/DD system, the BER is typically used to quantify the probability of making a bit decision error,

where the optical signals (transmitted as a pulse of light to indicate a “1” bit, and no light output for a “0” bit) are susceptible to various channel impairments and noise contributions [6, 42, 95]. For non-real-time data services, the average channel capacity determines the maximum achievable information rate averaged over all possible fading states; since the FSO channel is time-varying due to the turbulence- and PE-induced fluctuations, hence the information carrying capacity is also transient [33, 35, 158]. In the case of block fading (or quasi-static fading) channels, where the channel or the received irradiance intensity remains unchanged for a significantly long period of time, system outages will occur when the irradiance intensity falls below a threshold [24, 159]. Correspondingly, the outage capacity is a useful capacity measure, which presents the maximum rate of transmission, such that the probability of the system being in an outage meets a specified value [32].

3.4.1. Bit Error Rate

For an IM/DD FSO communication link using OOK modulation, the BER can be expressed as [6, 25, 42, 95, 160]:

$$P_e = P_X(0)P_X(e|0) + P_X(1)P_X(e|1)\ ; \tag{3.1}$$

where $P_X(0)$ and $P_X(1)$ denote the probabilities of transmitting “0” and “1” bits, respectively, and $P_X(e|0)$ and $P_X(e|1)$ resemble the conditional bit error probabilities when the transmitted bit is “0” or “1”. Conditioned on the channel state h, the following relation is then obtained:

$$P_X(e|0,h) = P_X(e|1,h) = Q\left(\sqrt{SNR(h)}\right); \tag{3.2}$$

where $Q(\cdot)$ is the Gaussian-Q function given by:

$$Q(y) = \frac{1}{\sqrt{2\pi}}\int_y^{\infty} \exp\left(\frac{-t^2}{2}\right) dt\ . \tag{3.3}$$

With reference to the expression for $SNR(h)$ defined by (2.2), it should be noted that the total noise contributions (i.e., shot noise, dark current noise, thermal noise and background noise) are taken into account by the statistical noise variance σ_n^2, and is assumed constant in the corresponding SNR calculations [6, 24, 34]. Considering the symmetry of the problem with $P_X(0) = P_X(1) = 0.5$ and $P_X(e|0) = P_X(e|1)$, the average BER can be determined by averaging over the PDF of h [94]:

$$P_e = \int_0^{\infty} f_h(h) Q\left(\sqrt{SNR(h)}\right) dh \,. \tag{3.4}$$

3.4.2. Probability of Outage

The instantaneous capacity corresponding to a channel state h is given by [24, 25, 156]:

$$C\big(SNR(h)\big) = \sum_{x=0}^{1} P_X(x) \int_{-\infty}^{+\infty} f(y|x,h) \times \log_2 \left[\frac{f(y|x,h)}{\sum_{m=0,1} f(y|x=m,h) P_X(m)}\right] dy \,; \tag{3.5}$$

where $P_X(x)$ is the probability of the bit being one ($x = 1$) or zero ($x = 0$), with $P_X(x = 0) = P_X(x = 1) = 0.5$, and $f(y|x,h)$ can be expressed as:

$$f(y|x,h) = \begin{cases} \dfrac{1}{\sqrt{2\pi\sigma_n^2}} \exp\left[-\dfrac{y^2}{2\sigma_n^2}\right], & x = 0 \\ \dfrac{1}{\sqrt{2\pi\sigma_n^2}} \exp\left[-\dfrac{(y - 2P_{\mathrm{FSO}}\gamma h)^2}{2\sigma_n^2}\right], & x = 1 \,. \end{cases} \tag{3.6}$$

Since the optical slow-fading channel is random and remains unchanged over a long block of bits, the time-varying channel capacity will not be sufficient to support a maximum data rate, when the instantaneous SNR falls below a threshold [25, 159]. Such occurrence,

known as system outage, can result in a loss of potentially up to 10^9 consecutive bits at a data rate of 10 Gbps, under deep fades scenarios that may last for ~1-100 ms [28]. In this case, the outage probability is an appropriate performance measure of the capacity, which represents the probability that the instantaneous channel capacity C falls below a transmission rate R_0, given by the relation:

$$P_{\text{out}} = \text{Prob}\big(C\big(SNR(h)\big) < R_0\big)\,. \tag{3.7}$$

Since $C(\cdot)$ is monotonically increasing with SNR, P_{out} is the cumulative density function of h evaluated at $h_0 = \sqrt{C^{-1}(R_0)\sigma_n^2/2P_{\text{FSO}}^2\gamma^2}$, thus can be determined equivalently from the expression [24]:

$$P_{\text{out}} = \int_0^{h_0} f_h(h)\,dh\,. \tag{3.8}$$

3.4.3. Average Channel Capacity

The average channel capacity represents the practically achievable information carrying rate (in bits per channel use) through the time-varying fading channel with an arbitrarily small probability of detection error. This can be approached by using channel codes of large block lengths, in order to capture the effects of the channel variations through the codewords [25]. The average capacity $\langle C \rangle$ for a binary-input continuous-output channel is defined as the maximum mutual information between the input to the channel x, and output from the channel y, where the maximum is taken over all input distributions [159, 161]. For a known channel at the receiver:

$$\langle C \rangle = \sum_{x=0}^{1} P_X(x) \int_{-\infty}^{\infty} \int_0^{\infty} f(y|x,h) f_h(h)$$

$$\times \log_2 \left[\frac{f(y|x,h)}{\sum_{m=0,1} f(y|x=m,h) P_X(m)} \right] dh dy \, ; \tag{3.9}$$

where $f(y|x,h)$ can be expressed as:

$$f(y|x,h) = \begin{cases} \frac{1}{\sqrt{2\pi\sigma_n^2}} \exp\left[-\frac{y^2}{2\sigma_n^2} \right], & x = 0 \\ \frac{1}{\sqrt{2\pi\sigma_n^2}} \exp\left[-\frac{(y - 2P_{\text{FSO}}\gamma h)^2}{2\sigma_n^2} \right], & x = 1 \, . \end{cases} \tag{3.10}$$

In the case of unknown channel at the receiver:

$$\langle C \rangle = \sum_{x=0}^{1} P_X(x) \int_{-\infty}^{\infty} f(y|x) \log_2 \left[\frac{f(y|x)}{\sum_{m=0,1} f(y|x=m) P_X(m)} \right] dy \, ; \tag{3.11}$$

where and $f(y|x)$ can be expressed as:

$$f(y|x) = \begin{cases} \frac{1}{\sqrt{2\pi\sigma_n^2}} \exp\left[-\frac{y^2}{2\sigma_n^2} \right], & x = 0 \\ \frac{1}{\sqrt{2\pi\sigma_n^2}} \int_0^{\infty} \exp\left[-\frac{(y - 2P_{\text{FSO}}\gamma h)^2}{2\sigma_n^2} \right] f_h(h) dh \, , & x = 1 \, . \end{cases} \tag{3.12}$$

3.5. Outage Analysis

Recall the proposed system model described in Section 2.2, with the block diagram of the SISO horizontal FSO communication link as presented in Figure 2.1. The FSO link design analysis is carried out under the influence of different operating conditions, such as the weather effects as signified by the visibility V and turbulence strength C_n^2, the PE loss with jitter variance σ_{pe}^2, and the propagation distance L. In addition, system design considerations, which include: the transmitter beam width w_0, receiver aperture diameter D, laser wavelength λ, data rate R_0, transmitted optical power P_{FSO}, and knowledge of CSI are investigated and compared with respect to the performance metrics. The relevant

parameters considered in the performance analysis are provided in Table 3.1; and assumed for the numerical results presented here, unless otherwise specified. These nominal settings are selected by carefully reviewing the relevant parameter values, which have been widely considered and scrutinized [24, 74-76, 90-93].

3.5.1. Outage Probability under Light Fog Condition

Figure 3.1 illustrates the probability of outage P_{out} in terms of the transmitter beam width w_0 for an achievable rate $R_0 = 0.5$ bits/channel use, under the light fog condition at $L = 1.0$ km; and for a variety of receiver aperture diameter D. The simulation settings and weather-dependent parameters considered in the outage analysis are defined in Table 3.1 and Table 3.2, respectively. Recalling the combined channel fading model in Section 2.4.4, P_{out} is obtained by substituting (2.74) into (3.8) for a range of w_0 values varying between 4 mm and 100 mm at a step size of 1 mm, whereby the weak turbulence case (i.e., $\sigma_R^2 = 0.1$)

Table 3.1: Parameters of the partially coherent FSO communication system.

Parameter	Symbol	Typical value
Laser wavelength	λ	1550 nm
Average transmitted optical power	P_{FSO}	10 mW
Photodetector responsivity	γ	0.5 A/W
Noise variance	σ_n^2	10^{-14} A^2
Receiver diameter	D	200 mm
Spatial coherence length	l_c	1.38 mm
Nominal beam width	w_0	50 mm
PE-induced jitter standard deviation	σ_{pe}	30 cm

Table 3.2: Weather-dependent parameters considered in the outage analysis.

Weather conditions	Visibility, V (km)	Atmospheric turbulence strength, C_n^2 (m$^{-2/3}$)	Rytov variance, σ_R^2 (at 1.0 km)
Light fog	0.642	5.0×10^{-15}	0.1
Clear weather	10.0	5.0×10^{-14}	1.0

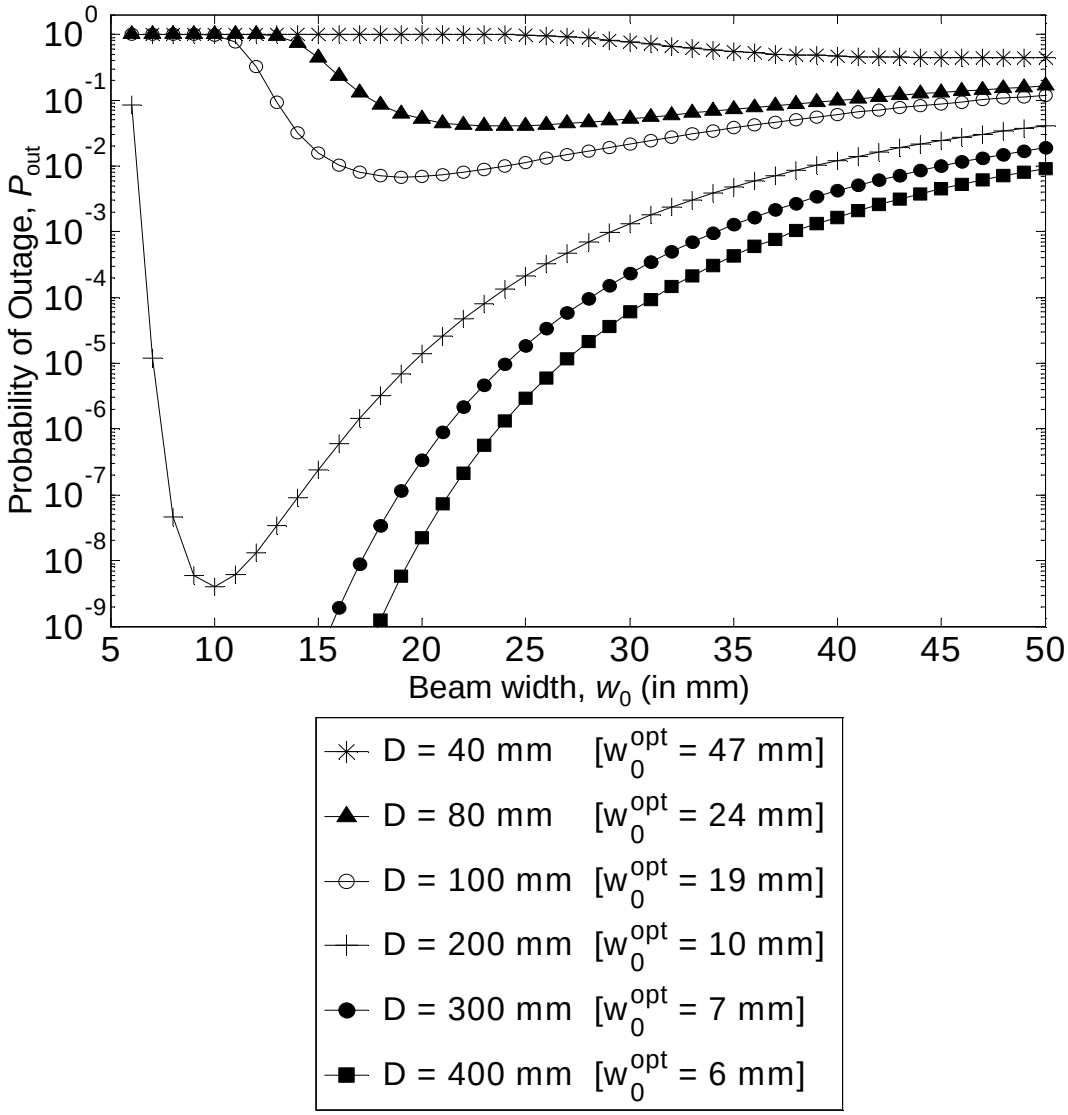

Figure 3.1: Probability of outage in terms of the transmitter beam width under the light fog condition, for $L = 1.0$ km and $R_0 = 0.5$ bits/channel use . For the different receiver aperture sizes D under examined, the optimum beam width w_0^{opt} have been identified and shown here.

is considered here. From Figure 3.1, it is noted that lower P_{out} can be achieved with larger values of D as a result of the aperture-averaging effect, which is evident from the reduction in the scintillation index. For instance, the system performance improves by ~8 orders of magnitude for $D = 200$ mm at $w_0 = 10$ mm, as compared to the remaining cases of D with smaller collecting areas, which experience complete system annihilation. In addition, the

numerical results show that the best performance can be obtained through the selection of an optimum beam width w_0^{opt} for a considered D value; and suggest that the best combination of D and w_0^{opt} enables optimal link design, as w_0^{opt} decreases with larger D. At $L >$ 1.5 km, the FSO link experiences complete system outage, which is non-recoverable albeit optimizing the system design parameters. This is mainly because the absorption and scattering effects due to the presence of atmospheric particles attenuates and destroys the optical beams propagating at longer link distances.

Next, Figure 3.2 depicts the trade-off between the probability of outage P_{out} and the maximum achievable transmission rate R_0, under the light fog condition at $L = 1.0$ km and for $\lambda = \{850, 1064, 1550\}$ nm. Based upon the assumed values of $D = 200$ mm and

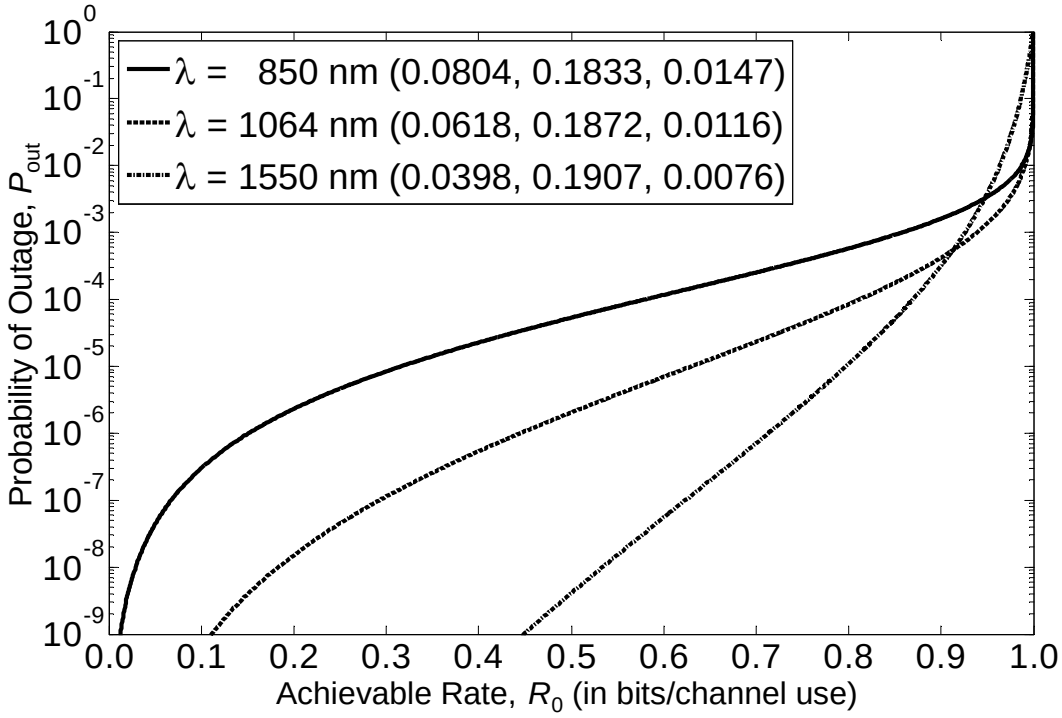

Figure 3.2: Trade-off between the outage probability and maximum achievable rate under the light fog condition, for $L = 1.0$ km, $D = 200$ mm, $w_0 = 10$ mm, and $\lambda = \{850, 1064, 1550\}$ mm. Numerical values in the figure legend refers to $\left(\sigma_I^2(0), A_g, \sigma_I^2(D)\right)$.

$w_0 = 10$ mm, P_{out} is determined through the substitution of (2.74) into (3.8) for all the considered R_0 values ranging from 0 to 1. It is observed that FSO links operating at $\lambda = 1550$ nm can achieve a significantly larger R_0 with reduced aperture-averaged scintillation index $\sigma_I^2(D)$, as compared to smaller laser wavelengths. For instance, at $P_{\text{out}} = 10^{-6}$, an achievable rate in excess of 0.7 bits/channel use is attainable at $\lambda = 1550$ nm, while much smaller R_0 of 0.15 bits/channel use and 0.45 bits/channel use are achieved at $\lambda = 850$ nm and $\lambda = 1064$ nm, respectively. This implies that the adopted wavelength is an important link design criterion for maximizing the transmission rate with low outage probability.

3.5.2. Outage Probability under Clear Weather Condition

Figure 3.3 presents the probability of outage P_{out} against the transmitter beam width w_0 for R_0 = 0.5 bits/channel use, under the clear weather condition at $L = 3.5$ km (see Table 3.2), where different values of D are considered. In the case of a stronger turbulence with $\sigma_R^2 = 1.0$, P_{out} is obtained by substituting (2.75) into (3.8) for different w_0 values ranging from 2 mm to 200 mm at a fixed interval of 2 mm. Under high-visibility atmospheric conditions, FSO links can achieve greater propagation distances. This is mainly because the optical beams are less susceptible to attenuation caused by absorption and scattering, as indicated by a higher h_l (= 0.7006), albeit requiring a larger w_0 to mitigate the impact of scintillation due to the strong turbulence and misalignment-induced fading. It is evident from the numerical results that a larger w_0^{opt} of 46 mm is required for $D = 200$ mm, as compared to the light fog condition (see Figure 3.1), in order to produce a more coherent laser beam with greater resilience to the scintillation effect. This in turn results in a larger beam spot size at the receiver, which mitigates the jitter-induced PE loss while enabling effective collection of the optical signal by the enlarged receiver aperture.

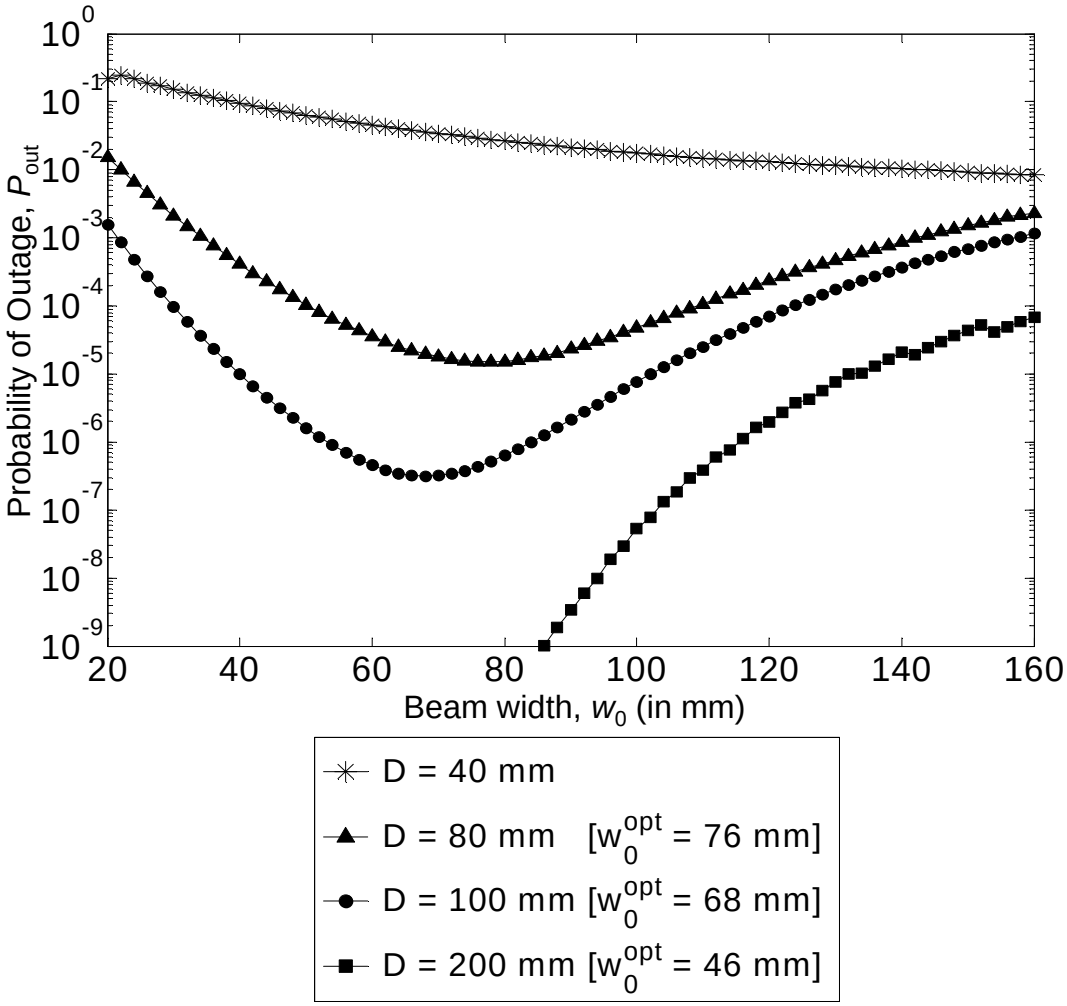

Figure 3.3: Probability of outage as a function of the transmitter beam width under the clear weather scenario, for $L = 3.5$ km and $R_0 = 0.5$ bits/channel use. The optimum beam width is identified and shown for various receiver aperture sizes, except for $D = 40$ mm which does not have an optimal value.

On the other hand, the optimal value is generally in excess of 60 mm for smaller aperture sizes under investigation, except for $D = 40$ mm, in which significant reduction in P_{out} is unattainable albeit manifold increase in w_0.

The trade-off between the probability of outage P_{out} and the maximum achievable transmission rate R_0 for $\lambda = \{850, 1064, 1550\}$ nm, is also examined for the high-visibility strong-turbulence scenario as shown in Figure 3.4. Taking into account the assumed

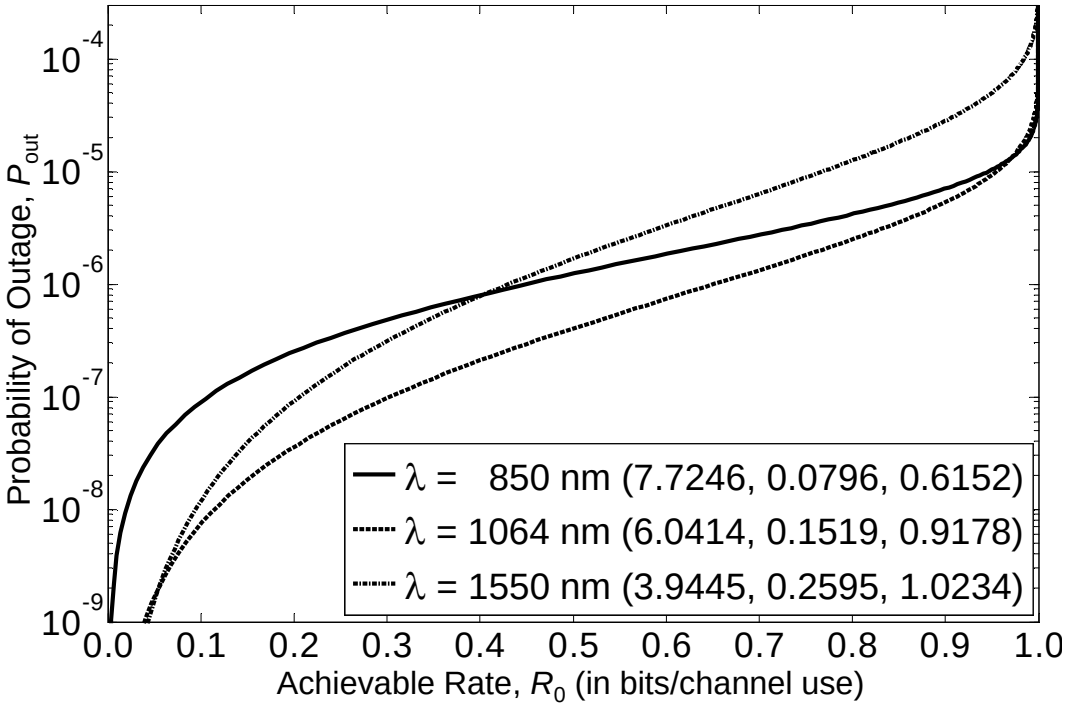

Figure 3.4: Trade-off between the outage probability and maximum achievable rate under the clear weather scenario, for $L = 3.5$ km, $D = 100$ mm, $w_0 = 50$ mm, and $\lambda = \{850, 1064, 1550\}$ mm. Numerical values in the figure legend refers to $\left(\sigma_I^2(0), A_g, \sigma_I^2(D)\right)$.

parameters of $L = 3.5$ km, $D = 100$ mm, and $w_0 = 50$ mm, P_{out} is found through the substitution of (2.75) into (3.8) for the different R_0 values varying between 0 and 1. The advantage of adopting a particular laser wavelength on the FSO link performance is less distinctive in this case. This observation can be explained by the fact that the optical channel fading characteristics have altered the propagation properties of the laser beam, thereby concluding that the optimization of capacity metrics is best achieved through proper selection of D and w_0 for a known λ and/or increasing the transmit power P_{FSO}.

3.6. The Aperture Averaging Effect

The effect of aperture-averaging on horizontal FSO communication links with spatially partially coherent laser beams is studied here, in order to examine the two

distinctive advantages of using enlarged receiver apertures, while taking into account numerous link design considerations. In principle, aperture averaging reduces the turbulence-induced scintillation level through the shifting of the relative frequency content of the irradiance power spectrum towards lower frequencies, which averages out the fastest fluctuations; and potentially mitigates the PE loss, as can be observed from the reduction in the normalized jitter $2\sigma_{pe}/D$.

Table 3.3: Weather-dependent parameters considered in the aperture-averaging studies.

Weather conditions	**Visibility, V (km)**	**Atmospheric turbulence strength, C_n^2 ($m^{-2/3}$)**	**Link distance, L (km)**	**Rytov variance, σ_R^2**
Light fog	0.642	5.0×10^{-15}	1.0	0.10
Moderate fog	0.480	2.0×10^{-15}	1.0	0.04
Dense fog	0.150	1.0×10^{-15}	1.0	0.02
Clear weather	10.0	5.0×10^{-14}	1.0	1.00
			4.5	15.69
			7.5	40.02
		3.1230×10^{-16}	7.5	0.25
		1.1244×10^{-14}		9.00
		1.8739×10^{-14}		15.00

3.6.1. Error Performance due to Atmospheric Effects

Figure 3.5 illustrates the average BER $\langle BER \rangle$ in terms of the average transmitted optical power P_{FSO}, under different light fog scenarios at $L = 1.0$ km, and for a range of D. The simulation settings and weather-dependent parameters considered in the aperture averaging studies are defined in Table 3.1 and Table 3.3, respectively. In the occurrence of low-visibility conditions with typically weak turbulences (i.e., $\sigma_R^2 \ll 1.0$), $\langle BER \rangle$ is calculated for range of P_{FSO} values by employing (2.74) and (3.3) in (3.4). It is noted that a lower $\langle BER \rangle$ can be achieved with much smaller transmit power requirement by utilizing receiver apertures of larger D; in which a substantial P_{FSO} reduction of >20 dB can be

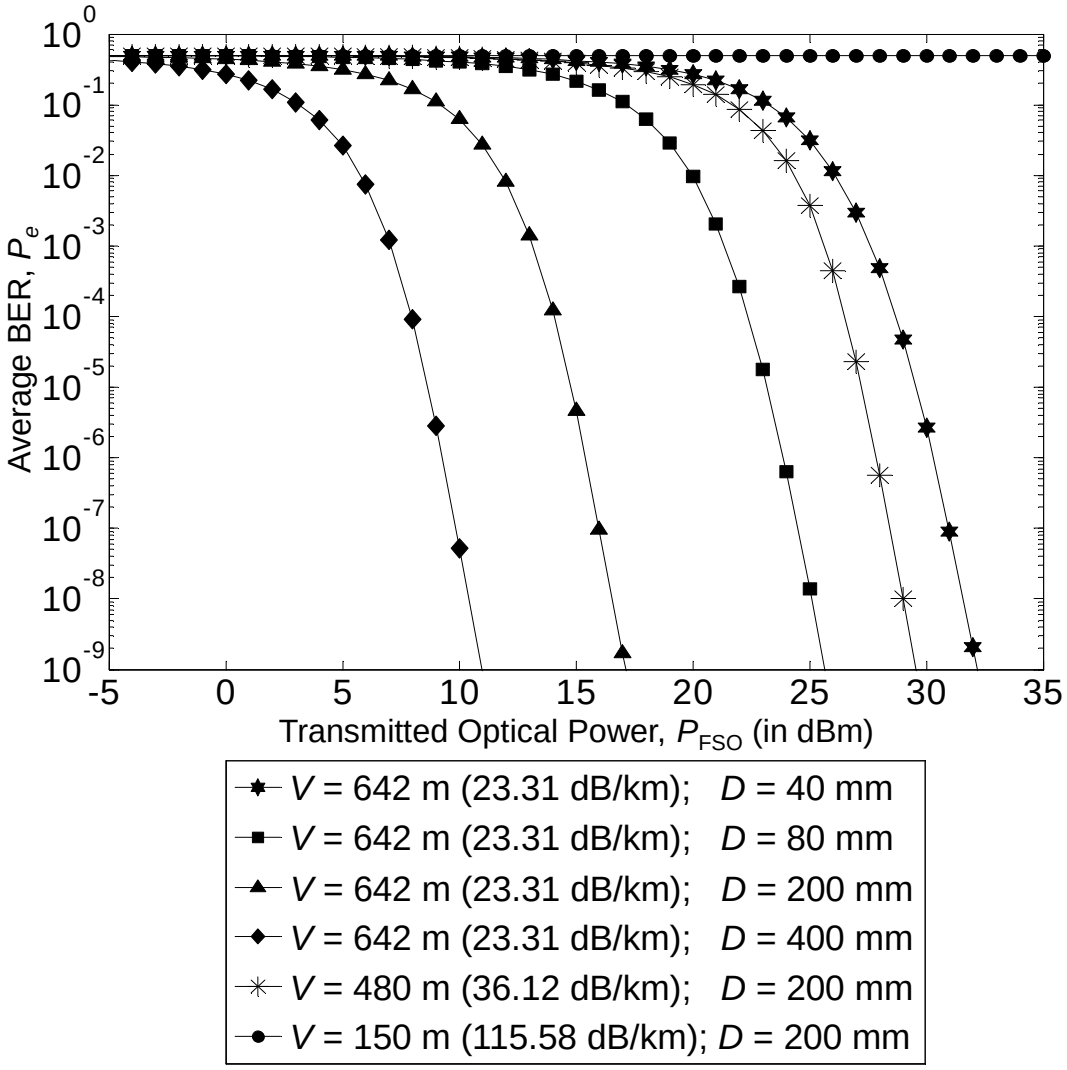

Figure 3.5: Average BER in terms of the transmitted optical power under different light fog conditions at $L = 1.0$ km. In the figure legend, the numerical values (in parenthesis) refer to the attenuation coefficient σ.

made possible with $D = 400$ mm, for $\langle BER \rangle = 10^{-9}$ and $V = 0.642$ km, as compared to the case of $D = 40$ mm. In addition, the system under study would require higher P_{FSO} under the moderate fog condition ($V = 0.480$ km), to compensate for the increase in atmospheric attenuation ($\sigma = 36.12$ dB/km); in which a greater P_{FSO} requirement of ~13 order-of-magnitude is observed for $\langle BER \rangle = 10^{-9}$, albeit the introduction of an enlarged receiver aperture with $D = 200$ mm. Under the most extreme low-visibility case ($V = 0.150$ km,

$\sigma = 115.58$ dB/km), the FSO link experiences complete system annihilation, which is non-recoverable albeit deliberately increasing the values of D and P_{FSO}.

Next, Figure 3.6 depicts the variation of the average BER $\langle BER \rangle$ against the average transmitted optical power P_{FSO}, for the clear weather conditions with $V = 10.0$ km. In particular, the fading reduction resulting from aperture averaging is evaluated for a range of considered D values, with $C_n^2 = 5.0 \times 10^{-14}$ m$^{-2/3}$ ($\sigma_R^2 = 1.00$) at $L = 1.0$ km; and the turbulence-induced scintillation effect is also observed for two other cases of L at 4.5 km ($\sigma_R^2 = 15.69$) and 7.5 km ($\sigma_R^2 = 40.02$). Please refer to Table 3.3 for complete details of the relevant weather-dependent parameters. In the event of stronger turbulences with $\sigma_R^2 \geq 1.0$ under clear weather conditions, $\langle BER \rangle$ is determined for range of P_{FSO} values by taking into account (2.75) and (3.3) in (3.4). In general, the FSO link has a lower P_{FSO} requirement as compared to the low-visibility cases (Figure 3.5) for the same system configuration, which is mainly due to the significantly lower atmospheric attenuation of $\sigma = 0.4508$ dB/km. The introduction of a receiver aperture with larger D enhances the link performance, in which P_{FSO} reduction in excess of 25 dB is observed for $\langle BER \rangle = 10^{-9}$ with $D = 400$ mm, as compared to the case of $D = 40$ mm. At greater link distances, the increase in scintillation level (indicated by larger σ_R^2) results in the skewing of the mean BER curve, exhibiting much smaller step size in $\langle BER \rangle$ reduction with respect to the same increment in the P_{FSO}. These observations are particularly prominent in the cases of smaller D, which can be explained by the alteration in the irradiance profile from a normally-distributed pattern towards a distribution with longer tails in the infinite direction. The skewness of the density distribution denotes the extent of the optical intensity fluctuations as the channel inhomogeneity increases.

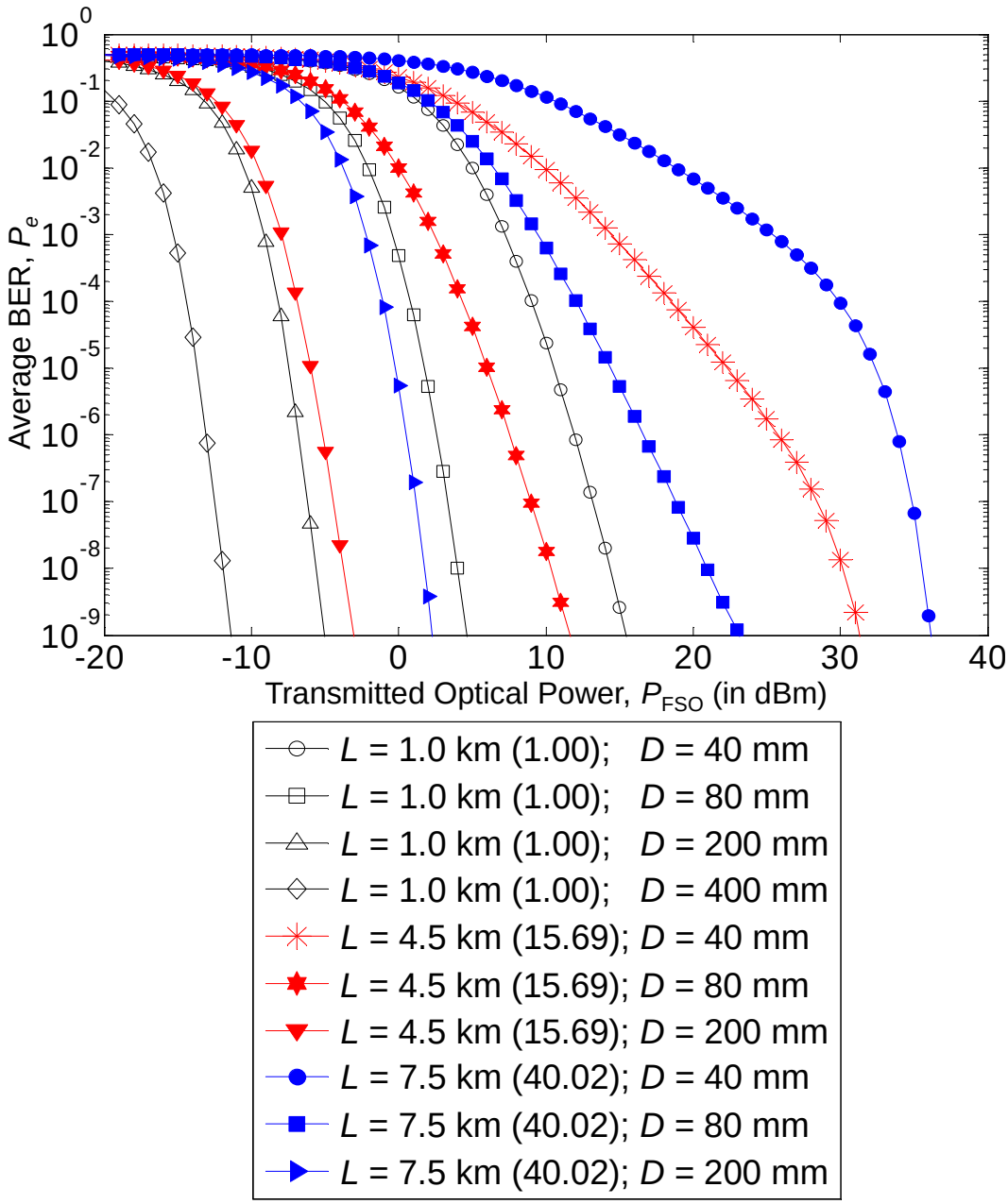

Figure 3.6: Average BER in terms of the transmitted optical power in the strong turbulence regime at $L = \{1.0, 4.5, 7.5\}$ km. In the figure legend, the numerical values (in parenthesis) refer to the Rytov variance σ_R^2.

Figure 3.7(a) presents the average BER $\langle BER \rangle$ as a function of the average electrical SNR $\langle SNR \rangle$, under the light fog condition with $V = 0.642$ km and $C_n^2 = 5.0 \times 10^{-15}$ m$^{-2/3}$ ($\sigma_R^2 = 0.1$) at $L = 1.0$ km (see Table 3.3); taking into account the effect of D and comparing with respect to the AWGN (i.e., no turbulence) case. The calculation of $\langle BER \rangle$

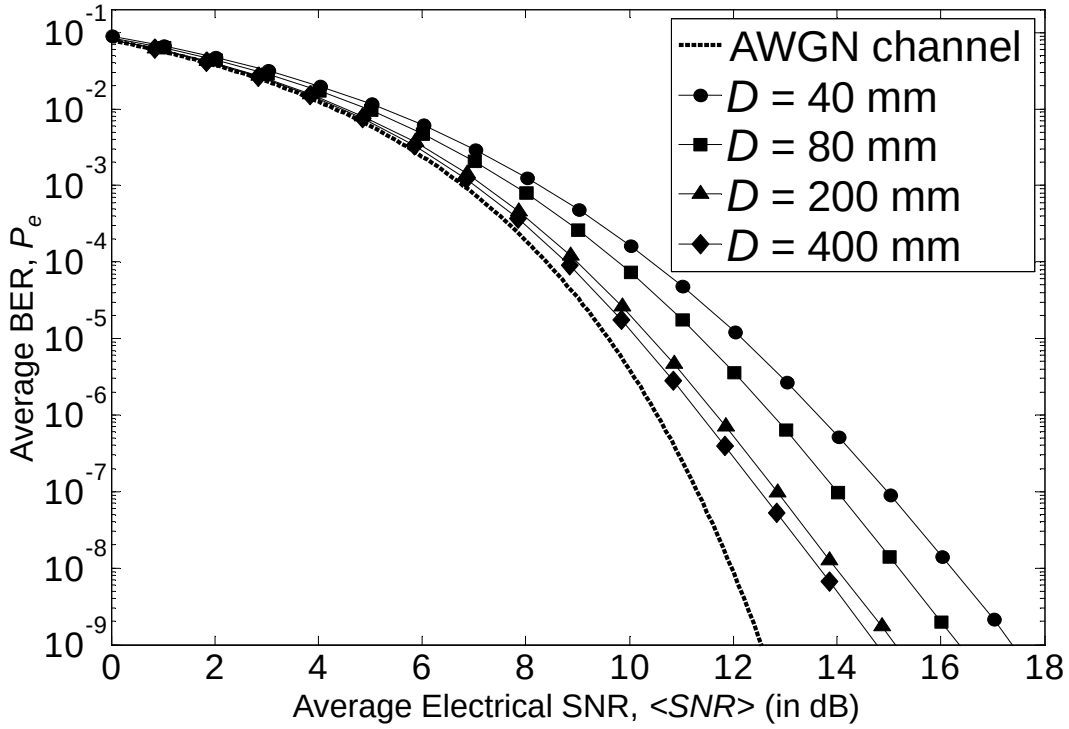

(a)

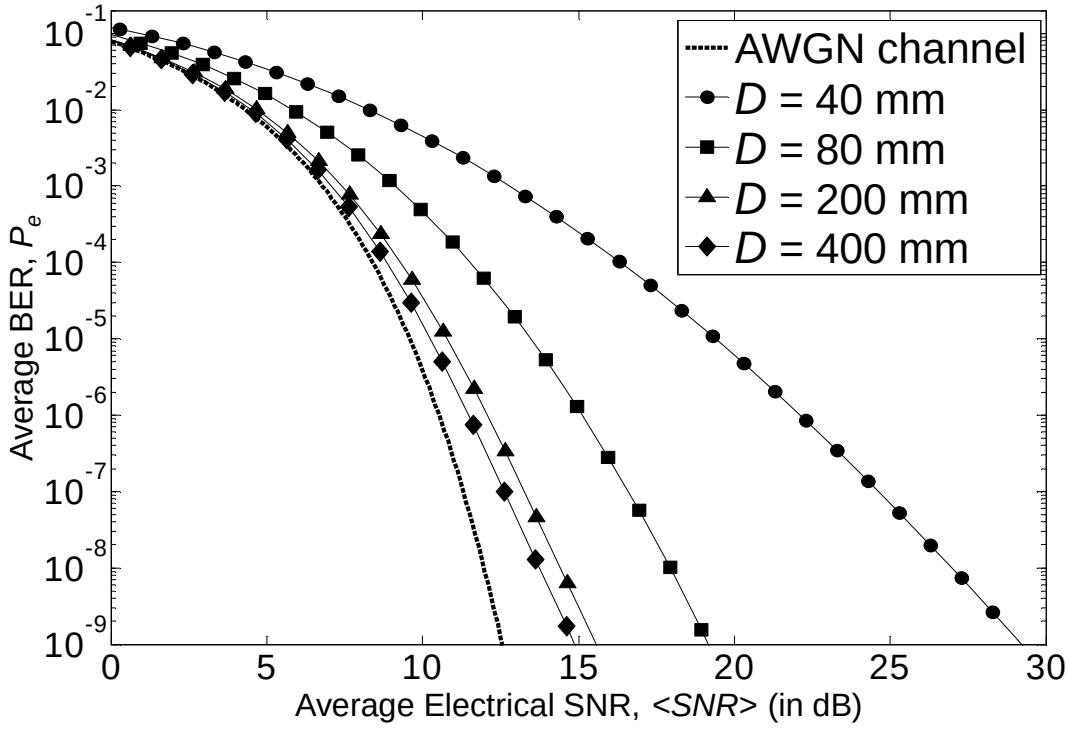

(b)

Figure 3.7: Average BER as a function of the average electrical SNR under the (a) light fog and (b) clear weather conditions at $L = 1.0$ km, taking into account the effect of D and comparing with the AWGN (non-turbulent) case.

presented in Figure 3.7(a) and Figure 3.7(b) involves the same approach used for Figure 3.5 and Figure 3.6, respectively; whereas the $\langle SNR \rangle$ values are found by integrating (2.2) over all the possible channel fading states h. The numerical results show that a two-fold reduction in the mean BER is observed for $\langle SNR \rangle = 15$ dB with $D = 400$ mm, as compared to the case of $D = 40$ mm; thus bringing the resulting $\langle BER \rangle$ curve closer to the ideal non-turbulent case, albeit deviating from the reference with a 2-dB gap in the mean SNR for achieving a $\langle BER \rangle$ of 10^{-9}. Performance enhancement due to aperture averaging is further prevalent in the strong turbulence regime ($V = 10.0$ km, $\sigma_R^2 = 1.0$ at $L = 1.0$ km) as depicted in Figure 3.7(b), whereby the resulting scintillation reduction potentially decreases the average BER by more than four order-of-magnitude for $\langle SNR \rangle > 15$ dB with $D = 400$ mm, as compared to the case of $D = 40$ mm. In effect, these observations can be justified by the shifting of the relative frequency content of the irradiance power spectrum toward lower frequencies due to the aperture averaging effect; in essence, averaging out the fastest fluctuations, thereby resulting in scintillation reduction and lower BER attainment [11, 40].

3.6.2. Average Channel Capacities due to Channel State Information

Figure 3.8(a) presents the average channel capacity $\langle C \rangle$ as a function of the average electrical SNR $\langle SNR \rangle$ for $D = \{40, 80, 200, 400\}$ mm, assuming the CSI is known to the receiver. The light fog condition is considered here, with $V = 0.642$ km, $C_n^2 = 5.0 \times 10^{-15}$ m$^{-2/3}$ ($\sigma_R^2 = 0.1$) at $L = 1.0$ km (see Table 3.3). In the case of a known channel at the receiver under weak turbulence condition, $\langle C \rangle$ is determined by substituting (2.74) and (3.10) into (3.9) for different values of $\langle SNR \rangle$. Under the visibility-impaired weak turbulence condition, a faster increase in the average capacity with respect to the $\langle SNR \rangle$ is observed, in which the maximum channel capacity is approached at higher mean SNR

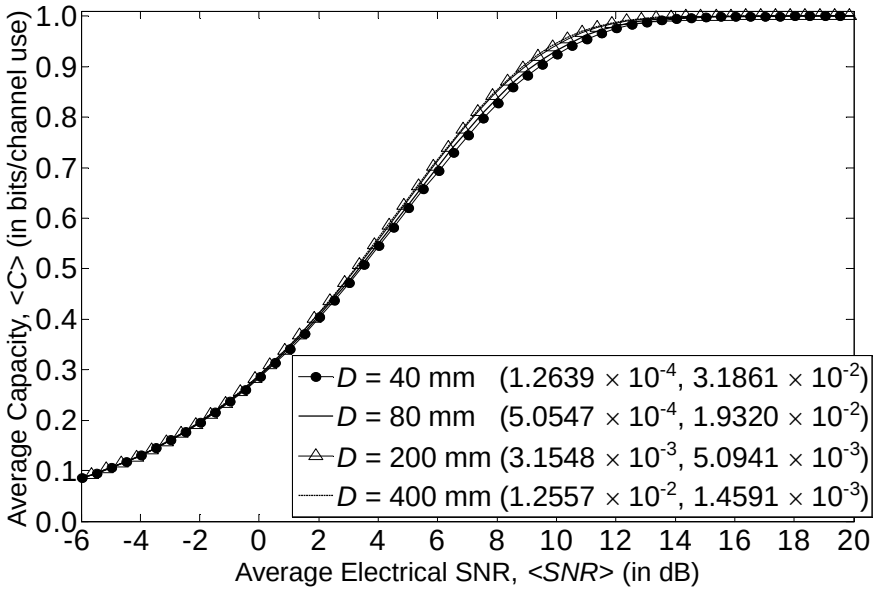

(a)

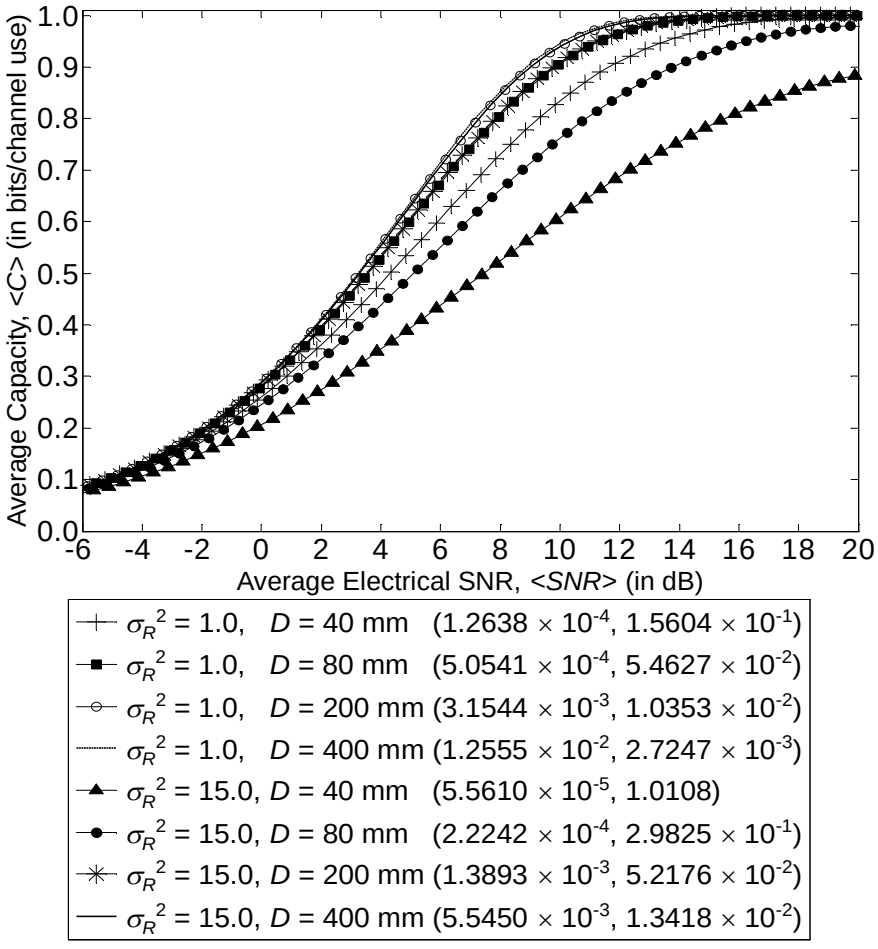

(b)

Figure 3.8: Average channel capacity as a function of the average electrical SNR for different receiver aperture dimension, under the (a) light fog ($V = 0.642$ km, $\sigma_R^2 = 0.1$ at $L = 1.0$ km); and (b) clear weather $V = 10.0$ km, $\sigma_R^2 = 1.0$ at $L = 1.0$ km, $\sigma_R^2 = 15.0$ at $L = 7.5$ km) conditions. The CSI is assumed known to the receiver.

values in excess of 14 dB. In addition, near-identical behaviour is noted for all the cases of D under investigation, albeit observing an increase in the fraction of collected power A_0 and a reduction in the aperture-averaged scintillation level $\sigma_I^2(D)$ (see figure legend). These observations reveal that $\langle C \rangle$ is almost independent of D, since the effects of scintillations and PEs are less dominant, as compared to the beam extinction resulting from the scattering and absorption of atmospheric particles, which can be compensated by increasing the transmit optical power of the laser beam.

The corresponding results for the clear weather scenarios are illustrated in Figure 3.8(b), with $V = 10.0$ km, $C_n^2 = 5.0 \times 10^{-14}$ m$^{-2/3}$ at $L = 1.0$ km ($\sigma_R^2 = 1.0$), and $C_n^2 = 1.8739 \times 10^{-14}$ m$^{-2/3}$ at $L = 7.5$ km ($\sigma_R^2 = 15.0$) (see Table 3.3). In the event of a known channel at the receiver for various moderate-to-strong turbulence cases, $\langle C \rangle$ is determined by substituting (2.75) and (3.10) into (3.9) for different values of $\langle SNR \rangle$. In comparison to the light fog condition (Figure 3.8(a)), it is evident that the average channel capacity is more susceptible to the adverse effects of atmospheric turbulence, which imposes a higher scintillation level and PE loss, as signified by a larger $\sigma_I^2(D)$ and ξ values, respectively. At $\sigma_R^2 = 1.0$, the average capacity increases at a relatively slower rate for $D = 40$ mm, as compared to the remaining cases; and then approaches the maximum channel capacity for $\langle SNR \rangle > 16$ dB. It is evident that maximum capacity enhancement can be attained with larger receiver apertures of $D = \{200, 400\}$ mm, in which near-optimal channel capacities of more than 0.99 bits/channel use are achieved for $\langle SNR \rangle \geq 14$ dB. Furthermore, a larger penalty on the FSO channel capacity is observed at a longer link distance of $L = 7.5$ km with $\sigma_R^2 = 15.0$, which is particularly pronounced for larger $\langle SNR \rangle$ values; where it is shown that there is significant variation in $\langle C \rangle$ for all the considered D values, with a maximum deviation of 0.31 bits/channel use at $\langle SNR \rangle = 14$ dB. It is noted that the average

capacity increases at a much slower rate for the cases of $D = \{40, 80\}$ mm, and approaches their respective values well below the maximum capacity. However, improvement in the channel capacity of more than 25% can be made possible for $\langle SNR \rangle$ in excess of 10 dB with $D = 400$ mm.

Figure 3.9 depicts the average capacity $\langle C \rangle$ against the average electrical SNR $\langle SNR \rangle$ for the weak and moderate-to-strong turbulence regimes, with $C_n^2 = 3.1230\times10^{-16}$ $m^{-2/3}$ ($\sigma_R^2 = 0.25$) and $C_n^2 = 1.1244\times10^{-14}$ $m^{-2/3}$ ($\sigma_R^2 = 9.00$), respectively (see Table 3.3). The effect of PEs, as signified by the normalized jitter $2\,\sigma_{pe}/D$, is examined for a variety of D values, with $L = 7.5$ km and $V = 10$ km; and for the cases of known (i.e., (3.9) and (3.10)) and unknown channels (i.e., (3.11) and (3.12)) at the receiver. In the weak turbulence regime (Figure 3.9(a)), a faster increase in the average capacity with respect to the SNR is observed, showing less variation between the known and unknown channel cases for all the considered D values; in which the maximum channel capacity is approached at higher SNR values in excess of 16 dB. The variation between known and unknown channels is larger for the moderate-to-strong turbulence scenario (Figure 3.9(b)), and is prevalent under the influence of PEs with $2\sigma_{pe}/D = 15.0$; where it is noted that an average capacity gap of ~0.15 bits/channel use at $\langle SNR \rangle = 14$ dB. This implies that greater penalty will be imposed upon the channel capacity under the combined effects of turbulence and PEs, and without knowledge of the channel state conditions. Nevertheless, the introduction of larger receiver aperture promotes capacity enhancement and potentially minimizes the observed gap; in which a notable improvement in $\langle C \rangle$ of ~0.46 bits/channel use can be achieved at $\langle SNR \rangle = 14$ dB with $D = 400$ mm, albeit not knowing the channel state at the receiver. In addition, $\langle C \rangle$ exhibits near-identical behaviour with negligibly small variation for both

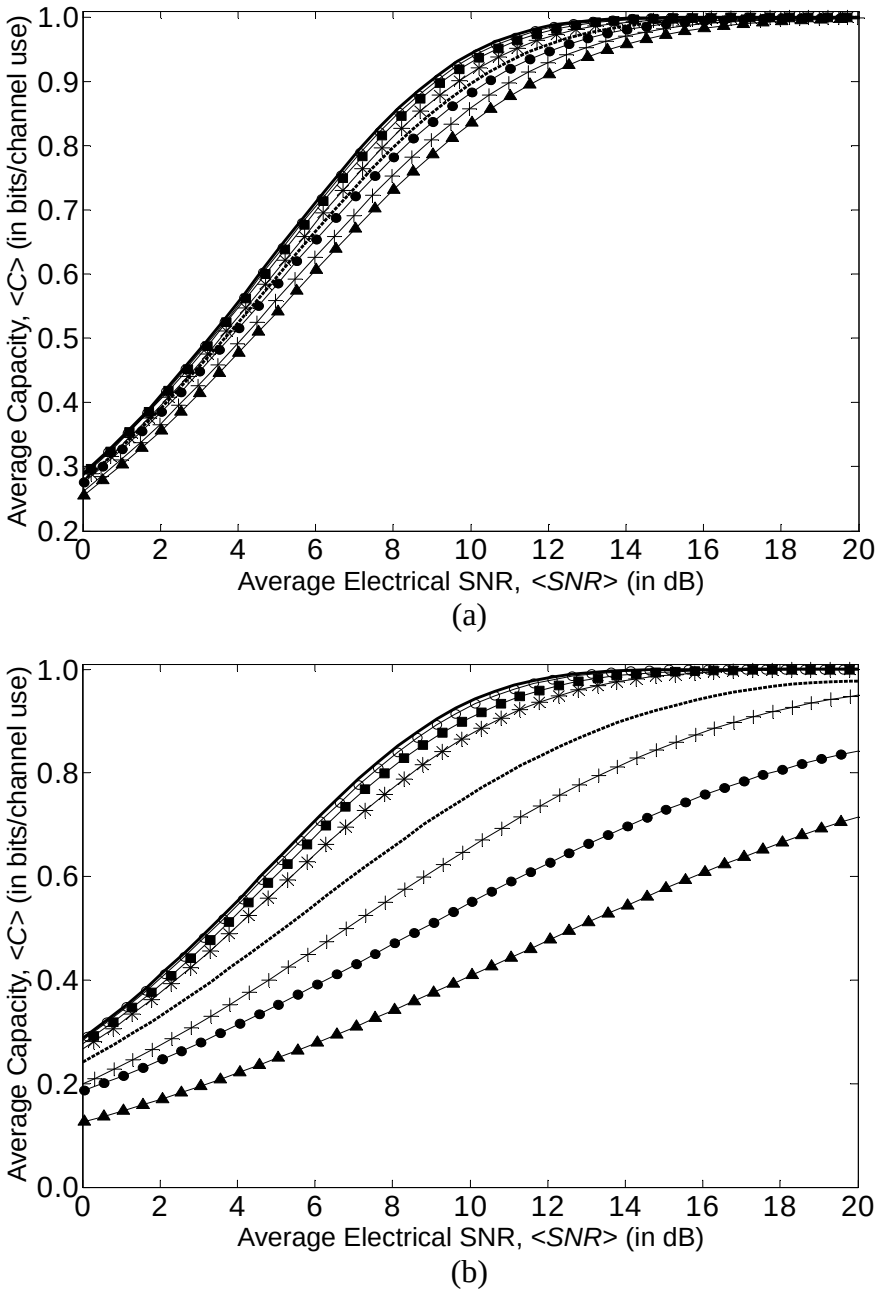

Figure 3.9: Average channel capacity in terms of the average electrical SNR for the (a) weak ($\sigma_R^2 = 0.25$) and (b) moderate-to-strong ($\sigma_R^2 = 9.00$) turbulence regimes, where $V = 10.0$ km and $L = 7.5$ km. The effect of PEs, as signified by the normalized jitter, is examined for the cases of known and unknown channels at the receiver.

channel cases with $D = 400$ mm; thus approaching an asymptotic limit of 1.0 bits/channel use for $\langle SNR \rangle \geq 14$ dB.

3.7. Beam Width Optimization

3.7.1. Dependence on Link Design Criteria

In Figure 3.10, the relationship between the transmitter beam width w_0 on the average channel capacity $\langle C \rangle$ (see (3.11) and (3.12)) is examined, in the presence of atmospheric turbulence and PEs, given that the channel state is unknown to the receiver. The weak ($\sigma_R^2 = 0.25$) and moderate-to-strong ($\sigma_R^2 = 9.00$) turbulence conditions are considered here, for $L = 7.5$ km, $V = 10.0$ km and $\langle SNR \rangle = 14$ dB. The simulation settings and weather-dependent parameters considered in the present beam width optimization studies are defined in Table 3.1 and Table 3.4, respectively. It is evident that the FSO channel capacity is susceptible to the adverse effects of turbulence-induced scintillations and PEs, in which this phenomenon is particularly prevalent in the moderate-to-strong turbulence case (Figure 3.10(b)); whereby the FSO link suffers performance degradation with a significant reduction of 0.55 bits/channel use, under the severe PE loss of $2\sigma_{pe}/D = 19.5$ for $w_0 = 4$ cm, as compared to the weak turbulence condition (Figure 3.10(a)) with a negligibly small variation of < 0.05 bits/channel use. Another interesting observation is made here, showing that the FSO channel capacity is in fact dependent on the beam width; and changing the w_0 value affects the achievable capacity under different atmospheric channel conditions. Correspondingly, this reveals the importance of finding an optimal w_0 value and adjusting the parameter to maximize $\langle C \rangle$; and hence, w_0 is a vital parameter in the FSO link design consideration.

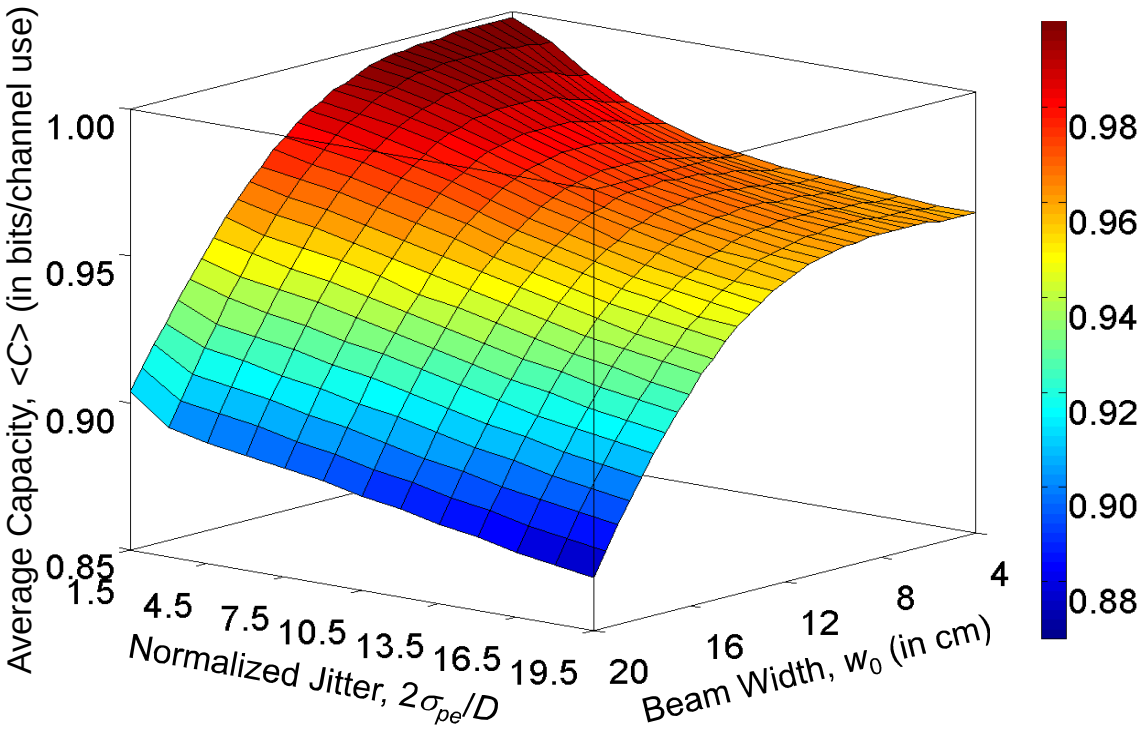

(a)

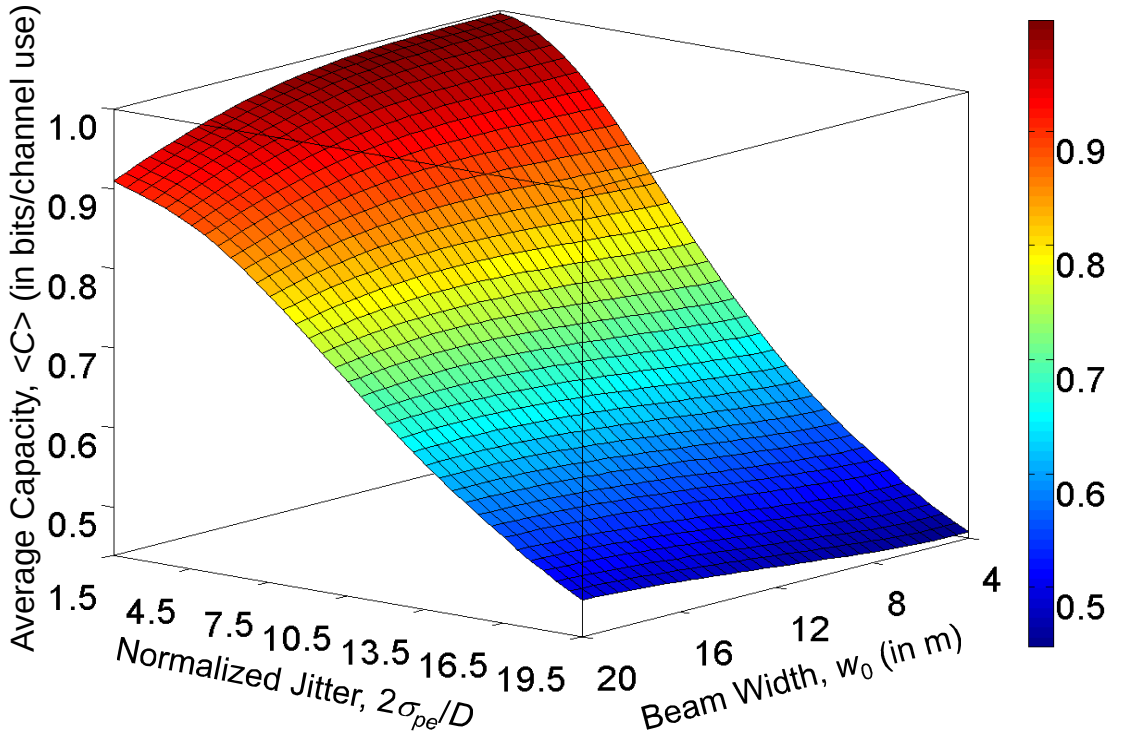

(b)

Figure 3.10: Relationship between the average channel capacity, transmitter beam width and PE loss, for $V = 10.0$ km, $L = 7.5$ km, $\langle SNR \rangle = 14$ dB, and an unknown channel at the receiver. The (a) weak ($\sigma_R^2 = 0.25$) and (b) moderate-to-strong ($\sigma_R^2 = 9.00$) turbulence cases are considered.

Table 3.4: Weather-dependent parameters considered in the beam width optimization studies.

	Visibility, V (km)	10.0		
	Atmospheric loss, σ	0.4665		
		Atmospheric turbulence strength, C_n^2 ($m^{-2/3}$)		
	Link distance, L (km)	**4.5**	**7.5**	**18.0**
Rytov variance, σ_R^2	0.10	3.1869×10^{-16}	1.2493×10^{-16}	2.5097×10^{-17}
	0.15	4.7804×10^{-16}	1.8739×10^{-16}	3.7645×10^{-17}
	0.20	6.3739×10^{-16}	2.4986×10^{-16}	5.0191×10^{-17}
	0.25	7.9659×10^{-16}	3.1232×10^{-16}	6.2739×10^{-17}
	0.30	9.5609×10^{-16}	3.7479×10^{-16}	7.5287×10^{-17}
	0.40	1.2748×10^{-15}	4.9971×10^{-16}	1.0038×10^{-16}
	0.50	1.5935×10^{-15}	6.2464×10^{-16}	1.2548×10^{-16}
	0.60	1.9122×10^{-15}	7.4957×10^{-16}	1.5058×10^{-16}
	0.70	2.2309×10^{-15}	8.7450×10^{-16}	1.7567×10^{-16}
	0.80	2.5496×10^{-15}	9.9942×10^{-16}	2.0077×10^{-16}
	0.90	2.8683×10^{-15}	1.1244×10^{-15}	2.2586×10^{-16}
	1.00	3.1869×10^{-15}	1.2493×10^{-15}	2.5097×10^{-16}
	1.50	4.7804×10^{-15}	1.8739×10^{-15}	3.7645×10^{-16}
	2.00	6.3739×10^{-15}	2.4986×10^{-15}	5.0191×10^{-16}
	3.00	9.5609×10^{-15}	3.7478×10^{-15}	7.5287×10^{-16}
	4.00	1.2748×10^{-14}	4.9971×10^{-15}	1.0038×10^{-15}
	5.00	1.5935×10^{-14}	6.2464×10^{-15}	1.2548×10^{-15}
	6.00	1.9122×10^{-14}	7.4957×10^{-15}	1.5058×10^{-15}
	7.00	2.2309×10^{-14}	8.7450×10^{-15}	1.7567×10^{-15}
	8.00	2.5496×10^{-14}	9.9942×10^{-15}	2.0077×10^{-15}
	9.00	2.8683×10^{-14}	1.1244×10^{-14}	2.2586×10^{-15}
	10.00	3.1870×10^{-14}	1.2493×10^{-14}	2.5097×10^{-15}
	12.00	3.8244×10^{-14}	1.4991×10^{-14}	3.0115×10^{-15}
	14.00	4.4618×10^{-14}	1.7490×10^{-14}	3.5134×10^{-15}
	16.00	5.0992×10^{-14}	1.9989×10^{-14}	4.0153×10^{-15}
	18.00	5.7366×10^{-14}	2.2487×10^{-14}	4.5172×10^{-15}
	20.00	6.3740×10^{-14}	2.4986×10^{-14}	5.0191×10^{-15}
	22.00	7.0114×10^{-14}	2.7484×10^{-14}	5.5211×10^{-15}
	24.00	7.6488×10^{-14}	2.9983×10^{-14}	6.0230×10^{-15}
	26.00	8.2862×10^{-14}	3.2481×10^{-14}	6.5249×10^{-15}
	28.00	8.9236×10^{-14}	3.4980×10^{-14}	7.0268×10^{-15}
	30.00	9.5610×10^{-14}	3.7478×10^{-14}	7.5287×10^{-15}
	32.00	1.0198×10^{-13}	3.9977×10^{-14}	8.0307×10^{-15}
	34.00	1.0836×10^{-13}	4.2476×10^{-14}	8.5326×10^{-15}
	36.00	1.1473×10^{-13}	4.4974×10^{-14}	9.0345×10^{-15}

In Figure 3.11, the present analysis is extended to investigate the effects of beam width on the average channel capacity under the influence of a variety of turbulence strength (as signified by σ_R^2 in (2.40)); taking into account the clear weather condition at $L = \{4.5, 7.5, 18.0\}$ km , with $V = 10$ km , $2\sigma_{pe}/D = 12.0$ and $\langle SNR \rangle = 14$ dB . At $L = 4.5$ km (Figure 3.11(a)), near-optimal $\langle C \rangle$ in excess of 0.85 bits/channel use can be approached in the weak turbulence regime ($\sigma_R^2 \leq 1.0$), with optical beams of smaller size ($w_0 = \{3, 8\}$ cm); whereas performance degradation is observed with increasing beam width. For instance, the average capacity suffers a substantial reduction of 0.48 bits/channel use when w_0 is intentionally increased from 3 cm to 24 cm at $\sigma_R^2 = 0.1$; and exhibits a rather persistent behaviour at $\langle C \rangle \approx 0.5$ bits/channel use, for σ_R^2 values ranging from 0.1 to 10.0, and increases thereafter albeit giving the worst performance for all the considered w_0 values. At a longer link distance of $L = 7.5$ km (Figure 3.11(b)), it is observed that smaller beam widths ($w_0 = \{5, 10\}$ cm) are desirable at $\sigma_R^2 \leq 1.0$ with $\langle C \rangle > 0.83$ bits/channel use , but gives the lowest average capacity attainment in the stronger turbulence regime of $\sigma_R^2 \geq 10.0$. In particular, it is noted that the optimal $\langle C \rangle$ can be achieved with $w_0 = 20$ cm in the intermediate turbulence regime of $\sigma_R^2 = 2.0$ to 7.0. The numerical results presented for the case of $L = 18.0$ km (Figure 3.11(c)) also exhibits similar behaviour, showing that $\langle C \rangle > 0.90$ bits/channel use can be achieved with $w_0 =$ 20 to 40 cm for $\sigma_R^2 \leq 5.0$, whereas performance degradation is observed for the remaining cases of $w_0 = \{60, 90\}$ cm, and vice versa. These observations can be explained by the fact that the PCB suffers substantial alteration in its beam profile/characteristics when propagating through free-space, which is mainly contributed by the combined effects of the turbulence-induced scintillation and beam wander; thereby resulting in the variation of the channel capacity for different σ_R^2. In addition, link distance remains as another important link design criterion, since greater L corresponds to stronger turbulence; which in turn

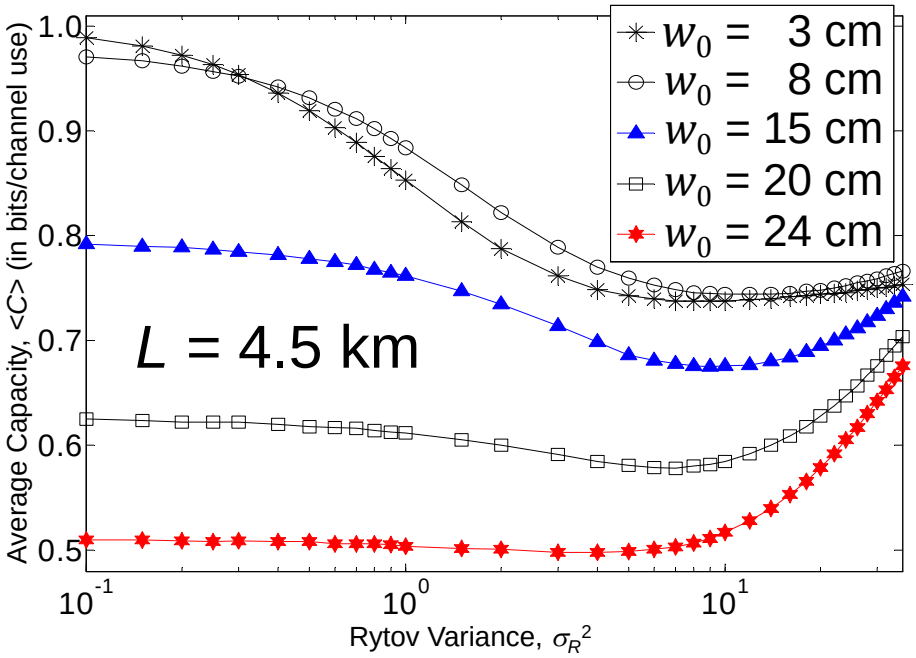

(a)

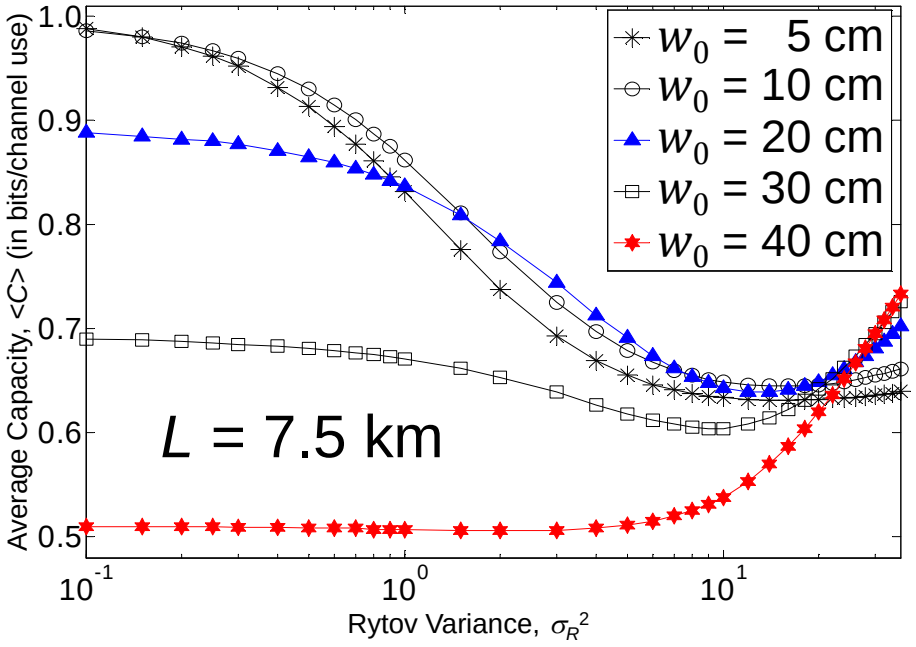

(b)

requires a larger optimal w_0 value for the cases of $L = 7.5$ km (Figure 3.11(b)) and $L = 18.0$ km (Figure 3.11(c)), as compared to $L = 4.5$ km (Figure 3.11(a)), under a significant PE loss of $2\sigma_{pe}/D = 12.0$, as evident from the observations made for $\sigma_R^2 \geq$

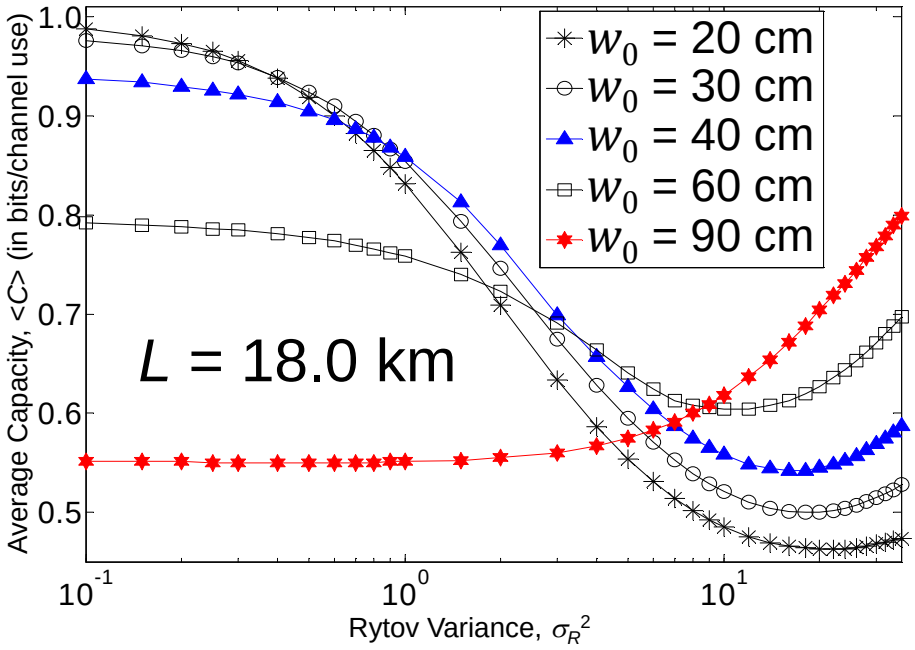

(c)

Figure 3.11: Average channel capacity against the Rytov variance for a variety of beam width settings. The clear weather scenario is considered at (a) $L = 4.5$ km, (b) $L = 7.5$ km, and (c) $L = 18.0$ km, where $V = 10.0$ km, $2\sigma_{pe}/D = 12.0$, and $\langle SNR \rangle = 14$ dB.

10.0. Therefore, beam width optimization is a feasible approach in promoting capacity enhancement for long-distance terrestrial FSO links, since larger transmitter beam radius improves the average channel capacity only in the stronger turbulence regime, while imposing severe performance degradation under weak-to-moderate turbulence conditions, and vice versa.

3.7.2. Optimum Beam Width

The characteristics of the optimum beam width w_0^{opt} for finding the best achievable average capacity $\langle C \rangle$ is examined, under the combined effects of different atmospheric channel conditions that are likely to occur in practice. These parameters are determined through an exhaustive search over their discrete sets, with the results as readily presented

in Figure 3.12. Figure 3.12(a) shows the variation of w_0^{opt} in terms of the turbulence strength (as signified by σ_R^2), for $L = 7.5$ km, $V = 10$ km, $\langle SNR \rangle = 14$ dB and different normalized jitter values of $2\sigma_{pe}/D = \{6.0, 9.0, 12.0, 15.0\}$; and the corresponding optimized $\langle C \rangle$ is depicted in Figure 3.12(b). In general, the w_0^{opt} values are relatively smaller when the effects of turbulence and PEs are less severe; whereby it is observed that w_0^{opt} is typically less than 15 cm for $\sigma_R^2 \leq 1.5$ and/or $2\sigma_{pe}/D \leq 6.0$, which corresponds to an optimal capacity in excess of 0.88 bits/channel use. In the weak turbulence regime, w_0^{opt} exhibits a linear incremental trend for all cases of $2\sigma_{pe}/D$ when $\sigma_R^2 \leq 2.0$; and shows vastly contrasting characteristics thereafter. An appealing observation is made here, showing a reduction in w_0^{opt} from 7.25 cm to 5.65 cm, as $2\sigma_{pe}/D$ varies from 6.0 to 15.0 at $\sigma_R^2 = 0.1$; thereby revealing the fact that the transmitter beam width can be made smaller albeit with increasing PE loss. Moreover, in the intermediate turbulence regime with σ_R^2 ranging from 2.0 to 10.0, w_0^{opt} exhibits small steps of decrease in its value for $2\sigma_{pe}/D = \{6.0, 9.0\}$; but shows a linear increase for the remaining cases, where the PE loss is more severe. This phenomena can be explained by the fact that the combined effects of turbulence-induced scintillations and PEs can result in an increase in the effective beam radius, given the condition that either one or both of these adversities are least dominant; which in turn reduces the sensitivity to optical intensity fluctuations, and thus a smaller w_0^{opt} value for maximizing $\langle C \rangle$. Nevertheless, w_0^{opt} must be increased accordingly for the strong turbulence case with $\sigma_R^2 > 10.0$, in which such incremental trend changes from a more linear to an exponential behaviour with larger $2\sigma_{pe}/D$; since increasing the receiver beam size of a PCB enables the reduction in the scintillations and PEs. As evident from Figure 3.12(b), the FSO channel capacity is highly susceptible to the adverse effects of atmospheric turbulence, and suffers greater performance degradation for larger PE loss

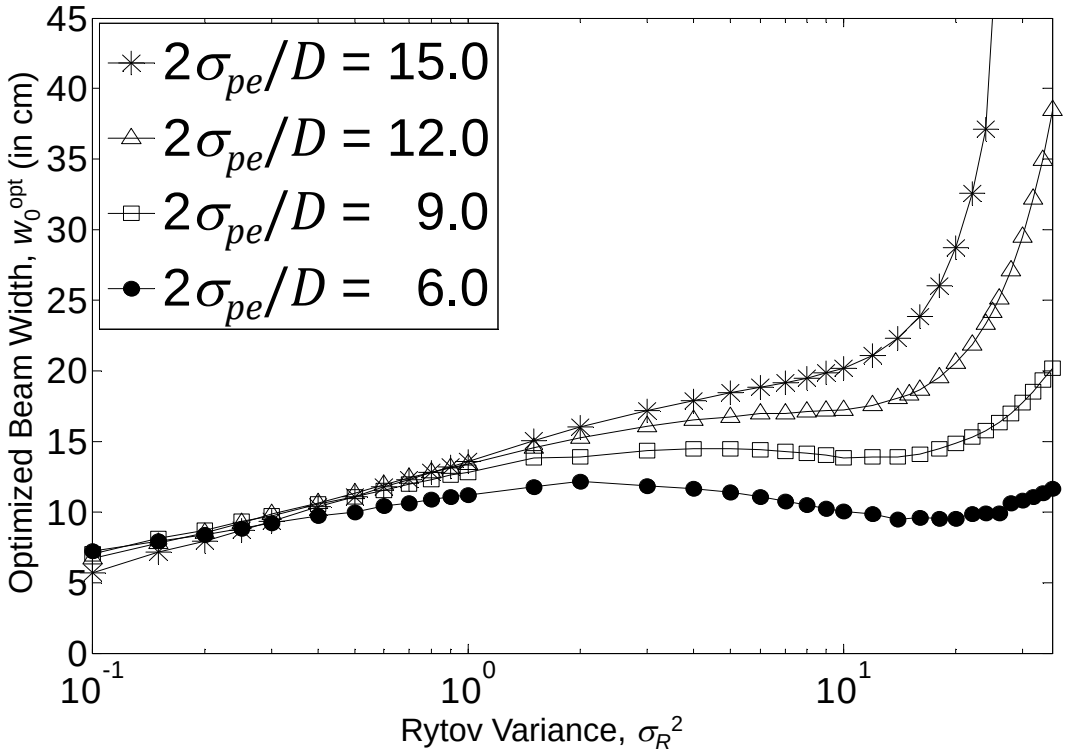

(a)

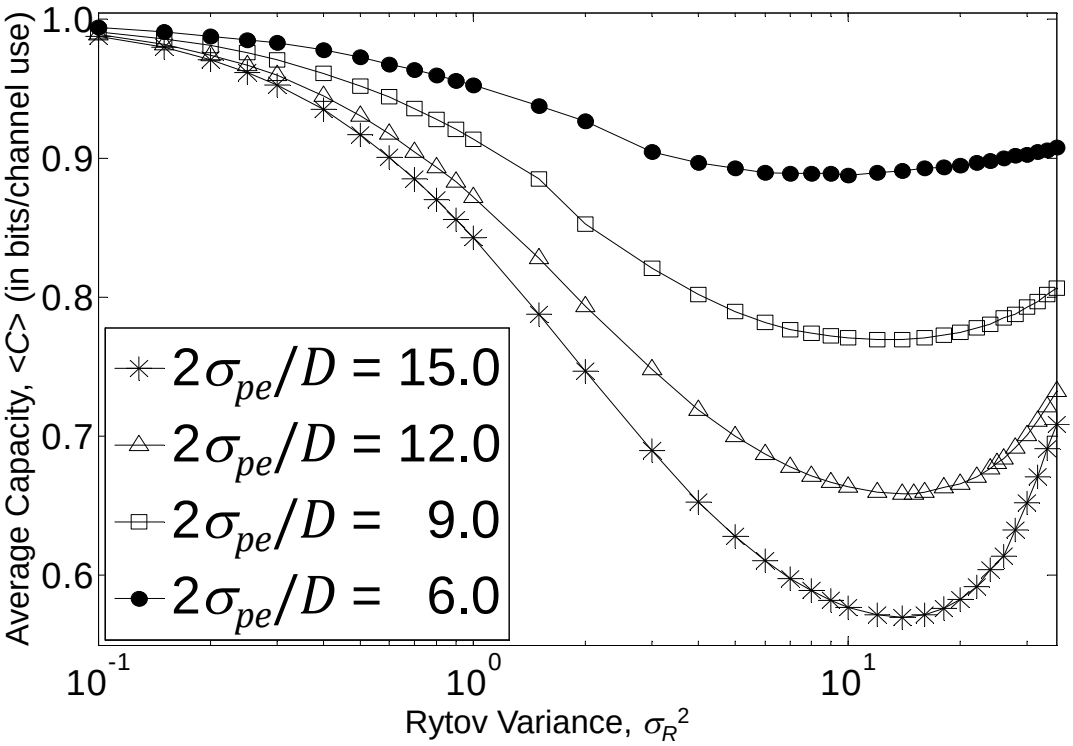

(b)

Figure 3.12: The optimal (a) beam width and (b) average channel capacity with respect to the Rytov variance under the clear weather condition, for $2\sigma_{pe}/D = \{15.0, 12.0, 9.0, 6.0\}$ at $\langle SNR \rangle = 14$ dB; where $V = 10.0$ km, $L = 7.5$ km, and the channel state is unknown to the receiver.

albeit performing beam width optimization; whereby a notable reduction in $\langle C \rangle$ is observed for all the considered $2\sigma_{pe}/D$ values, with a maximum variation of 0.11, 0.22, 0.33 and 0.42 bits/channel use, respectively. Furthermore, a slight improvement in the FSO channel capacity is noticed for $\sigma_R^2 > 10.0$, since increasing the beam width and transmit optical power (to give $\langle SNR \rangle = 14$ dB) alters the PCB into a relatively coherent laser beam, which is more resilient to the strong turbulence conditions.

3.8. Summary

This chapter has examined the performance of partially coherent FSO communication links from the information theory perspective, taking into account the adverse effects of atmospheric loss, turbulence-induced scintillations and PEs. In particular, a spatially partially coherent Gaussian-beam wave and important link design criteria have been jointly considered, in which the latter consists of the receiver aperture dimension and its resulting aperture averaging effect, transmitter beam width, link range, knowledge of CSI, and weather conditions. By using the combined optical slow-fading channel model to describe the optical channel characteristics, a comprehensive analysis of the error performance, average channel capacity and outage probability of the FSO system have been presented. Moreover, the lowest-order Gaussian-beam wave model has been introduced in the proposed study, to characterize the propagation properties of the optical signal through random turbulent medium in an accurate manner; taking into account the diverging and focusing of the PCB, and the scintillation and beam wander effects arising from the atmospheric turbulent eddies. Correspondingly, the proposed study have presented a holistic perspective for optimal planning and design of horizontal FSO links employing spatially partially coherent laser beams.

It has been demonstrated that a lower outage probability and improved BER can be achieved with the introduction of a larger receiver aperture due to the aperture-averaging effect, which effectively mitigates the scintillations and PE loss. From the outage analysis, it is evident that there exist an optimum beam width for a considered receiver aperture size and known laser wavelength, which must be selected according to changing weather condition for optimizing the outage capacity. While higher transmit power potentially enhances the error performance of the FSO system for moderate-to-high visibility scenarios, complete system outage occurs at link distances greater than 1.5 km under the visibility-limiting light fog condition, and is non-recoverable albeit optimizing the system parameters. In the aperture-averaging studies, the numerical results have shown that greater penalty will be imposed upon the average channel capacity under the combined effects of turbulence and PEs, particularly when the channel state is unknown at the receiver. With the introduction of an enlarged receiver aperture, a notable average capacity improvement of up to 0.46 bits/channel use can be achieved for a mean SNR of 14 dB in the moderate-to-strong turbulence regime, albeit without knowledge of the channel state conditions. Furthermore, it has been noted that the PCB properties are substantially altered when propagating through free-space, and revealed the importance of finding an optimal beam width to maximize the average capacity. Several appealing observations have been made in this study, showing that the beam width can be reduced to improve the FSO channel capacity, albeit in the presence of turbulence-induced scintillations and PEs, given the condition that either one or both of these adversities are least dominant. Nevertheless, the beam width must be increased accordingly in the strong turbulence regime, whereby such incremental trend changes from a more linear to an exponential behaviour; since increasing the beam width and transmit optical power (to give a mean SNR of ~14 dB) alters the PCB into a relatively coherent laser beam, thus becoming more resilient to the

strong turbulence conditions. Therefore, beam width optimization is a feasible approach in promoting capacity enhancement for long-distance terrestrial FSO links; since the beam parameter is subject to the combined effects of turbulence and PEs, and its optimal value must be adjusted according to varying channel conditions. The notable observations and findings highlighted in this chapter have motivated the development of two feasible optimization techniques, which will be presented in Chapter 4.

CHAPTER 4

Optimization of a Partially Coherent Gaussian Beam

4.1. Introduction

The best achievable channel capacities of spatially partially coherent FSO communication links can be approached through optimum selection of the important link design parameters, such as the transmitter beam width and receiver aperture diameter, while taking into account the contributing effects of different operating conditions. Through the extensive performance studies presented in Chapter 3, new optimization techniques are developed and introduced in the present chapter, as feasible methods to mitigate the degrading impacts of turbulence-induced scintillations and PEs, thereby enabling performance enhancement of the system under study.

In this chapter, the relevant literatures pertaining to PCB optimization in FSO links

are discussed in Section 4.2, clearly highlighting the limitations and open research issues of the mentioned research works; which in turn substantiates the outlining of the main contributions of the proposed optimization techniques in Section 4.3. Based upon the aforementioned system and channel models in Section 2.2 and Section 2.4, respectively, the average channel capacity in the event of unknown CSI at the receiver (as defined by (3.11) and (3.12)) is employed as a useful performance metric, in order to carry out joint investigation of the effects of a PCB and aperture averaging in Section 4.4. Numerical results reveal the inherent advantages of the aperture-averaging effect in mitigating the scintillations and PE loss; and demonstrate that there exists optimality in the transmitter beam width under different atmospheric channel conditions, thereby motivating the development of a theoretical beam width optimization model. In Section 4.5, joint beam width and spatial coherence length optimization is proposed to maximize the FSO channel capacity, under the combined influences of atmospheric turbulence and PEs, while taking into account the aperture-averaging effect. In particular, an optimization metric is developed to determine the optimum beam divergence at the receiver for maximizing the average capacity. The concluding remarks are then provided in Section 4.6.

4.2. Background and Motivation

In [72], Schulz examined the problem of maximizing the received mean signal intensity, and established conditions for the mutual intensity of a transmitted beam, in order to identify the optimal beam with respect to the two optimization criteria of maximal mean intensity and minimal scintillation index. It was shown that a fully coherent laser beam maximizes the expected intensity, whereas a PCB mitigates the scintillation effects. Chen *et al.* [73] proposed an optimization criterion for the initial coherence degree of lasers, based on the PDF of the irradiance fluctuations, which maximizes the received

irradiance that occurs with the highest probability. In addition, a method for adaptive initial coherence was given to use the criterion in practical applications. Voelz and Xiao [162] presented a performance metric to investigate the optimization of the transverse coherence length as a function of a variety of link parameters and scenarios, which balances the effects of beam spread and scintillation, for achieving near-optimal FSO link performance. In [74], Borah and Voelz examined the problem of coherence length optimization in the weak turbulence regime, in which the conditions for achieving improvement in the outage probability were described; taking into account the effects of various parameters, comprising the phase front radius of curvature, transmission distance, wavelength and beam width. Nevertheless, the effects of PEs and aperture averaging were not considered in the above-mentioned optimization studies. In [75], Liu *et al.* proposed a theoretical model to investigate the average channel capacity optimization in the presence of atmospheric turbulence and PEs, and showed that both the transmitter beam divergence angle and beam waist can be tuned to maximize the average capacity for a given transmitted laser power, subjected to the dependence on the jitter and operation wavelength, respectively. However, the degree of partial (spatial) coherence of the laser source was not taken into account in the beam model, since the beam divergence angle is a function of the transmitter beam waist, for a given system setup and atmospheric turbulence. Cang and Liu [76] presented the expressions of large- and small-scale log-irradiance flux variance for a PCB propagating through the non-Kolmogorov turbulence channel. The achievable average channel capacity was observed for the cases of moderate-to-strong fluctuations, taking into account specific parameters encompassing conditions of atmospheric turbulence, receiver aperture diameter and spatial coherence of the laser source; but PEs and beam optimization were not considered in the study.

4.3. Main Contributions of Research

Joint investigation of the effects of a spatially partially coherent Gaussian beam and aperture averaging is presented from the information theory perspective, in order to examine the resulting impact of the PCB parameters and receiver aperture diameter on the average channel capacity of the FSO link, in the presence of turbulence-induced scintillations and PEs. Numerical results show that the FSO channel capacity is highly susceptible to the adverse effects of scintillations and PEs; and confirm the two distinctive advantages of introducing an enlarged receiver aperture (i.e., reducing the scintillation and mitigating the PE loss), and the interest of optimizing the beam width to maximize the average capacity, especially in the moderate-to-strong turbulence regime. Correspondingly, a theoretical beam width optimization model is proposed in this research study, which takes advantage of a simple mathematical solution to determine the optimum beam width. While an exact closed-form expression for the optimum beam width is unavailable, it is demonstrated that the parameter value can be alternatively obtained through the numerical method. Based on the theoretical model, several appealing observations are made and reported for the first time through the proposed work, showing that a larger optimum beam width is required under more severe PE losses in the stronger turbulence regimes, in which such incremental trend changes from a more linear to a near-exponential behaviour with increasing turbulence strength. When the effect of PEs is less prevalent, the optimum beam width is relatively smaller compared to the weaker turbulence cases.

Subsequent investigation studies on the characteristics of spatially partially coherent Gaussian laser beams propagating through the atmospheric turbulence channel reveal the relationship between the beam width and spatial coherence length to optimize the PCB. Therefore, a joint beam width and spatial coherence length optimization technique is

proposed to maximize the average channel capacity in partially coherent FSO links, under the combined effects of turbulence and PEs, while taking into account the aperture-averaging effect. Furthermore, an optimization metric, known as the beam spreading gain is developed to examine the behaviour of the optimum beam divergence, by providing a feasible translation of the joint optimal transmitter beam parameters into an analogous level of divergence of the received optical beam. It is demonstrated that the PCBs are desirable in the weak-to-moderate turbulence regimes, and reveals the need for adjusting the beam width and the spatial coherence length in order to optimize the beam divergence by a factor of the beam spreading gain. On the other hand, coherent laser beams operating at a high transmit power exhibit greater resilience to the strong turbulence conditions; and are preferred in this case, as indicated by the significant reduction in the proposed optimization metric. The near-ideal average capacity is best achieved through the introduction of an enlarged receiver aperture and joint PCB optimization, which effectively mitigates the adverse effects of scintillations and PEs.

4.4. Theoretical Beam Width Optimization Model

4.4.1. Performance Analysis

Figure 4.1 illustrates the average channel capacity $\langle C \rangle$ (see (3.11) and (3.12)) as a function of the average electrical SNR $\langle SNR \rangle$ for a range of normalized jitter $2\sigma_{pe}/D$, to examine the effects of aperture-averaging and PEs in the case of unknown CSI at the receiver. Unless otherwise specified, the default parameters considered in the presented results throughout this section are defined accordingly in Table 3.1 and Table 3.4 [24, 76]. The two cases of weak and moderate-to-strong turbulence regimes are considered here, with $C_n^2 = 3.1230\times10^{-16}$ m$^{-2/3}$ ($\sigma_R^2 = 0.25$) and $C_n^2 = 1.1244\times10^{-14}$ m$^{-2/3}$ ($\sigma_R^2 = 9.00$),

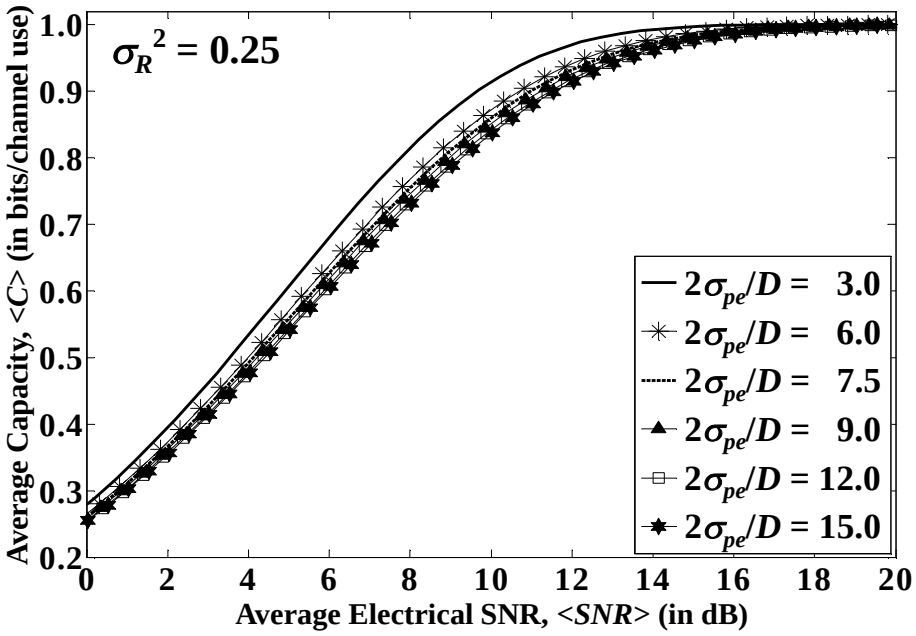

(a)

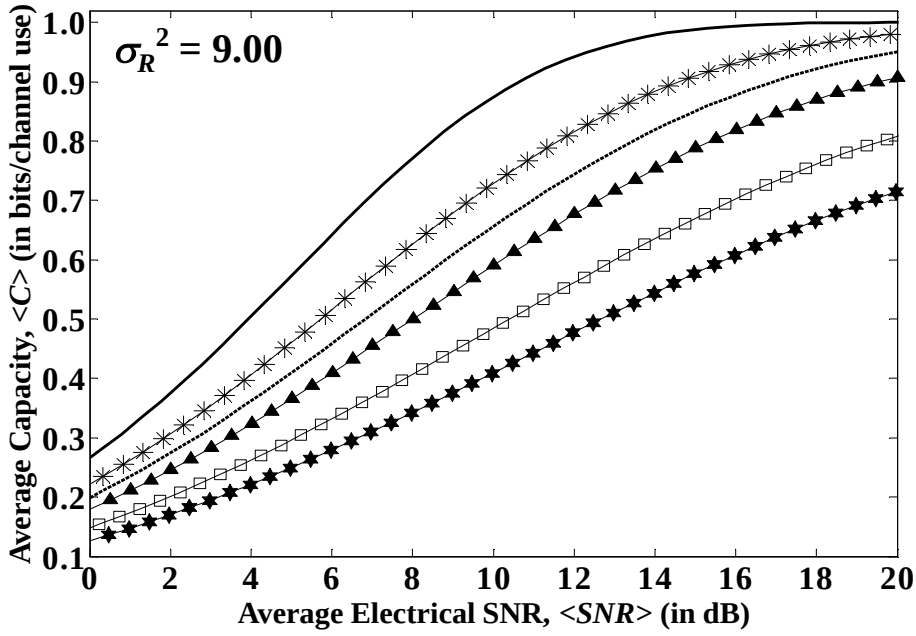

(b)

Figure 4.1: Average channel capacity in terms of the average electrical SNR for different normalized jitter values, under the: (a) weak ($\sigma_R^2 = 0.25$), and (b) moderate-to-strong ($\sigma_R^2 = 9.00$) turbulence conditions.

respectively at a link distance $L = 7.5$ km. Under the weak turbulence condition (Figure 4.1(a)), a faster increase in $\langle C \rangle$ with respect to $\langle SNR \rangle$ is observed for all considered

$2\sigma_{pe}/D$ values, where the maximum channel capacity is approached at SNR values greater than 16 dB. Moreover, the variation in $\langle C \rangle$ is less significant for the different cases of $2\sigma_{pe}/D$ at $\sigma_R^2 = 0.25$, as compared to the moderate-to-strong turbulence scenario ($\sigma_R^2 = 9.00$) in Figure 4.1(b). For the latter case, a significant improvement in $\langle C \rangle$ is obtained by increasing the receiver aperture diameter D. In effect, the benefits of increasing the receiver aperture size is twofold – reducing the scintillation by shifting the relative frequency content of the irradiance power spectrum towards lower frequencies; and mitigating the PE loss, as indicated by the reduction in the normalized jitter. For instance, it is noted from Figure 4.1(b) that an average channel capacity improvement of more than 0.4 bits/channel use can be achieved at $\langle SNR \rangle = 14$ dB (corresponding to a bit error rate of $\approx 10^{-6}$), by increasing D from 40 mm to 200 mm, thereby resulting in a near-optimal $\langle C \rangle$ of 0.98 bits/channel use for $2\sigma_{pe}/D = 3.0$. Furthermore, $\langle C \rangle$ approaches the asymptotic limit of 1.0 bits/channel use for $\langle SNR \rangle > 16$ dB, which is unattainable for the remaining cases.

Figure 4.2 depicts the average channel capacity $\langle C \rangle$ against the transmitter beam width w_0 for a range of $2\sigma_{pe}/D$ at $\langle SNR \rangle = 14$ dB, taking into account the two turbulence cases of $\sigma_R^2 = \{0.25, 9.00\}$. From Figure 4.2(a), it is observed that the optimal w_0 value is mainly concentrated in the region of 4 cm to 15 cm under the weak turbulence condition, whereby the achievable average capacity is typically in excess of 0.92 bits/channel use. In addition, $\langle C \rangle$ exhibits less variation with $2\sigma_{pe}/D$ for a given w_0, as compared to the moderate-to-strong turbulence scenario in Figure 4.2(b), where significant capacity variations of > 0.4 bits/channel use are seen for $w_0 = 4$ to 15 cm. It is further noted that the optimal w_0 values are larger, as compared to the former case. These observations indicate the high susceptibility of the FSO channel capacity to the adverse effects of

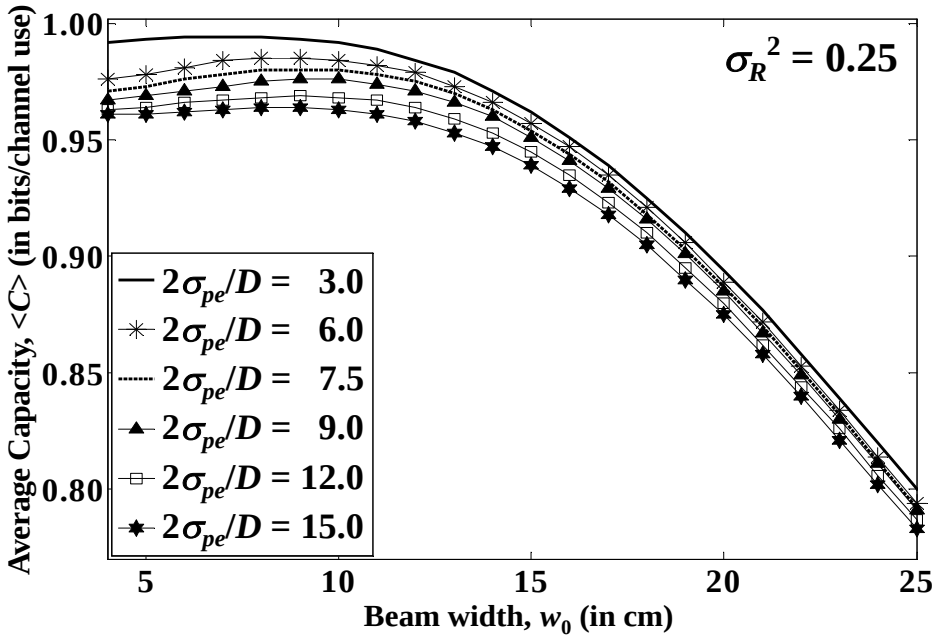

(a)

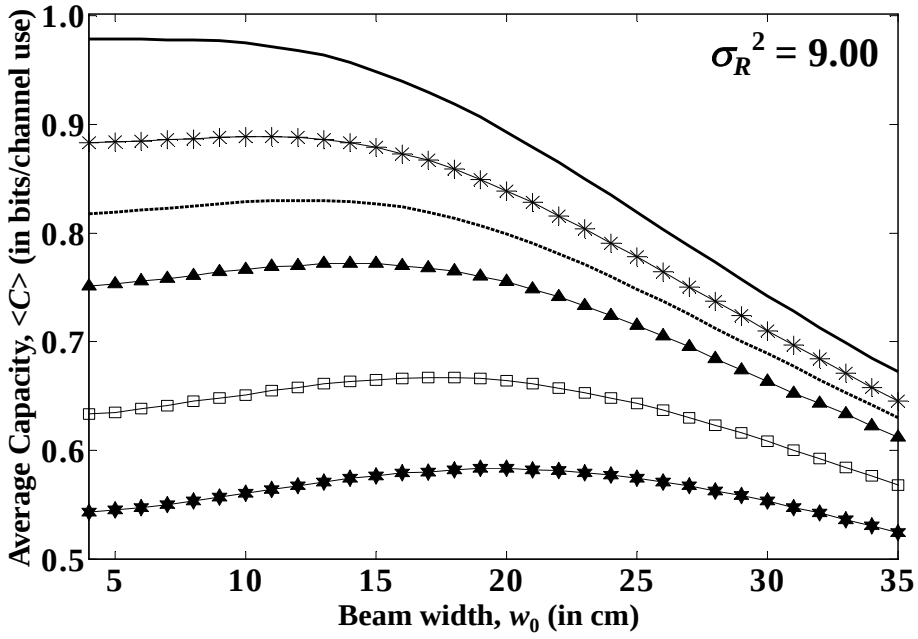

(b)

Figure 4.2: Average channel capacity as a function of the beam width for a variety of normalized jitter settings at $\langle SNR \rangle = 14$ dB. The (a) weak ($\sigma_R^2 = 0.25$) and (b) moderate-to-strong ($\sigma_R^2 = 9.00$) turbulence cases are considered.

scintillations and PEs, and confirm the interest of optimizing the beam width w_0 to maximize $\langle C \rangle$, especially in the moderate-to-strong turbulence regime.

4.4.2. Theoretical Model

Correspondingly, a theoretical model is developed to determine the optimum beam width w_0^{opt} for maximizing the average channel capacity $\langle C \rangle$. In principle, w_0^{opt} can be derived analytically by taking the relation as follows:

$$\frac{d\langle C \rangle}{dw_0} = 0 \, . \tag{4.1}$$

Considering an exact closed-form expression for w_0^{opt} is currently unavailable, the author demonstrates that the parameter can be alternatively solved using the numerical method. It is shown accordingly in Figure 4.3(a) w_0^{opt} as a function of $2\sigma_{pe}/D$ at $\langle SNR \rangle = 14$ dB for $\sigma_R^2 = \{0.25, 1.50, 9.00, 15.00, 20.00\}$; and the corresponding optimized $\langle C \rangle$ are presented in Figure 4.3(b). As expected from the results of Figure 4.1 (a), the FSO channel capacity is less affected by the PE loss under the weak turbulence condition ($\sigma_R^2 = 0.25$), where $\langle C \rangle$ is generally larger than 0.95 bits/channel use for all $2\sigma_{pe}/D$. In addition, minor variations in the w_0^{opt} values are observed, with values ranging from 4 cm to 10 cm. More specifically, w_0^{opt} exhibits very small steps of increment for $2\sigma_{pe}/D = 2.0$ to 9.0 and decreases thereafter, which is a vastly contrasting behaviour compared to the other turbulence cases. For $\sigma_R^2 = 1.50$, the decrease in $\langle C \rangle$ is rather linearly proportional to $2\sigma_{pe}/D$ with a maximum variation of ~0.25 bits/channel use; whereas w_0^{opt} shows a gradual but much larger increase compared to $\sigma_R^2 = 0.25$, and subsequently exhibits a monotonic behaviour for $2\sigma_{pe}/D \geq 14.0$. In addition, it is evident that $\langle C \rangle$ becomes more susceptible to PEs with increased turbulence strength. This phenomenon is particularly prevalent in the stronger turbulence regimes with $\sigma_R^2 = \{9.00, 15.00, 20.00\}$, where a maximum variation of more than 0.48 bits/channel use is noted. An interesting observation is made here, showing that a larger w_0^{opt} is required under more severe PE losses of $2\sigma_{pe}/D \geq 9.0$, in

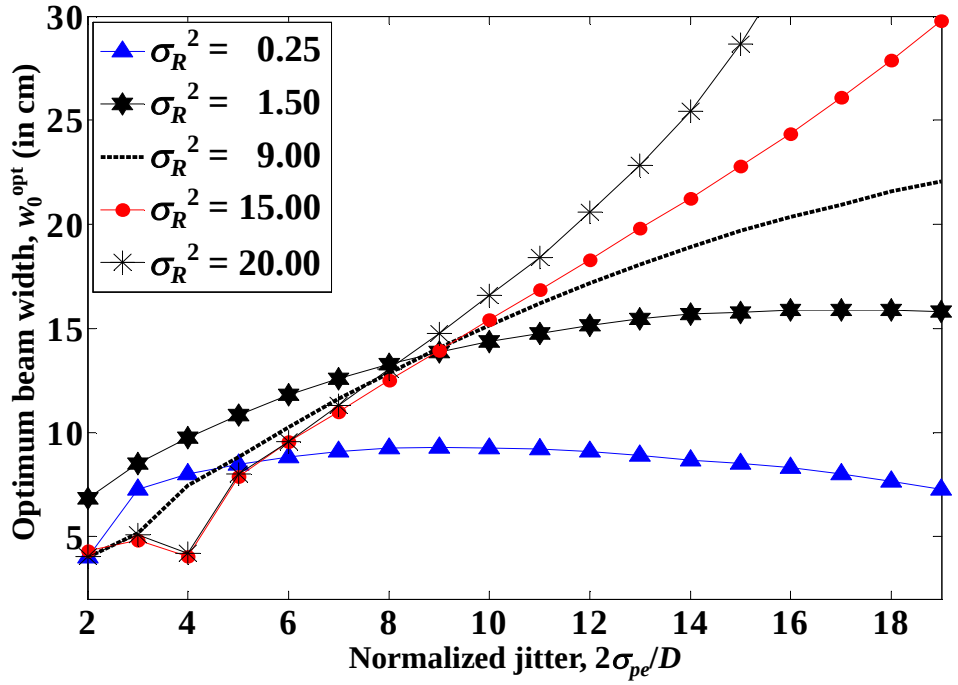

(a)

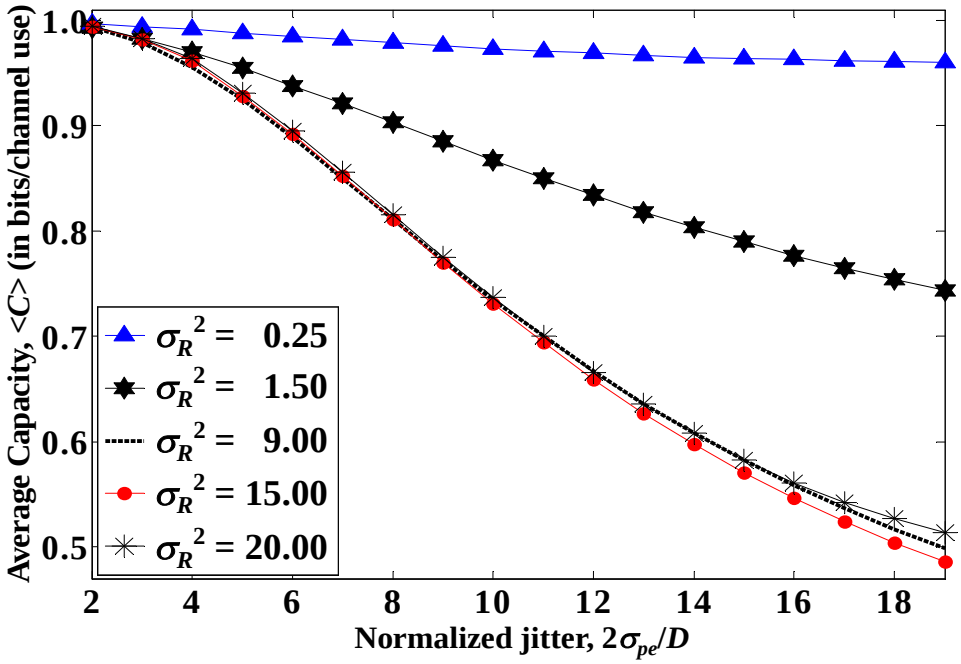

(b)

Figure 4.3: The optimal (a) beam width and (b) average channel capacity against the normalized jitter at $\langle SNR \rangle = 14$ dB , for various turbulence strengths of $\sigma_R^2 = \{0.25, 1.50, 9.00, 15.00, 20.00\}$.

which such incremental trend changes from a more linear to a near-exponential behavior for larger σ_R^2. In particular, when the effect of PEs is less prevalent with $2\sigma_{pe}/D \leq 5.0$,

w_0^{opt} is relatively smaller compared to the weaker turbulence cases. This can be explained by the fact that stronger turbulence result in an increase in the effective beam radius, which reduce the sensitivity to PE fluctuations, thereby giving a smaller w_0^{opt}.

4.5. Joint Beam Width and Spatial Coherence Length Optimization

4.5.1. Performance Analysis

Figure 4.4(a) depicts the average channel capacity $\langle C \rangle$ against the average electrical SNR $\langle SNR \rangle$ for a range of spatial coherence length l_c, under the weak turbulence condition with $C_n^2 = 3.1230 \times 10^{-16}$ m$^{-2/3}$ ($\sigma_R^2 = 0.25$) at a link distance $L = 7.5$ km. The variation of $\langle C \rangle$ with respect to l_c at $\langle SNR \rangle = 14$ dB (corresponding to a bit-error-rate of $\approx 10^{-6}$) for numerous w_0 settings is shown in Figure 4.4(b). Unless otherwise specified, the default values for other considered parameters in this section are as defined in Table 3.1 and Table 3.4. From Figure 4.4(a), it is evident that a higher channel capacity can be achieved with PCBs of smaller l_c, particularly at larger SNR values, as compared to the case of coherent laser beams, where $\langle C \rangle < 0.1$ bits/channel use albeit increasing the SNR. On the other hand, it is observed from Figure 4.4(b) that for $\langle SNR \rangle = 14$ dB, $\langle C \rangle$ exhibits a variation of > 0.5 bits/channel use between the l_c extremes, for all considered w_0 values. In general, w_0 does not have a significant impact on $\langle C \rangle$ for $l_c \leq 0.005$ m, but causes performance degradation by a factor of more than two for the coherent case.

Figure 4.5 shows the corresponding results for the moderate-to-strong turbulence scenario ($\sigma_R^2 = 9.00$), which exhibits similar characteristics as that of the weak turbulence case, with some variation highlighted as follows. It is noted in Figure 4.5(a) that the increase in $\langle C \rangle$ is rather linearly proportional to $\langle SNR \rangle$ for all cases of l_c; and PCBs of

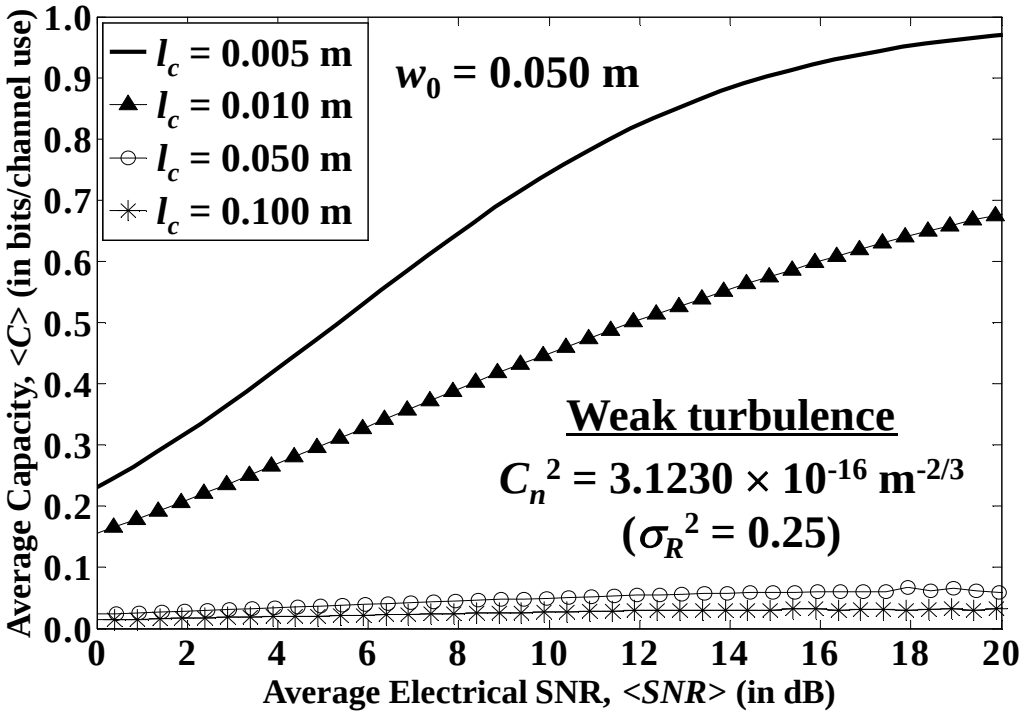

(a)

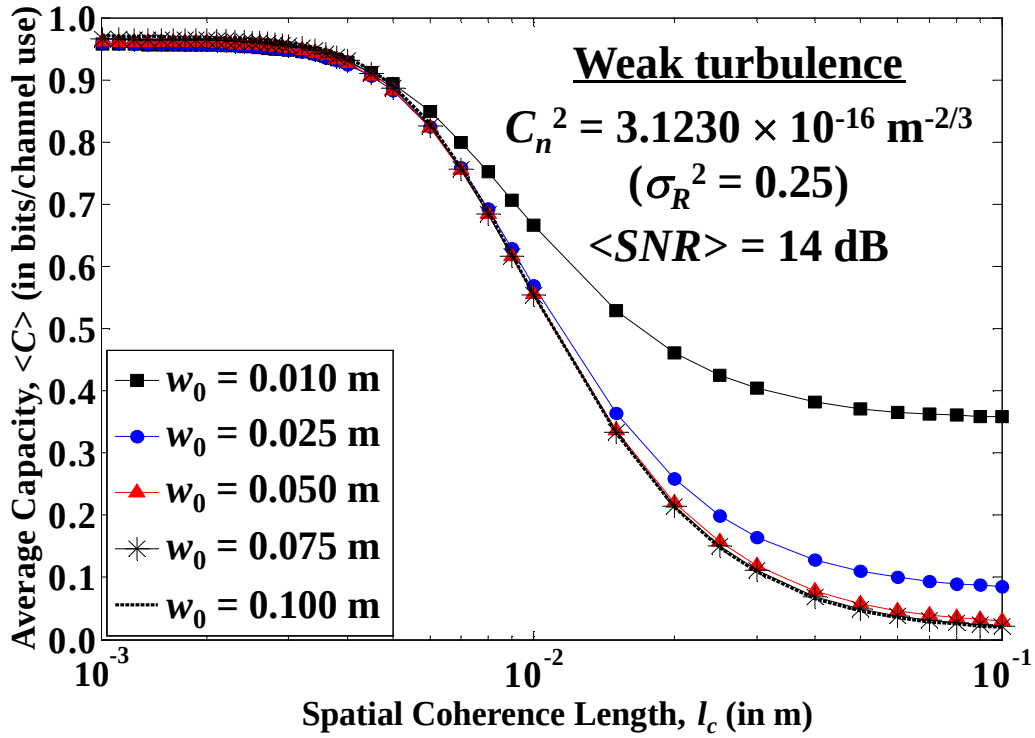

(b)

Figure 4.4: Average channel capacity in terms of (a) the average electrical SNR for different spatial coherence lengths; and (b) the spatial coherence length for a variety of beam width settings, at $\langle SNR \rangle = 14$ dB. The weak turbulence case is considered, with $\sigma_R^2 = 0.25$.

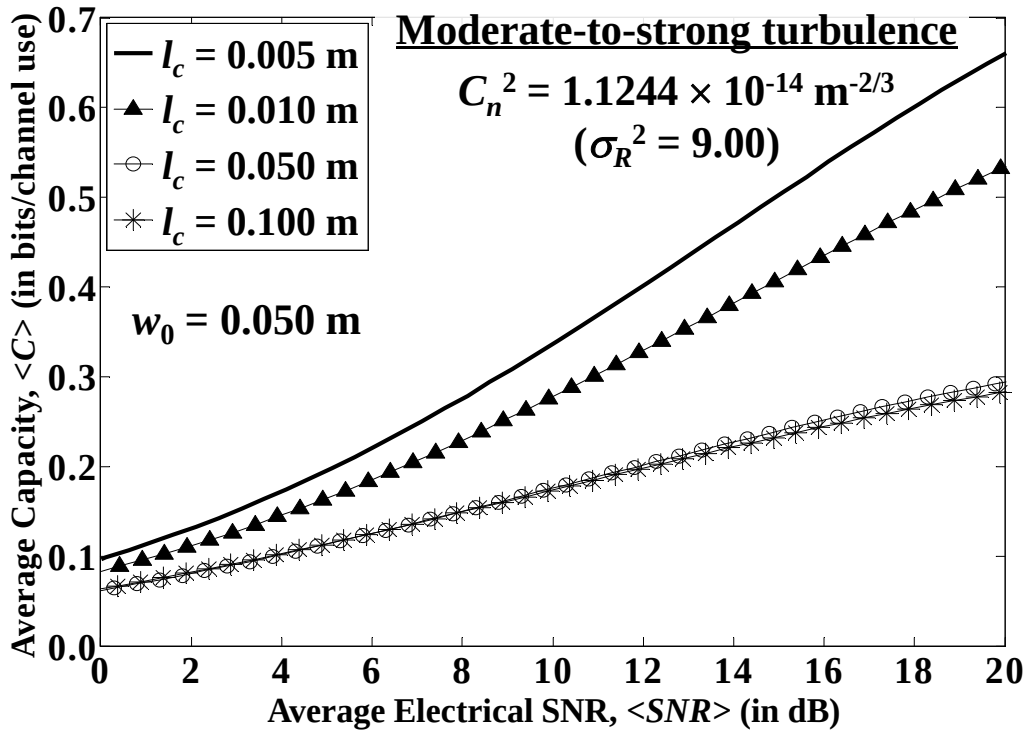

(a)

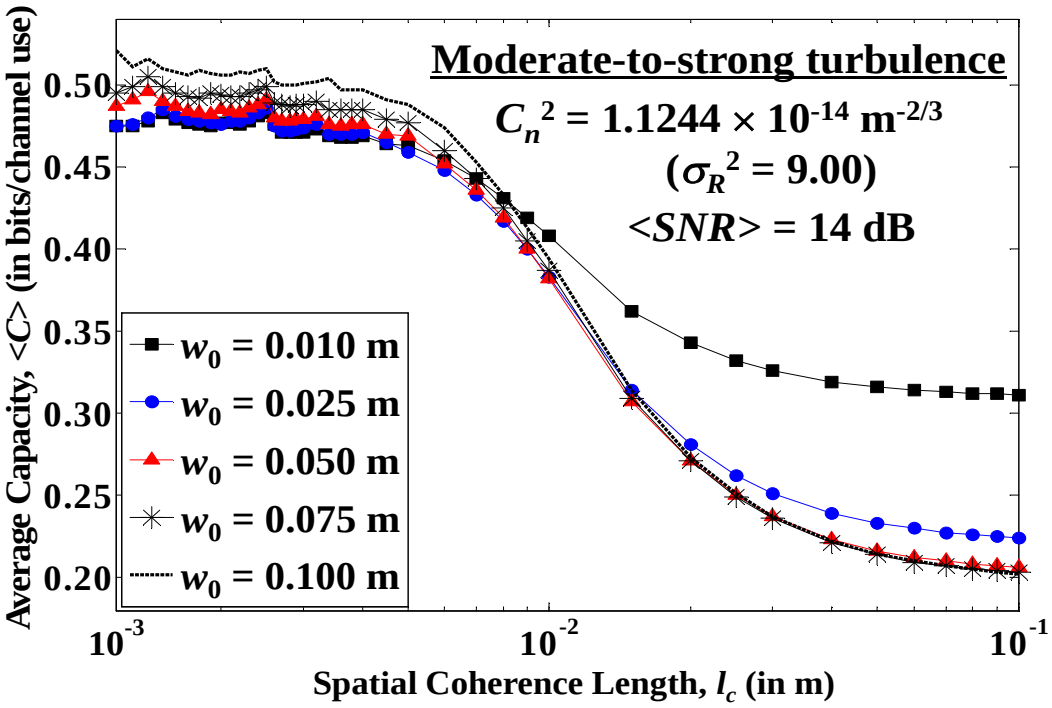

(b)

Figure 4.5: Corresponding results showing the average channel capacity against (a) the spatial coherence length, and (b) the beam width at $\langle SNR \rangle = 14$ dB, for the moderate-to-strong turbulence case ($\sigma_R^2 = 9.00$).

smaller l_c are still desirable in the intermediate turbulence regime, which is evident from the relatively higher capacity attainment for $l_c = \{0.005, 0.010\}$ m, particularly at larger SNR values. In Figure 4.5(b), it is observed that the variation of $\langle C \rangle$ with respect to l_c exhibits similar characteristics as that of the weak turbulence case, but the maximum variation in $\langle C \rangle$ between the l_c extremes decreases, with values ranging between 0.2 and 0.3 bits/channel use for all cases of w_0.

Figure 4.6 illustrates the corresponding results for the strong turbulence case with $C_n^2 = 4.4974 \times 10^{-14}$ m$^{-2/3}$ ($\sigma_R^2 = 36.00$), which exhibits a vastly contrasting behavior compared to the weak and intermediate turbulence scenarios. It is noted in Figure 4.6(a) that a large l_c is preferred, but near-ideal $\langle C \rangle$ can only be attained via a substantial increase in the SNR. This shows the importance of using a coherent laser source with a high transmit power to optimize the capacity. From Figure 4.6(b) (and other turbulence cases, although not shown here), it is observed that the maximum variation in $\langle C \rangle$ between the l_c extremes decreases significantly for stronger turbulence. In addition, an optimal $\langle C \rangle$ of 0.67 bits/channel use occurs for $l_c \geq 0.04$ m and $w_0 \geq 0.05$ m at $\langle SNR \rangle$ of 14 dB. The presented results justify the necessity for the joint optimization of w_0 and l_c, to determine the best achievable $\langle C \rangle$ under most turbulence conditions that are likely to occur in practice. For instance, through an exhaustive search over the discrete sets, the optimal values of $[w_0; l_c]^{\text{opt}}$ = [0.10; 0.0012], [0.10; 0.0012] and [0.05; 0.0600] have been determined, for the weak ($\sigma_R^2 = 0.25$), intermediate ($\sigma_R^2 = 9.00$) and strong ($\sigma_R^2 = 36.00$) turbulence conditions, respectively.

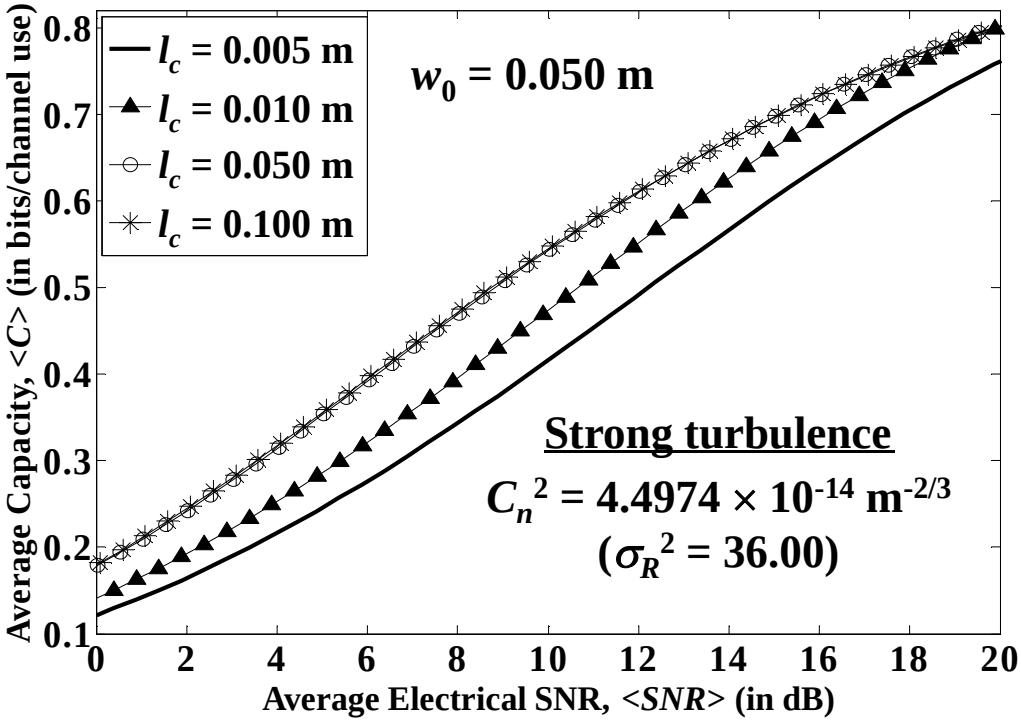

(a)

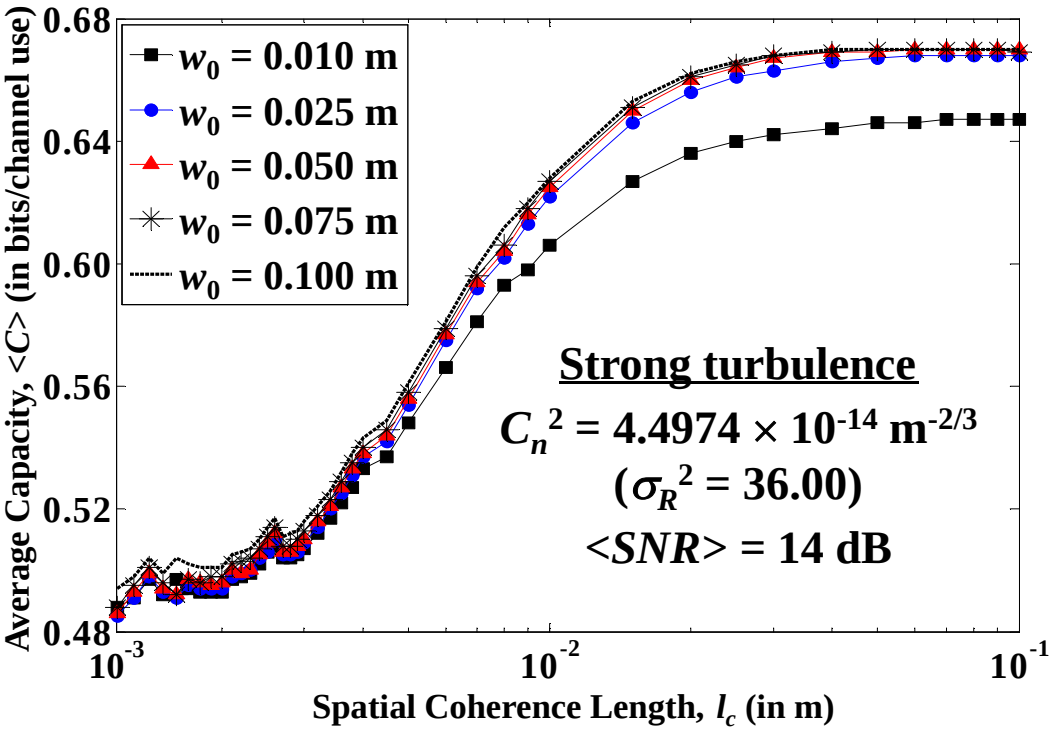

(b)

Figure 4.6: Corresponding results showing the average channel capacity against (a) the spatial coherence length, and (b) the beam width at $\langle SNR \rangle = 14$ dB, for the strong turbulence case ($\sigma_R^2 = 36.00$).

4.5.2. Optimization Metric

In addition to the joint optimization technique, an optimization metric is developed to investigate the characteristics of the optimum beam divergence, with respect to the changes in the atmospheric turbulence strengths and PEs. In principle, the beam spreading gain as defined by:

$$A_{\zeta}^{\text{opt}} = \frac{w_{z_{eq}}^{\text{opt}}}{w_{z_{eq}}^{\text{nom}}}\ , \tag{4.2}$$

provides a feasible translation of the joint optimal transmitter beam parameters $[w_0; l_c]^{\text{opt}}$ into an analogous level of divergence of the optical beam at the receiving-end, with reference to the nominal coherent case of $[w_0; l_c]^{\text{nom}}$ = [0.05; 0.10]. Figure 4.7 shows the optimized $\langle C \rangle$ as a function of σ_R^2 for $\langle SNR \rangle = 14$ dB. The effect of PEs, resembled by the normalized jitter $2\sigma_{pe}/D$, is examined for a variety of D. The average channel capacity for the cases of divergent and coherent beams with $[w_0; l_c]$ = [0.05; 0.01] and [0.05; 0.10], respectively, and the A_{ζ}^{opt} values are indicated for $2\sigma_{pe}/D = 15.0$. It is observed that near-ideal $\langle C \rangle$ can be approached for $\sigma_R^2 \leq 1.0$, by reducing the degree of spatial coherence, thus resulting in $A_{\zeta}^{\text{opt}} > 20$. In addition, the optimal $\langle C \rangle$ and A_{ζ}^{opt} decrease for larger σ_R^2, in which similar behavior are observed for other $2\sigma_{pe}/D$ cases. This suggests that PCBs are desirable in the weak-to-moderate turbulence regime, and reveals the need for adjusting w_0 and l_c to optimize the beam divergence by a factor of A_{ζ}^{opt}, thus maximizing $\langle C \rangle$.

Coherent laser beams (with A_{ζ}^{opt} approaching 1.0) operating at a high transmit power are more feasible under strong fluctuations conditions. The introduction of a larger receiver aperture and joint optimization of w_0 and l_c enhances the capacity with $\langle C \rangle > 0.8$ bits/channel use for $2\sigma_{pe}/D = \{7.5, 6.0, 3.0\}$. In principle, increasing the

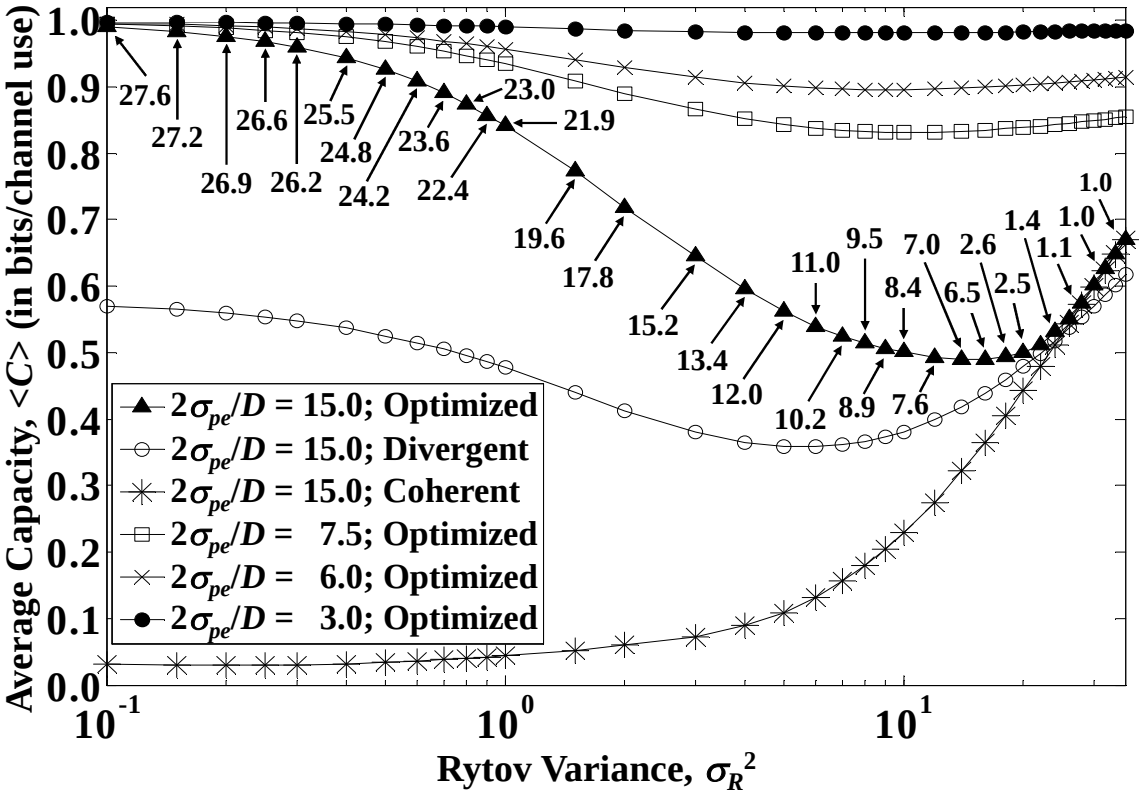

Figure 4.7: The optimal average channel capacity in terms of the Rytov variance, for $2\sigma_{pe}/D = \{15.0, 7.5, 6.0, 3.0\}$ at $\langle SNR \rangle = 14$ dB. The cases of $[w_0; l_c] = [0.05; 0.01]$ (divergent) and [0.05; 0.10] (coherent), and the values for A_ζ^{opt} are depicted for $2\sigma_{pe}/D = 15.0$.

receiver aperture mitigates the PE loss, as indicated by the reduction in $2\sigma_{\text{pe}}/D$. It also shifts the relative frequency content of the irradiance power spectrum towards lower frequencies due to aperture averaging, essentially averaging out the fastest fluctuations, thereby reduces the scintillation.

4.6. Summary

This chapter has presented joint investigation of the effects of spatially partially coherent Gaussian laser beam and aperture averaging on the performance of FSO communication systems from the information theory perspective, taking into account the impairments resulting from atmospheric turbulence and PEs. Numerical results have

shown that the aperture-averaging effect potentially mitigates the turbulence-induced scintillations and PE loss; and confirmed the interest of optimizing the beam width to maximize the average channel capacity. Correspondingly, a theoretical beam width optimization model has been developed, which takes advantage of a simple mathematical solution to determine the optimum beam width of the PCB, for maximizing the FSO channel capacity in the presence of turbulence and PEs. It has been demonstrated that the parameter value can be obtained through the numerical method, since an exact closed-form expression for the optimum beam width is unavailable. In particular, several appealing observations have been made and reported for the first time through the proposed work, showing that a larger optimum beam width is required under more severe PE losses in the stronger turbulence regimes, in which such incremental trend changes from a more linear to a near-exponential behaviour with increasing turbulence strengths. When the effect of PEs is less prevalent, the optimum beam width is relatively smaller compared to the weaker turbulence cases. Furthermore, it has been shown that the FSO channel capacity can be increased by up to twofold, for a given jitter variance, through the combination of an enlarged receiver aperture and the beam width optimization technique, particularly in the moderate-to-strong turbulence regimes.

Next, a joint beam width and spatial coherence length optimization technique has been proposed to maximize the average channel capacity in partially coherent FSO links over atmospheric turbulence channels with PEs, while taking into account the aperture-averaging effect. The beam spreading gain has been developed as a useful metric to examine the characteristics of the optimum beam divergence, by providing a feasible translation of the joint optimal beam parameters into an analogous level of divergence of the resulting optical beam. It has been demonstrated that the PCBs are desirable in the weak-to-moderate turbulence regime, which in turn revealed the importance of adjusting

the beam width and spatial coherence length to optimize the beam divergence by a factor of the beam spreading gain; whereas highly coherent laser beams are preferred under strong fluctuations conditions, as can be observed from the notable reduction in the proposed optimization metric. Therefore, optimal average channel capacity can be achieved through the introduction of a larger receiver aperture and joint PCB optimization, which effectively mitigates the scintillation effects and PE loss.

CHAPTER 5

Experimental Demonstration of the Effects of Aperture Averaging and Beam Width under Controlled Turbulence Condition

5.1. Introduction

In-depth theoretical analysis and simulation studies presented in Chapters 3 and 4 have discussed and highlighted the importance of proper selection of the transmitter beam width and receiver aperture size, as a feasible method in mitigating the degrading impacts incurred by the atmospheric turbulent channel to optimize the achievable FSO channel capacities. Correspondingly, an experimental work is carried out and presented in the present chapter, in order to demonstrate the joint effects of aperture averaging and beam width on the FSO communication system, taking into account the influence of turbulence-induced scintillation effect (i.e., the presence of thermal gradient within the FSO channel). While practical demonstration of the aperture-averaging phenomenon can be found in a handful of relevant research work [71, 163-165], the proposed study reports here for the

first time the characterization of the combined effects of aperture averaging and beam width for a Gaussian laser beam under laboratory-controlled turbulence conditions. In particular, the probability density distributions of the received optical signal are generated from the acquired data, in order to examine the extent of signal fluctuations resulting from the reduction of the receiver aperture size and the increase of scintillation, for different beam width settings. Taking into account numerous transmitter beam radius, turbulent channel conditions and receiver aperture dimensions in the experiment, the subsequent analysis reveals that the aperture-averaging factor exhibits a linear behaviour with respect to the changes in the point-received scintillation index.

A comprehensive survey of the relevant research work pertaining to the practical demonstration of the aperture-averaging effect is presented in Section 5.2, and the main contributions of the proposed experimental study are justified accordingly in Section 5.3. The experimental setup and the methodology and post-analysis required to carry out the practical work are thoroughly elaborated in Sections 5.4 and 5.5, respectively; in which the latter provides detailed explanation on the data acquisition process (in Section 5.5.1), generation of the probability density distributions (in Section 5.5.2), prediction of the beam width (in Section 5.5.3), and computation of the turbulence strength parameters (in Section 5.5.4). Next, Section 5.6 reviews the relevant model performance indicators to perform the GOF test, which include the mean bias error, root mean square error, t-statistic, correlation coefficient and coefficient of determination. The experimental results are presented and discussed in Section 5.7, whereby the characteristics of the received optical signal resulting from the variation of receiver aperture dimension, turbulence strength and beam width are examined through the corresponding probability density distributions in Section 5.7.1. In Section 5.7.2, the combined effects of aperture averaging and beam width are observed through the aperture-averaging factor, in which it is demonstrated that the relationship

between the aperture-averaging factor and point-received scintillation index can be approximated by a first-order linear regression model. Furthermore, Section 5.7.3 evaluates the performance enhancement attainable with an aperture-averaged optical receiver, in comparison to a finite point receiver. Finally, the key concluding remarks are summarized in Section 5.8.

5.2. Background and Motivation

In [71], Churnside developed approximate expressions for the aperture-averaging factor of optical scintillation for the weak and strong turbulence regimes, and then performed a series of experiments to validate some of these relationships. Taking into account a fixed beam width setting with a beam divergence of 1.2 mrad and an array of receiver apertures with various dimensions, it was shown that these simple approximations are within a factor of two of the measurements. While not all parameter regimes were feasible in the experiments, the author demonstrated seemingly good agreement between the predicted and measured values for spherical wave propagation through a weak turbulence channel with small and large inner scales. Through comparison with the experimental results, it is apparent that there is a mismatch with the strong turbulence theory, and the data do not exhibit clear separation of scales as predicted by the asymptotic theory; thus concluding that the latter scenario has not occurred at the turbulence level during the experiment, which can be produced with extremely large apertures.

Perlot and Fritzsche [163] investigated the aperture averaging of optical scintillations through the evaluation of irradiance flux statistics, which are extracted from a sequence of pupil intensity pattern images captured with a charge-coupled device (CCD)-based camera. In addition, the spatial and temporal behaviour of the optical intensities are observed in the

presence of significant transverse wind and short link distances (<1 km), which can be directly related to the “frozen turbulence” phenomenon. However, the experimental setup and measurement techniques are subjected to various constraints and drawbacks, which in turn restrict the choice of turbulence scenarios that can be investigated in the corresponding study. For instance, the recording of scintillations by the CCD camera may not be accurate under the influence of strong wind, mainly because the limited frame rate of the low-noise camera cannot follow the fluctuations and time averaging that occurs over the CCD integration time. Other factors that may severely distort the statistical evaluation include: the size of the entrance pupil, the upper bound set on the intensity correlation length, and the limitation in the quantization process of the CCD camera. Furthermore, saturation of the intensity at the highest digital number of the imaging device corrupts the scintillation index estimation; whereas the lack of resolution for intensity values near zero causes much difficulty in the modelling of the PDF and prediction of the fade probabilities. Based upon the presented scenarios, the intensity fluctuations and aperture averaging factor derived from the experimental data agreed fairly well with those predicted by theory. While a strong correlation between the temporal and spatial intensity covariance functions has been observed in this work, the attempt of extending this space/time equivalence to the second-order statistics of the aperture-averaged power remains unsuccessful.

Utilizing a slightly diverged 1550-nm Gaussian laser beam operating at a transmitted optical power of ~22 dBm with a measured beam divergence of 0.46 mrad (at full angle), Vetelino *et al.* [164] carried out field measurements to collect irradiance data simultaneously using three receiving apertures of different sizes for investigating the aperture-averaging effects. The path average values of important atmospheric parameters were inferred from the measurements and scintillation theory, and then used to reproduce the experimental data with numerical simulations and develop the parameters for the

theoretical PDFs. Correspondingly, the irradiance fluctuations of the Gaussian beam wave propagating through the atmosphere along a horizontal path, near the ground, in the moderate-to-strong turbulence regime, were examined based upon the probability density distributions for the three apertures at two different cases of the moderate and strong turbulences. In addition, the probability density distributions of the measured irradiance are compared with the simulated data and the theoretical lognormal and gamma-gamma turbulence models. For this particular experimental setup, it was observed that the spherical wave theory produces comparable results for the statistics of the optical laser beam. In the moderate-to-strong fluctuation regime, the gamma-gamma PDF provides a good fit to the irradiance fluctuations collected by finite-sized apertures that are significantly smaller than the coherence radius; whereas the fluctuations appear to be lognormal distributed for apertures larger than or equal to the coherence radius.

In [166, 167], the performance of FSO communication link is experimentally investigated under the weak atmospheric turbulence conditions, by using a dedicated indoor atmospheric chamber to generate and control the scintillation effect in the laboratory. The viability and application of the laboratory atmospheric chamber in emulating the turbulence scenarios on outdoor environment are examined and validated through a series of methodologies, which include: (1) characterization and calibration of the atmospheric chamber; (2) comparison of recorded measurements with respect to the theoretical prediction, showing good match between these datasets; (3) demonstration of methods to generate the turbulence and control its level; and (4) derivation of the relation between the experimental environment and outdoor FSO link to ensure total reciprocity. In this work, it was shown that the turbulence-induced scintillations severely affects the link availability of FSO communication systems due to the sharp response of the BER performance; and the analysis and demonstration presented a step forward to characterize

the atmospheric channel in an indoor environment, which is by nature complex and unpredictable. The developed laboratory atmospheric chamber has been used in numerous relevant experimental studies, which reported the characterization and modelling of the FSO communication channel [168, 169] and performance evaluation of the FSO system [170-172] under the influence of different atmospheric conditions (e.g., fog, turbulence and smoke).

As evident from the aforementioned field-based experimental studies, the characterization and measurements involving the effects of atmospheric turbulence under diverse weather conditions are indeed very challenging, mainly due to the long waiting time to observe and experience reoccurrence of different atmospheric events, which may possibly take weeks or months. In addition, the link alignment and adjustment and prediction of numerous important system design and weather-dependent parameters are much difficult to perform in actual field measurements, thereby limiting the variety and range of variables that could be considered in the experiments.

5.3. Main Contributions of Research

Taking advantage of the dedicated laboratory atmospheric chamber and viability of introducing more extensive methodologies with a wider scope of design consideration in the indoor environment, the proposed study presents the joint investigation and practical demonstration of the effects of aperture averaging and beam width on the FSO link under laboratory-controlled atmospheric turbulence conditions. It should be noted that the phase diffuser is not considered in this experimental work, mainly because the author would like to observe and confirm the relationships between the transmitter beam width, receiver aperture dimension and turbulence strength, which are characterized for the first time here.

Correspondingly, the proposed study can be extended in a more progressive manner by taking into account multiple variables in the experiments, which in turn requires more sophisticated equipments, such as a variable phase diffuser and optical beam profiler.

Based upon a carefully designed experiment setup to reproduce the turbulence-induced scintillation effects typically encountered in the FSO communication channel in the outdoor environment, a series of experiments and data acquisition are performed in the study. In particular, a range of receiver aperture dimensions, beam width settings and turbulence strengths are considered. Correspondingly, the measurement data goes through the post-analysis processes, which include: (1) generation of the probability density distributions of the received optical signal; (2) estimation of the beam radius (i.e., spot size) of the Gaussian laser beam; (3) calculation of the relevant turbulence strength parameters, such as the refractive index structure parameter, Rytov variance and scintillation index; and (4) validation of the empirical behaviour with respect to the theoretical or proposed models through the GOF tests.

The aperture-averaging effect is examined and characterized through the probability density distributions of the received optical signal, which are then compared with the predicted lognormal and gamma-gamma turbulence models; showing relatively good agreement between the observed density distributions and theoretical PDFs, as evident from the GOF test statistics. In the presence of stronger turbulence scenarios, optical fluctuations occur predominantly with decreasing receiver aperture sizes, resulting from the diminishing effects of aperture averaging; which are indicated by larger values of scintillation index and greater dispersion in the signal density distributions. In addition, a smaller spot size of the optical laser beam leads to stronger fluctuations in the received optical signal, mainly due to the aggravation of the turbulence-induced beam wander and

scintillation effects; thereby substantiating the theoretical argument that partially coherent Gaussian laser beam of larger beam width potentially mitigates the undesirable impacts of the FSO channel.

Moreover, the aperture-averaging factor predicted from the measurement data exhibits similar trend as the theoretical plane wave model with increasing scaled aperture size, for all the considered beam width settings. Subsequent analysis reveals that the relationship between the aperture averaging factor and point-received scintillation index can be represented by a first-order linear regression model. The coefficients of the regression model are determined through curve fitting technique, and used as appropriate measures to observe and compare the variation in the behaviour by adjusting the aperture size and beam width. The resulting GOF test statistics are presented to validate the accuracy of the linear regression model in describing this empirical-based relationship.

Furthermore, a comparison of the measured Q-factor between an aperture-averaged optical receiver and its corresponding finite point receiver show that performance enhancement of manifold gain can be achieved with increasing scaled aperture size. Therefore, the introduction of an enlarged receiver aperture improves the effective collection of the received optical signal, and potentially mitigates the turbulence-induced beam wander and scintillation effects.

5.4. Experiment Setup for Turbulence Channel

Figure 5.1 depicts the block diagram of the experimental setup for the proposed study, with the relevant parameters summarized in Table 5.1. In accordance to the theoretical treatments in the former chapters, the IM/DD and NRZ-OOK technique is

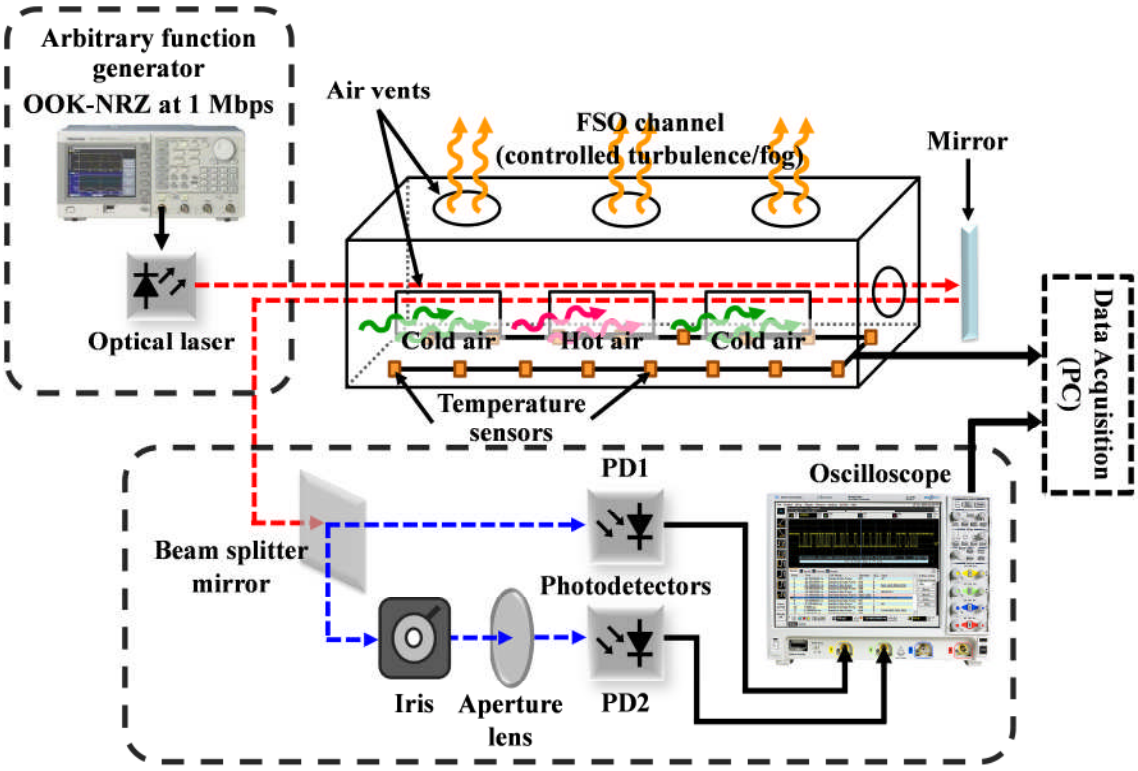

Figure 5.1: Block diagram of the experiment setup.

considered in the system under study. Binary OOK bits at 1 Mbps are generated using the Tektronix AFG3252C arbitrary function generator, and modulated onto the instantaneous intensity of a Gaussian beam-wave emitted by an optical laser source operating at a wavelength of 785 nm (i.e., near-infrared) with a 3 mW circular beam. The spot size w_0 of the optical laser beam can be varied by adjusting the aperture lens attached to the device.

The laboratory atmospheric chamber is constructed by cascading eight individual compartments to give a dimension of 550 cm × 30 cm × 30 cm, in which each segment has air vents (at the side and/or top) to allow air circulation. With the use of external fans, hot and cold air are feed into the atmospheric chamber in the direction perpendicular to the propagation path of the optical laser beam. This in turn creates temperature gradient within the chamber for emulating the atmospheric turbulence typically encountered on outdoor

Table 5.1: Parameters of the FSO transmitter and receiver in the experiment setup.

Parameter		Value
Transmitter		
Data source	Modulation format	NRZ-OOK
	Bit rate	1 Mbps
Laser diode	Peak wavelength	785 nm
	Output power	3 mW
	Beam profile	Circular
	Class	3B
Receiver		
Optical lens	Diameter	40 mm
	Focal length	100 mm
Iris	Maximum diameter opening	40 mm
Photodetector	Module	Thorlabs PDA10A-EC
	Detector	Silicon *p-i-n*
	Spectral range of sensitivity	200 – 1100 nm
	Active area	0.8 mm^2
	Typical spectral sensitivity	0.45 A/W at 750 nm
	Dark offset	10 mV
	Transimpedance gain	5×10^3 V/A

FSO channel. The cold air is maintained at the room temperature ranging from 20 °C to 25 °C, whereas the hot air is controlled with the external heating source to vary the temperature between 20 °C and 90 °C. Temperature sensors are placed throughout the chamber to measure and record the instantaneous temperatures at different locations along the length of the channel, which are vital measurements for estimating the relevant atmospheric turbulence parameters. At the other end of the atmospheric chamber, a mirror is used to reflect the optical laser beam back to the transmitter side, thereby extending the link range to approximately 11 m, such that stronger turbulence scenarios can be produced and observed in the experiment.

At the receiving-end, a beam splitter mirror [114] separates (typically by half) the incident optical laser beam (at a 45° angle) into a transmitted beam and reflected beam at

right angle; in which the former beam is received directly by a Thorlabs PDA10A-EC [173] Si amplified photodetector (i.e., PD1). The reflected beam goes through the adjustable iris opening, which defines the receiver aperture diameter D; and then collected and focused by the aperture lens before reaching the second photodetector (i.e., PD2) that is identical to PD1. The electrical output of the photodetectors are viewed and captured using an Agilent DSO9254A high-frequency digital oscilloscope, whereby complete post-analysis are subsequently performed on these measurement data to obtain the relevant parameters.

5.5. Methodology and Post-Analysis

5.5.1. Data Acquisition

For a chosen beam width setting, measurements are performed and recorded to obtain the amplitude distribution of the optical laser beam, in which the value of the beam width can be estimated; and multiple data runs are carried out to ensure consistency in the measurement data. For each data run, six turbulence conditions are produced, and the received optical signals of both finite point-received and aperture-averaged paths for a variety of receiver aperture diameter $D = \{3, 6, 10, 15, 20, 30, 40\}$ mm are captured for 20 datasets in each turbulence case. The raw measurement data then goes through a series of post-processes using Matlab, which include data alignment, low-pass filtering, down-sampling and bit thresholding, in order to recover the transmitted binary OOK-NRZ data. These extensive measurements enable the calculation of the scintillation indices ($\sigma_I^2(D)$ and $\sigma_I^2(0)$) and aperture-averaging factor A_g and generation of the signal probability density distributions with good accuracy. At 17 different locations throughout the laboratory atmospheric chamber, temperature measurements are recorded simultaneously with a time interval of 5 s during each data run to capture the temperature variations along

the chamber; thus allowing the computation of the important turbulence-related parameters, which include the refractive index structure parameter C_n^2 and Rytov variance σ_R^2.

5.5.2. Generation of the Probability Density Distributions

The complete datasets acquired from the individual turbulence scenario for each data run are taken into account in the generation of probability density distributions of the aperture-averaged received optical signal (see part (a) of Figure 5.5 to Figure 5.8 and Figure A.1 to Figure A.8 (in Appendix A)) and the natural logarithm of the corresponding normalized signal (i.e., part (b) of the mentioned figures). To produce the signal density distributions, the mean value is subtracted from the post-processed measurement data, which are then categorized into their respective histogram bins with a fixed bin width of 5 mV; and the resulting probability densities are obtained by dividing the number of data points in each bin by the bin width and the total number of data points. The natural logarithm of the normalized optical intensities are calculated and sorted into their respective histogram bins for obtaining the normalized log intensity PDFs. These PDFs are used to observe and compare the characteristics of the received optical signal with respect to the theoretical lognormal and gamma-gamma turbulence models, particularly in capturing the behaviour in the tails of the PDFs. The bin sizes are varied for different cases of D, with values ranging between 0.025 and 0.25 due to the vastly widening of the dispersion in the PDF for smaller values of D, thereby eliminating the discrepancies resulting from fluctuations in the density values and/or empty histogram bins. The mid-point of the normalized log intensities are used as the corresponding log-intensity value for the experimental probability density when plotting the PDF.

5.5.3. Prediction of the Beam Width

For a particular beam width setting, the optical intensities of the Gaussian laser beam at numerous transversal distance points are measured and recorded preceding the first data run, in order to obtain the amplitude profile of the optical beam. Based upon the theoretical Gaussian-beam wave model, the experimental normalized beam intensities can be determined; in which w_0 (of the radial axis) is predicted at $-\ln[I/\max(I)] = 1.0$. In the proposed experimental study, three beam width settings have been chosen and estimated as $w_0 = \{2.7731, 4.5174, 5.4609\}$ mm, as depicted in Figure 5.2 to Figure 5.4, respectively.

5.5.4. Computation of the Turbulence Strength Parameters

Recall the discussion on optical turbulences in the atmospheric channel resulting in the scintillation effects in Section 2.4.2.2, which highlights the adoption of the Kolmogorov energy cascade theory in describing such phenomenon. The temperature measurements recorded during each data run are taken into account in the estimation of the temperature structure constant C_T^2 by using (2.32), which is then substituted into (2.38) to determine the refractive index structure parameter C_n^2. Correspondingly, the Rytov variance σ_R^2 can be obtained from (2.40). Based on (2.39), the measured received optical signals are used in the calculation of the aperture-averaged and finite point-received scintillation indices $\sigma_I^2(D)$ and $\sigma_I^2(0)$, which are required for finding the aperture-averaging factor A_g.

5.6. Model Performance Indicators

The GOF test encompasses a series of calculations to examine the discrepancies, statistical significance and/or correlation between the experimental data and theoretical

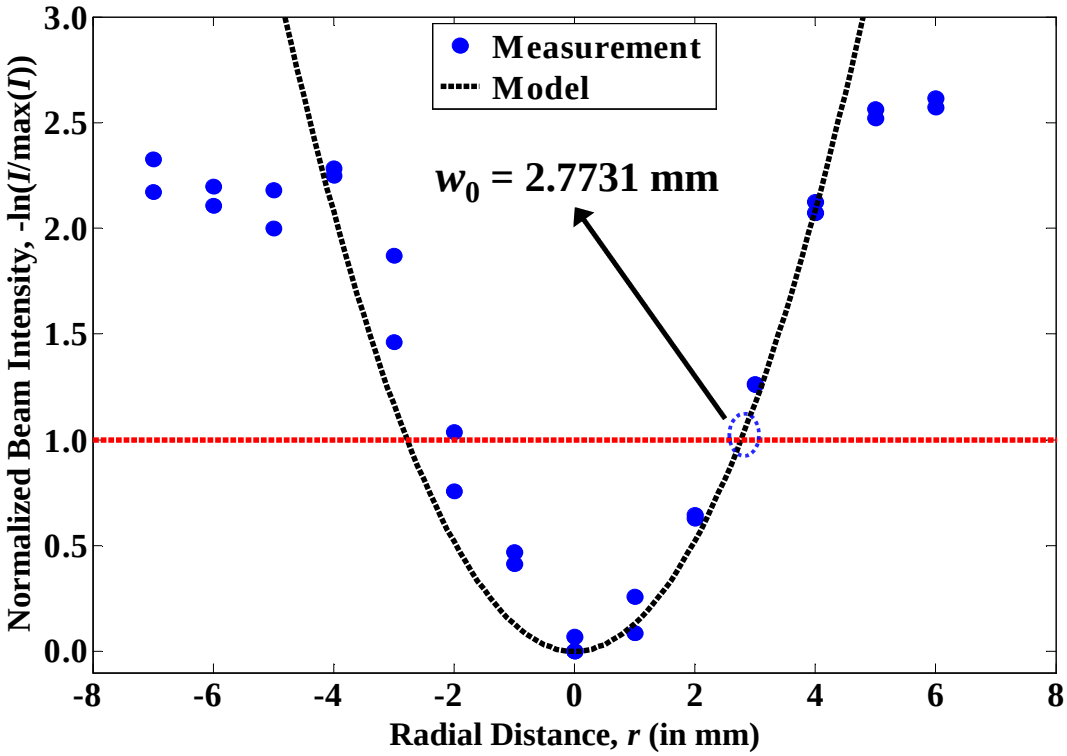

Figure 5.2: Normalized beam intensity as a function of the radial distance, in which the predicted beam width of the Gaussian beam is $w_0 = 2.7731$ mm.

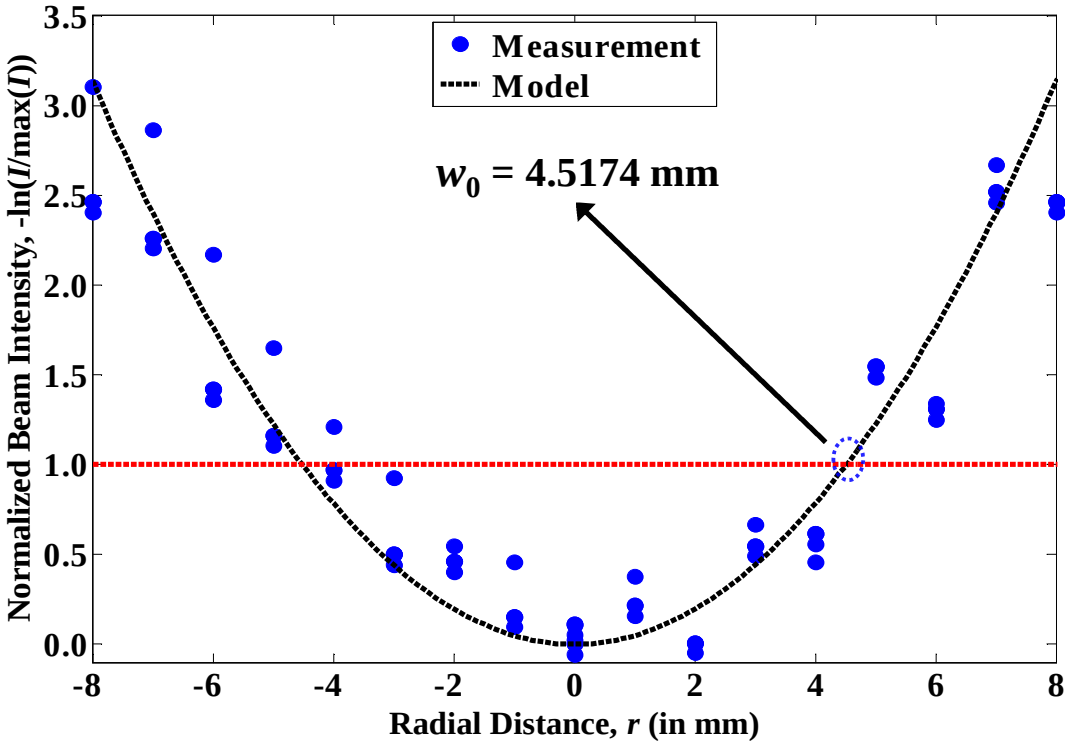

Figure 5.3: Normalized beam intensity as a function of the radial distance, in which the predicted beam width of the Gaussian beam is $w_0 = 4.5174$ mm.

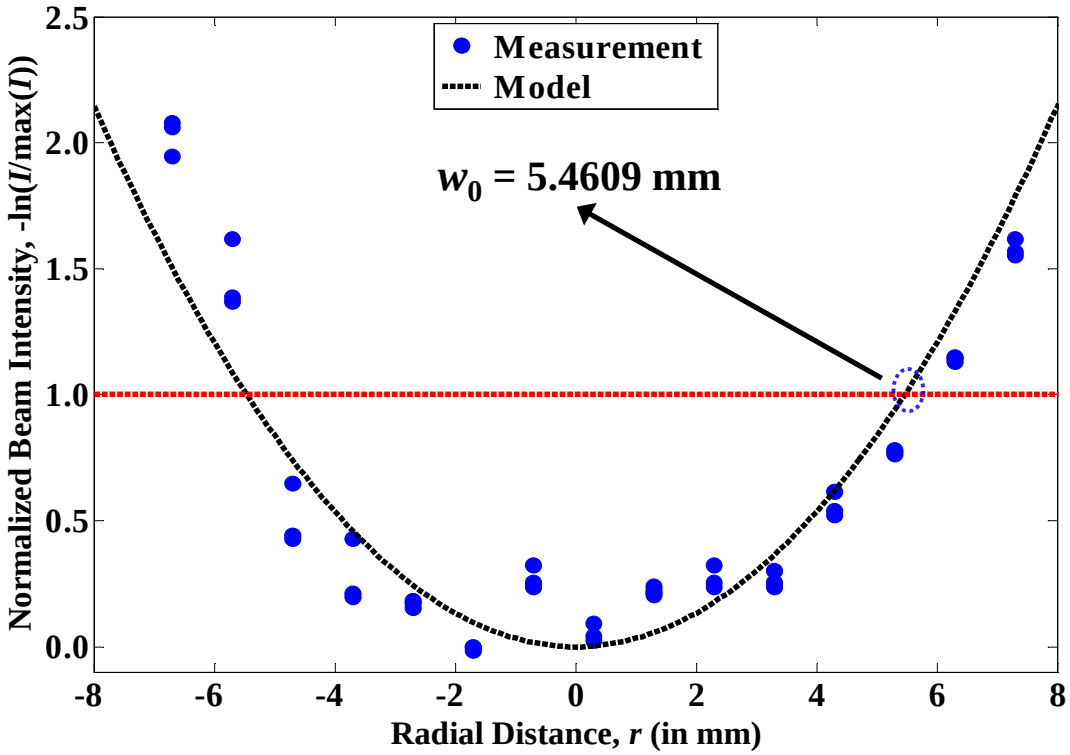

Figure 5.4: Normalized beam intensity as a function of the radial distance, in which the predicted beam width of the Gaussian beam is $w_0 = 5.4609$ mm.

models through various model performance indicators, which include: the mean bias error (*MBE*), root mean square error (*RMSE*), t-statistic (t_s), correlation coefficient (R), and coefficient of determination (*R*-square). The *MBE* is defined through the relation [174]:

$$MBE = \frac{1}{N}\sum_{i=1}^{N}(y_i - x_i) \ ; \tag{5.1}$$

where y_i denotes the i^{th} predicted value from the functional representation, x_i represents the i^{th} observed value (i.e., experimental data), and N indicates the total number of observations. This performance metric provides information pertaining to the long-term performance of the model under investigation, in which a positive value of the indicator corresponds to the degree of overestimation in the theoretically predicted values, and vice versa. In general, a smaller magnitude of *MBE* is desirable, implying that the overall

deviation of the theoretical and/or proposed model with respect to the measurement data is less significant and that the model is applicable to the study. Another parameter of interest is the *RMSE* given by [174]:

$$RMSE = \sqrt{\frac{1}{N}\sum_{i=1}^{N}(y_i - x_i)^2} \ . \tag{5.2}$$

In contrast to the *MBE*, the *RMSE* provides information pertaining to the short-term performance of the functional representation, since the calculation involves a term-by-term comparison of the actual deviation between the calculated and observed values. Similarly, a smaller *RMSE* value indicates a better model performance. The separate use of the *MBE* and *RMSE* in assessing the model performance may lead to incorrect findings, because it may be possible to have a large *RMSE* value while simultaneously getting a significantly smaller *MBE* value from the test, and vice versa.

Taking into account the inconvenience and possible inaccuracy of utilizing separate statistical performance indicators to evaluate a model's performance, the t-statistic t_s has been introduced by Stone in [175], which formulated a relation for the indicator by incorporating the *MBE* and *RMSE* into the numerical expression as follows:

$$t_s = \sqrt{\frac{(N-1)MBE^2}{RMSE^2 - MBE^2}} \ . \tag{5.3}$$

This statistical indicator takes into account the dispersion of the results, which is neglected when the *MBE* and *RMSE* are considered separately. In addition, the t-statistic is a useful indicator to measure the statistical significance of a model's estimates at a particular confidence interval. However, a critical value t_c has to be identified from the standard statistical table (e.g., $t_c\left(\frac{\alpha_t}{2}\right)$ at the α_t-level of significance, and $(N-1)$ degrees of

freedom (DF)) [176] as presented in Appendix B, in order to validate the statistical significance of a model's estimates. Therefore, it can be inferred that the model under study is statistically significant at the $(1-\alpha_t)$ confidence level, when the calculated t_s value falls within the interval defined between $-t_c$ and t_c (i.e., the acceptance region under the reduced normal-distribution curve). On the contrary, the indicator with a calculated value beyond the defined interval (i.e., the critical region) implies that the hypothesis, which presumes the parameter selection has improved the model can be rejected.

The correlation coefficient measures the strength of the bivariate relationship between the variables x and y based on the average of all distance products separating individual data points from the two sample means, which are adjusted accordingly by dividing the distances with their respective standard deviations to avoid scale distortions. Taking into account the concurrent computation of the sample standard deviations, the correlation coefficient R can be determined through the relation [177]:

$$R = \frac{\sum_{i=1}^{N} x_i y_i - N\bar{x}\bar{y}}{\sqrt{(\sum_{i=1}^{N} x_i^2 - N\bar{x}^2)(\sum_{i=1}^{N} y_i^2 - N\bar{y}^2)}}\ ; \tag{5.4}$$

where $\bar{x}$ and $\bar{y}$ denote the mean of the N observed (i.e., actual measurement data) and predicted (i.e., theoretical models) values, respectively. In principle, the correlation coefficient ranges between -1 to 1; where $R > 0$ indicates a positive linear relationship between the x and y datasets, $R < 0$ suggests a negative linear relationship (i.e., anti-correlation), and R values close to or equal to 0 implies no linear relationship between the datasets. Furthermore, the coefficient of determination R-square is a useful indicator to evaluate how successful the fit of a functional representation is in explaining the variation of the measurement data, as defined by the equation as follows [178]:

$$R\text{-square} = 1 - \frac{\sum_{i=1}^{N}(x_i - y_i)^2}{\sum_{i=1}^{N}(x_i - \bar{x})^2} \ . \tag{5.5}$$

The calculated *R*-square value ranges from 0 to 1, in which a value closer to unity signifies a better fit of the mathematical model to the observed values. For instance, an *R*-square value of 0.8624 indicates that the fit is able to justify 86.24% of the total variation in the data about the mean.

5.7. Experimental Results and Discussion

5.7.1. Probability Density Distributions of the Received Optical Signal

Figure 5.5(a) presents the probability density distributions of the received optical signals encompassing both data bits '0' and '1', for $D = \{40, 30, 20, 15, 10, 6, 3\}$ mm and $w_0 = 2.7731$ mm, in the presence of a weak turbulence condition with $\sigma_R^2 = 0.1738$ ($C_n^2 = 1.5272 \times 10^{-11}$ m$^{-2/3}$). These histograms clearly depict the characteristics of the received optical signals, showing the distinctive characteristics of the signal density distributions for the cases of $D = \{40, 30, 20\}$ mm, in which the signal amplitude profiles for both '0' and '1' bits are almost identical and equidistant on both sides of the zero mark. Nevertheless, such distinctive features of the signal distributions diminish with decreasing values of D, as evident from the reduction in the separation distance between the respective peaks towards the centre and a wider dispersion in the density distributions. These observations are further substantiated by increasing values of $\sigma_I^2(D)$, varying from a negligibly small value of 0.0042 (for $D = 40$ mm) to a relatively large value of 0.4360 (for $D = 3$ mm). In particular, it can be seen that the signal profiles for bit '0' becomes more broadened and skewed with longer tails towards the positive direction, when D is varied from 15 mm to 3 mm; thereby inferring that the optical intensities resembling bit '0' are

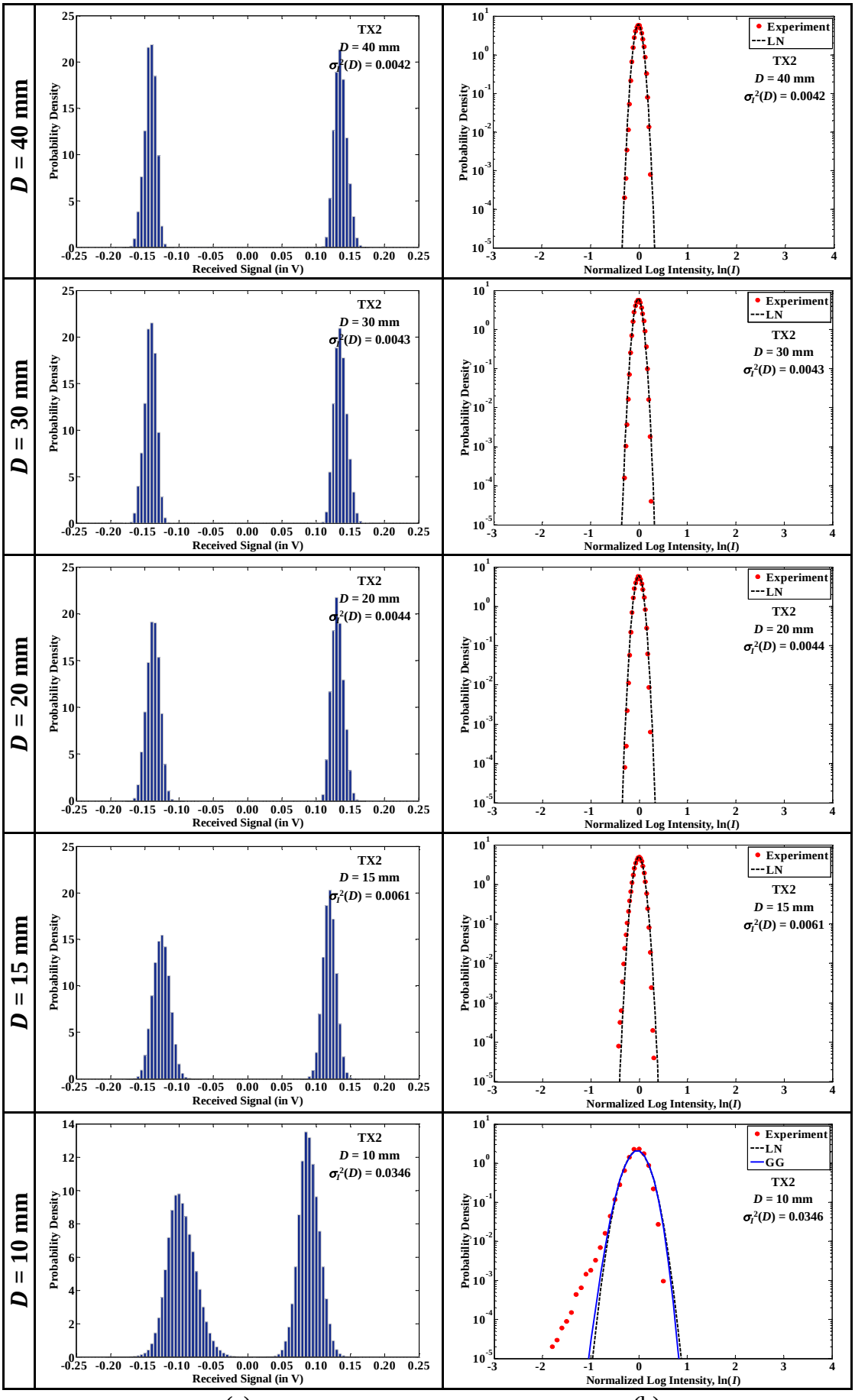
D = 40 mm
TX2
D = 40 mm
σI²(D) = 0.0042
Probability Density
Received Signal (in V)
Experiment
LN
Normalized Log Intensity, ln(I)
D = 30 mm
TX2
D = 30 mm
σI²(D) = 0.0043
D = 20 mm
TX2
D = 20 mm
σI²(D) = 0.0044
D = 15 mm
TX2
D = 15 mm
σI²(D) = 0.0061
D = 10 mm
TX2
D = 10 mm
σI²(D) = 0.0346
GG
(a)
(b)

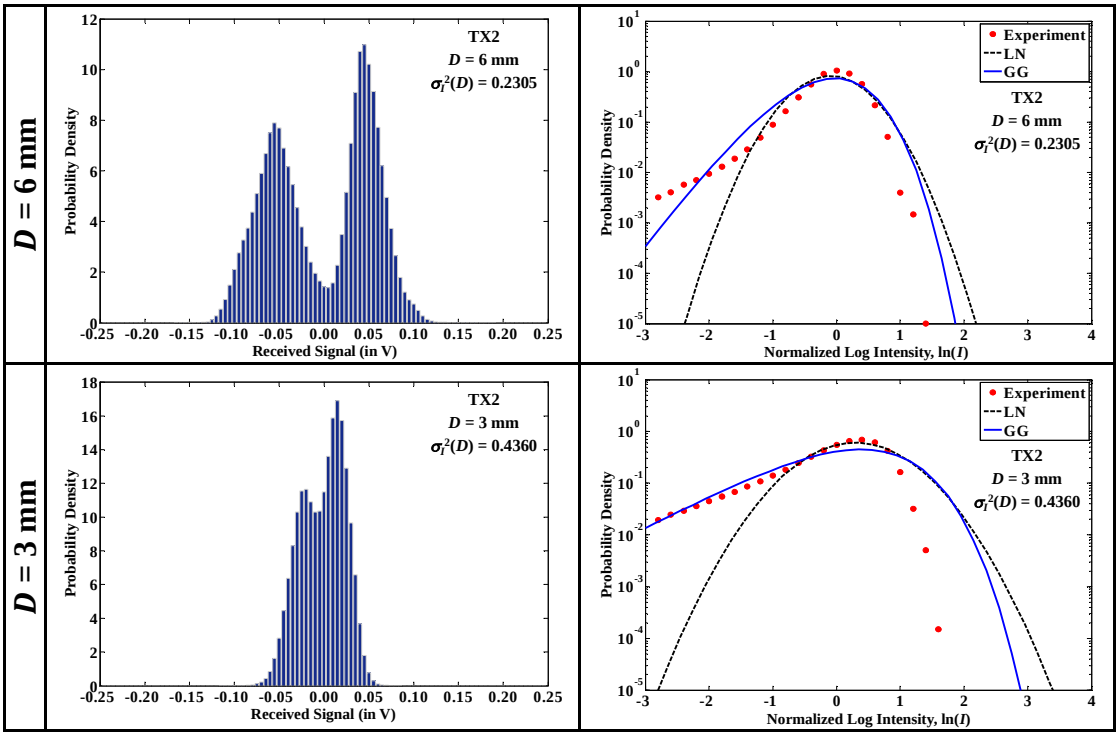

Figure 5.5: (a) Received signal distribution for different receiver aperture diameters of $D = \{40, 30, 20, 15, 10, 6, 3\}$ mm and beam width setting of $w_0 = 2.7731$ mm, with turbulence at $\sigma_R^2 = 0.1738$ ($C_n^2 = 1.5272 \times 10^{-11}$ m$^{-2/3}$); and (b) comparisons of the normalized log irradiance PDF between the experimental data and the theoretical models.

more susceptible to the turbulence-induced scintillation and aperture-averaging effect, as compared to bit '1'. In the limiting cases of $D = \{6, 3\}$ mm, it is noted that the signal amplitude reduces significantly (with mean values ranging between ± 50 mV), mainly due to the diminishing effects of aperture-averaging, thus resulting in the merging of the signal profiles for bits '0' and '1' towards the zero mark. Consequently, the heavy signal distortions incurred by the degrading impacts of turbulence and reduced aperture size make these data bits indistinguishable from each other, inevitably causing an increase in the BER due to the higher likelihood of detection error, particularly for the case of $D = 3$ mm.

The variations of the signal density distributions in terms of different considered values of D at $w_0 = 2.7731$ mm, are examined for a stronger turbulence case of $\sigma_R^2 = 0.5165$ ($C_n^2 = 4.5382 \times 10^{-11}$ m$^{-2/3}$), as illustrated in Figure 5.6(a). In general, the broadening of the probability density distributions are more pronounced for all considered values of D, in comparison to the signal amplitude profiles depicted in Figure 5.5(a); which corresponds to relatively larger $\sigma_I^2(D)$ values, ranging from 0.0389 (for $D = 40$ mm) to 0.5000 (for $D = 3$ mm). In addition, the separation distance between the peaks of the signal profiles for bits '0' and '1' reduces rapidly with decreasing values of D; in which the merging of the respective distributions occurs for $D \leq 15$ mm, thereby causing the data bits to be indistinguishable from one another and imposing penalty upon the error performance. Under the worst case scenarios of $D = \{6, 3\}$ mm, the received optical signals are mainly concentrated within the ± 20 mV and ± 10 mV regions, respectively; implying that the use of small-size aperture lens does not effectively collect and focus the received optical signals. Moreover, the small collection area of the receiver aperture is unable to compensate for the fluctuations and jittering of the optical laser beam introduced by the turbulence-induced beam wander and scintillation effects, particularly when a narrow beam width is considered. The corresponding analysis has been extended to investigate various turbulence cases of $\sigma_R^2 = \{0.1851, 0.2322, 0.2374, 0.3797\}$; in which the probability density distributions of the received optical signal for a series of D, and comparisons of the normalized log irradiance PDF between the experimental data and theoretical models are available in Appendix A.1.

The distribution of the normalized log intensity $\ln(I)$ presents a viable alternative to observe and compare the characteristics of the optical intensities, particularly in depicting the behaviour in the tails of the PDFs resulting from fluctuations and jittering of the optical

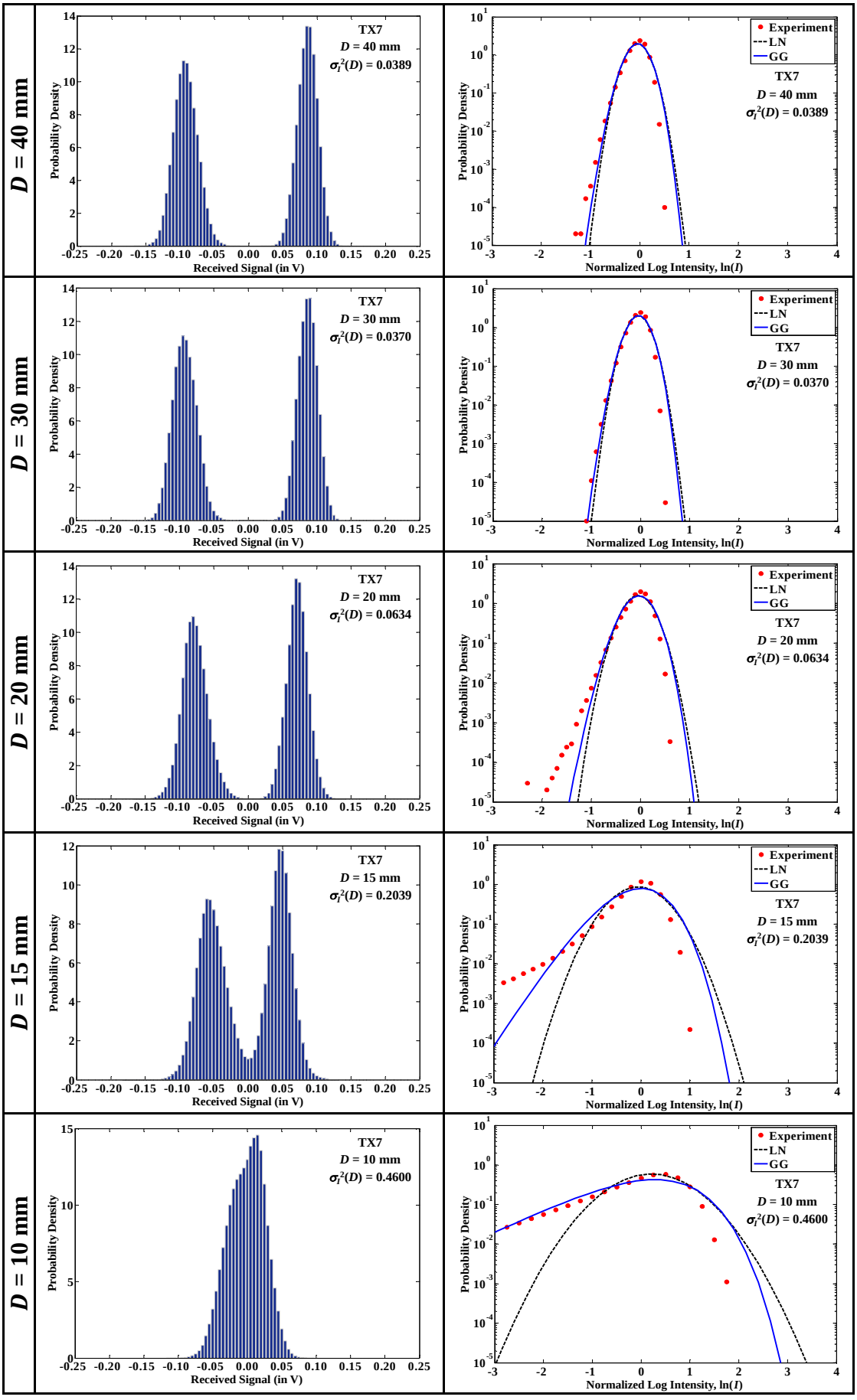
D = 40 mm
D = 30 mm
D = 20 mm
D = 15 mm
D = 10 mm
TX7
D = 40 mm
σ_I²(D) = 0.0389
D = 30 mm
σ_I²(D) = 0.0370
D = 20 mm
σ_I²(D) = 0.0634
D = 15 mm
σ_I²(D) = 0.2039
D = 10 mm
σ_I²(D) = 0.4600
Probability Density
Received Signal (in V)
Experiment
LN
GG
Normalized Log Intensity, ln(I)
(a)
(b)

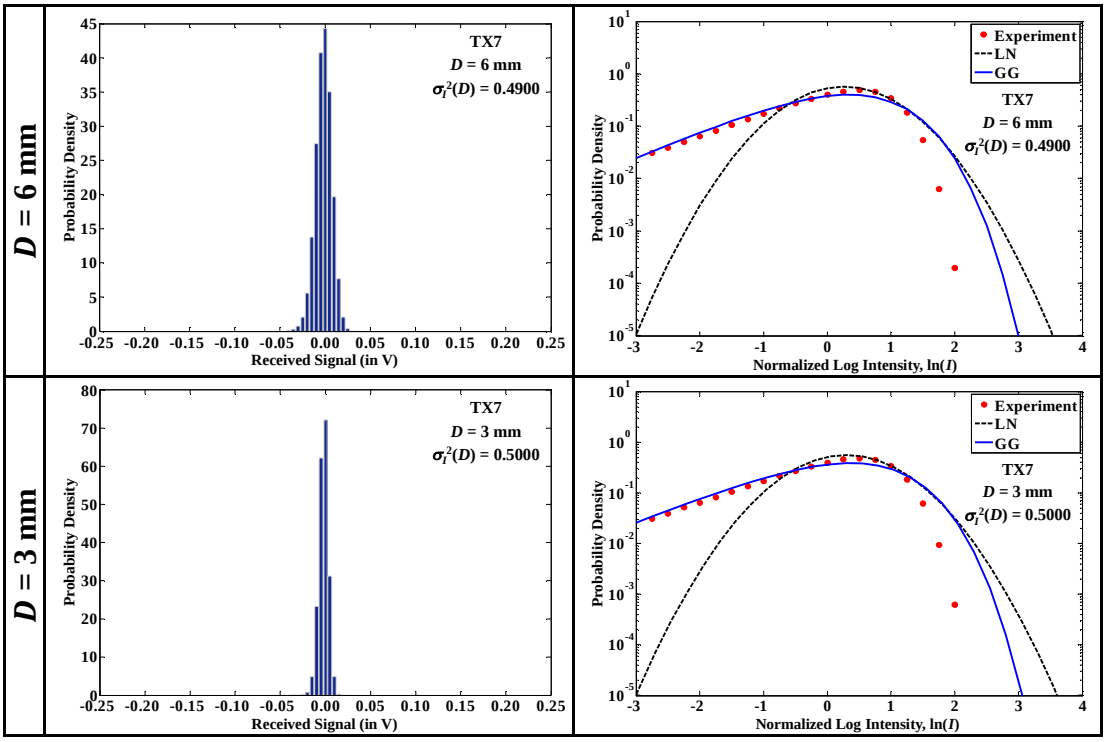

(a) (b)

Figure 5.6: (a) Received signal distribution for different receiver aperture diameters of $D = \{40, 30, 20, 15, 10, 6, 3\}$ mm and beam width setting of $w_0 = 2.7731$ mm, with turbulence at $\sigma_R^2 = 0.5165$ ($C_n^2 = 4.5382 \times 10^{-11}$ m$^{-2/3}$); and (b) comparisons of the normalized log irradiance PDF between the experimental data and the theoretical models.

laser beam. Based upon the experimental data for generating the signal density distributions in Figure 5.5(a) and Figure 5.6(a), the corresponding normalized log intensity PDFs are produced and shown accordingly in Figure 5.5(b) and Figure 5.6(b) for the turbulence cases of $\sigma_R^2 = \{0.1738, 0.5165\}$, respectively. In Figure 5.5(b), it is noted that the experimental data for the considered values of $D = \{40, 30, 20, 15\}$ mm can be described by the theoretical lognormal model with good accuracy; whereby optical fluctuations are almost negligible for these cases, as evident from the relatively small aperture-averaged scintillation indices of $\sigma_I^2(D) = \{0.0042, 0.0043, 0.0044, 0.0061\}$. The changing patterns of the PDFs in Figure 5.5(b) reveal an inherent shifting of the mean towards the negative direction (i.e., left) of the PDF with smaller D values, and the

broadening of the signal profiles (as highlighted in Figure 5.5(a)) is reflected accordingly in the PDFs. In the presence of more severe optical fluctuations for the cases of $D = \{6, 3\}$ mm, the negative tails of the PDFs are significantly elevated; in which such behaviour is resembled by the gamma-gamma model with better accuracy, as compared to the lognormal model. The comparisons made through these observations are further validated through a series of GOF tests with results as presented in Table 5.2. The correlation coefficient R is generally in excess of 0.94 for all considered values of D, and the *MBE* approximate to zero with desirable *RMSE* ranging between 0.0694 and 0.5124; thereby inferring a strong correlation with small discrepancies between the experimental data and theoretical models albeit slightly underestimating the observations (as indicated by negative values of the *MBE*). In addition, the resulting test statistics of the Student t-test indicate that t_s are confined within the acceptance region with their respective critical values t_c (defined for specific DF) provided in Table 5.2, which in turn suggests that the theoretical lognormal and/or gamma-gamma models are able to represent the observations

Table 5.2: The corresponding statistical test results depicting the GOF between the experimental data and the lognormal and gamma-gamma models, for a variety of receiver aperture diameter $D = \{40, 30, 20, 15, 10, 6, 3\}$ mm and beam width $w_0 = 2.7731$ mm, at $\sigma_R^2 = 0.1738$.

D (mm)	Model	MBE	$RMSE$	Student t-Test (95% Confidence Level)			R
				DF	t_c	t_s	
40	LN	-3.8832E-05	0.5124	42	2.0181	0.0003	0.9711
30	LN	-1.9739E-05	0.4969	44	2.0154	0.0002	0.9720
20	LN	-5.9444E-05	0.5318	42	2.0181	0.0005	0.9676
15	LN	-2.3607E-05	0.0777	58	2.0017	0.0016	0.9992
10	LN	-2.2032E-04	0.1021	46	2.0129	0.0103	0.9921
	GG	-1.3261E-04	0.0977	46	2.0129	0.0065	0.9933
6	LN	-2.7974E-05	0.0780	93	1.9858	0.0025	0.9540
	GG	-3.5103E-06	0.0838	90	1.9867	0.0003	0.9537
3	LN	-9.1700E-04	0.0495	96	1.9850	0.1283	0.9641
	GG	-6.8555E-04	0.0694	91	1.9864	0.0694	0.9416

at the 0.05 significance level (i.e., 95% confidence level).

Figure 5.6(b) shows that the normalized log irradiance PDFs are generally more broadened at $\sigma_R^2 = 0.5165$, as compared to the weak turbulence scenario of $\sigma_R^2 = 0.1738$ (in Figure 5.5(b)); and suffers a greater shift towards the left of the distributions with decreasing values of D. Moreover, the extent of the signal fluctuations for $D \leq 15$ mm can be seen from the substantial elevation in the negative tails of the PDFs, which is appropriately accounted by the gamma-gamma model, as evident from the GOF test statistics in Table 5.3. While both the theoretical lognormal and gamma-gamma models present strong correlation with $R > 0.94$ and slight underestimation of the experimental data with negative *MBE* values for all cases under study, the resulting test statistics reveal a better fit of the latter model due to the relatively lower *RMSE* and t_s values attained.

Table 5.3: The corresponding statistical test results depicting the GOF between the experimental data and the lognormal and gamma-gamma models, for a variety of receiver aperture diameter $D = \{40, 30, 20, 15, 10, 6, 3\}$ mm and beam width $w_0 = 2.7731$ mm, at $\sigma_R^2 = 0.5165$.

D (mm)	Model	MBE	$RMSE$	Student t-Test (95% Confidence Level)			R
				DF	t_c	t_s	
40	LN	-4.7793E-04	0.1856	36	2.0281	0.0109	0.9747
	GG	-3.0760E-04	0.1744	35	2.0301	0.0075	0.9791
30	LN	-4.2916E-04	0.1768	32	2.0369	0.0097	0.9803
	GG	-2.6936E-04	0.1665	32	2.0369	0.0065	0.9840
20	LN	-5.3501E-04	0.2039	51	2.0076	0.0134	0.9427
	GG	-3.2677E-04	0.1891	51	2.0076	0.0088	0.9529
15	LN	-3.8423E-04	0.0920	88	1.9873	0.0280	0.9449
	GG	-2.0988E-04	0.0956	86	1.9879	0.0147	0.9466
10	LN	-3.4383E-04	0.0542	78	1.9908	0.0396	0.9529
	GG	-1.7582E-04	0.0535	76	1.9917	0.0205	0.9521
6	LN	-1.0274E-04	0.0451	80	1.9901	0.0146	0.9719
	GG	-2.3774E-05	0.0302	81	1.9897	0.0050	0.9831
3	LN	-1.1087E-04	0.0434	80	1.9901	0.0163	0.9731
	GG	-3.1569E-05	0.0342	80	1.9901	0.0342	0.9791

For a larger value of $w_0 = 4.5174$ mm, the probability density distributions of the received optical signals are presented in Figure 5.7(a), taking into account a variety of receiver aperture dimensions and a turbulence scenario with $\sigma_R^2 = 0.9359$ ($C_n^2 = 8.2225 \times 10^{-11}$ $m^{-2/3}$). The signal density distributions of both data bits '0' and '1' exhibit distinctive characteristics for the cases of $D \geq 15$ mm, in which the signal amplitude profiles are near-identical (with mean values of ± 150 mV albeit showing slight reduction with decreasing values of D) and equally spaced on either sides of the zero mark. This implies that the received optical intensities resembling bits '0' and '1' are less susceptible to optical fluctuations and/or attenuation, as reflected by the extremely narrow opening of the normalized log intensity PDF (see Figure 5.7(b)) and negligibly small $\sigma_I^2(D)$ values, ranging from 0.0038 (for $D = 40$ mm) to 0.0051 (for $D = 15$ mm); thus making these data bits clearly distinguishable and resulting in minimum bit detection error. Nevertheless, the broadening of the signal profile becomes pronounced with reduced aperture size of the optical receiver, particularly for the cases of $D \leq 10$ mm; in which the distributions of bit '0' exhibit more skewness with longer tails extending toward the positive direction, as evident from the sharp increment in $\sigma_I^2(D) = \{0.0370, 0.1308, 0.2121\}$. While the respective peaks of the density distributions of bits '0' and '1' remains perceptible for all the observations in Figure 5.7(a), the merging of the signal distributions occurs mainly in the regions near the zero mark for the cases of $D = \{6, 3\}$ mm. It is apparent that the transmitted binary data are susceptible to severe signal distortion due to turbulence under the diminishing aperture-averaging effect, and may not be properly recovered from the weaker optical signals, thus imposing penalty upon the BER.

In the case of a strong turbulence with $\sigma_R^2 = 1.3356$ ($C_n^2 = 1.1734 \times 10^{-10}$ $m^{-2/3}$), the distinctive pattern of the density distributions of data bits '0' and '1' (in Figure 5.8(a)) is

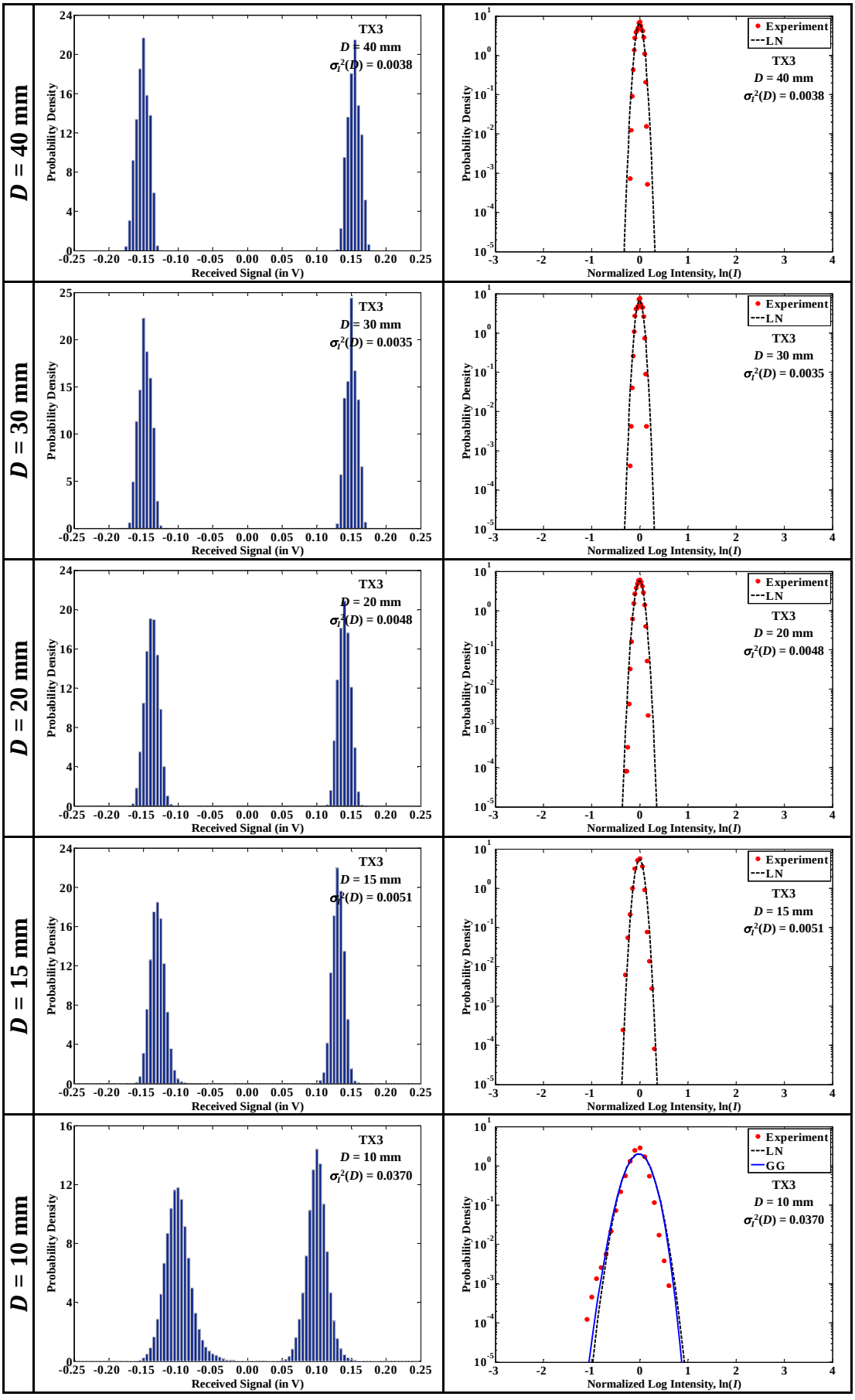
D = 40 mm
D = 30 mm
D = 20 mm
D = 15 mm
D = 10 mm
Probability Density
Received Signal (in V)
Normalized Log Intensity, ln(I)
TX3
D = 40 mm
σ_I²(D) = 0.0038
D = 30 mm
σ_I²(D) = 0.0035
D = 20 mm
σ_I²(D) = 0.0048
D = 15 mm
σ_I²(D) = 0.0051
D = 10 mm
σ_I²(D) = 0.0370
Experiment
LN
GG

(a) (b)

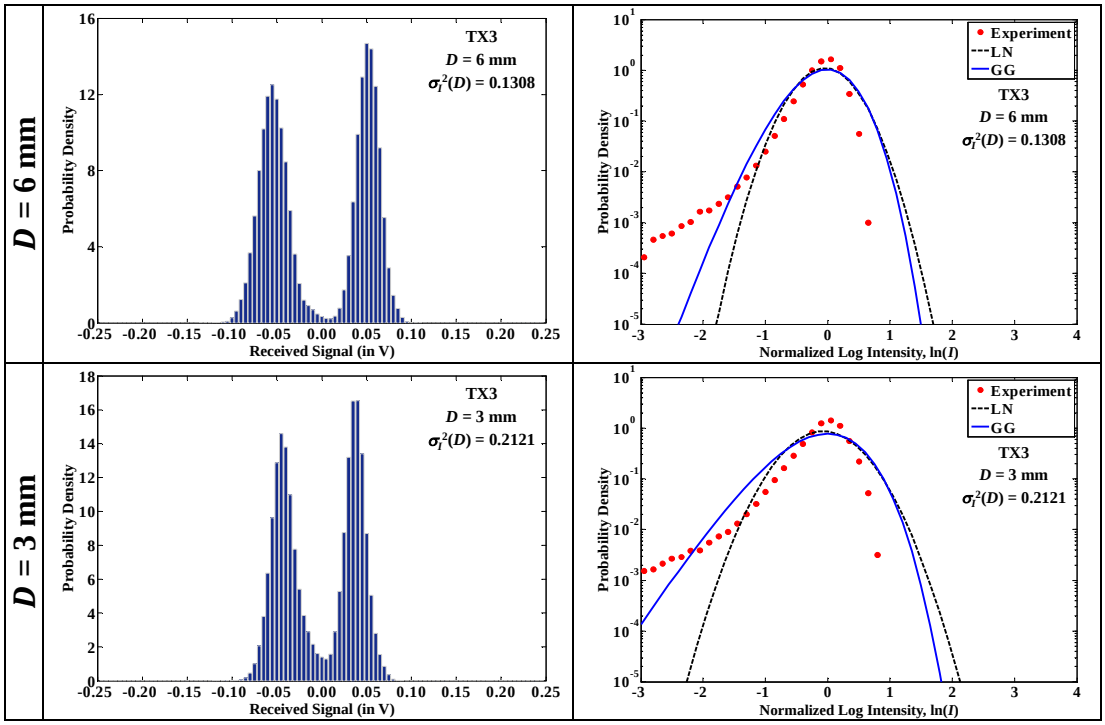

Figure 5.7: (a) Received signal distribution for different receiver aperture diameters of $D = \{40, 30, 20, 15, 10, 6, 3\}$ mm and beam width setting of $w_0 = 4.5174$ mm, with turbulence at $\sigma_R^2 = 0.9359$ ($C_n^2 = 8.2225 \times 10^{-11}$ m$^{-2/3}$); and (b) comparisons of the normalized log irradiance PDF between the experimental data and the theoretical models.

observed for $D = \{40, 30, 20\}$ mm with negligibly small values of $\sigma_I^2(D) = \{0.0049, 0.0043, 0.0058\}$, which clearly depicts the near-identical and distant separation (with mean amplitudes of ± 150 mV) of the respective signal profiles. The occurrence of such distinct characteristics in the signal amplitude profiles can be explained by the enhancement introduced by the aperture-averaging effect, which enables the effective collection of the optical signal and promotes the mitigation of the scintillation and beam wander. Under the diminishing effect of aperture averaging with decreasing values of D, the changing pattern of the histograms reveals that the signal distributions becomes broadened and gradually merges towards the zero mark, particularly for $D \leq 10$ mm, while the respective peaks of bits '0' and '1' still remains perceptible. The observed variations in

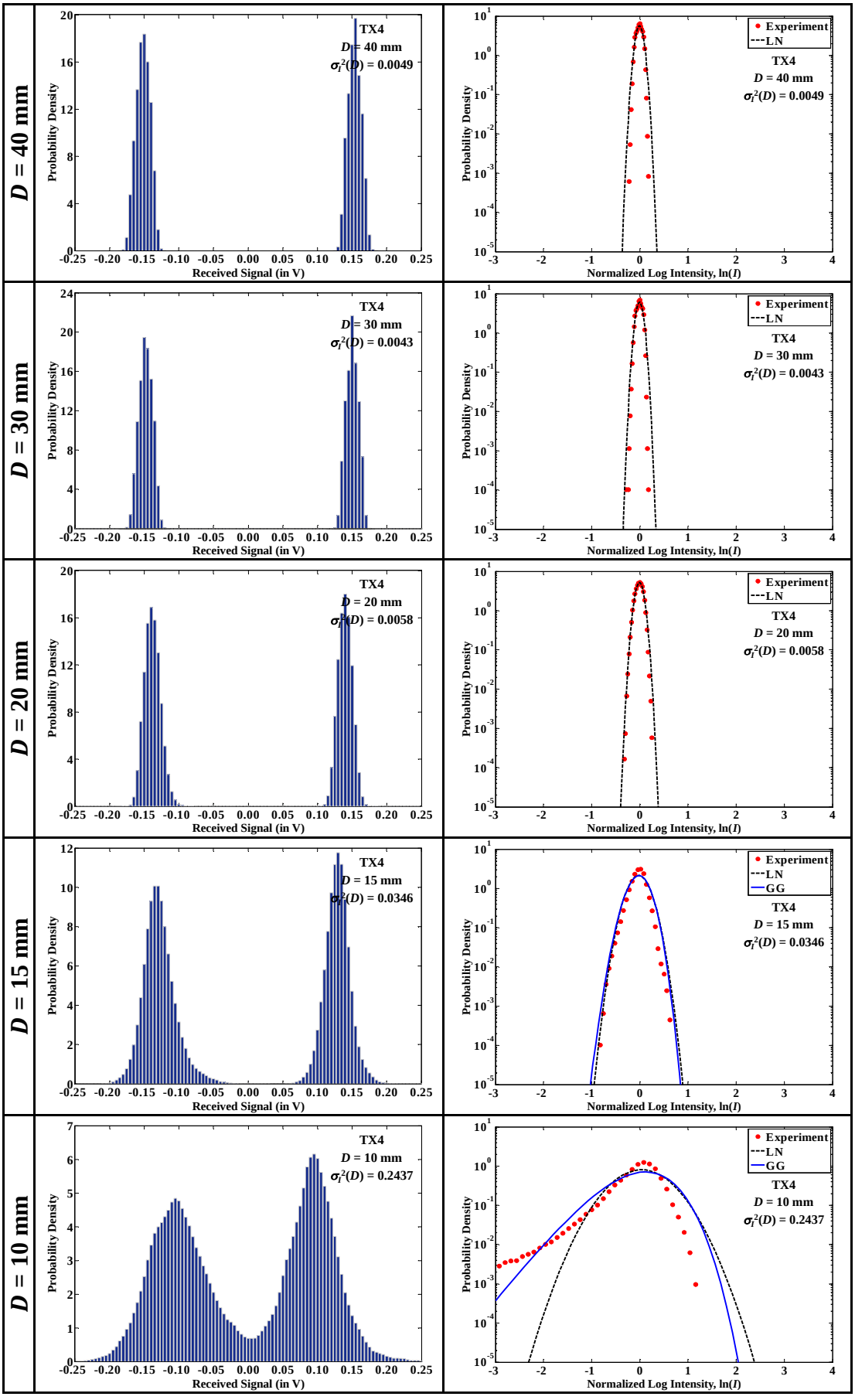
D = 40 mm
D = 30 mm
D = 20 mm
D = 15 mm
D = 10 mm
Probability Density
Received Signal (in V)
Normalized Log Intensity, ln(I)
TX4
D = 40 mm
σ_I²(D) = 0.0049
D = 30 mm
σ_I²(D) = 0.0043
D = 20 mm
σ_I²(D) = 0.0058
D = 15 mm
σ_I²(D) = 0.0346
D = 10 mm
σ_I²(D) = 0.2437
Experiment
LN
GG

(a) (b)

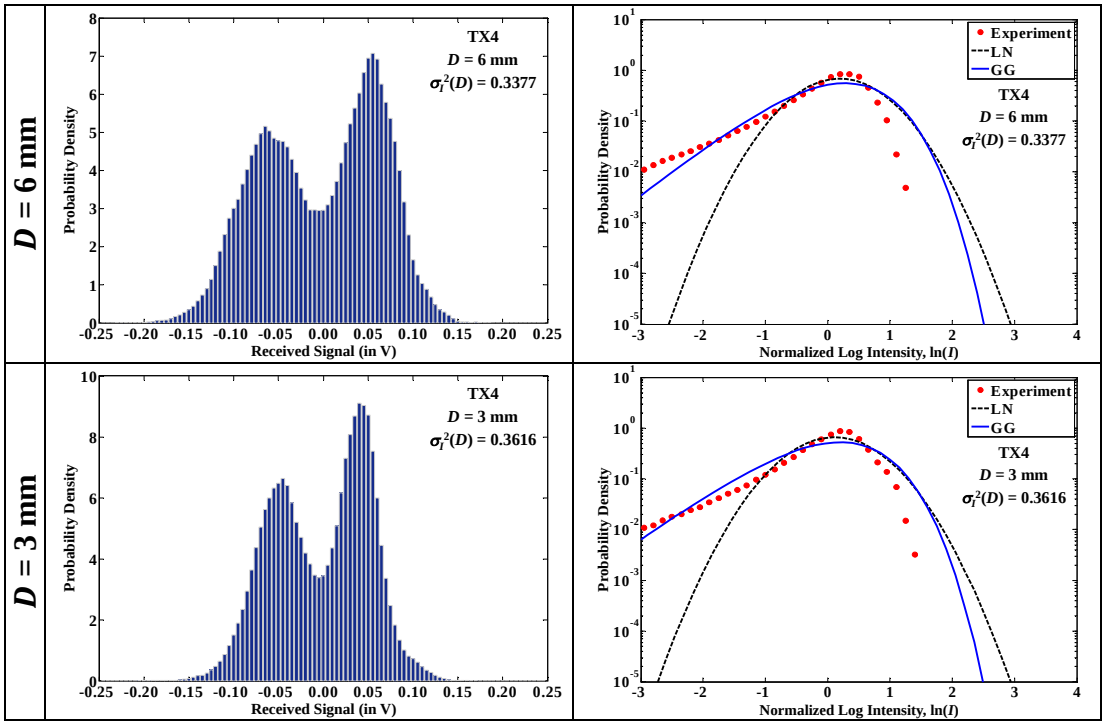

(a) (b)

Figure 5.8: (a) Received signal distribution for different receiver aperture diameters of $D = \{40, 30, 20, 15, 10, 6, 3\}$ mm and beam width setting of $w_0 = 4.5174$ mm, with turbulence at $\sigma_R^2 = 1.3356$ ($C_n^2 = 1.1734 \times 10^{-10}$ m$^{-2/3}$); and (b) comparisons of the normalized log irradiance PDF between the experimental data and the theoretical models.

the signal amplitude profiles are in accordance to the rapid increase of $\sigma_I^2(D)$ from 0.0346 (for $D = 15$ mm) to 0.3616 (for $D = 3$ mm). In comparison to the observations for $w_0 = 2.7731$ mm in Figure 5.5 and Figure 5.6 depicting more aggravated $\sigma_I^2(D)$ values and greater dispersion in the PDFs with reduced aperture size, it is demonstrated that larger spot size of the optical laser beam is capable of mitigating the signal fluctuations and jitter-induced PEs resulting from the scintillation and beam wander effects, particularly when smaller geometries of the receiver aperture are considered in the system. The corresponding experimental results encompassing the signal density distributions and comparisons of the normalized log intensity PDFs with GOF test statistics are presented in Appendix A.2, for other turbulence cases of $\sigma_R^2 = \{0.8323, 1.7114, 2.2139, 2.5616\}$.

In the cases of $D \geq 15$ mm at $\sigma_R^2 = 0.9359$, the distinctive features observed in the histograms of the received optical signals are reflected upon the extremely narrow opening of the normalized log intensity PDFs in Figure 5.7(b). These observations present very good agreement with the theoretical lognormal model applicable to the weak turbulence conditions, as validated from the GOF test statistics provided in Table 5.4. It should be noted that the relatively larger values of the *RMSE* for $D \geq 15$ mm (similarly observed in Table 5.5 for $\sigma_R^2 = 1.3356$) can be explained by the concentration of majority of the experimental data near the peak of the PDFs with density values approaching 1.0. Nevertheless, the correlation coefficient of these cases with $R > 0.97$ and negligibly small values of *MBE* and $t_s = \{0.0650, 0.0844, 0.0880, 0.0000\}$ within the acceptance region (at 95% confidence level) of the hypothetical t-test confirms the close relationship between the experimental data and theoretical model. Similar to previous observations made in Figure 5.5(b) and Figure 5.6(b), the PDFs presents an inherent shift towards the left of the

Table 5.4: The corresponding statistical test results depicting the GOF between the experimental data and the lognormal and gamma-gamma models, for a variety of receiver aperture diameter $D = \{40, 30, 20, 15, 10, 6, 3\}$ mm and beam width $w_0 = 4.5174$ mm, at $\sigma_R^2 = 0.9359$.

***D* (mm)**	**Model**	***MBE***	***RMSE***	**Student t-Test (95% Confidence Level)**			***R***
				DF	t_c	t_s	
40	LN	-6.6740E-03	0.4356	36	2.0281	0.0650	0.9840
30	LN	-1.2329E-02	0.6026	34	2.0322	0.0844	0.9721
20	LN	-4.7295E-03	0.2344	38	2.0244	0.0880	0.9968
15	LN	-1.5752E-06	0.3843	26	2.0555	0.0000	0.9821
10	LN	-5.7783E-05	0.2926	32	2.0369	0.0008	0.9598
	GG	-2.6515E-05	0.2917	32	2.0369	0.0004	0.9613
6	LN	-2.1154E-03	0.1292	93	1.9858	0.1146	0.9490
	GG	-1.7730E-03	0.1411	92	1.9861	0.0880	0.9396
3	LN	-3.0065E-03	0.1204	106	1.9826	0.1869	0.9347
	GG	-2.7745E-03	0.1404	102	1.9835	0.1479	0.9111

distributions with increasing values of $\sigma_I^2(D)$; and the broadening of the signal amplitude profiles are evident from a wider opening of the PDFs for the cases of $D \leq 10$ mm, in which the experimental data reveal the elevation at the negative tails of the PDFs. For the limiting cases of $D \leq 10$ mm, the corresponding GOF test statistics in Table 5.4 suggest a strong correlation between the experimental data and theoretical models with R values varying between 0.9111 and 0.9613; and a better fit of the theoretical gamma-gamma model with respect to the observations, as indicated by the relatively smaller values of the *MBE*, *RMSE* and/or t_s.

On the other hand, Figure 5.8(b) presents similar but more aggravated characteristics in the normalized log intensity PDFs under the strong turbulence scenario with $\sigma_R^2 = 1.3356$; depicting a strong correlation ($R > 0.92$) and small discrepancies ($MBE \approx 0$) between the observed and predicted data, as shown in Table 5.5. Under the diminishing

Table 5.5: The corresponding statistical test results depicting the GOF between the experimental data and the lognormal and gamma-gamma models, for a variety of receiver aperture diameter $D = \{40, 30, 20, 15, 10, 6, 3\}$ mm and beam width $w_0 = 4.5174$ mm, at $\sigma_R^2 = 1.3356$.

D (mm)	Model	MBE	$RMSE$	Student t-Test (95% Confidence Level)			R
				DF	t_c	t_s	
40	LN	-7.2454E-03	0.3726	39	2.0227	0.0870	0.9924
30	LN	-3.0289E-03	0.3787	44	2.0154	0.0375	0.9893
20	LN	-3.0171E-04	0.1204	46	2.0129	0.0120	0.9983
15	LN	-1.7741E-04	0.3778	45	2.0141	0.0023	0.9417
	GG	-1.0289E-04	0.3924	45	2.0141	0.0013	0.9354
10	LN	-7.2028E-04	0.0983	141	1.9769	0.0626	0.9429
	GG	-4.8014E-04	0.1165	135	1.9777	0.0352	0.9239
6	LN	-3.3257E-03	0.0659	121	1.9798	0.3945	0.9528
	GG	-3.2513E-03	0.0867	117	1.9804	0.2933	0.9240
3	LN	-1.8229E-03	0.0631	123	1.9794	0.2277	0.9556
	GG	-1.6086E-03	0.0876	117	1.9804	0.1446	0.9218

effect of aperture-averaging, the differing behaviour of the PDFs reveal a greater shift towards the negative direction and more broadening in their respective distributions, with significant elevation in the negative tails of the PDFs for $D \leq 10$ mm. The t-statistics reveal a better fit of the theoretical gamma-gamma model at the 0.05 significance level, as can be seen from the desirable *MBE* and *RMSE* results and relatively smaller values of $t_s = \{0.0013, 0.0352, 0.2933, 0.1446\}$ for $D \leq 15$ mm; thus confirming the accuracy of the model in describing the optical fluctuations and beam jitter due to turbulence.

5.7.2. The Effects of Aperture Averaging and Beam Width

In Figure 5.9, the characteristics of the aperture-averaging factor A_g as a function of the scaled aperture size $d = \sqrt{kD^2/4L}$ is collectively examined and are compared for the considered values of $w_0 = \{2.7731, 4.5174, 5.4609\}$ mm, with respect to the theoretical plane wave model having an approximate formula defined by [11]:

$$A_g \approx \left[1 + 1.062\left(\frac{D^2 k}{4L}\right)\right]^{-7/6} . \tag{5.6}$$

In general, the predicted values of A_g from the experimental data exhibits similar trend as the theoretical plane wave model with increasing scaled aperture size, albeit fluctuating on both the lower and upper sides of the theoretical estimation, for all the considered beam width settings; thus demonstrating a fair agreement in terms of their changing patterns. The extent of these observed variations accounting for different turbulence conditions are defined by the boundaries of the error bars, with the corresponding mean values indicated by their respective markers.

Figure 5.10 depicts the relationship between the aperture averaging factor A_g and point-received scintillation index $\sigma_I^2(0)$, taking into account various parameters

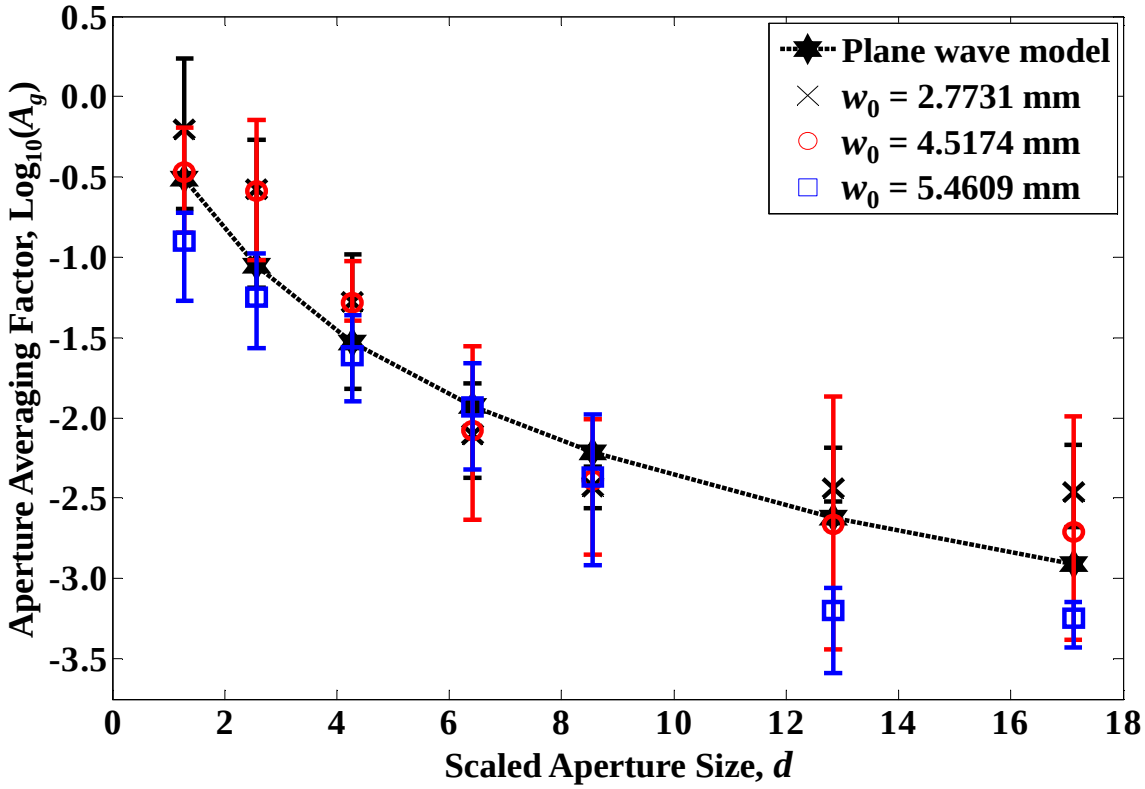

Figure 5.9: The variation of the aperture-averaging factor in terms of scaled aperture size for different beam width settings of $w_0 = \{2.7731, 4.5174, 5.4609\}$ mm, in comparison with the theoretical plane wave model.

encompassing the receiver aperture diameters of $D = \{40, 30, 20, 15, 10\}$ mm and beam width setting of $w_0 = 2.7731$ mm. The aperture-averaging factor exhibits a decreasing trend for larger values of $\sigma_I^2(0)$, in which such empirical relationship can be described by a first-order linear regression model with good accuracy, as defined by the relation:

$$\mathrm{Log}_{10}(A_g) = C_1 \mathrm{Log}_{10}(\sigma_I^2(0)) + C_0 \,. \tag{5.7}$$

The coefficients (i.e., C_0 and C_1) of the linear regression model presented in Table 5.6 are determined through the curve fitting technique, and used as appropriate measures to observe and compare the variation in the respective behaviour by adjusting the receiver aperture size and beam width. While near-identical characteristics are noted for the cases of $D = \{40, 30\}$ mm, it is evident that such linear behaviour presents an inherent upward

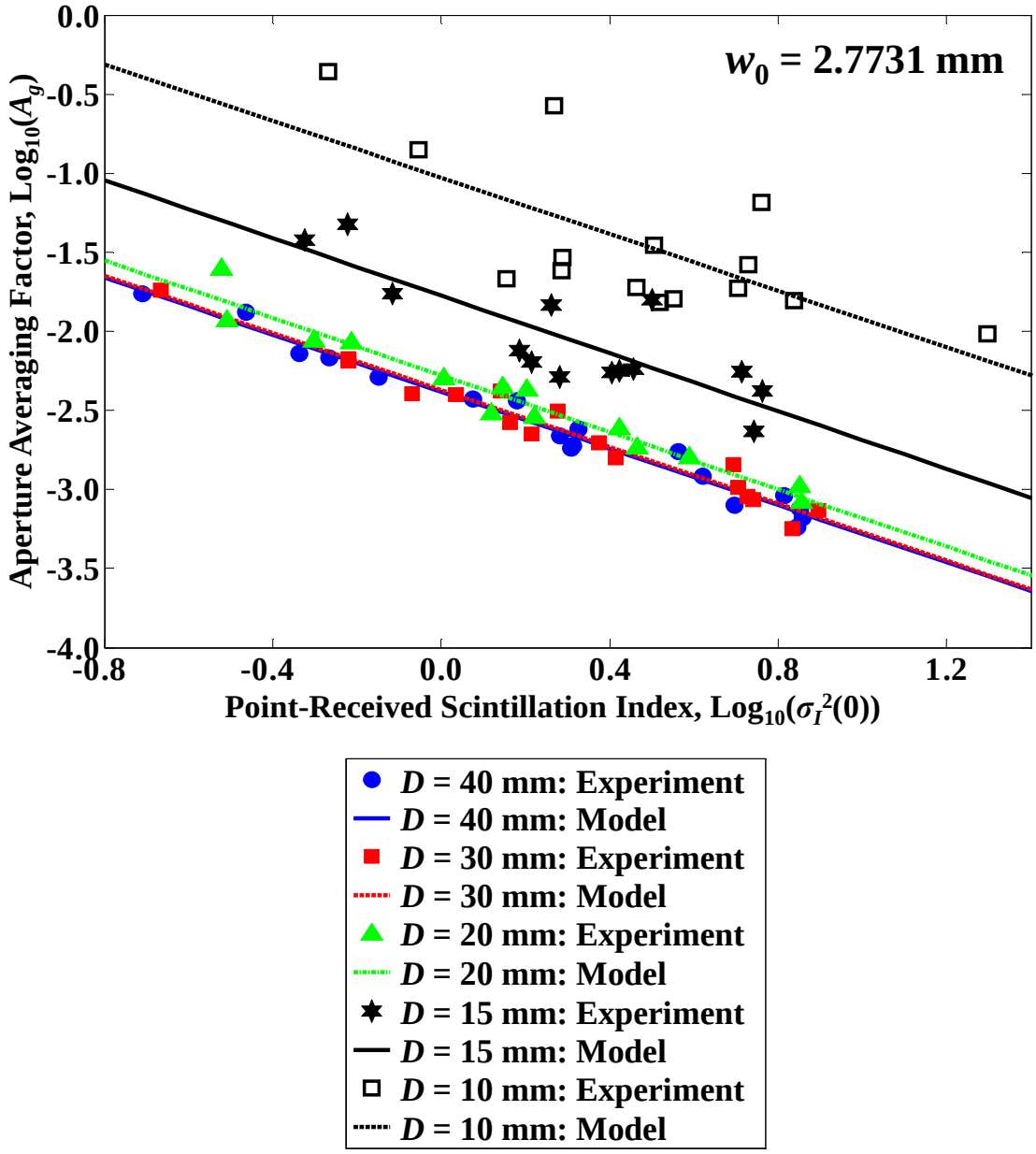

Figure 5.10: Relationship between the aperture averaging factor and point-received scintillation index, which can be described by a first-order linear regression model. The considered parameters include $D = \{40, 30, 20, 15, 10\}$ mm and $w_0 = 2.7731$ mm.

shift for smaller values of $D = \{15, 10\}$ mm, as reflected upon the increasing values of C_0 (i.e., intercept) from -2.3813 to -1.0275 and relatively constant values of $C_1 = \{\text{-}0.8991, \text{-}0.9003, \text{-}0.9043, \text{-}0.9119, \text{-}0.8943\}$ (i.e., slope) with negligibly small deviations. The resulting GOF test statistics in Table 5.6 reveal that the first-order linear regression model represents this empirical-based relationship with high accuracy for

Table 5.6: The coefficients of the first-order linear regression model for the various considered receiver aperture diameter of $D = \{40, 30, 20, 15, 10\}$ mm and beam width setting of $w_0 = 2.7731$ mm. The resulting test statistics of the *R*-square and *RMSE* are presented here, to evaluate the accuracy of the linear regression model in describing the empirical-based relationship between the aperture-averaging factor and scintillation index.

D (mm)	Regression Coefficients		R-square	$RMSE$
	C_0	C_1		
40	-2.3813	-0.8991	0.9764	0.0666
30	-2.3698	-0.9003	0.9636	0.0745
20	-2.2763	-0.9043	0.9552	0.0845
15	-1.7751	-0.9119	0.7025	0.1961
10	-1.0275	-0.8943	0.4945	0.3354

$D \geq 20$ mm; in which such good agreement is validated by *R*-square values greater than 0.95, and very small discrepancies with $RMSE = \{0.0666, 0.0745, 0.0845\}$. Nevertheless, the close relationship between the experimental data and first-order linear regression model reduces with decreasing values of $D = \{15, 10\}$ mm, as evident from the decreasing *R*-square $= \{0.7025, 0.4945\}$ (implying a moderate fit of the regression model) and increasing $RMSE = \{0.1961, 0.3354\}$ (indicating a larger variation between the experimental data and proposed model).

In the case of $w_0 = 4.5174$ mm as shown in Figure 5.11, near-identical characteristics are observed for the cases of $D = \{40, 30\}$ mm, as denoted by the relatively constant regression coefficients of $C_0 = \{-2.3949, -2.3908\}$ and $C_1 = \{-0.9184, -0.9164\}$ in Table 5.7; in which the resulting GOF test statistics reveal a very good agreement of the first-order linear regression model with *R*-square $= \{0.9513, 0.9353\}$ and $RMSE = \{0.0594, 0.0629\}$. For smaller values of $D \leq 20$ mm, the linear model is slightly elevated at a fixed increment for all considered values of $\sigma_I^2(0)$; which is noted from the slight

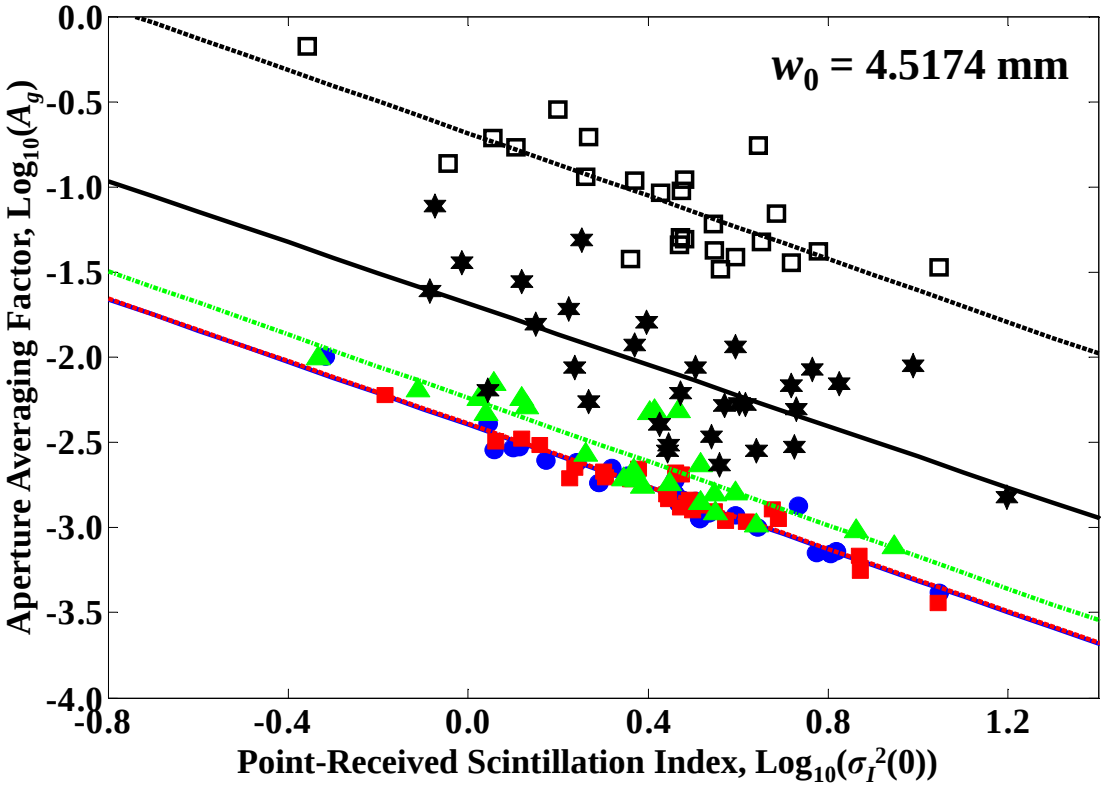

Figure 5.11: Relationship between the aperture averaging factor and point-received scintillation index, which can be described by a first-order linear regression model. The considered parameters include $D = \{40, 30, 20, 15, 10\}$ mm and $w_0 = 4.5174$ mm.

Table 5.7: The coefficients of the first-order linear regression model for the various considered receiver aperture diameter of $D = \{40, 30, 20, 15, 10\}$ mm and beam width setting of $w_0 = 4.5174$ mm. The resulting test statistics of the *R*-square and *RMSE* are presented here, to evaluate the accuracy of the linear regression model in describing the empirical-based relationship between the aperture-averaging factor and scintillation index.

D (mm)	Regression Coefficients		*R*-square	*RMSE*
	C_0	C_1		
40	-2.3949	-0.9184	0.9513	0.0594
30	-2.3908	-0.9164	0.9353	0.0629
20	-2.2397	-0.9319	0.7682	0.1480
15	-1.6851	-0.8993	0.4551	0.2942
10	-0.6832	-0.9257	0.6252	0.2044

increase of C_0 = -2.2397 and relatively constant value of C_1 = -0.9319, as compared to the previous cases of D. In particular, such linear relationship presents significant elevation for the cases of $D = \{15, 10\}$ mm; as evident from the substantial increase in the regression coefficients of $C_0 = \{\text{-}1.6851, \text{-}0.6832\}$ and $C_1 = \{\text{-}0.8993, \text{-}0.9257\}$, which is more pronounced than the observations for $w_0 = 2.7731$ mm. This implies that the diminishing effects of aperture-averaging resulting from the use of aperture lens with smaller collecting area impose greater fluctuations and jittering of the optical laser beam at the receiving-end of the FSO system, which in turn corresponds to larger aperture-averaging factor, with maximum approaching values seen at $\sigma_I^2(0) \leq 0.25$ for $D = 10$ mm. While the relatively larger values of $RMSE = \{0.1480, 0.2942, 0.2044\}$ suggest greater deviations between the experimental data and empirical model for $D \leq 20$ mm, the resulting R-square $= \{0.7682, 0.4551, 0.6252\}$ indicate a moderate fit of the linear regression model with respect to the measurements.

In Figure 5.12, similar characteristics are observed for $D = \{40, 30\}$ mm with $w_0 = 5.4609$ mm, in comparison to the previous cases of $w_0 = \{2.7731, 4.5174\}$ mm; whereby the relative constant regression coefficients are given by $C_0 = \{\text{-}2.2292, \text{-}2.1029\}$ and $C_1 = \{\text{-}1.0182, \text{-}1.0082\}$. It is further noted that these coefficients (in Table 5.8) exhibit incremental trends with decreasing values of D; in which a larger intercept (C_0) of the regression model implies an inherent elevation in the observed linear relationship, whereas a larger slope (C_1) indicates a larger A_g for smaller $\sigma_I^2(0)$, and vice versa. In general, the GOF test statistics reveal good agreement between the experimental data and linear regression model for all cases of D, with desirable R-square values ranging from 0.6776 to 0.9582 and *RMSE* varying between 0.0742 and 0.2470. Based upon the results highlighted in Figure 5.10 to Figure 5.12, several appealing observations are made here. In

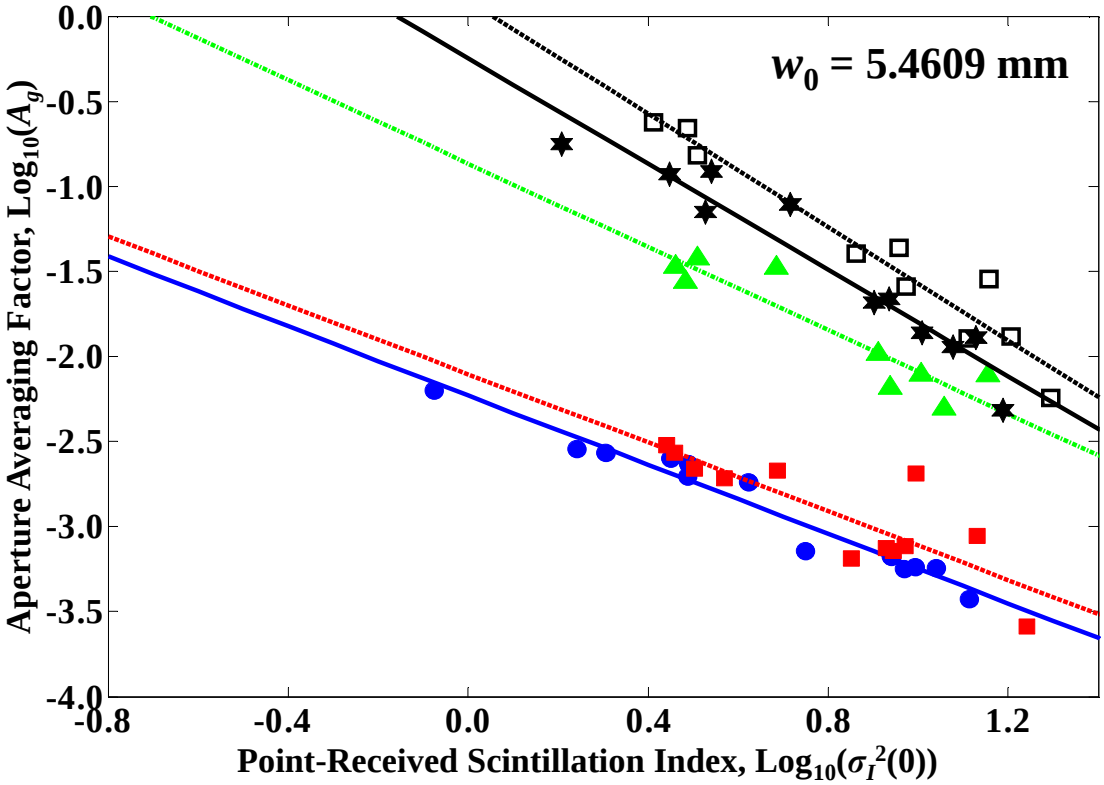

Figure 5.12: Relationship between the aperture averaging factor and point-received scintillation index, which can be described by a first-order linear regression model. The considered parameters include $D = \{40, 30, 20, 15, 10\}$ mm and $w_0 = 5.4609$ mm.

Table 5.8: The coefficients of the first-order linear regression model for the various considered receiver aperture diameter of $D = \{40, 30, 20, 15, 10\}$ mm and beam width setting of $w_0 = 5.4609$ mm. The resulting test statistics of the *R*-square and *RMSE* are presented here, to evaluate the accuracy of the linear regression model in describing the empirical-based relationship between the aperture-averaging factor and scintillation index.

D (mm)	Regression Coefficients		*R*-square	*RMSE*
	C_0	C_1		
40	-2.2292	-1.0182	0.9582	0.0742
30	-2.1029	-1.0082	0.7023	0.1704
20	-0.8659	-1.2254	0.6776	0.2470
15	-0.2447	-1.5583	0.8588	0.1931
10	0.0921	-1.6645	0.9368	0.1319

the presence of turbulences within the FSO channel, the spot size of the optical laser beam should be increased accordingly, while utilizing an enlarged receiver aperture, in order to enable the effective collection of the optical signal and the mitigation of optical fluctuations and beam jittering introduced by the scintillation and beam wander effects, respectively. The proposed experimental study demonstrates the necessity of selecting and/or adjusting appropriate transmitter beam radius and receiver aperture dimension, in order to mitigate the undesirable channel effects under changing turbulence conditions of the system under study; and hence justifies the importance of the optimization of relevant system design parameters, as have been proposed and discussed in the former Chapter 3 and Chapter 4.

5.7.3. Performance Evaluation

Figure 5.13 examines and compares the performance enhancement that can be achieved by an aperture-averaged optical receiver of different scaled aperture size d with respect to its corresponding finite point receiver, through the evaluation of the Q-factor given by [179]:

$$Q = \frac{\bar{I}_1 - \bar{I}_0}{\sigma_1 - \sigma_0} \; ; \tag{5.8}$$

where $\bar{I}_1$ and $\bar{I}_0$ denote the average received optical signals resembling the data bits '1' and '0', and σ_1 and σ_0 corresponds to the respective standard deviations. The considered parameters include different turbulence strengths indicated by the Rytov variances of $\sigma_R^2 = \{0.1738, 0.1851, 0.5165\}$ and $w_0 = 2.7731$ mm. These observations suggest that performance enhancement of manifold gain in excess of 10 order-of-magnitude can be achieved by an aperture-averaged optical receiver with increasing scaled aperture size; in which a maximum Q-factor of ~16 for $d > 6$ is obtained, under a weak turbulence

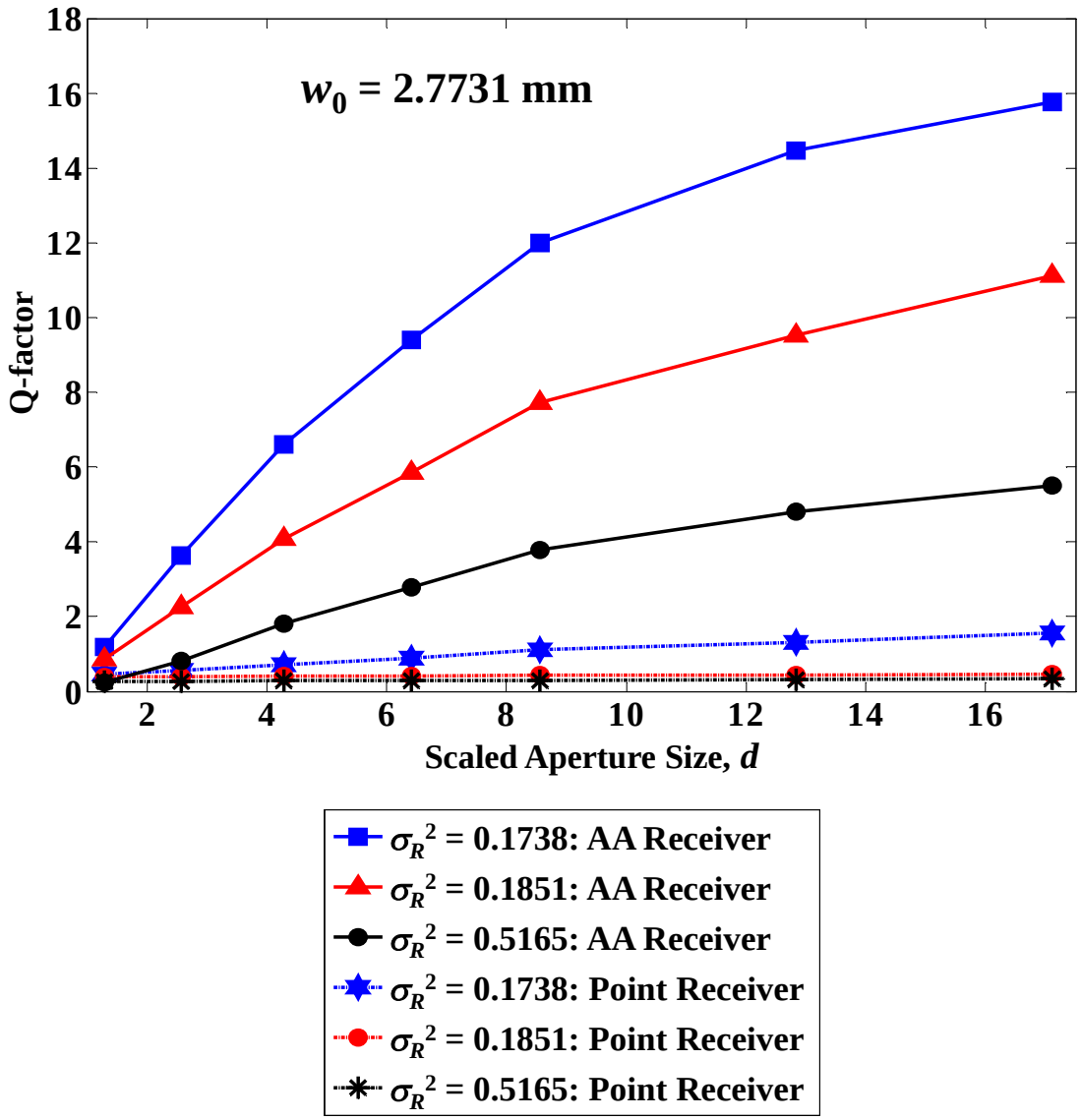

Figure 5.13: Comparison of the measured Q-factor against the scaled aperture size between an aperture-averaged optical receiver and its corresponding finite point receiver, taking into account different strength-of-turbulence with $\sigma_R^2 = \{0.1738, 0.1851, 0.5165\}$. The considered beam size is $w_0 = 2.7731$ mm.

condition with $\sigma_R^2 = 0.1738$. Moreover, a maximum Q-factor of ~12 is achievable at $\sigma_R^2 = 0.1851$, whereas a link improvement of < 6 order-of-magnitude can be attained for a stronger turbulence case of $\sigma_R^2 = 0.5165$. In conclusion, the introduction of an enlarged receiver aperture improves the effective collection of the received optical signal, and potentially mitigates the fluctuations and jittering of the optical laser beam resulting from the turbulence-induced beam wander and scintillation effects.

5.8. Summary

This chapter has presented the joint investigation and practical demonstration of the effects of aperture averaging and beam width on the FSO link under laboratory-controlled atmospheric turbulence conditions. The aperture-averaging effect has been examined and characterized through the probability density distributions of the received optical signal, and compared with respect to the theoretical lognormal and gamma-gamma turbulence models. In particular, these histograms have presented several appealing observations in the proposed experimental study, clearly depicting the distinctive characteristics of the signal density distributions for enlarged receiver apertures under weak turbulence conditions. In the presence of stronger turbulence scenarios, it has been shown that optical fluctuations occur predominantly with decreasing receiver aperture sizes. The corresponding study has demonstrated that a smaller spot size of the optical laser beam leads to stronger fluctuations and jitter-induced PEs in the received optical signal, resulting from the aggravation of the beam wander and scintillation effects; which in turn substantiated the theoretical argument that partially coherent Gaussian laser beam of larger beam width potentially mitigates the undesirable impacts of the FSO channel. In addition, the distribution of the normalized log intensity have been considered here, in order to observe and compare the characteristics of the optical intensities, particularly in capturing the behaviour in the tails of the PDFs resulting from fluctuations and jittering of the optical laser beam. It has been observed that the changing patterns of the PDFs reveal an inherent shifting of the mean towards the negative direction of the PDF with smaller receiver aperture size, and the broadening of the signal amplitude profiles is reflected accordingly in the PDFs. In the presence of more severe optical fluctuations, the negative tails of the PDFs are significantly elevated; in which such behaviour is resembled by the theoretical gamma-gamma turbulence model with better accuracy.

The characteristics of the aperture-averaging factor as a function of the scaled aperture size have been collectively examined and compared for different beam width settings; demonstrating similar trend as the theoretical plane wave model, albeit fluctuating on both the lower and upper sides of the theoretical estimation. Through extensive analysis of the experimental data, it has been shown that the aperture-averaging factor exhibits a decreasing trend for larger values of point-received scintillation index; in which this empirical-based relationship can be represented by a first-order linear regression model with good accuracy. The coefficients of the regression model have been determined through curve fitting technique, and used as appropriate measures to observe and compare the variation in the linear behaviour by adjusting the aperture size and beam width. It is evident that such linear behaviour presents an inherent upward shift with reducing aperture dimension, which is particularly pronounced for larger beam widths, thereby inferring that the use of optical laser source with increased beam spot size must be accompanied with an enlarged receiver aperture. Furthermore, a comparison of the measured Q-factor between an aperture-averaged optical receiver and its corresponding finite point receiver has shown that manifold gain in the link performance can be achieved with increasing scaled aperture size. These findings confirm that the introduction of an enlarged receiver aperture enhances the effective collection of the received optical signal and potentially mitigates the turbulence-induced beam wander and scintillation effects. In conclusion, the proposed experimental study have demonstrated the necessity of selecting and/or adjusting appropriate transmitter beam radius and receiver aperture dimension, in order to mitigate the undesirable channel effects under changing turbulence conditions. Correspondingly, the outcome of the proposed experimental study justifies the importance of the optimization of relevant system design parameters, as have been proposed and discussed in Chapters 3 and 4.

CHAPTER 6

Hybrid FSO/RF Communication Systems

6.1. Introduction

FSO communications remains as one of the least deployed broadband technologies, albeit its tremendous potential in resolving the “last mile” issues, due to its capability of achieving near-optimal capacity comparable to fibre-optic cabling with a minimal cost and time of deployment [81]. In accordance to the extensive background studies and performance analysis presented in Chapters 2 and 3, respectively, it is well-understood that the widespread deployment of the FSO technology is severely hampered by the adverse effects of beam extinction and scintillation due to unpredictable weather conditions (such as fog, haze, smog, etc.) and the atmospheric turbulence (caused by the refractive index fluctuations due to the presence of thermal gradients in the atmosphere), respectively. These natural phenomena inevitably result in a significant optical power attenuation and

link distance reduction, thus falling short of the desired carrier-grade availability of 99.999%. In particular, Kim and Korevaar [27] reported that the atmospheric attenuation of laser power is a random function of the weather, which can vary from 0.2 dB/km in exceptionally clear weather (i.e., 50 km visibility) to 350 dB/km in very dense fog (i.e., 50 m visibility); and evaluated the degrading impacts on the link range and availability for both enterprise- and carrier-class FSO systems through link budget analysis and historical weather data. Consequently, this has motivated numerous research efforts particularly in the most recent decade to design and implement a more superior hybrid FSO/RF communication system, which takes advantage of the media diversity technique by integrating a lower data-rate RF channel in conjunction with the FSO channel [82-85, 180]. With the enhanced duality feature to switch between the two technology options, this approach potentially combats the deterioration of signal quality and link outages, by sustaining minimum data communication through the complementary RF link, for the period when the primary FSO link is unavailable due to the adverse atmospheric conditions.

This chapter first presents an extensive literature survey on the relevant research works pertaining to hybrid FSO/RF communication systems in Section 6.2; which addresses the most recent advances in technology and methodologies and performance evaluation involving the switching and data transmission between the two available technology options. In Section 6.3, the system and channel models pertaining to the hybrid FSO/RF systems are described; whereas a specific case study on the application of hybrid systems for next generation Metrozones is investigated in Section 6.4. In the latter, the background studies, rationale, network architecture and main contributions of the proposed work with regards to the green Metrozones concept are clearly highlighted. In addition, a detailed explanation on the proposed H-BTS system architecture design is provided, in which the BAS control protocol and resource prioritization algorithm for enabling the

SWoD mechanism, cooperative inter-cell support and prioritized switching in the hybrid backhaul links will be discussed here. Numerical results from the feasibility studies, encompassing the BTS daily traffic profile simulation and outage analysis of the hybrid FSO/RF systems are highlighted and justified accordingly in Section 6.5. Finally, concluding remarks are presented in Section 6.6.

6.2. Review of Literature

Relevant research studies [27, 52-57] from the most recent decade revealed that media diversity scheme presents a more viable and effective mitigation technique under extreme weather conditions. The most prominent alternative utilizes a complementary RF link operating at a lower data rate, to extend the link range while maintaining desired availability when the primary FSO system suffers temporary signal degradation or complete system annihilation due to the adverse weather effects. The rationale pertaining to the development of such hybrid FSO/RF systems is based upon theoretical and experimental validations [27, 53], which reflect the symbiotic relationship between these technology options in complementing one another's weaknesses. This is mainly because fog and rain drastically affect the FSO and RF links, respectively, but only insignificantly vice versa, and rarely occur simultaneously.

From an information theoretic point-of-view, the hybrid FSO/RF system under consideration can be conceptualized as a system architecture having a pair of independent, non-ergodic channels with random states, as depicted in Figure 6.1 [181]. In this system, a source (such as audio, video, or speech) is transmitted through the parallel fluctuating channels so as to minimize the average distortion. Based on the generalized system architecture as illustrated in Figure 6.1, an encoder must map a source sequence **s** into a

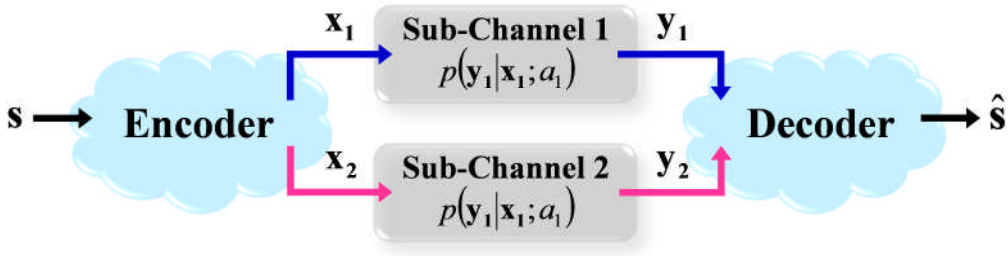

Figure 6.1: Conceptual illustration of a parallel diversity system architecture having a pair of independent, non-ergodic channels with random states [181].

(a)

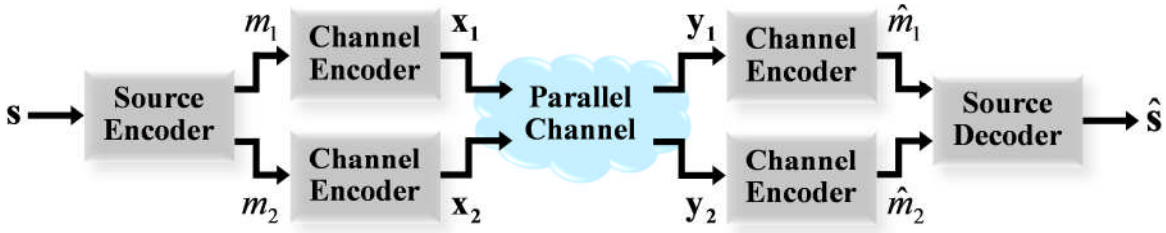

(b)

Figure 6.2: (a) Channel coding diversity; and (b) source coding diversity [181].

pair of channel inputs $\mathbf{x_1}$ and $\mathbf{x_2}$ without knowing the channel states a_1 and a_2, while a decoder is required at the receiving-end to map the channel outputs along with knowledge of the channel states into an estimate of the source $\hat{\mathbf{s}}$. In principle, the two most common approaches to code over multiple parallel channels involve exploiting diversity in the source coding and channel coding regimes (Figure 6.2), respectively, in which the latter technique is widely studied in the context of hybrid FSO/RF systems. In the channel coding diversity system (Figure 6.2(a)), $\mathbf{s}$ is encoded into $\hat{\mathbf{s}}$ by a single description (SD) source encoder, which is subsequently encoded into $(\mathbf{x_1}, \mathbf{x_2})$ by the channel encoder and

transmitted across a parallel channel. On the other hand, the source coding diversity system (Figure 6.2(b)) encodes **s** into $\hat{\mathbf{s}}_1$ and $\hat{\mathbf{s}}_2$ by a multiple description (MD) source encoder, where the corresponding $\hat{\mathbf{s}}_i$ (for i = 1, 2) is then separately encoded into $\mathbf{x}_i$ by a channel encoder and transmitted across the appropriate channel. For channel coding diversity, the capability of the receiver in producing reliable error-free recovery of **s** is dependent on the overall channel quality, thus implying that the encoded source can be reconstructed with significant reliability as long as the total channel quality is high enough (even if one of the channels is bad) to support the transmission rate. On the contrary, source coding diversity relies upon the quality of individual contributing channels to produce accurate signal estimation at the receiver, in which either scenario may result in: (1) low-fidelity source reconstruction if one description can be recovered from either channel (i.e., the remaining description is unrecoverable due to bad channel quality); or (2) high-fidelity source reconstruction if both descriptions are successfully decoded from the contributing channels with desirable channel quality.

A commercial hybrid FSO/RF system was introduced by AirFiber Inc. in a Whitepaper [53] by Bloom and Hartley. The proposed hybrid solution integrates FSO and 60 GHz millimetre wave (MMW) technologies to mutually mitigate each other's weakness, in order to provide a true carrier grade (99.999%) wireless, redundant, unlicensed system capable of ranges greater than 1 km in all weather conditions. A redundant link controller (RLC) was designed to optimize the hybrid implementation through its seamless handover capability between technology options and correction for temporary blockages, thereby sustaining zero bit error under worst-case scenario of rapid switching between propagation links due to changing weather conditions or presence of obstructions on either path. The RLC maintains data integrity on a frame-by-frame basis by observing both FSO and MMW paths using cyclic redundancy check (CRC), and subsequently forwards the

matching frame via the desired channel to the receiving-end. Since the frames are pipelined, there is absolutely no bit loss or delay incurred upon the system. Measurements data acquired from multiple FSO-only systems and the hybrid FSO/RF solution showed that the former experienced severe link interruption due to fog while the latter performed flawlessly with BER of 10^{-9} at 800 m, switching seamlessly between FSO and MMW under varying atmospheric conditions.

Subsequently, Vangala and Pishro-Nik [56] highlighted more research challenges pertaining to media diversity schemes, which include: (1) inefficient utilization of bandwidth and wastage of channel resources due to duplication of the message on both FSO and RF channels; (2) greater circuit and system complexity, increased design cost and synchronization issues due to the need for multiple encoders and decoders; and (3) the requirement for adaptation of codes to the varying channel conditions on both the links and efficient data transmission mechanism for optimal channel utilization. Hence, the authors proposed a coding paradigm based on non-uniform (multi-channel) rate-compatible punctured low-density parity-check (LDPC) codes, which employs a single encoder and decoder that can vary the code-rate based on the channel conditions, in order to optimize the capacity of the combined FSO and RF channels while maintaining carrier-grade reliabilities. The non-uniformity of the code is very effective in dealing with the bursty nature of the channels, while rate-adaptation provides efficient utilization of the time-varying channels. However, the proposed coding scheme relies upon the knowledge of the instantaneous channel conditions at the transmitter for proper adjustment of the percentage of punctured nodes, which in turn define code rates for FSO and RF transmission. Analytical and simulation results indicated that the proposed channel code can provide significant BER improvement by several orders of magnitude, and optimize the throughput due to the increase in channel availability.

Similarly, Tapse and Borah [55] have considered hybrid communication systems comprising parallel FSO and RF links for LDPC-coded data transmission, in which the former is employed as the primary channel due to its much higher data carrying capacity, while only a small fraction of the data is diverted through the latter. Characterization of the hybrid channel justified that the proposed solution can minimize the optical link's threshold and produce a significant gain in the channel capacity, thereby extending the scope of operation of the FSO-only systems over a wider range of adverse atmospheric conditions. It is evident that the channel capacity can be nearly doubled in the low optical SNR region by just using the RF link only 5% of the time. Furthermore, the authors presented a detailed convergence study based on the density evolution strategy and Gaussian approximation technique, which is then applied to derive the conditions for convergence of the message passing algorithm in terms of minimum data carrying rate through the RF link. The authors suggested that the proposed hybrid FSO/RF link can provide more flexibility in RF spectrum allocation and utilization by replacing certain RF-only links, and can be extended and applied to other hybrid channels, such as wireline/FSO links and acoustic/RF links in underwater channels.

In [54], He and Schober introduced a robust coding scheme for hybrid FSO/RF channels in the absence of CSI at the transmitter; and showed that greater robustness to the weather impairments and fading phenomena can be obtained with joint bit-interleaved coded modulation of the bit steams transmitted over the FSO and RF sub-channels. An asymptotic performance analysis has been carried out in this work, which in turn revealed that properly designed convolutional codes and assignment patterns can exploit the diversity offered by the independent sub-channels. In addition, an efficient search procedure for the corresponding convolutional codes and assignment patterns has been developed; in which an upper bound for the code rate of the proposed hybrid system has

been derived, to guarantee the existence of codes achieving full diversity. Furthermore, the optimal power assignment criteria has been provided for the cases of maximum RF and/or limiting FSO transmit power, which demonstrated that the RF link can be beneficial even if the maximum RF transmit power is limited. Taking into account typical system and channel parameters, the corresponding frame error rate and cut-off rate results confirmed the excellent performance of the proposed hybrid FSO/RF scheme for various weather conditions, outperforming previously proposed methods employing simple repetition code and selection diversity.

Then, Zhang *et al.* [57] developed a soft-switching scheme for hybrid FSO/RF links using short-length Raptor codes, unlike earlier works which considered the less efficient selection or hard-switching method and LDPC or bit-wise Raptor coding. In this approach, Raptor encoded packets are sent simultaneously through FSO and RF links, such that the encoder does not require knowledge of CSI and the code-rate between both links are adapted automatically based on the weather conditions but with very limited channel feedback. In particular, novel degree distributions for short-length Raptor codes are designed to implement FSO links at high data rates and a low decoding cost. In addition, the overhead inherent in sending the interconnection information of each packet is considered explicitly, rather than assuming that the transmitter and receiver have synchronized random generators. Furthermore, the authors demonstrated the practicality of soft-switching in hybrid FSO/RF links through the hardware implementation of a Raptor encoder and decoder using a field-programmable gate array (FPGA). The hardware implementation is capable of achieving a 714 Mbps data throughput with a 97 mW power consumption and 26360 gate circuit scale. This enables the Raptor encoder/decoder hardware to be deployed in existing hybrid systems with much convenience at an affordable extra cost. The performance of the switching algorithms in hybrid FSO/RF links

and achievable rate improvement over hard-switching systems are investigated via simulation; taking into account parameters of a 1 Gbps FSO link and a 96 Mbps Worldwide Interoperability for Microwave Access (WiMAX) RF link, and realistic channel model based on the 2007 climate data of three Canadian cities. Simulation results revealed that the short-length Raptor codes are capable of achieving average data rates in excess of 430 Mbps at a transmission distance of 2 km, as compared to the hard-switching method with an achievable data rate of 109 Mbps. Therefore, the authors concluded that the soft-switching hybrid FSO/RF links based on short-length Raptor codes are both practical and efficient in coordinating the concurrent utilization of these channels.

In [182], Letzepis *et al.* proposed a hybrid FSO/RF channel model based on parallel block fading channels [161], by incorporating the differences in signalling rates and atmospheric fading effects present in the FSO and RF links; and examined the fundamental limits of the hybrid channel from an information theoretic perspective. First, the outage probability in the large SNR regime is analyzed for the case when CSI is only available at the receiver, in order to obtain the SNR exponent or outage diversity of the hybrid system for general scintillation distributions. Since the exponent is unavailable in closed form for this case, the authors derived simple expressions from which it can be computed numerically. Then, by using the special case when transmission consists of single FSO and RF blocks, the closed form expression for the SNR exponent in terms of each component channel's SNR exponent, the ratio of component channel bits to total bits, and the overall binary code rate of the system are further obtained. It has been shown that the highest outage diversity is attainable, given that the hybrid binary code rate is set smaller than the minimum of the two component channel's maximum binary code rates. On the other hand, the SNR exponent is dominated by the worst of the two component channel's SNR exponents, if the hybrid binary code rate is set larger than the maximum of the two

component channel's maximum binary code rates. Furthermore, the authors considered the case when perfect CSI is known at both the transmitter and receiver, in which the optimal power allocation strategy that minimizes the outage probability is developed, subject to peak and average power constraints. The proposed solution reduces to a non-convex optimization problem, due to the power scaling of the FSO channel; and hence, a sub-optimal power allocation strategy is proposed, which is much simpler to implement and has the same SNR exponent as the optimal power allocation. It has been proven that the sub-optimal solution achieves significant power savings (on the order of tens of dBs), as compared to uniform power allocation; and has the same SNR exponent as optimal power allocation.

In [52], AbdulHussein *et al.* proposed the application of a rateless coded automatic repeat request scheme for hybrid FSO/RF communication systems, with distinct features as follows: (a) enables the realization of the potential advantages due to parallel FSO and RF channels without the need for redesign or reconfiguration of the transmitter-side coding or modulation, and (b) adapts seamlessly to the changes in rate supported by the channel. The authors established the pertinent modulation-constrained information-theoretic limits for the hybrid FSO/RF channel, and demonstrated via simulation that a single moderate-length Raptor code design potentially achieves realized rates approaching these limits under a wide range of channel conditions. It has been shown that the adjustment of code rate prior to transmission will lead to rate loss and codeword outage depending on the rate of channel fluctuation; and concluded that the proposed rateless coding approach with rate adaptation capabilities at the transmitter provides performance advantages over fixed-rate coding schemes [56] for hybrid FSO/RF systems in conditions of strong atmospheric turbulence.

While the relevant literatures have presented in-depth theoretical analysis on the performance of hybrid FSO/RF communication systems from the information theory perspective, there has been a lack of work emphasizing on the design, analysis and optimization of the soft-switching mechanism for the hybrid system. In addition, it is necessary to take into account critical system design considerations, such as real-time data traffic demand and fluctuating channel quality of the parallel links due to varying weather conditions. Furthermore, none of the literatures have examined the feasibility of introducing the FSO communications to complement the RF technology in the existing macro-cellular networks, as a high-speed and efficient wireless backhauling solution under the combined influences of network load and weather effects. The deployment of hybrid FSO/RF backhaul links in wireless broadband networks is poised to address two key conflicting challenges currently faced by network operators: (1) the exponential surge in mobile data traffic volumes in the recent decade, resulting in severe bandwidth capacity crunch and wireless traffic bottleneck; and (2) the non-negligible presence of power-hungry BTSs and the mushrooming of APs, directly contributing to the enormous power consumption and significant carbon emissions.

6.3. System Description

6.3.1. System Model

Figure 6.3 presents the block diagram of a point-to-point hybrid FSO/RF system, highlighting the most fundamental link built-up for the system under study without the introduction of hard- and/or soft-switching mechanisms. It can be conceptually described as a system architecture having a pair of independent, non-ergodic channels with random states [181], in which a source **s** (audio, video, or speech) is transmitted through the parallel fluctuating channels. In the absence of source encoding (i.e., $\mathbf{s} = \mathbf{m_1} = \mathbf{m_2}$), a

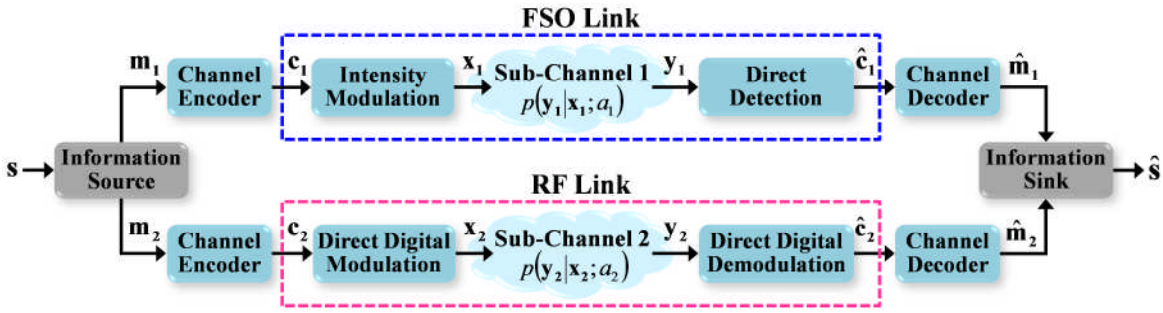

Figure 6.3: Block diagram of a point-to-point hybrid FSO/RF system.

channel encoder is required to encode the original information $\mathbf{m_1}$ (respectively, $\mathbf{m_2}$) into a codeword $\mathbf{c_1}$ (resp., $\mathbf{c_2}$) without knowing the channel state a_1 (resp., a_2). The encoded signal goes through the modulation process to produce $\mathbf{x_1}$ (resp., $\mathbf{x_2}$) and then propagates through free-space. On the other hand, a channel decoder is employed at the receiving-end along with knowledge of the channel state to produce an estimate of the source $\hat{\mathbf{m}}_\mathbf{1}$ (resp., $\hat{\mathbf{m}}_\mathbf{2}$) from the demodulated codeword $\hat{\mathbf{c}}_\mathbf{1}$ (resp., $\hat{\mathbf{c}}_\mathbf{2}$).

In principle, the channel model for the proposed hybrid FSO/RF system can be described as a combination of two individual LOS FSO and RF channels. It is assumed that both FSO and RF sub-systems are single-input single-output (SISO) systems. The FSO channel is analytically described using the combined optical slow-fading channel model as discussed in Section 2.4.4, and the relevant parameters are provided in Table 3.1. The RF channel model is presented in Section 6.3.2 as follows, in which the relevant RF link design parameters and weather-dependent indicators are shown accordingly in Table 6.1.

6.3.2. RF Channel Model

The large bandwidth availability of the unlicensed 60 GHz MMW spectrum has attracted a vast variety of wireless applications and services with the potential of high data throughputs, albeit hampered by the adverse atmospheric channel effects [183, 184] and

Table 6.1: The RF link design parameters and weather-dependent indicators.

RF System		
Parameter	**Symbol**	**Typical Value**
Carrier frequency	f_c	60 GHz
Transmitted RF power	P_{RF}	10 mW
Bandwidth	B	250 MHz
Transmit antenna gain	G_{Tx}	44 dBi
Receive antenna gain	G_{Rx}	44 dBi
Attenuation (due to oxygen)	a_{oxy}	15.1 dB/km
Noise power spectral density	N_0	-114 dBm/MHz
Receiver noise figure	N_F	5 dB

Weather-Dependent Parameters of the Hybrid FSO/RF System			
Weather Conditions	V **(km)**	a_{rain} **(dB/km)**	C_n^2 **(m$^{-2/3}$)**
Light fog	0.642	0.0	2.0×10^{-15}
Moderate rain (12.5 mm/h)	2.80	5.6	5.0×10^{-15}
Heavy rain (25 mm/h)	1.90	10.2	4.0×10^{-15}

transceiver hardware limitations [185, 186]. These include mobile broadband and cellular systems, wireless backhaul networks, fixed wireless access, wireless local area networks, ubiquitous personal communication networks, portable multimedia streaming and vehicular networks [183, 184]. The 60 GHz communications is highly susceptible to the atmospheric attenuation, in which the classical Friis free-space path loss formula suggests that this channel effect can potentially result in a 20-40 dB power penalty, as compared to unlicensed communication at operating frequencies below 6 GHz [184]. In addition, the MMW signal suffers from atmospheric absorption due to rain drops, water vapour and oxygen, which depends on the atmospheric conditions such as pressure, temperature and density; accounting for an additional 7-15.5 dB/km power loss in the received signal [183]. The MMW signal attenuation can be further aggravated by the presence of rain droplets, particularly when the atmosphere becomes saturated, in which different empirical models predict additional atmospheric attenuation between 8-18 dB/km for a given rainfall rate of 50 mm/hour [183].

A point-to-point RF link operating at an unlicensed carrier frequency of 60 GHz with direct digital modulation using the quadrature amplitude modulation (QAM) technique [185, 186], as illustrated in Figure 6.4, is considered as a complementary link to the FSO channel.

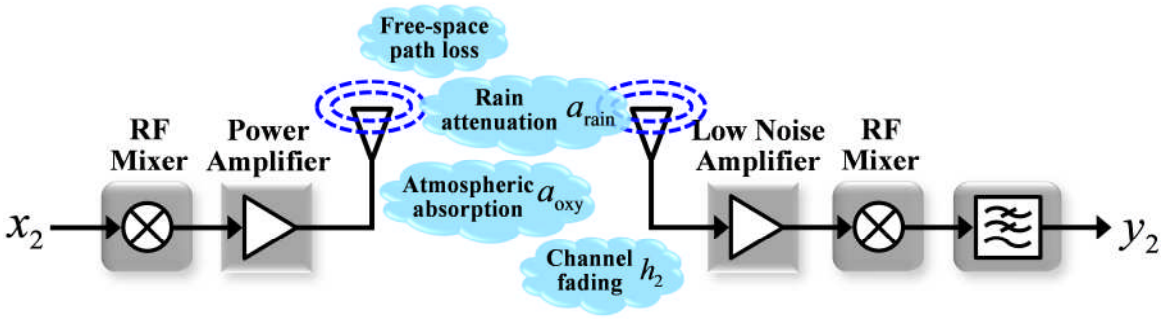

Figure 6.4: Block diagram of a point-to-point 60 GHz RF system.

The received signal of the RF channel is given by [54]:

$$y_2 = \sqrt{P_{\mathrm{RF}}}\sqrt{g_{\mathrm{RF}}}h_2 x_2 + n_{o,\mathrm{RF}}\,, \tag{6.1}$$

where P_{RF} is the RF transmit power, g_{RF} is the average power gain of the RF link, h_2 is the RF fading gain, x_2 is the modulated RF signal, and $n_{o,\mathrm{RF}}$ is the complex AWGN with variance $\sigma^2_{n,\mathrm{RF}}$.

The effective gain of the RF system g_{RF} can be modelled as [187]:

$$g_{\mathrm{RF}}[\mathrm{dB}] = G_{\mathrm{Tx}} + G_{\mathrm{Rx}} - 20\log_{10}\left(\frac{4\pi L}{\lambda_2}\right) - a_{\mathrm{oxy}}L - a_{\mathrm{rain}}L\,, \tag{6.2}$$

where G_{Tx} and G_{Rx} represent the transmit and receive antenna gains (in dB), respectively, λ_2 denotes the wavelength of the RF system, and a_{oxy} and a_{rain} resemble the attenuations due to oxygen absorption and rain (both in dB/km), respectively. The RF noise variance

is given by $\sigma_{n,\mathrm{RF}}^2\,[\mathrm{dB}] = BN_0 + N_\mathrm{F}$, where B is the signal bandwidth, N_0 is the noise power spectral density (in dBm/MHz), and N_F is the receiver noise figure.

The fading gain h_2 can be modelled as Rician distributed, with the PDF given by [188]:

$$f_2(h_2) = \frac{2(K+1)h_2}{\Omega}\exp\left(-K - \frac{(K+1)h_2^2}{\Omega}\right) I_0\left(2h_2\sqrt{\frac{K(K+1)}{\Omega}}\right), \tag{6.3}$$

where Ω is the received signal power, and the Rician factor K is the ratio of the power of the LOS component to the power of the diffuse component. The Rician factor is a useful measure of the communication link quality; and is dependent on various factors, such as link distance, antenna height and the environment, and may also change with time [54, 188].

Correspondingly, the SNR of the RF link can be determined from the relation as follows [54]:

$$SNR_{\mathrm{RF}}(h_2) = \frac{P_{\mathrm{RF}} g_{\mathrm{RF}} h_2^2}{\sigma_{n,\mathrm{RF}}^2}\ . \tag{6.4}$$

6.4. Case Study: H-BTS Architecture with Joint FSO/RF Wireless Backhauling and Basic Access Signalling

6.4.1. Background and Motivation

The unequivocality of global man-made climate change has attracted substantial governmental and political intervention [189, 190] across the world to address the urgency of this phenomena. Correspondingly, the conservation efforts striving for greener

technology options [191, 192], energy-efficient solutions [193, 194], and carbon emissions savings opportunities [5, 195] have been gradually leveraged upon the research communities [196], industrial companies [192, 197] and regulatory bodies [191] toward realizing a global low carbon society. Statistics released by the Global eSustainability Initiative (GeSI) [195] reveal that worldwide carbon emissions will rise from 40 billion tonnes (Gt) carbon dioxide equivalent (CO_2e) per annum (pa) in 2002 to approximately 53 $GtCO_2e$ by 2020. In particular, the information and communications technology (ICT) sector has been identified as one of the key areas in mitigating the world's carbon footprint due to its astounding direct contribution of 2% by consuming 3% of the worldwide energy with a growth rate of 6% pa [193, 198]. In addition to the expected growth in mature developed markets, the explosive growth in the number of mobile, fixed and broadband subscribers on a global basis, which is attributable to the emerging ICT demand in developing countries [195], inevitably requires extensive mobile networks supported by greater amount of power-hungry base transceiver stations (BTSs) and mobile switching centres. As a result, this incurs enormous stress upon network operators to suppress the resulting infrastructure carbon footprint with a projected growth from 133 million tonnes (Mt) CO_2 to 299 $MtCO_2$ by 2020 at an annual incremental rate of 5%.

The evolution of wireless mobile communications has witnessed a dynamic shift in technology adoption trends among relevant industry drivers since the early 1980s, which in turn influenced the behaviour of end users with regards to the acceptance of new technologies and services, spending pattern and demand for connectivity [199-201]. A microscopic perspective of these observed trends indicate that mobile service provisioning and user requirements for connectivity, has transitioned from fundamental coverage and adequate mobility for making simple voice call, towards more sophisticated services demanding ubiquity, all-in-one voice, data and video convergent solutions, and enhanced

efficiency of transmission (implying higher capacity at lower cost). As efficient radio technologies such as software-defined radio [202, 203], smart antennas [204-206], wireless mesh networking [207, 208] and interference cancellation techniques [209, 210] approach maturity and deployed in commercial markets, the penetration of green “criteria” into existing solutions would definitely come into effect over the next two decades to justify the telecommunications industry’s accountability and responsibility to the environment and society [192, 197, 211]. This would ultimately result in the transformation into clean, energy-efficient and complete wireless communication networks, without compromising the Quality of Service (QoS) for the mobile users or imposing negative impacts upon the deployment costs for network operators, equipment manufacturers and content providers.

Greenfield deployment of wireless macro-cellular networks typically require up to tens of thousands of BTSs, in order to provide ubiquitous coverage and seamless communication while coping with the capacity demand for voice and high-speed data and video traffic. This in turn poses immense pressure on network operators to suppress the greenhouse emissions and mushrooming operational expenditure (OPEX) due to the dominant energy requirement at radio base stations [195, 198, 212, 213]. At present, an estimated 24,000 BTSs are deployed in existing third generation (3G) network throughout the UK with a total power consumption of 300 GWh/year for providing coverage to a population in excess of 80%, in which these statistics would double up to extend the network for national coverage [198]. The roll-out of the 4G cellular wireless standards in the near future is poised to set the peak capacity requirements up to 1 Gbps, in order to provide a comprehensive and secure all-internet protocol (IP) based solution to a multitude of mobile broadband facilities, such as ultra-broadband internet access, voice over IP (VoIP), online gaming services and streamed multimedia applications. The incessantly exploding mobile data traffic volumes due to burgeoning smart devices, applications and

changing user behaviour has resulted in severe bandwidth capacity crunch, in which the peak-to-average gap is forecasted to rise to 90 times its current size by 2015 with the adoption of 4G technologies [213].

This detrimental impact has attracted extensive research efforts to look into new radio access network (RAN) architectural paradigm [213, 214], which optimizes the existing macrocell site infrastructure and introduces new sub-networking layers at the micro-/picocell level. Correspondingly, the benefits of overlaying smaller cells can be attained, which include: (1) capacity enhancement by a factor of 1600 [213] compared to other methods, such as improving spectrum efficiency and increasing cell site transmit power; (2) improved service continuity and ubiquity; (3) even distribution of network load; and (4) minimal cost for network extension compared to deploying traditional macro BTSs for the same purpose, due to cheaper micro-/picocell architectures. As Metrozones deployments would typically require 3-6 microcells and/or 8-14 picocells per macrocell site for 3G/4G service provisioning [213], energy-efficient mechanisms and green approaches are vital for sustainable operation of these Metrozones, in order to address two contradictory phenomena – (1) the non-negligible presence of power-hungry and expensive ground-based BTSs, and the mushrooming of APs for uniform blanket coverage; and (2) the significant CO2 emissions contributing to the world's carbon footprint.

6.4.2. The Green Metrozones Concept

6.4.2.1. The Rationale

The diffusion of smaller cells into traditional macro-cellular networks presents a feasible, energy-efficient and cost-effective alternative, to shift the access network closer to the mobile user terminals (MUTs) as compared to other methods, such as improving the

spectrum efficiency and increasing cell site transmit power [196, 213]. Correspondingly, manifold gain in the mobile data capacity can be achieved to curtail the impact of the prevailing bandwidth capacity crunch phenomena. This will inevitably drive the deployment of at least an order-of-magnitude more micro-/picocells for providing a uniformly distributed capacity density across a mobile service area [196]. As a result, the requirement for new data-centric RAN architecture solutions with a higher degree of network flexibility and reconfigurability must be addressed.

On the other hand, the existing macro-cellular BTS infrastructures are retained and upgraded to enhance the network performance and scalability, while promoting a significant reduction in the site costs. These BTSs with integrated routing and mesh networking capabilities can be deployed at the macro tier, to enable rapid, flexible and low-cost connectivity to the core network via the packet-based multi-hop communication, as compared to wired backhaul solutions, such as leased T1/E1 copper lines and optical fiber links [215]. The evolving trends in emerging 4G wireless mobile broadband networks reveals preferences for smaller cells to boost the capacity and migration towards cost-effective packet-based wireless backhauling solutions. This has led to the inter-dependency between macro- and sub-cells, which has attracted the Metrozones concept to cope with the massive growth in the number of mobile subscribers and high-speed data services, while complementing the operators' escalating deployment and operational costs.

6.4.2.2. Network Architecture

In principle, the network topology of Metrozones is conceptually similar to a two-tier infrastructure/backbone wireless mesh network (WMN) [208, 213], which comprises two main hierarchy – the macro-cellular tier and sub-networking layer, as illustrated in Figure 6.5.

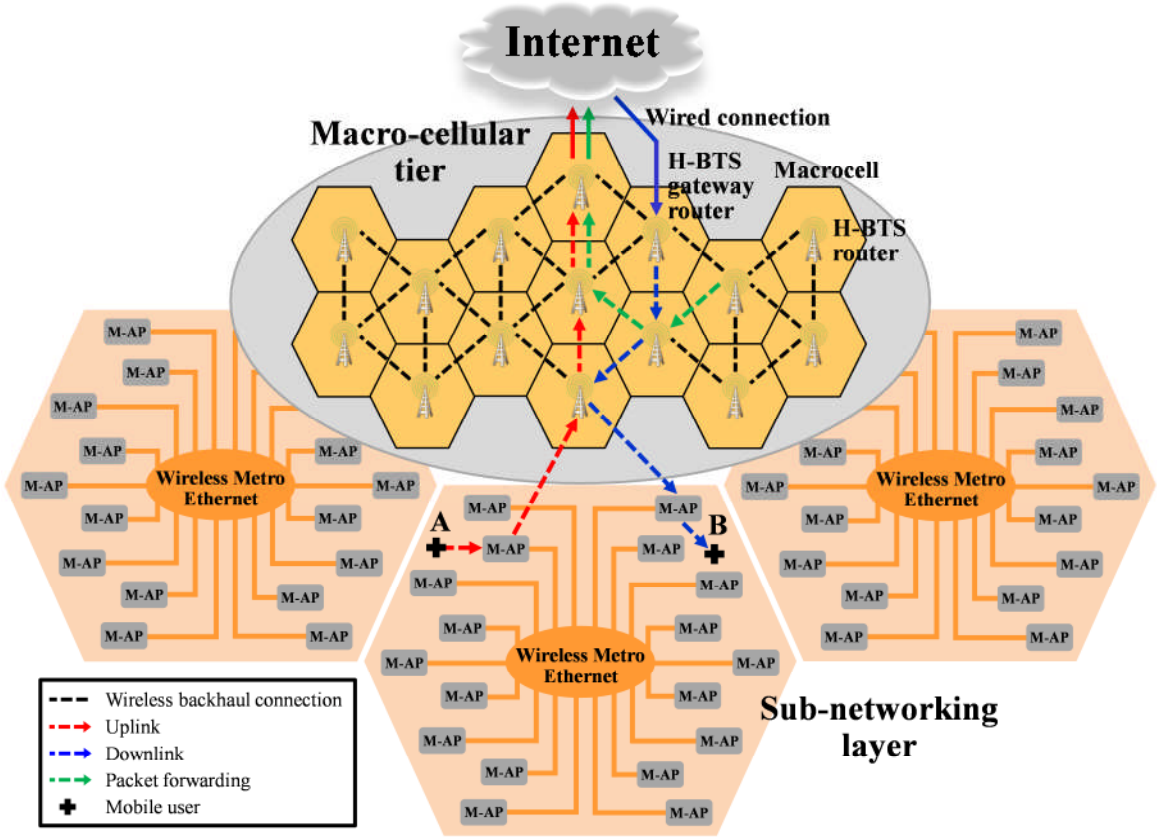

Figure 6.5: Network architecture of the green Metrozones concept.

The macro tier is populated by the BTS infrastructures with no mobility, less power constraint, sophisticated computational functions and integrated routing capabilities to perform wireless mesh backhauling. A fraction of BTSs with the gateway (GW) or the bridge functions has wired connection to the Internet, representing sources/sinks in the WMN, thereby enabling connectivity to the wired backbone facilities at a much lower cost and with flexible networking options [208, 215]. These BTSs automatically establish and maintain the connectivity among themselves, to form interconnected self-configuring, self-healing wireless backhaul links within the WMN. The data traffic is en route to and from the wired Internet entry points via multi-hop communication among mesh nodes using efficient routing protocols, thus promoting link reliability and load balancing in the macro tier.

At the sub-networking layer, M-APs providing coverage to smaller micro-/picocells within each macrocell form a cluster, which is connected to the BTS via the wireless Metro Ethernet [216], thereby forming a point-to-multipoint connection. Inter-cell coordination is managed in an autonomous manner based on the self-organizing network (SON) [217, 218] principles, whereby the M-APs form self-configuring, self-optimizing and self-healing clusters, in order to maximize the network performance and to deliver enhanced user perceived quality through numerous integrated approaches. These include optimization of the network parameters under interference and overload conditions; mitigation of quality degradation that may arise from inaccuracies of network planning or equipment faults; and rapid and efficient fault identification and compensation.

6.4.3. Main Contributions of Study

Gigabit Ethernet (GigE) backhauling solutions in next generation 4G networks will largely be based on the MMW and licensed E-Band technologies (i.e., 50/60 GHz and 80 GHz bands, respectively), for supporting bandwidth-intensive data operations in the enterprise and urban markets with shorter link requirements of 3-5 km [215, 219]. The high operating frequencies of these technologies promotes antenna directivity with a very narrow beam width (4.7° and 1.2° at 60 GHz and 80 GHz, respectively). This unveils numerous technical advantages in mesh-configured wireless backhaul networks, such as throughput enhancement, interference mitigation, superior security and a high frequency reuse rate [219]. Nonetheless, the high susceptibility of MMW radios to rain attenuation presents a greater challenge to network operators in optimizing their backhaul solutions, in order to deliver GigE speeds with a desired carrier-grade availability of 99.999%, not affected by local meteorological conditions [219, 220]. The performance of both FSO and RF links are susceptible to the adverse effects of meteorological and other natural

conditions. Therefore, hybrid FSO/RF systems [27, 53, 54, 57] present the most prominent alternative to enable these technologies in complementing one another's weaknesses, since fog and rain drastically affect the FSO and RF links, respectively, but only insignificantly vice versa, and rarely occur simultaneously.

In the present study, new H-BTS system architecture for the green Metrozones is proposed, which takes advantage of the symbiotic relationship between the FSO and RF technologies, by integrating these communication links at the macro-cellular tier. This corresponds to high data-rate transmission with lower transmit power and less susceptibility to interference, thereby delivering high-capacity, power-efficient wireless backhauling solution under most weather conditions and varying data traffic load. A radio resource management (RRM) module encompassing a resource prioritization mechanism is designed and introduced into the system hub of the proposed H-BTS architecture. This is to maintain a good control and optimal on-demand resource allocation to both the wireless backhaul and RF access networks, and to establish sustainable wireless backhaul link availability via essential switching between the FSO and RF communication links, taking into account various factors such as the fluctuating traffic demand, spectral bandwidth occupancy, network load, QoS and channel conditions. Furthermore, a BAS scheme employing a default low data-rate, low-power radio is considered, which necessitates the discovery, registration and monitoring of active M-APs, to enable two distinctive features: the SWoD mechanism and cooperative inter-cell support. The SWoD mechanism minimizes the number of operating radio access interfaces (RAIs) and enhances potential energy savings by putting idling/under-utilized RAIs and M-APs into sleep mode, particularly in low traffic scenarios. The cooperative inter-cell support offloads the M-APs located at the macrocell edge to neighbouring H-BTSs with more resource availability, thus enabling more even distribution of the network load across a particular topology.

6.4.4. Basic Access Signalling Control Protocol

Figure 6.6 illustrates the system hub of the proposed H-BTS system architecture, which comprises the RRM module and BAS scheme, to achieve potential energy savings through resource monitoring, optimal decision making and priority-based resource allocation. In principle, the BAS scheme utilizes a default low data-rate, low-power radio operating on a dedicated frequency band for exchanging control messages between the H-BTS and M-APs, thus separating the control channel from the high-bandwidth, high-power data transport channel. The proposed out-of-band control signalling scheme promotes enhancement in resource monitoring through the discovery and registration of new M-APs and monitoring of these nodes within the BTS coverage, in which a neighbour list is generated and dynamically updated in accordance to the M-AP activities. The flow diagram in Figure 6.7 provides an overview of the BAS mechanism, in which the main operations are described as follows:

1) M-AP discovery: A H-BTS ($\mathcal{H}_{(i)}$, for $i = \{1, 2, \dots\}$) with resource availability uses the default BAS radio to broadcast control signal (*CTRL_PKT*) on a periodical basis to its M-AP cluster, in which the M-APs are denoted as $\mathcal{M}_{(i,j)}$, for $j = \{1, 2, \dots\}$. Upon receiving the control signal, a new M-AP ($\mathcal{M}_{(i,\ell)}$, for $\{\ell \in j\}$) responds by sending a request (*REQ_PKT*) to $\mathcal{H}_{(i)}$ and awaits acknowledgement (*ACK_ID*) to proceed with the next phase.

2) M-AP registration: $\mathcal{M}_{(i,\ell)}$ requires *ACK_ID* to initiate the registration procedure, in which the registration information (*REG_PKT*) comprising M-AP identity (*MAP_ID*), status (*MAP_STAT*), location (*MAP_ADD*), and number MUTs attached (*MAP_USER*), is transmitted to $\mathcal{H}_{(i)}$ and relayed to the resource database for updating the neighbour list.

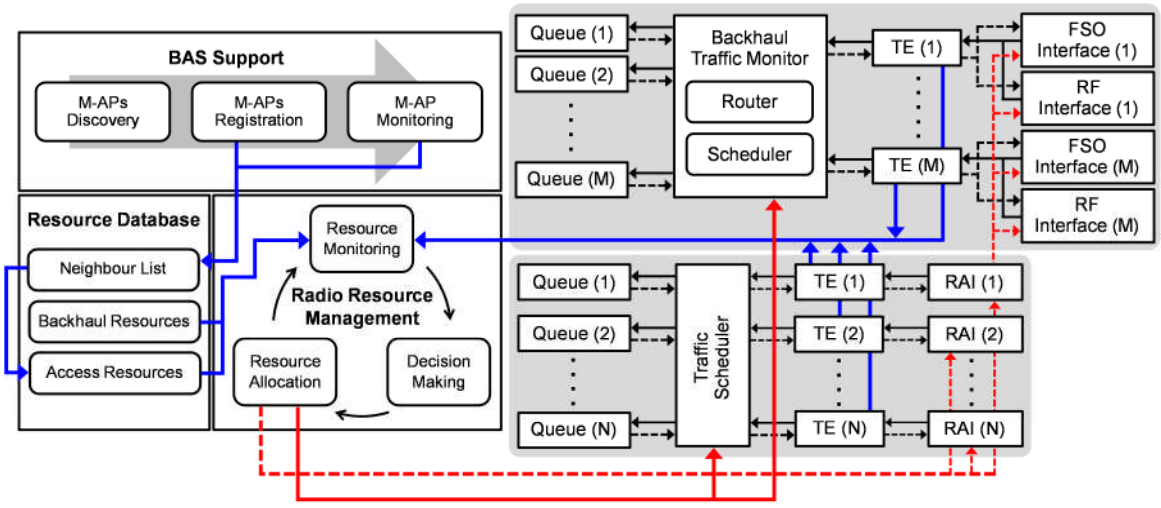

Figure 6.6: The proposed H-BTS system architecture.

Upon successful completion of M-AP registration, RRM will trigger an RAI (*RAI_TRIG_ON*) to establish a communication link with the newly reported M-AP.

3) M-AP monitoring: In this phase, the active M-APs will update their information in the resource database by sending update packet (*UPDATE_PKT*) to the H-BTS. If an M-AP remains inactive for an interval exceeding t_{idle} s, the node will send a request to the H-BTS to update its status information and disconnect idling RAIs (*RAI_TRIG_OFF*), in which the M-AP is then placed into the sleep mode. Correspondingly, under-utilized radio access interfaces at H-BTS can be switched off (during low traffic demand), and then reinstated based upon the M-AP request via the BAS scheme. This in turn promotes higher energy efficiency by optimizing the operation of RAIs at the sub-networking layer with the proposed SWoD mechanism.

6.4.5. Resource Prioritization Mechanism

The RRM module involves resource/information monitoring, decision making and priority-based resource allocation, in which these mechanisms are jointly managed and

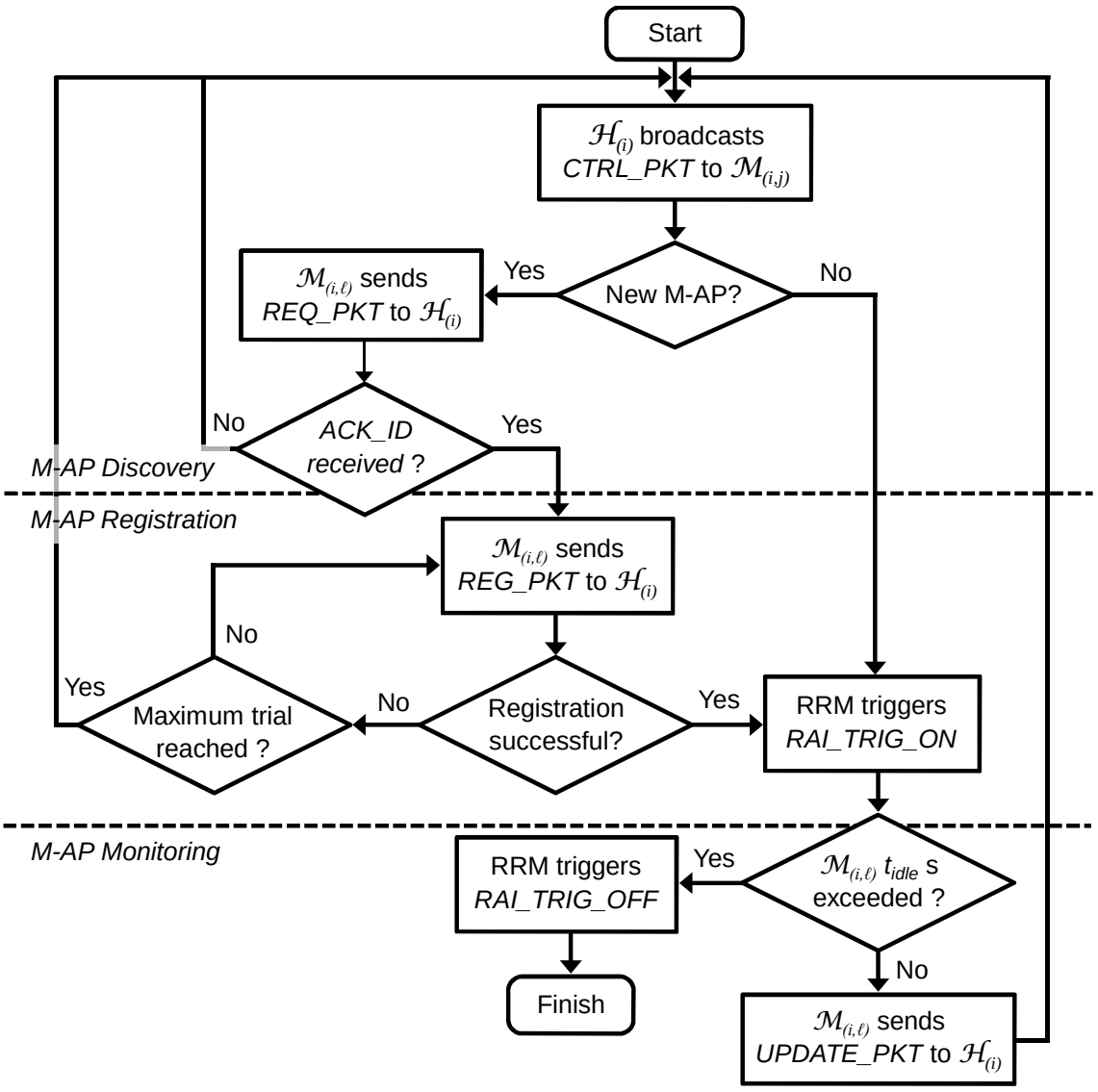

Figure 6.7: Flow diagram of the proposed BAS control protocol.

executed by the proposed resource prioritization mechanism as shown in Figure 6.8. In principle, the information/resources observed and/or managed by the RRM module can be categorized into pre-determined and time-varying factors [221]. These are monitored and gathered separately for the macro-cellular and sub-networking layers, due to the vastly varying propagation conditions and different communication purposes with contrasting application and QoS constraints.

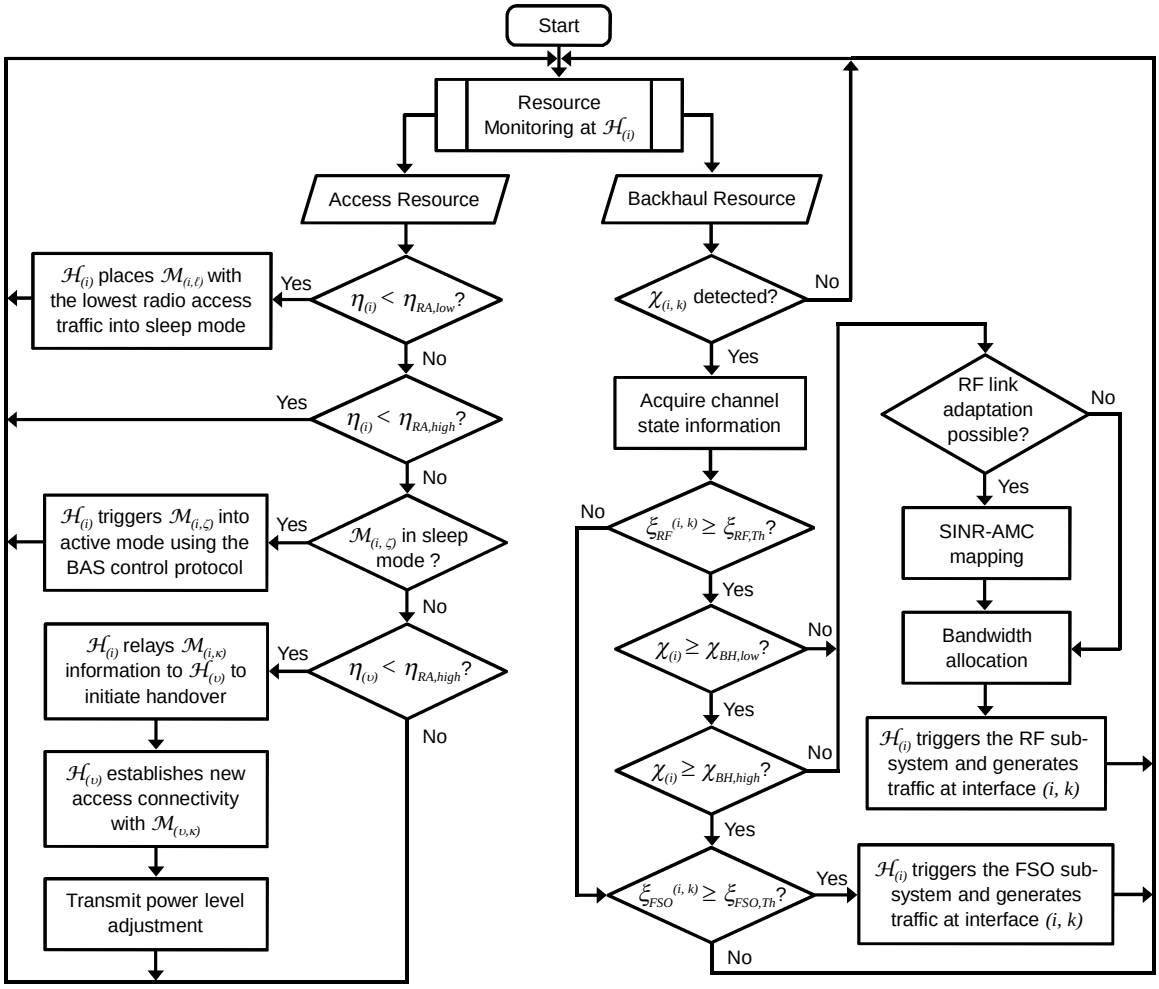

Figure 6.8: Flow diagram of the proposed resource prioritization mechanism.

Within the sub-networking layer to enable last-mile radio access, the updated neighbour list produced by the BAS scheme (Figure 6.7) and the network load (observed by the traffic estimators (TEs) at each interface, i.e., TE(1), ... TE(N)) present an important time-varying access resource, which influences the decision of the RRM to enforce the SWoD mechanism in one of the following modes:

1) Sleep mode: is enabled under two possible scenarios – (i) $\mathcal{M}_{(i,\ell)}$ inactivity for a time interval exceeding t_{idle} s; and (ii) the total access traffic demand at $\mathcal{H}_{(i)}$ approaches the lower threshold ($\eta_{(i)} < \eta_{RA,low}$). In the latter case, $\mathcal{H}_{(i)}$ sends a request to $\mathcal{M}_{(i,\ell)}$ with

the lowest radio access traffic, in order to disconnect the communication link (which requires the triggering of *RAI_TRIG_OFF*) and place the targeted $\mathcal{M}_{(i,\ell)}$ into sleep mode. The self-organizing capabilities of the M-AP clusters enable the selected M-AP to aggregate the end users residing within its coverage area to neighbouring micro-/picocells. Upon successful offloading of the radio access traffic, the M-AP responds with a procedural acknowledgement using the dedicated BAS control protocol and subsequently enters into sleep mode, thereby conserving energy during low traffic demand by minimizing $\mathcal{M}_{(i,\ell)}$ and number of operating RAIs at $\mathcal{H}_{(i)}$.

2) Active mode: is triggered under two possible circumstances – (i) successful registration of newly discovered $\mathcal{M}_{(i,\ell)}$; and (ii) total access traffic demand at $\mathcal{H}_{(i)}$ approaches the upper threshold ($\eta_{(i)} \geq \eta_{RA,high}$) with sleeping M-APs ($\mathcal{M}_{(i,\zeta)}$) within the $\mathcal{M}_{(i,j)}$ cluster. In the second condition, $\mathcal{H}_{(i)}$ triggers $\mathcal{M}_{(i,\zeta)}$ into active mode via the BAS scheme, in which the high-power high-speed RAIs (of the previously sleeping M-APs) are switched on for distributing the data traffic to the $\mathcal{M}_{(i,j)}$ cluster.

3) Handover mode: is considered when the $\mathcal{M}_{(i,j)}$ cluster is insufficient to cope with the excessive access traffic demand at $\mathcal{H}_{(i)}$, while adjacent $\mathcal{H}_{(\upsilon)}$ can utilize its resource availability to enhance load balancing within the cellular network. Thus implying the criteria to initiate M-AP handover as follows – (1) $\mathcal{M}_{(i,\zeta)} = \{\emptyset\}$; (2) $\eta_{(i)} \geq \eta_{RA,high}$; and (3) $\eta_{(\upsilon)} < \eta_{RA,high}$. This cooperative inter-cell support triggers the highly congested $\mathcal{H}_{(i)}$ to relay the information of selected M-AP(s) located at the macrocell edge (resembled by $\mathcal{M}_{(i,\kappa)}$) to $\mathcal{H}_{(\upsilon)}$, which then employs the low-power BAS radio to establish new access connectivity with $\mathcal{M}_{(\upsilon,\kappa)}$ ($\in \mathcal{M}_{(\upsilon,j)}$). Hence, the RAIs of $\mathcal{M}_{(\upsilon,\kappa)}$ are switched on, and transmit power level adjustments may be required.

At the macro layer, the CSI ($\xi_{RF}^{(i,k)}$, $\xi_{FSO}^{(i,k)}$) and total backhaul traffic demand ($\chi_{(i)}$) are vital time-varying resource metrics monitored by $\mathcal{H}_{(i)}$, which are acquired using a simple feedback path and the TEs (i.e., TE(1), ... TE(M)), respectively. Upon detection of a backhaul traffic (for uplink or packet forwarding services) at the interface (i,k), under the normal-to-low data transfer volume condition with $\chi_{(i)} < \chi_{BH,high}$, the RF sub-system at the interface (i,k) with channel quality exceeding its signal-to-interference-and-noise ratio (SINR) threshold ($\xi_{RF}^{(i,k)} \geq \xi_{RF,Th}$) is employed as the desired backhaul link, in which $\mathcal{H}_{(i)}$ triggers the high-power backhaul radio and generates data traffic at the interface. The resource prioritization algorithm checks for the possible RF link adaptation and performs SINR-to-adaptive modulation and coding (AMC) mapping for optimizing the link performance. Furthermore, the algorithm enables the complementary FSO sub-system under two scenarios: (1) $\xi_{RF}^{(i,k)} < \xi_{RF,Th}$ which may occur due to the rain attenuation; and (2) $\chi_{(i)} \geq \chi_{BH,high}$ due to the excessive backhaul load. While AMC schemes may not be a feasible approach for FSO systems employing the IM/DD method, FSO link adaptation is possible with the error control coding technique, in which the channel encoder adapts the codeword length in accordance to the measured SINR.

6.5. Feasibility Studies

The following feasibility studies are carried out to examine the time-varying characteristics of the macro-cellular BTSs daily traffic load; and to carry out outage analysis for evaluating the performance of the proposed hybrid FSO/RF system under different weather conditions.

6.5.1. Daily Traffic Profile of the BTS

The daily traffic pattern of a BTS can be approximated by a modified sinusoidal profile given by [222]:

$$\lambda_T(t) = \frac{1}{2^{\psi}}\left[1 + \sin\left(\frac{\pi}{12} + \varphi\right)\right]^{\psi} + \rho_T(t)\ , \tag{6.5}$$

where $\lambda_T(t)$ denotes the instantaneous normalized traffic (in unit of Erlangs), $\psi = \{1, 3\}$ determines the abruptness of the traffic profile, φ is a uniform random variable with interval $[0, 2\pi]$, which determines the distribution of the traffic pattern among the BTSs, and $\rho_T(t)$ is a Poisson distributed random process which models the random fluctuations of the traffic [222].

Our simulation studies indicate that the above approximation does not model the random fluctuating behavior of the data traffic in a realistic manner, compared to real measurements [223, 224]. It is suggested that the abruptness in the traffic profile can be generated as a sum of sinusoids, in which the modified expression is given by:

$$\Lambda_T(t) = \sum_{i=1}^{N} \lambda_{T,\,i}(t)\ . \tag{6.6}$$

In this work, the traffic pattern is adequately modeled as a sum of eight sinusoids (i.e., $N = 8$).

Figure 6.9 shows the daily traffic pattern approximated for four BTSs, in which it is noted that BTSs generally exhibit a lower traffic requirement in the early morning (0:00 hr to 4:00 hr) and the late evening (20:00 hr to 24:00 hr) with a normalized traffic < 0.3 Erlangs, as compared to peak hours during the day (i.e., 9:00 hr to 16:00 hr) with data traffic approaching the maximum load. These observations suggest that the proposed

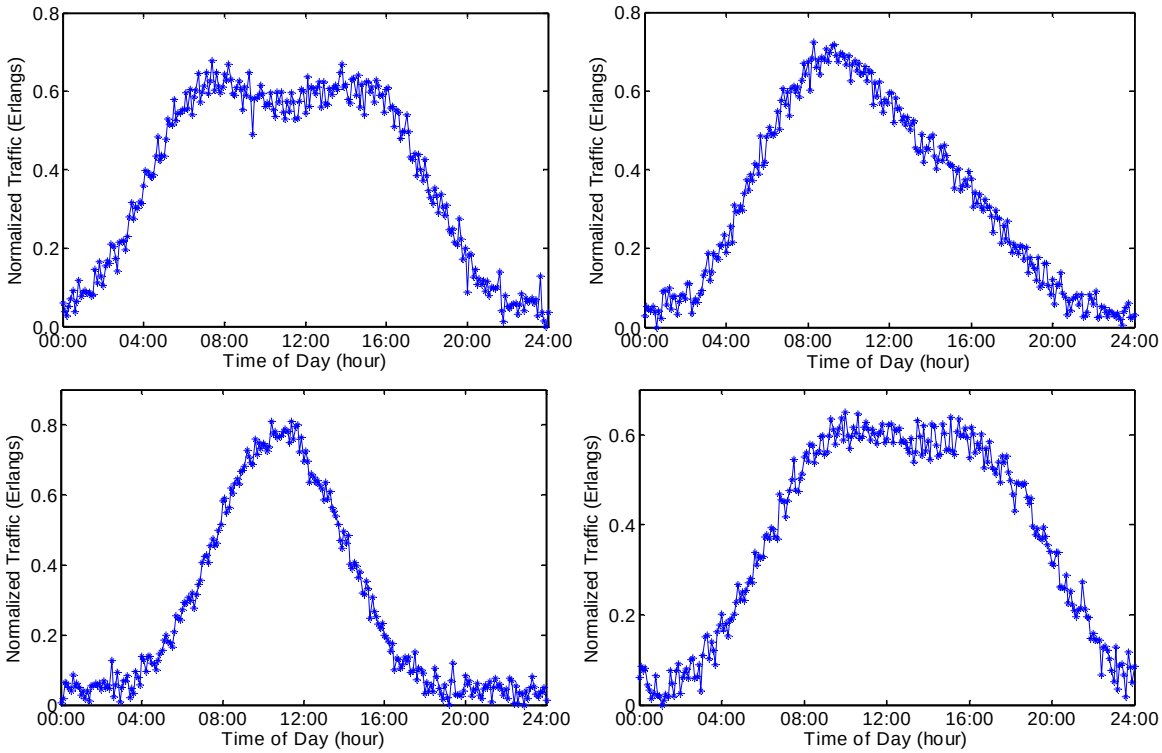

Figure 6.9: The resulting daily traffic pattern approximated for four BTSs.

SWoD mechanism and cooperative inter-cell support would be of great benefit in promoting potential energy savings during the low traffic period, by placing idling/under-utilized RAIs and M-APs into sleep mode. Under heavy traffic scenarios, the proposed features of the H-BTS architecture would enable best decision-making for on-demand resource allocation, thereby maintaining even distribution of network load across a particular topology.

6.5.2. Performance of the Hybrid FSO/RF System

The outage performance of the hybrid FSO/RF system is examined under the impairments of various weather effects. The outage probability P_{out} of the FSO channel is evaluated based on (3.5) to (3.8), as previously defined in Section 3.4.2. Similarly, the P_{out} for the RF sub-system can be determined from the expression in (3.8) with the cumulative

distribution function (CDF) of $h = h_2$ evaluated at $h_0 = \sqrt{C^{-1}(R_0)\sigma_{n,\mathrm{RF}}^2 / P_{\mathrm{RF}} g_{\mathrm{RF}}}$; whereby the fading gain h_2 is modelled as Rician distributed and defined by (6.3), and the instantaneous capacity is given by (3.5) with the conditional PDF defined as follows:

$$f(y|x, h = h_2) = \begin{cases} \dfrac{1}{\sqrt{2\pi\sigma_{n,\mathrm{RF}}^2}} \exp\left[-\dfrac{y^2}{2\sigma_{n,\mathrm{RF}}^2}\right], & x = 0 \\ \dfrac{1}{\sqrt{2\pi\sigma_{n,\mathrm{RF}}^2}} \exp\left[-\dfrac{\left(y - \sqrt{P_{\mathrm{RF}} g_{\mathrm{RF}}} h_2\right)^2}{2\sigma_{n,\mathrm{RF}}^2}\right], & x = 1\,. \end{cases} \tag{6.7}$$

Figure 6.10 depicts the P_{out} for the FSO and RF links at varying link distance L under different weather conditions, based on the simulation settings as defined in Table 6.1. The weather effects are characterized through numerous parameters including the visibility V, rain attenuation a_{rain}, and turbulence strength C_n^2 [24, 54, 57]. Our results show that the FSO system is capable of maintaining a link range in excess of 2.0 km at $P_{\text{out}} = 10^{-6}$ for $R_0 = 0.5$ bits/channel use, under moderate (12.5 mm/h) and heavy (25.0 mm/h) rain conditions, while the RF link suffers significant link reduction with $L < 0.5$ km. This reveals the vast potential of the FSO link in enabling a very high-speed wireless backhauling under the adverse effects of rain. Under the low visibility ($V = 0.642$ km) condition, the FSO link suffers severe performance degradation with $L < 1.0$ km at $P_{\text{out}} = 10^{-6}$, and experiences system outage probability of 1.0 for $L > 1.5$ km. The RF link can be employed as a complementary alternative to establish backhaul communication, albeit at a relatively lower data rate and link quality. Hence, the inherent advantage of both FSO and RF systems in complementing one another under the effects of rain and fog, respectively, reflects the symbiotic relationship between these technology options.

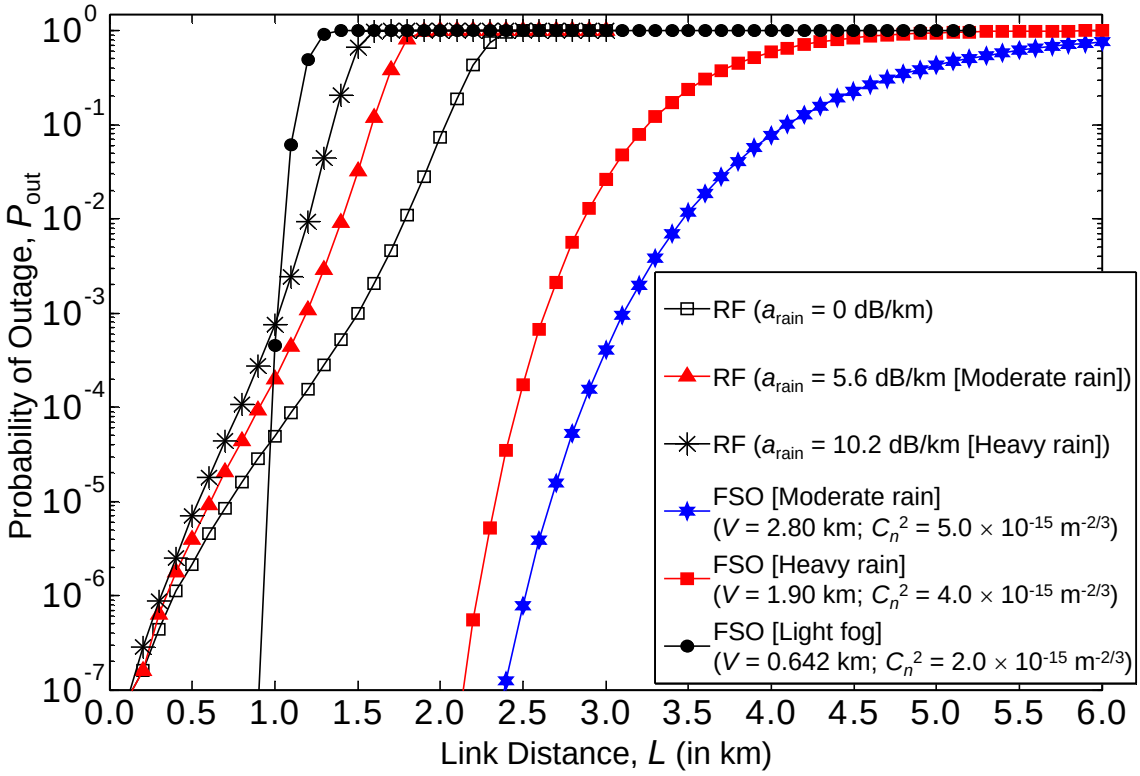

Figure 6.10: Outage probability of the FSO and RF links at varying link distance L, for $R_0 = 0.5$ bits/channel use, under different weather conditions.

6.6. Summary

In this chapter, new H-BTS system architecture has been proposed for the green Metrozones. Taking advantage of the symbiotic relationship between the FSO and RF technologies, the hybrid FSO/RF systems have been integrated at the macro-cellular tier, to enable high-capacity, power-efficient wireless backhauling under most weather conditions and varying data traffic load. In addition, the RRM module encompassing the resource prioritization mechanism has been introduced into the system hub of the proposed H-BTS architecture. This is to maintain a good control and optimal on-demand resource allocation to both the wireless backhaul and RF access networks, and to establish sustainable wireless backhaul link availability via essential switching between the FSO and RF communication links. Moreover, the BAS scheme employing a default low data-rate, low-power radio has

been considered, which necessitates the discovery, registration and monitoring of active M-APs, in order to enable two distinctive features: the SWoD mechanism and cooperative inter-cell support. The SWoD mechanism minimizes the number of operating RAIs and enhances potential energy savings by putting idling/under-utilized RAIs and M-APs into sleep mode, particularly in low traffic scenarios. The cooperative inter-cell support offloads the M-APs located at the macrocell edge to neighbouring H-BTSs with more resource availability, thus enabling more even distribution of the network load across a particular topology.

Furthermore, feasibility studies have been carried out to examine the time-varying characteristics of the BTS daily traffic profile, and to evaluate the outage performance of the proposed hybrid FSO/RF systems under different weather conditions. In particular, it has been demonstrated via simulation that the BTSs typically exhibit a lower traffic requirement (< 0.3 Erlangs) in the early morning and late evening, as compared to peak hours during the day with data traffic approaching the maximum load; thereby substantiating the significance of the proposed SWoD mechanism and cooperative inter-cell support. The corresponding outage analysis have revealed the vast potential of the FSO link in enabling a very high-speed wireless backhauling under the adverse effects of rain; whereas the RF link can be employed as a complementary alternative to establish backhaul communication, albeit at a relatively lower data rate and link quality. These observations concluded the inherent advantage of both FSO and RF sub-systems in complementing one another under the effects of rain and fog, respectively; thus reflecting the symbiotic relationship between these technology options. Finally, findings from the present work have revealed that adaptation and optimization at the link- and system-level are vital for Metrozones deployment, due to the occurrence of numerous time-varying factors in real networks, which include: (1) random fluctuations in the daily traffic profile

of the BTSs; (2) mobility of the user terminals which affects the user density (hence, the network load) across the topology; and (3) time-series characteristics of the channel state due to the influence of atmospheric conditions, such as rain, fog, haze and turbulence.

CHAPTER 7

Conclusions and Future Work

7.1. Conclusions

In this research project, extensive theoretical analysis and simulation studies have been carried out to investigate the FSO communication link impairments imposed by the combined effects of atmospheric loss, turbulence and PEs. Through the acquisition of in-depth knowledge pertaining to the characteristics and inherent limitations of the system under study, new optimization and enhancement techniques based upon the partially coherent Gaussian beam and media diversity have been proposed and presented in this thesis. In addition, experimental demonstration has been performed in laboratory-controlled atmospheric environment to substantiate the proposed theoretical and simulation studies.

The performance of partially coherent FSO communication links has been investigated from the information theory perspective in Chapter 3, taking into account the adverse effects of atmospheric loss, turbulence-induced scintillations and PEs. In particular, a spatially partially coherent Gaussian-beam wave and important link design criteria have been jointly considered, in which the latter consists of the receiver aperture dimension and its resulting aperture averaging effect, transmitter beam width, link range, knowledge of CSI, and weather conditions. By adopting the Gaussian-Schell beam and combined optical slow-fading channel models, the error performance, average channel capacity and outage probability of the FSO system have been thoroughly examined. The outage analysis has demonstrated that optimization of the outage capacity is best performed through proper selection of the beam width and receiver aperture size for a known laser wavelength and/or increasing the transmit power. From the aperture-averaging studies, it is evident that greater penalty will be imposed upon the average capacity in the presence of turbulence and PEs, particularly when the channel state is unknown at the receiver, which in turn can be compensated through the utilization of an enlarged receiver aperture. In addition, numerical results have shown that the PCB properties are substantially altered when propagating through free-space, and the optimum beam width of the optical laser source must be determined and adjusted according to varying channel conditions. Therefore, beam width optimization presents a feasible approach in promoting capacity enhancement for long-distance horizontal FSO communication links.

Joint investigation of the effects of spatially partially coherent Gaussian laser beam and aperture averaging on the performance of FSO communication systems has been presented in Chapter 4, in order to examine the resulting impact of the PCB parameters and receiver aperture diameter on the average channel capacity of the FSO link, under the combined influences of atmospheric turbulence and PEs. Numerical results have

demonstrated that the FSO channel capacity is highly susceptible to the adverse effects of scintillations and PEs, and validated the two distinctive advantages of introducing an enlarged receiver aperture (i.e., reducing the scintillation and mitigating the PE loss). In addition, the corresponding observations have confirmed the necessity and interest of optimizing the beam width to maximize the FSO channel capacity, especially in the moderate-to-strong turbulence regime. As a result, a theoretical beam width optimization model has been developed in this work, which takes advantage of a simple mathematical solution to determine the optimum beam width of the PCB for maximizing the FSO channel capacity. By solving the theoretical model through the numerical method, it is evident that a larger optimum beam width is required under more severe PE losses in the stronger turbulence regimes, in which such incremental trend changes from a more linear to a near-exponential behaviour with increasing turbulence strengths. When the effect of PEs is less prevalent, the optimum beam width is relatively smaller compared to the weaker turbulence cases. For a given jitter variance, an average capacity improvement by up to twofold is achievable through the joint adoption of an enlarged receiver aperture and the beam width optimization technique, particularly in the moderate-to-strong turbulence regime.

Subsequent investigation studies on the characteristics of partially coherent Gaussian beams propagating through the atmospheric turbulence channel have revealed the relationship between the beam width and spatial coherence length to optimize the PCB. Correspondingly, a joint beam width and coherence length optimization of partially coherent Gaussian beam has been proposed in Chapter 4, in order to maximize the average capacity in FSO systems over atmospheric turbulence channels with PEs. In particular, the effects of aperture-averaging on the average capacity of FSO links employing PCBs have been reported for the first time through this work. An optimization metric termed as the

beam spreading gain has been introduced to enable feasible translation of the joint optimal transmitter beam parameters into an analogous divergence/spreading gain of the received optical beam. Through the proposed metric, the optimum beam divergence can be determined with much simplicity, and hence the optimal capacity. It has been demonstrated that the PCBs are desirable in the weak-to-moderate turbulence regime, which in turn revealed the importance of adjusting the beam width and spatial coherence length to optimize the beam divergence by a factor of the beam spreading gain. On the other hand, highly coherent optical laser beams are preferred under strong fluctuations conditions, as can be observed from the notable reduction in the proposed optimization metric. In principle, increasing the receiver aperture mitigates the PE loss; and shifts the relative frequency content of the irradiance power spectrum towards lower frequencies due to aperture averaging, essentially averaging out the fastest fluctuations, thereby reduces the scintillation. Hence, the introduction of an enlarged receiver aperture and joint optimization technique enhances the FSO channel capacity under most turbulence conditions that are likely to occur in practice.

The effects of aperture averaging and beam width on the FSO link have been jointly investigated and practically demonstrated in an experimental work (in Chapter 5), which has been carried out under laboratory-controlled atmospheric turbulence conditions. The aperture-averaging effect has been examined and characterized through the probability density distributions and normalized log intensity PDFs of the received optical signal, and compared with respect to the theoretical lognormal and gamma-gamma turbulence models. Based upon the changing patterns of the generated histograms, it is evident that optical intensity fluctuations occur predominantly with decreasing receiver aperture sizes, and a smaller spot size of the optical laser beam leads to stronger fluctuations and PE-induced beam jitter in the received optical signal. These observations substantiate the theoretical

argument that partially coherent Gaussian laser beam of larger beam width potentially mitigates the undesirable impacts of the FSO channel. In addition, the distributions of the normalized log intensity have revealed an inherent shifting of the mean towards the negative direction and broadening of the PDF with smaller receiver aperture size. In the presence of more severe optical fluctuations as indicated by larger aperture-averaged scintillation index, the negative tails of the PDFs are significantly elevated, in which such behaviour is resembled by the theoretical gamma-gamma turbulence model with better accuracy.

Next, extensive analysis of the experimental data has been performed and shown that the aperture-averaging factor exhibits a decreasing trend for larger values of point-received scintillation index, which can be represented by a first-order linear regression model with good accuracy. The observed linear relationship presents an inherent upward shift with reducing aperture dimension, which is particularly pronounced for larger beam widths, thereby inferring that the use of optical laser source with increased beam spot size must be accompanied with an enlarged receiver aperture. Furthermore, a comparison of the measured Q-factor between an aperture-averaged optical receiver and its corresponding finite point receiver has shown that manifold gain in the link performance can be achieved with increasing scaled aperture size. These findings confirm that the introduction of an enlarged receiver aperture enhances the effective collection of the received optical signal and potentially mitigates the turbulence-induced beam wander and scintillation effects. In conclusion, this experimental study has demonstrated the necessity of selecting and/or adjusting appropriate transmitter beam radius and receiver aperture dimension, in order to mitigate the undesirable channel effects under changing turbulence conditions. Correspondingly, the outcome of this practical work justifies the importance of the

optimization of relevant system design parameters, as have been proposed and discussed in Chapters 3 and 4.

The viability of deploying the channel/media diversity technique in the FSO systems has been investigated through a case study in Chapter 6, in which the H-BTS system architecture has proposed for the green Metrozones. Taking advantage of the symbiotic relationship between the FSO and RF technologies, the hybrid FSO/RF system has been integrated at the macro-cellular tier, to enable high-capacity, power-efficient wireless backhauling under most weather conditions and varying data traffic load. In addition, the RRM module encompassing the resource prioritization mechanism has been designed and introduced into the system hub of the proposed H-BTS architecture. This is to maintain a good control and optimal on-demand resource allocation to both the wireless backhaul and RF access networks, and to establish sustainable wireless backhaul link availability via essential switching between the FSO and RF communication links. Furthermore, the BAS scheme employing a default low data-rate, low-power radio has been considered, which necessitates the discovery, registration and monitoring of active M-APs, in order to enable two distinctive features: the SWoD mechanism and cooperative inter-cell support. The SWoD mechanism minimizes the number of operating RAIs and enhances potential energy savings by putting idling/under-utilized RAIs and M-APs into sleep mode, particularly in low traffic scenarios. The cooperative inter-cell support offloads the M-APs located at the macrocell edge to neighbouring H-BTSs with more resource availability, thus enabling more even distribution of the network load across a particular topology. Findings from the present work have indicated that adaptation and optimization at the link- and system-level are vital for Metrozones deployment, due to the occurrence of numerous time-varying factors in real networks, which include: (1) random fluctuations in the daily traffic profile of the BTSs; (2) mobility of the user terminals which affects the user density (hence, the

network load) across the topology; and (3) time-series characteristics of the channel state due to the influence of atmospheric conditions, such as rain, fog, haze and turbulence.

7.2. Recommendations for Future Work

This thesis has contributed to the design, analysis and optimization of terrestrial FSO communication systems based upon a partially coherent Gaussian beam and media diversity technique, which have progressively uncovered more research opportunities and areas of improvement pertaining to the system under study.

A comprehensive design benchmark for optimal planning and design of horizontal FSO links has been presented in Chapter 3, which demonstrated the necessity of performing optimization on the system to obtain the best achievable channel capacities under different atmospheric channel effects resulting from turbulence-induced scintillations and PEs. Based upon the proposed optimization techniques in Chapter 4, new adaptive and robust optimization approaches capable of making proper adjustments to the relevant system design parameters can be incorporated to the existing system. This requires the investigation of more efficient combinatorial optimization algorithms such as the Hungarian method [225] and the careful design of multivariate training sequences, in order to maximize the FSO channel capacities under varying channel conditions without incurring excessive delay and processing overhead upon the system.

As evident from the results presented and discussed in Chapter 5, the theoretical lognormal turbulence model is only valid for the cases of weak turbulences and relatively large receiver aperture diameters; whereas the gamma-gamma model presents better tractability for stronger turbulence scenarios, albeit depicting a slight mismatch with

decreasing aperture sizes. Correspondingly, the probability density distributions of the received optical signal presented in Chapter 5 can be utilized to investigate and develop new tractable atmospheric channel model under most turbulent conditions, which takes into account the combined effects of aperture averaging and beam width. Furthermore, the linear regression analysis performed in this experimental work can be further extended to multiple regression analysis [176], in order to examine the inter-relationship of the relevant system design parameters and their statistical significance in the regression model.

While Chapter 6 has demonstrated the viability of deploying hybrid FSO/RF communication links as a high-speed and efficient backhauling solution in the wireless macro-cellular networks, more extensive simulation studies are required to observe and validate the real-time performance of the proposed H-BTS system architecture and algorithms. Through the development of reliable simulation models, numerous time-varying factors of the Metrozones and relevant design considerations can be appropriately taken into account, such that a comprehensive design benchmark for Metrozones deployment can be presented; thereby enabling adaptation and optimization at the link- and system-level to be performed in a more realistic manner. Correspondingly, further enhancement to the proposed resource prioritization mechanism and BAS scheme can be made possible. In addition, the feasibility of the proposed H-BTS system architecture for the green Metrozones can be evaluated through the monitoring of the total power consumption and potential energy savings [5], in which the development of new performance metric will be required. Furthermore, capacity and throughput analysis can be carried out to justify the performance improvement achievable from the proposed system.

In the recent decade, radio-on-FSO (RoFSO) communication systems [12] are rapidly gaining popularity as an efficient, high-capacity and cost-effective solution for

transferring RF signals, in order to facilitate the wireless broadband connectivity through seamless convergence of optical fibre and FSO communication networks. It is envisaged that the RoFSO technology can be adopted and integrated in hybrid FSO/RF systems for potential deployment in wireless macro-cellular networks and other fixed-wireless applications, in which the possible design and optimization approaches identified are outlined as follows:

(1) Investigation of viable and robust system architecture design for the hybrid links, which is adaptable to varying channel characteristics, such as channel coding diversity, source coding diversity and joint source-channel diversity techniques [181];

(2) Design of dynamic load partitioning and switching algorithms, based upon the traffic demand, channel conditions and status of the two links; and

(3) Joint AMC adaptation of the parallel channels [81], and adaptive rate optimization such as the reconfigurable rateless coding scheme [226, 227] encompassing an adjustable encoding strategy without perfect channel knowledge at the transmitter.

Appendix A

Additional Experimental Results

A.1 Received Signal Distribution and Comparisons of the Normalized Log Irradiance PDF for Experimental Data with Beam Width of 2.7731 mm

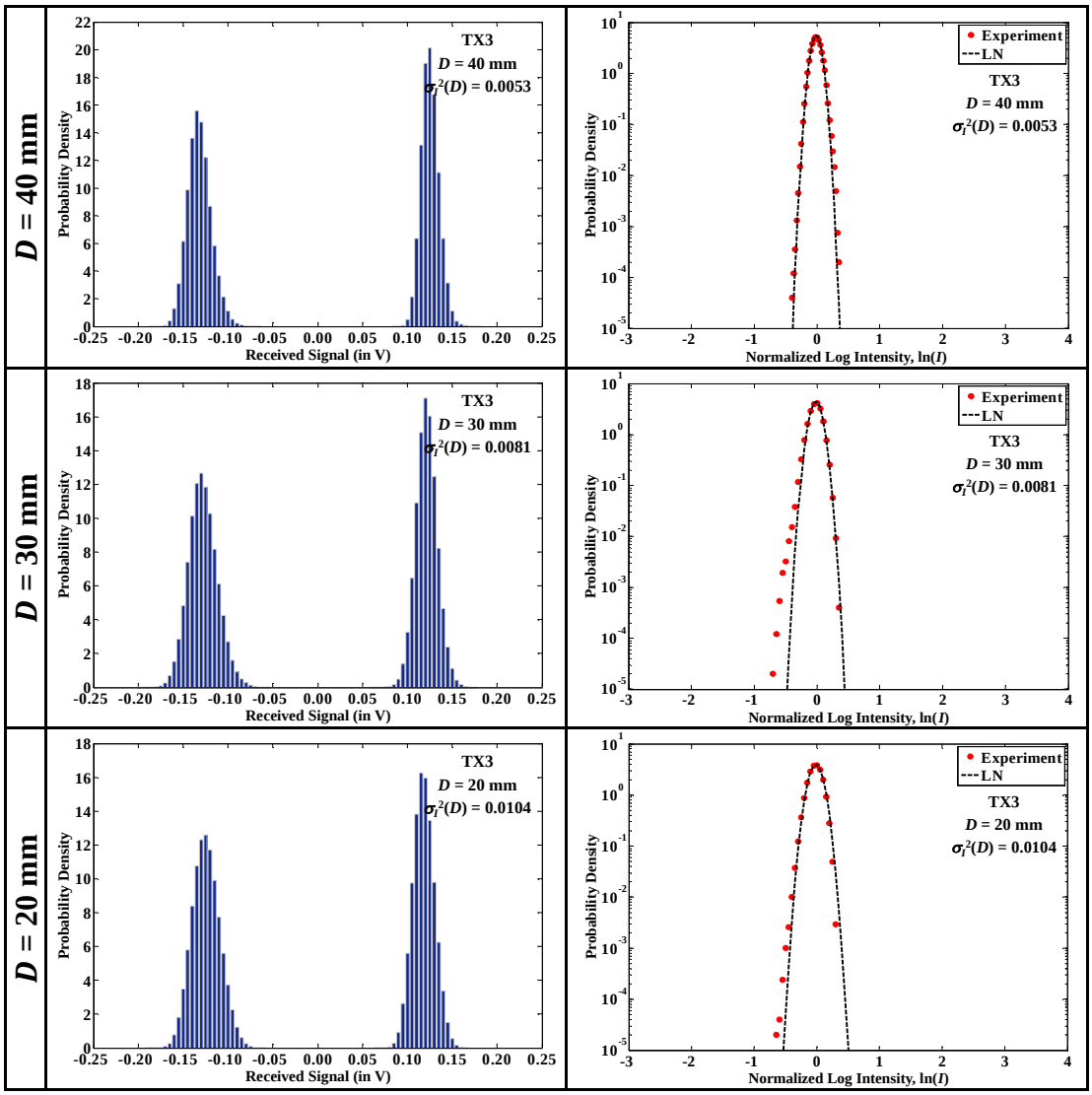

(a) (b)

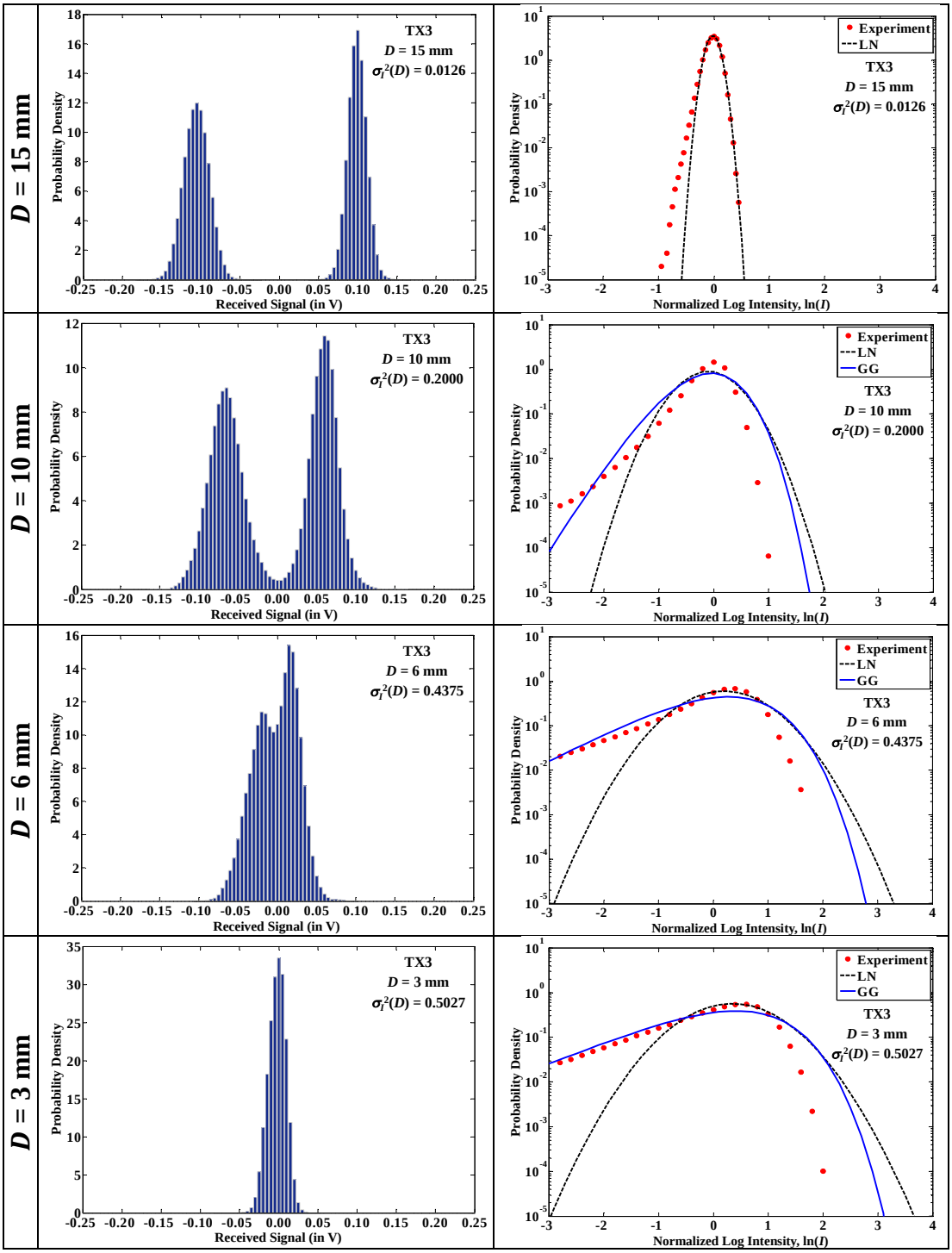

Figure A.1: (a) Received signal distribution for different receiver aperture diameters of $D = \{40, 30, 20, 15, 10, 6, 3\}$ mm and beam width setting of $w_0 = 2.7731$ mm, with turbulence at $\sigma_R^2 = 0.1851$ ($C_n^2 = 1.6266 \times 10^{-11}$ m$^{-2/3}$); and (b) comparisons of the normalized log irradiance PDF between the experimental data and the theoretical models.

Table A.1: The corresponding statistical test results depicting the GOF between the experimental data and the lognormal and gamma-gamma models, for a variety of receiver aperture diameter $D = \{40, 30, 20, 15, 10, 6, 3\}$ mm and beam width $w_0 = 2.7731$ mm, at $\sigma_R^2 = 0.1851$.

D (mm)	Model	MBE	$RMSE$	Student t-Test (95% Confidence Level)			R
				DF	t_c	t_s	
40	LN	-1.3536E-07	0.4067	60	2.0003	0.0000	0.9751
30	LN	-3.9827E-07	0.5324	42	2.0181	0.0000	0.9277
20	LN	-3.7145E-04	0.0713	38	2.0244	0.0227	0.9986
15	LN	-3.2755E-06	0.0770	54	2.0049	0.0002	0.9982
10	LN	-3.9598E-04	0.1255	79	1.9905	0.0204	0.9290
	GG	-2.1437E-04	0.1384	77	1.9913	0.0100	0.9174
6	LN	-3.7549E-04	0.0462	98	1.9845	0.0569	0.9677
	GG	-2.0168E-04	0.0663	93	1.9858	0.0213	0.9443
3	LN	-4.1589E-04	0.0429	99	1.9842	0.0685	0.9699
	GG	-2.3995E-04	0.0487	96	1.9850	0.0348	0.9618

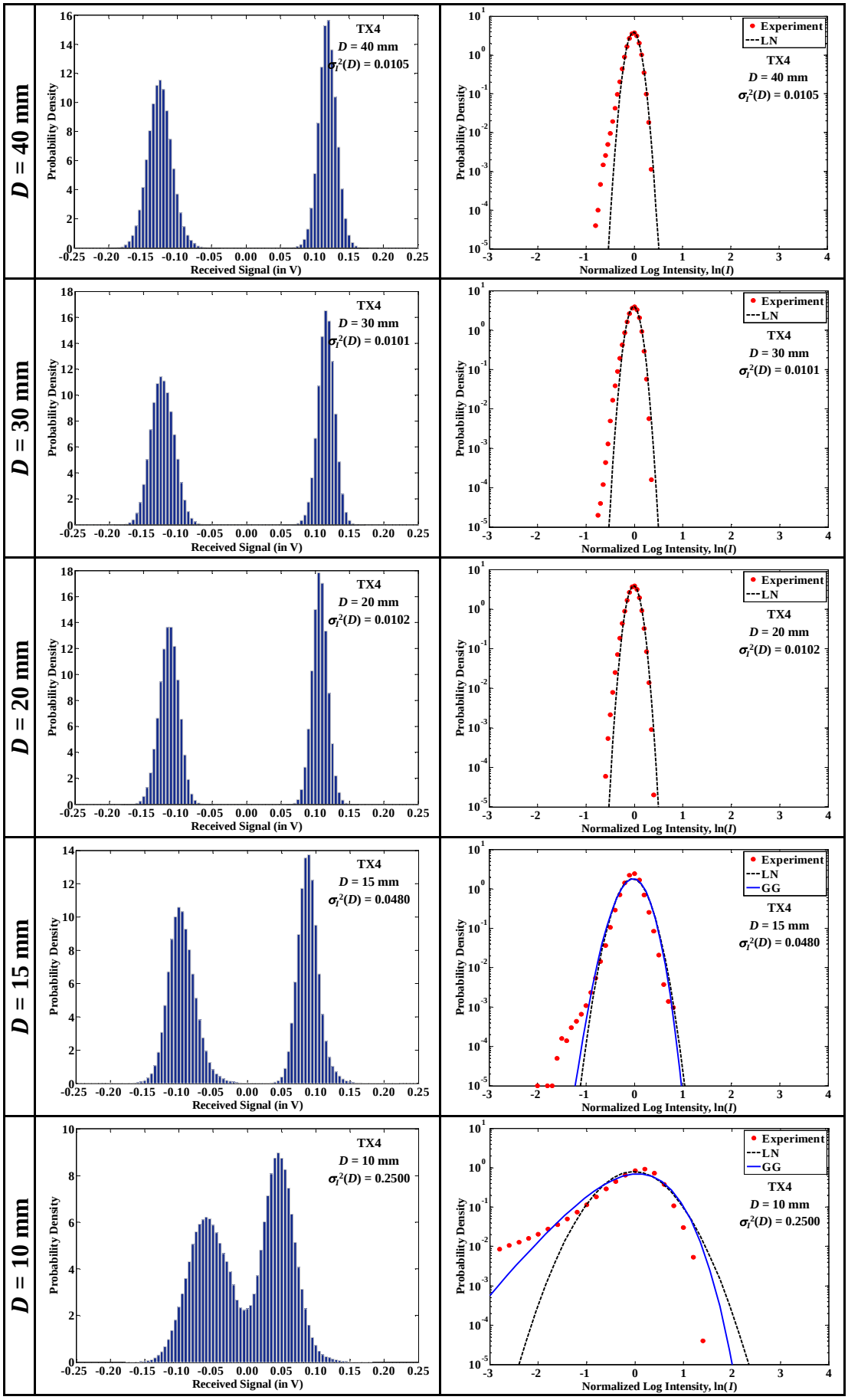
D = 40 mm
D = 30 mm
D = 20 mm
D = 15 mm
D = 10 mm
Probability Density
Received Signal (in V)
Normalized Log Intensity, ln(I)
TX4
D = 40 mm
σ_I²(D) = 0.0105
D = 30 mm
σ_I²(D) = 0.0101
D = 20 mm
σ_I²(D) = 0.0102
D = 15 mm
σ_I²(D) = 0.0480
D = 10 mm
σ_I²(D) = 0.2500
Experiment
LN
GG
(a)
(b)

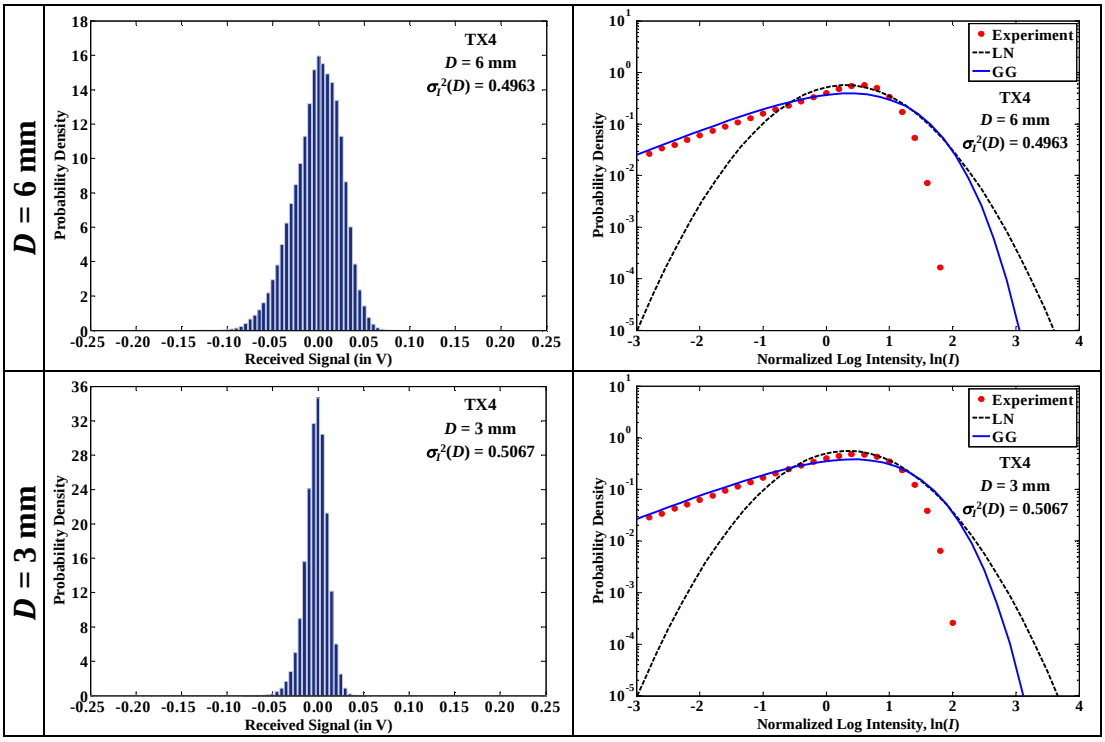

(a) (b)

Figure A.2: (a) Received signal distribution for different receiver aperture diameters of $D = \{40, 30, 20, 15, 10, 6, 3\}$ mm and beam width setting of $w_0 = 2.7731$ mm, with turbulence at $\sigma_R^2 = 0.2322$ ($C_n^2 = 2.0399 \times 10^{-11}$ m$^{-2/3}$); and (b) comparisons of the normalized log irradiance PDF between the experimental data and the theoretical models.

Table A.2: The corresponding statistical test results depicting the GOF between the experimental data and the lognormal and gamma-gamma models, for a variety of receiver aperture diameter $D = \{40, 30, 20, 15, 10, 6, 3\}$ mm and beam width $w_0 = 2.7731$ mm, at $\sigma_R^2 = 0.2322$.

***D* (mm)**	**Model**	***MBE***	***RMSE***	**Student t-Test (95% Confidence Level)**			***R***
				DF	t_c	t_s	
40	LN	-4.9050E-05	0.0657	46	2.0129	0.0036	0.9991
30	LN	-3.8219E-05	0.0756	44	2.0154	0.0024	0.9985
20	LN	-5.0765E-06	0.0727	40	2.0211	0.0003	0.9987
15	LN	-3.9020E-06	0.2016	52	2.0066	0.0001	0.9654
	GG	-9.7359E-07	0.1993	52	2.0066	0.0000	0.9676
10	LN	-3.5488E-05	0.0956	94	1.9855	0.0025	0.8242
	GG	-3.4281E-06	0.0856	92	1.9861	0.0003	0.9284
6	LN	-9.4837E-04	0.0476	97	1.9847	0.1394	0.9106
	GG	-7.2178E-04	0.0518	94	1.9855	0.0975	0.9559
3	LN	-4.1668E-04	0.0440	98	1.9845	0.0670	0.9096
	GG	-2.4100E-04	0.0333	98	1.9845	0.0512	0.9802

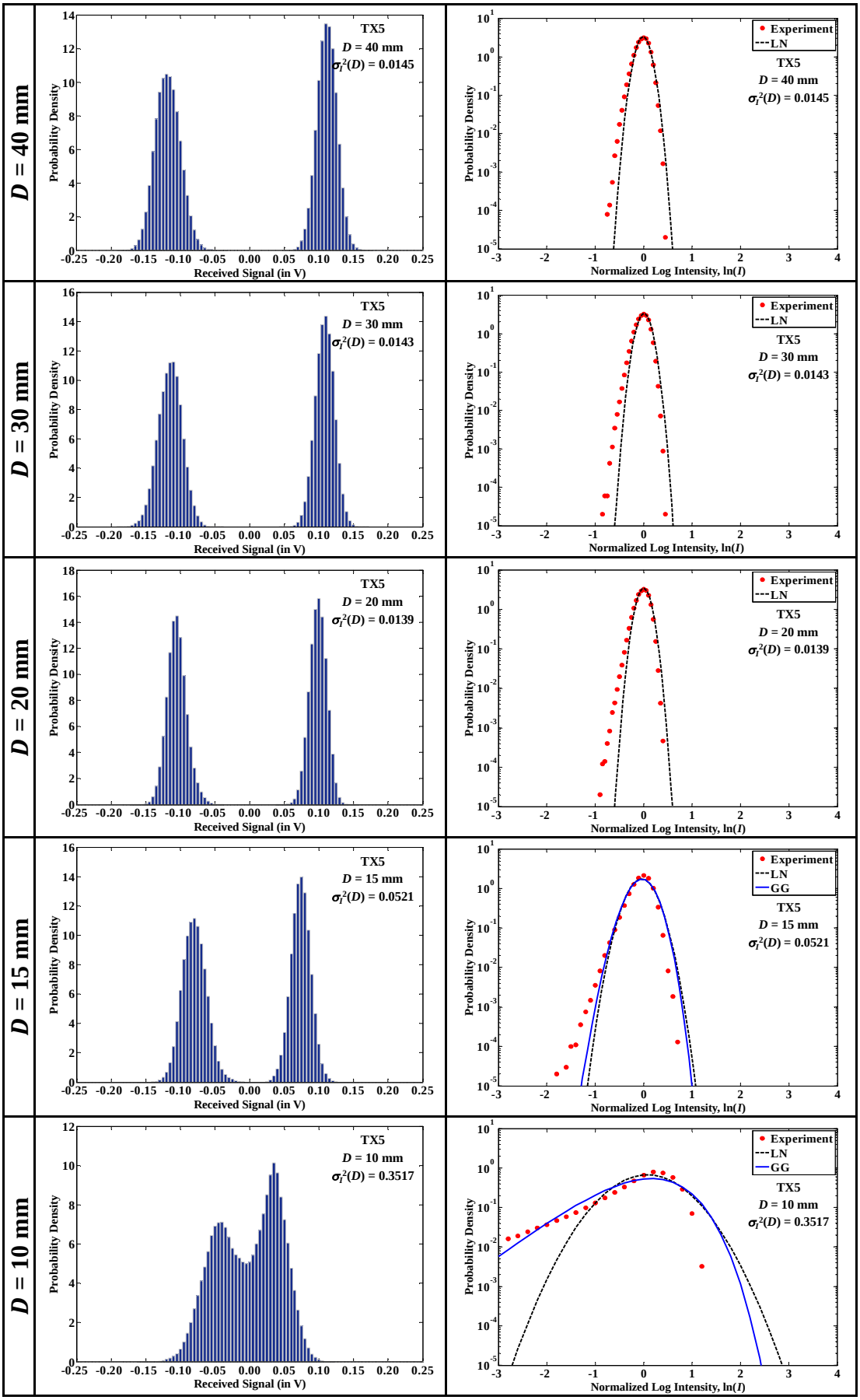
D = 40 mm
D = 30 mm
D = 20 mm
D = 15 mm
D = 10 mm
Probability Density
Received Signal (in V)
Normalized Log Intensity, ln(I)
TX5
D = 40 mm
σI2(D) = 0.0145
D = 30 mm
σI2(D) = 0.0143
D = 20 mm
σI2(D) = 0.0139
D = 15 mm
σI2(D) = 0.0521
D = 10 mm
σI2(D) = 0.3517
Experiment
LN
GG
(a)
(b)

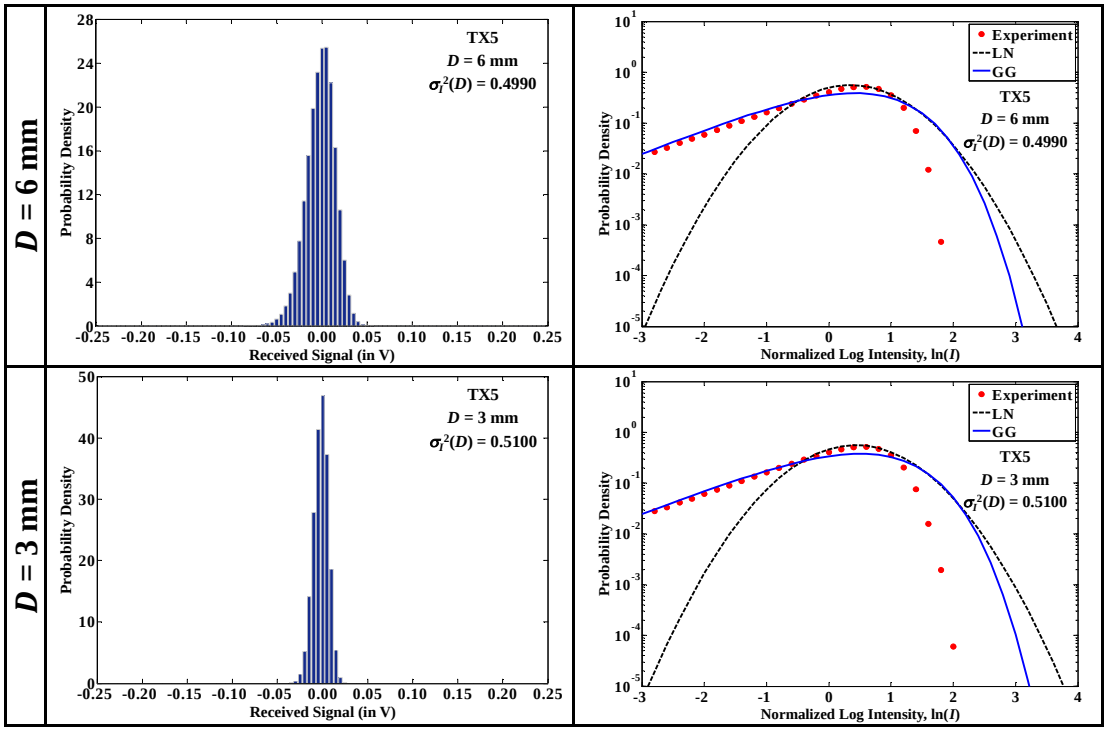

(a) (b)

Figure A.3: (a) Received signal distribution for different receiver aperture diameters of $D = \{40, 30, 20, 15, 10, 6, 3\}$ mm and beam width setting of $w_0 = 2.7731$ mm, with turbulence at $\sigma_R^2 = 0.2374$ ($C_n^2 = 2.0858 \times 10^{-11}$ m$^{-2/3}$); and (b) comparisons of the normalized log irradiance PDF between the experimental data and the theoretical models.

Table A.3: The corresponding statistical test results depicting the GOF between the experimental data and the lognormal and gamma-gamma models, for a variety of receiver aperture diameter $D = \{40, 30, 20, 15, 10, 6, 3\}$ mm and beam width $w_0 = 2.7731$ mm, at $\sigma_R^2 = 0.2374$.

***D* (mm)**	**Model**	***MBE***	***RMSE***	**Student t-Test (95% Confidence Level)**			***R***
				DF	t_c	t_s	
40	LN	-1.3033E-05	0.1242	48	2.0106	0.0005	0.9943
30	LN	-3.1304E-05	0.1014	32	2.0369	0.0012	0.9962
20	LN	-3.6554E-04	0.6469	32	2.0369	0.0023	0.8224
15	LN	-4.7309E-05	0.1823	51	2.0076	0.0013	0.9629
	GG	-1.9503E-05	0.1714	51	2.0076	0.0006	0.9690
10	LN	-1.9894E-03	0.0592	92	1.9861	0.2280	0.9583
	GG	-1.7812E-03	0.0717	89	1.9870	0.1687	0.9468
6	LN	-9.4923E-04	0.0438	97	1.9847	0.1516	0.9708
	GG	-7.2276E-04	0.0435	95	1.9853	0.1164	0.9689
3	LN	-9.3425E-04	0.0510	99	1.9842	0.1297	0.9568
	GG	-7.1072E-04	0.0484	97	1.9847	0.1039	0.9577

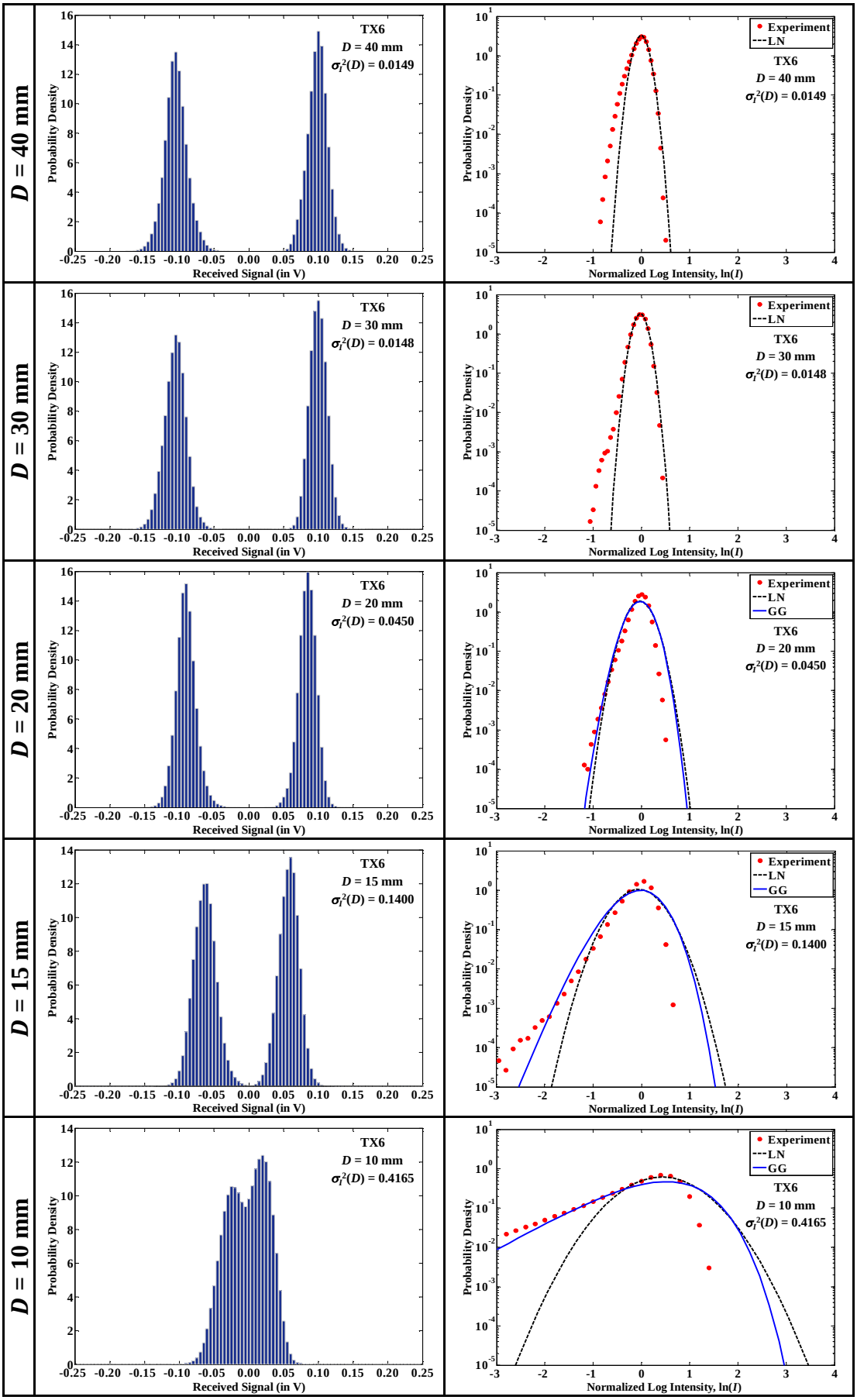
D = 40 mm
D = 30 mm
D = 20 mm
D = 15 mm
D = 10 mm
Probability Density
Received Signal (in V)
Normalized Log Intensity, ln(I)
TX6
D = 40 mm
σI2(D) = 0.0149
D = 30 mm
σI2(D) = 0.0148
D = 20 mm
σI2(D) = 0.0450
D = 15 mm
σI2(D) = 0.1400
D = 10 mm
σI2(D) = 0.4165
Experiment
LN
GG
(a)
(b)

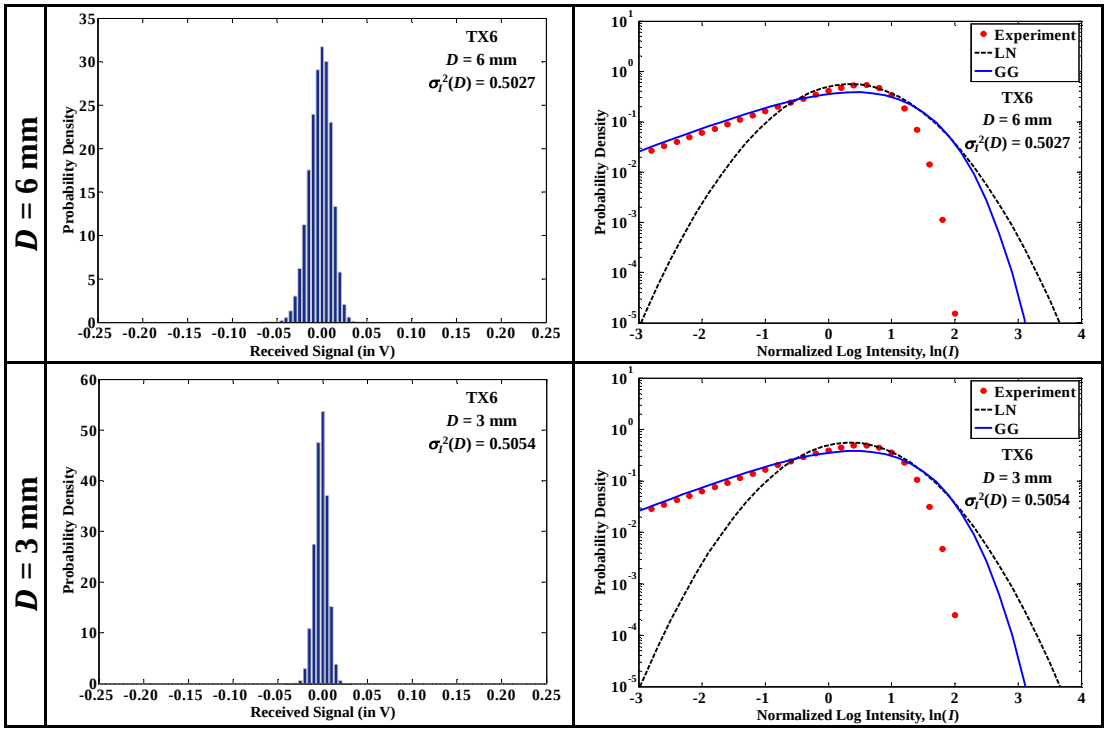

(a) (b)

Figure A.4: (a) Received signal distribution for different receiver aperture diameters of $D = \{40, 30, 20, 15, 10, 6, 3\}$ mm and beam width setting of $w_0 = 2.7731$ mm, with turbulence at $\sigma_R^2 = 0.3797$ ($C_n^2 = 3.3359 \times 10^{-11}$ m$^{-2/3}$); and (b) comparisons of the normalized log irradiance PDF between the experimental data and the theoretical models.

Table A.4: The corresponding statistical test results depicting the GOF between the experimental data and the lognormal and gamma-gamma models, for a variety of receiver aperture diameter $D = \{40, 30, 20, 15, 10, 6, 3\}$ mm and beam width $w_0 = 2.7731$ mm, at $\sigma_R^2 = 0.3797$.

D (mm)	Model	MBE	$RMSE$	Student t-Test (95% Confidence Level)			R
				DF	t_c	t_s	
40	LN	-1.6963E-06	0.1831	46	2.0129	0.0000	0.9878
30	LN	-1.4046E-05	0.0618	50	2.0086	0.0011	0.9984
20	LN	-1.2369E-03	0.3738	44	2.0154	0.0162	0.9235
	GG	-8.8286E-04	0.3648	44	2.0154	0.0119	0.9309
15	LN	-3.3021E-03	0.1638	64	1.9977	0.1176	0.9367
	GG	-2.8091E-03	0.1753	63	1.9983	0.0935	0.9301
10	LN	-4.1654E-03	0.0605	94	1.9855	0.4728	0.9474
	GG	-4.1955E-03	0.0708	91	1.9864	0.4067	0.9286
6	LN	-4.1561E-04	0.0436	99	1.9842	0.0675	0.9695
	GG	-2.3967E-04	0.0463	96	1.9850	0.0366	0.9649
3	LN	-4.1647E-04	0.0447	98	1.9845	0.0658	0.9712
	GG	-2.4069E-04	0.0366	98	1.9845	0.0465	0.9761

A.2 Received Signal Distribution and Comparisons of the Normalized Log Irradiance PDF for Experimental Data with Beam Width of 4.5174 mm

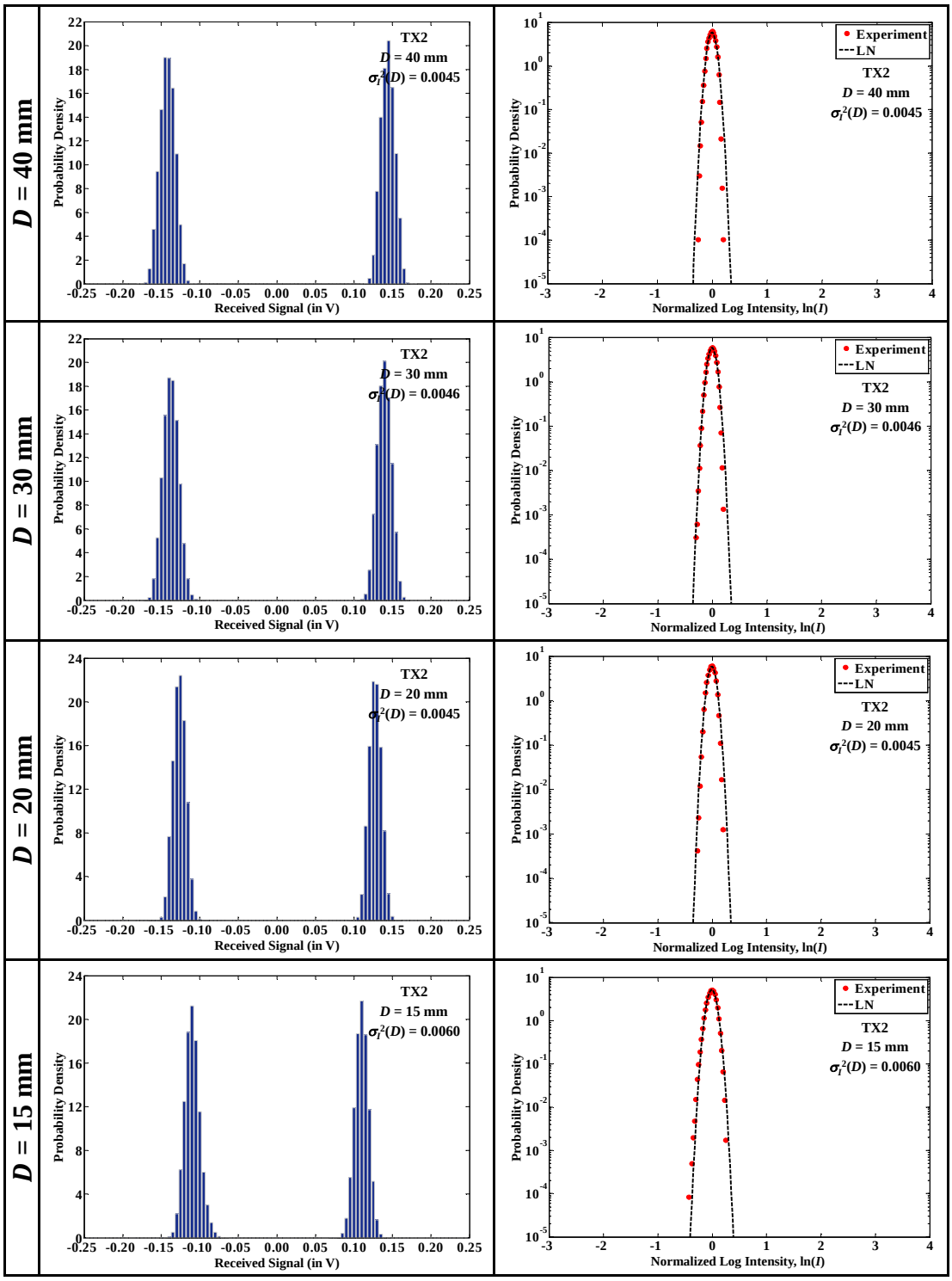

(a) (b)

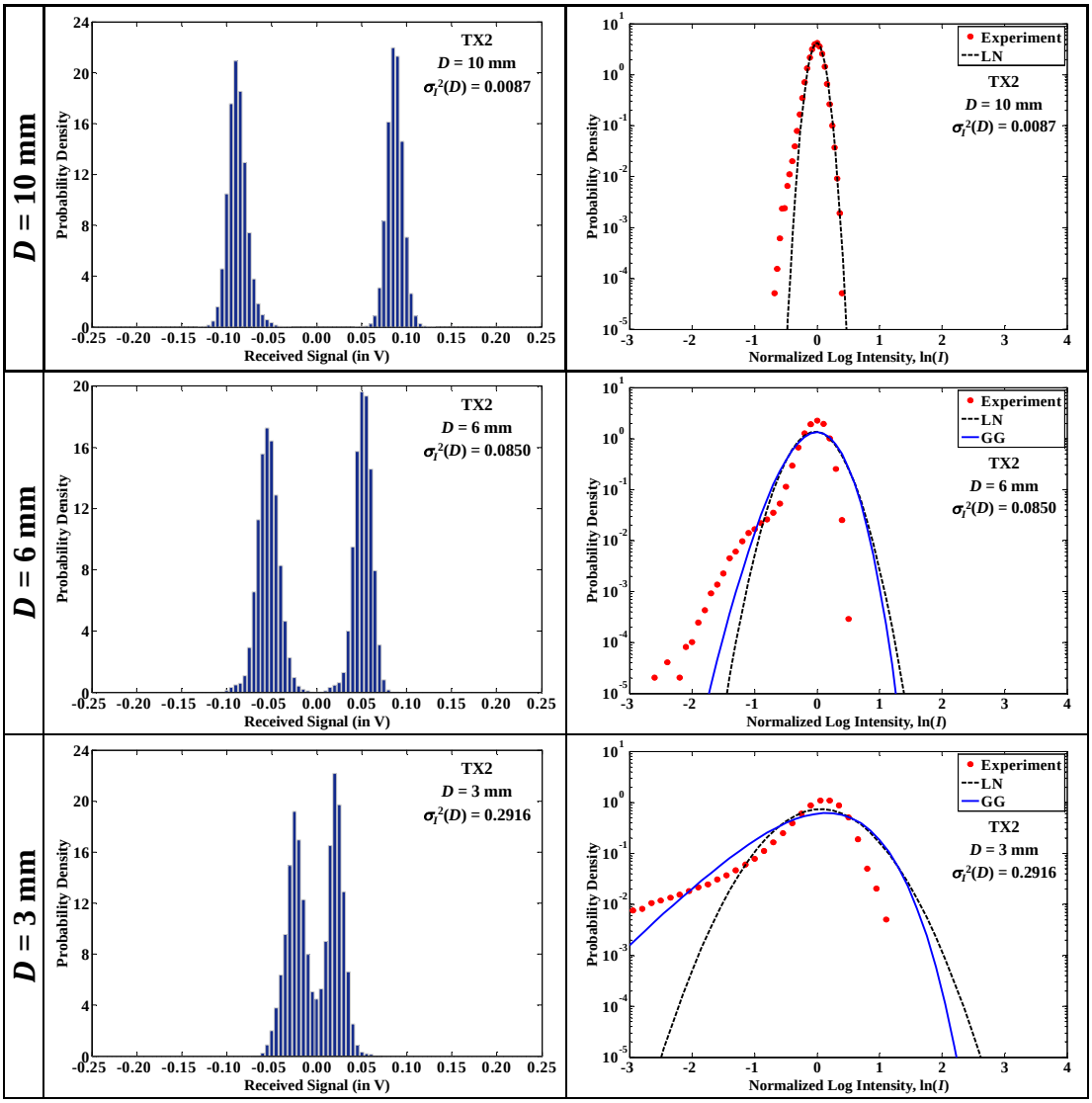

Figure A.5: (a) Received signal distribution for different receiver aperture diameters of $D = \{40, 30, 20, 15, 10, 6, 3\}$ mm and beam width setting of $w_0 = 4.5174$ mm, with turbulence at $\sigma_R^2 = 0.8323$ ($C_n^2 = 7.3127 \times 10^{-11}$ m$^{-2/3}$); and (b) comparisons of the normalized log irradiance PDF between the experimental data and the theoretical models.

Table A.5: The corresponding statistical test results depicting the GOF between the experimental data and the lognormal and gamma-gamma models, for a variety of receiver aperture diameter $D = \{40, 30, 20, 15, 10, 6, 3\}$ mm and beam width $w_0 = 4.5174$ mm, at $\sigma_R^2 = 0.8323$.

D (mm)	Model	MBE	$RMSE$	Student t-Test (95% Confidence Level)			R
				DF	t_c	t_s	
40	LN	-1.3170E-03	0.1860	46	2.0129	0.0340	0.9975
30	LN	-1.2851E-03	0.1375	50	2.0086	0.0467	0.9980
20	LN	-1.0372E-03	0.1829	38	2.0244	0.0247	0.9973
15	LN	-3.1996E-04	0.1001	52	2.0066	0.0163	0.9985
10	LN	-1.2948E-06	0.0667	54	2.0049	0.0001	0.9991
6	LN	-7.7545E-03	0.2845	53	2.0057	0.1468	0.9222
	GG	-6.9717E-03	0.2963	52	2.0066	0.1267	0.9156
3	LN	-3.2735E-03	0.1030	116	1.9806	0.2462	0.9245
	GG	-3.1612E-03	0.1292	110	1.9818	0.1895	0.8817

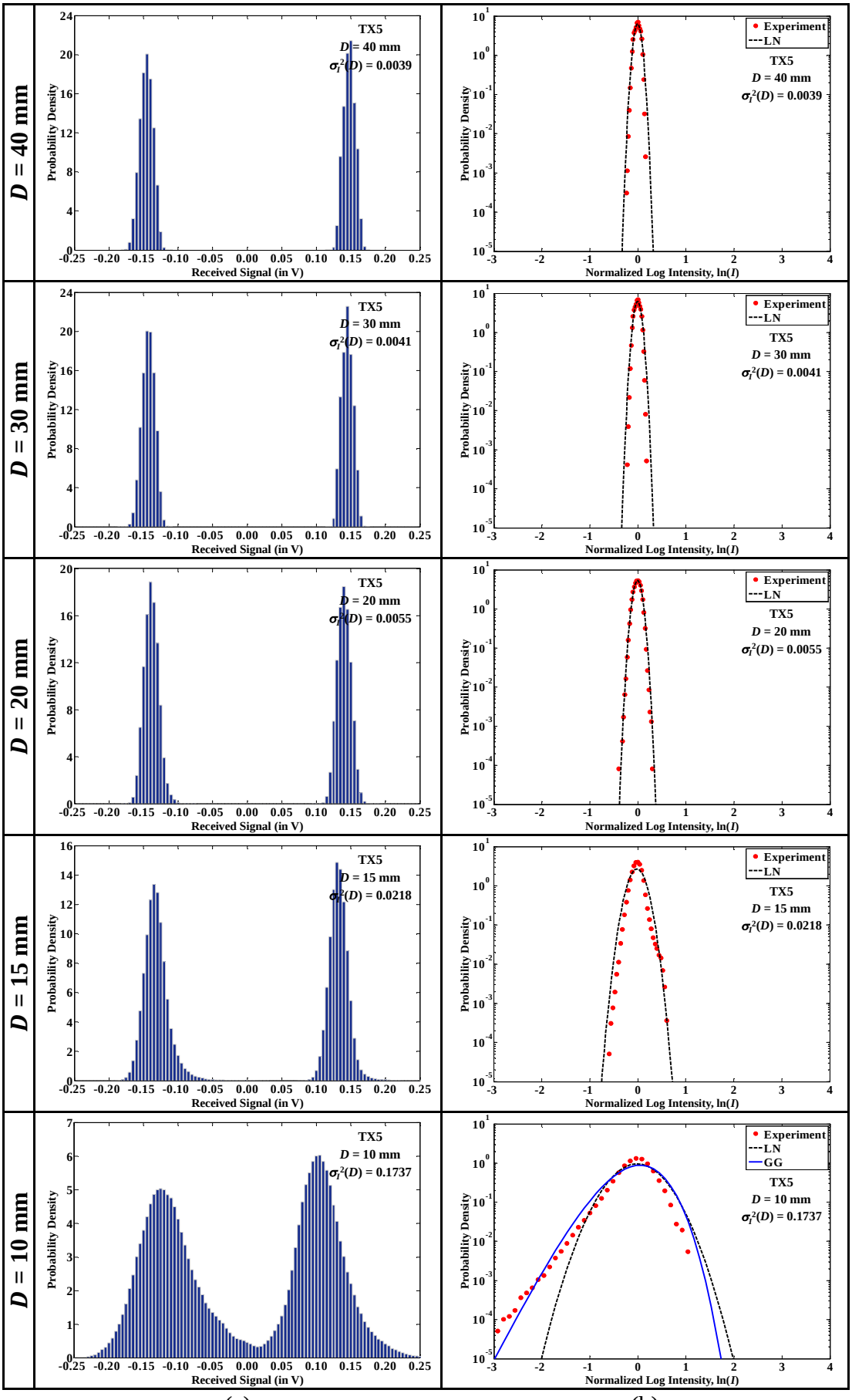
D = 40 mm
D = 30 mm
D = 20 mm
D = 15 mm
D = 10 mm
TX5
D = 40 mm
σ_I²(D) = 0.0039
D = 30 mm
σ_I²(D) = 0.0041
D = 20 mm
σ_I²(D) = 0.0055
D = 15 mm
σ_I²(D) = 0.0218
D = 10 mm
σ_I²(D) = 0.1737
Probability Density
Received Signal (in V)
Normalized Log Intensity, ln(I)
Experiment
LN
GG
(a)
(b)

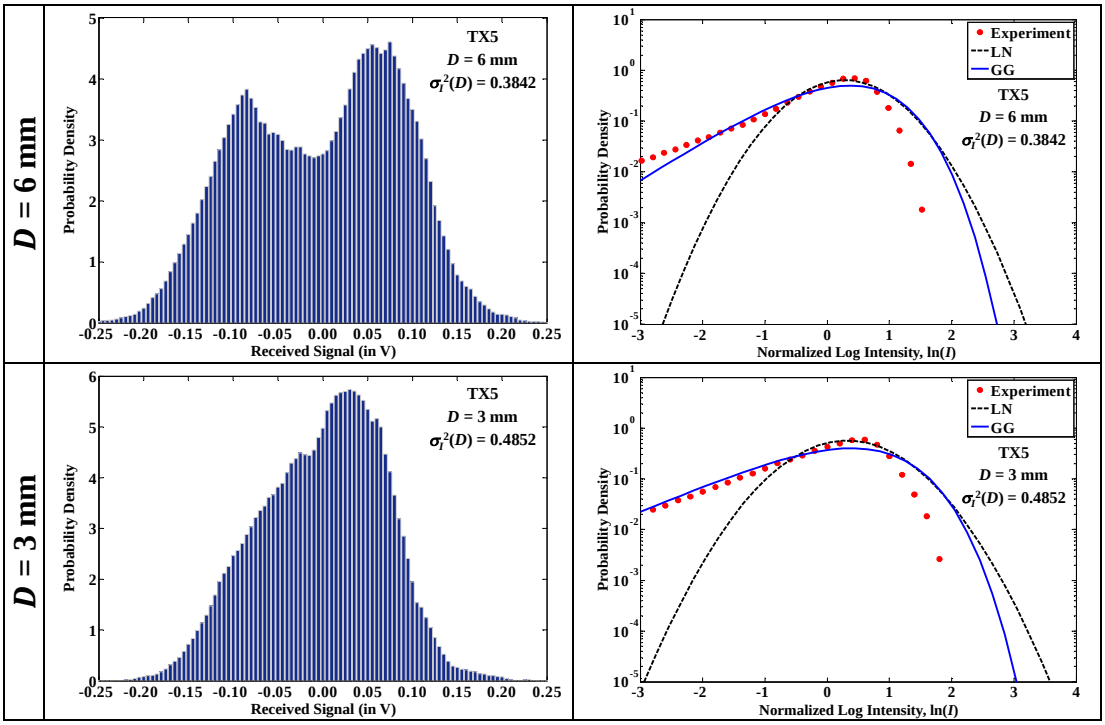

Figure A.6: (a) Received signal distribution for different receiver aperture diameters of $D = \{40, 30, 20, 15, 10, 6, 3\}$ mm and beam width setting of $w_0 = 4.5174$ mm, with turbulence at $\sigma_R^2 = 1.7114$ ($C_n^2 = 1.5036 \times 10^{-10}$ m$^{-2/3}$); and (b) comparisons of the normalized log irradiance PDF between the experimental data and the theoretical models.

Table A.6: The corresponding statistical test results depicting the GOF between the experimental data and the lognormal and gamma-gamma models, for a variety of receiver aperture diameter $D = \{40, 30, 20, 15, 10, 6, 3\}$ mm and beam width $w_0 = 4.5174$ mm, at $\sigma_R^2 = 1.7114$.

D (mm)	Model	MBE	$RMSE$	Student t-Test (95% Confidence Level)			R
				DF	t_c	t_s	
40	LN	-5.6804E-03	0.3369	40	2.0211	0.0754	0.9921
30	LN	-3.0324E-03	0.3183	40	2.0211	0.0426	0.9944
20	LN	-1.6187E-05	0.1035	52	2.0066	0.0008	0.9988
15	LN	-3.0340E-05	0.5013	55	2.0040	0.0003	0.9450
10	LN	-6.0564E-04	0.0967	91	1.9864	0.0429	0.9696
	GG	-3.4427E-04	0.1199	89	1.9870	0.0197	0.9533
6	LN	-1.9445E-03	0.0553	104	1.9830	0.2537	0.9582
	GG	-1.7455E-03	0.0672	101	1.9837	0.1875	0.9390
3	LN	-9.4322E-04	0.0455	98	1.9845	0.1452	0.9663
	GG	-7.1631E-04	0.0540	94	1.9855	0.0929	0.9547

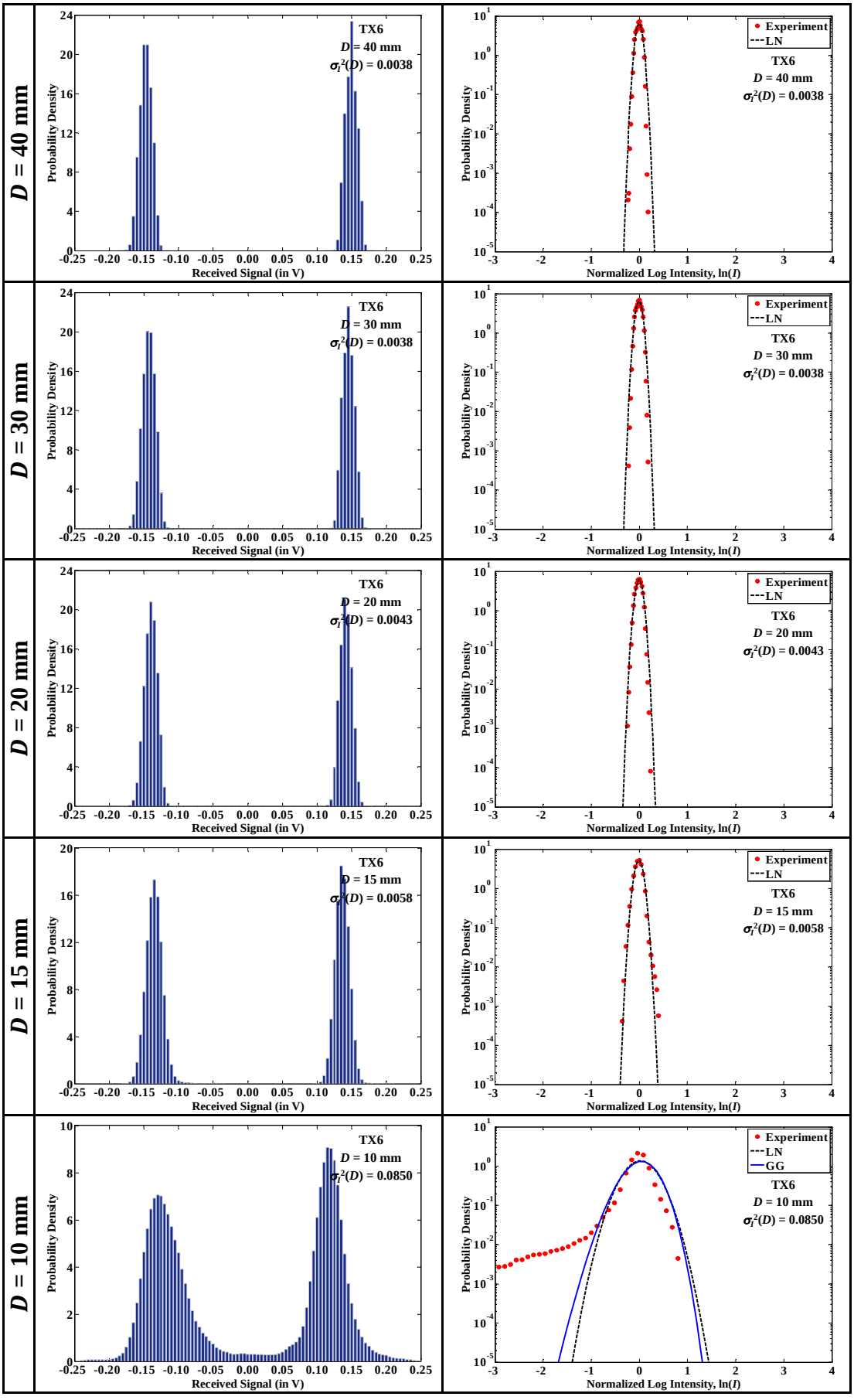
D = 40 mm
D = 30 mm
D = 20 mm
D = 15 mm
D = 10 mm
Probability Density
Received Signal (in V)
Normalized Log Intensity, ln(I)
TX6
D = 40 mm
σ_I²(D) = 0.0038
D = 30 mm
σ_I²(D) = 0.0038
D = 20 mm
σ_I²(D) = 0.0043
D = 15 mm
σ_I²(D) = 0.0058
D = 10 mm
σ_I²(D) = 0.0850
Experiment
LN
GG

(a) (b)

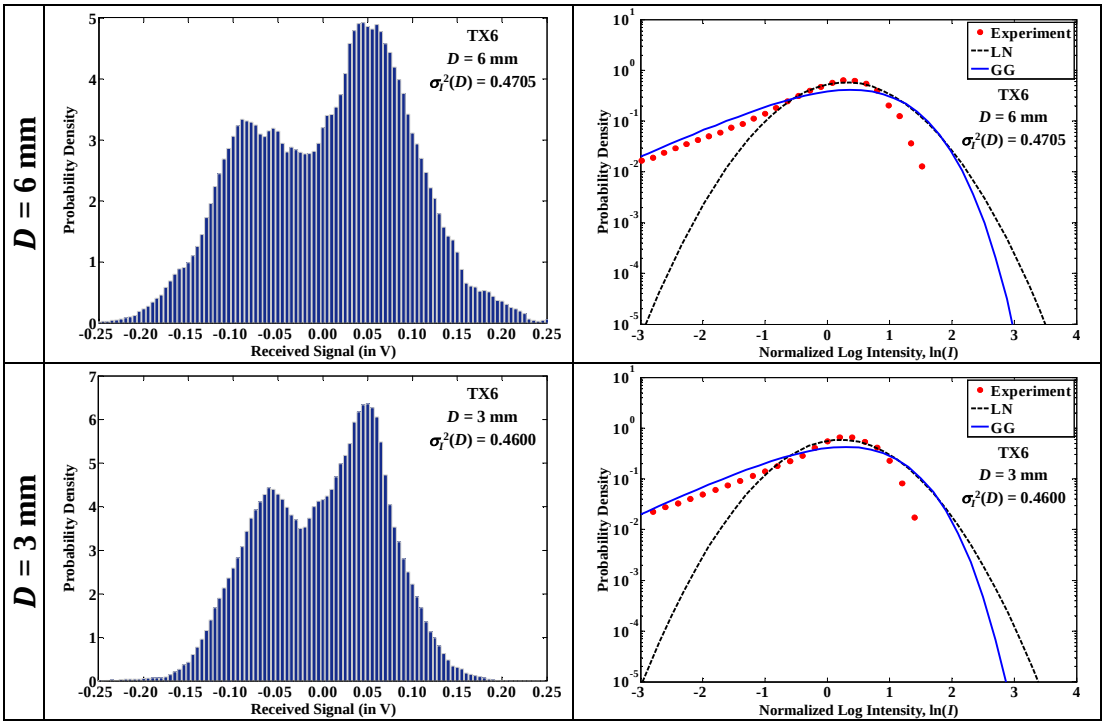

(a) (b)

Figure A.7: (a) Received signal distribution for different receiver aperture diameters of $D = \{40, 30, 20, 15, 10, 6, 3\}$ mm and beam width setting of $w_0 = 4.5174$ mm, with turbulence at $\sigma_R^2 = 2.2139$ ($C_n^2 = 1.9451 \times 10^{-10}$ m$^{-2/3}$); and (b) comparisons of the normalized log irradiance PDF between the experimental data and the theoretical models.

Table A.7: The corresponding statistical test results depicting the GOF between the experimental data and the lognormal and gamma-gamma models, for a variety of receiver aperture diameter $D = \{40, 30, 20, 15, 10, 6, 3\}$ mm and beam width $w_0 = 4.5174$ mm, at $\sigma_R^2 = 2.2139$.

***D* (mm)**	**Model**	***MBE***	***RMSE***	**Student t-Test (95% Confidence Level)**			***R***
				DF	t_c	t_s	
40	LN	-1.7028E-03	0.4088	42	2.0181	0.0191	0.9887
30	LN	-5.0816E-03	0.4304	40	2.0211	0.0528	0.9876
20	LN	-2.6767E-04	0.2215	38	2.0244	0.0053	0.9963
15	LN	-5.2253E-07	0.1756	38	2.0244	0.0000	0.9951
10	LN	-1.5852E-04	0.1466	134	1.9778	0.0090	0.9365
	GG	-8.4877E-05	0.1550	133	1.9780	0.0046	0.9284
6	LN	-3.7020E-03	0.0560	104	1.9830	0.4777	0.9518
	GG	-3.6373E-03	0.0724	98	1.9845	0.3626	0.9271
3	LN	-2.0542E-03	0.0495	94	1.9855	0.2847	0.9626
	GG	-1.8622E-03	0.0685	89	1.9870	0.1863	0.9386

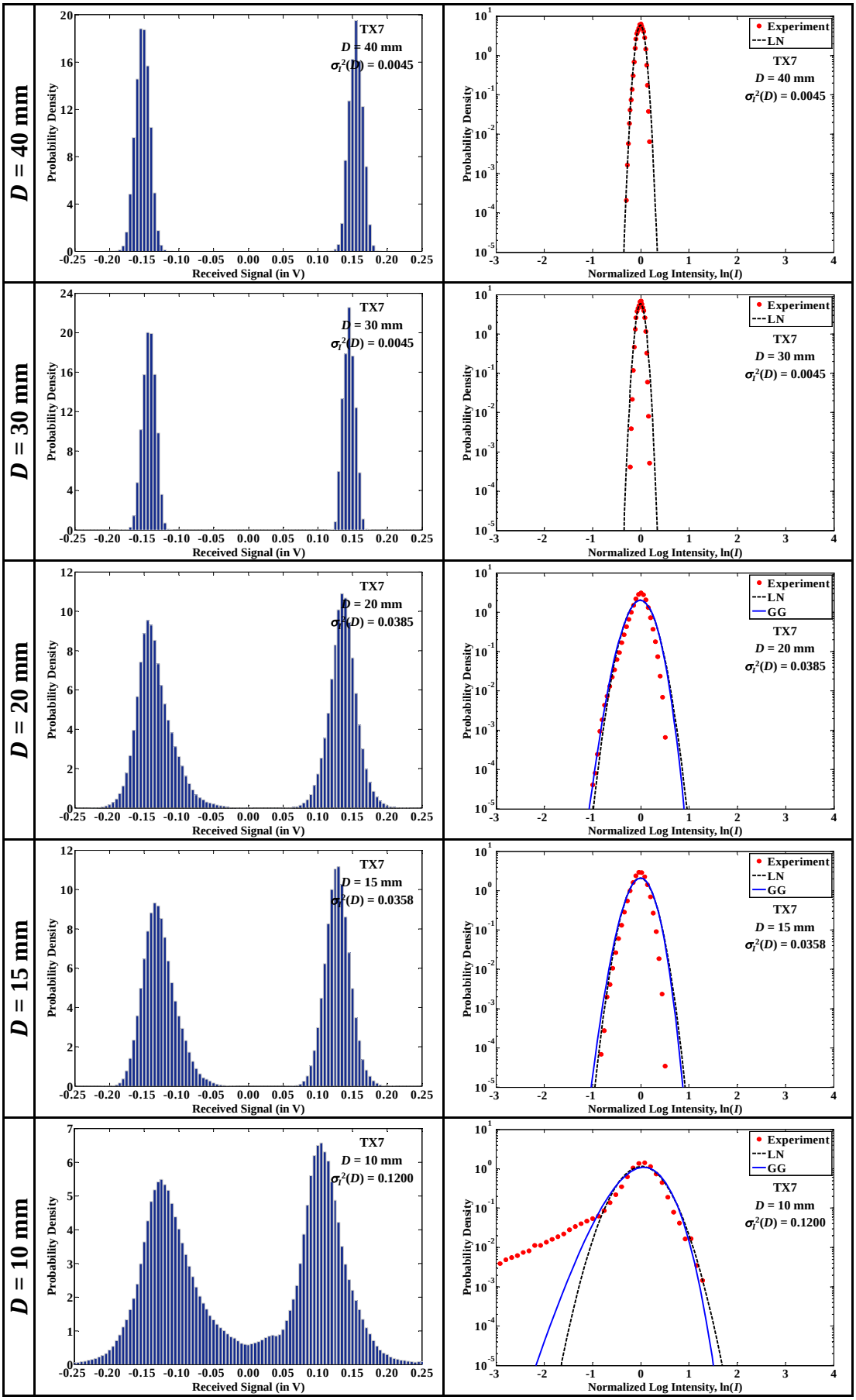
D = 40 mm
D = 30 mm
D = 20 mm
D = 15 mm
D = 10 mm
Probability Density
Received Signal (in V)
Normalized Log Intensity, ln(I)
TX7
D = 40 mm
σ_I²(D) = 0.0045
D = 30 mm
σ_I²(D) = 0.0045
D = 20 mm
σ_I²(D) = 0.0385
D = 15 mm
σ_I²(D) = 0.0358
D = 10 mm
σ_I²(D) = 0.1200
Experiment
LN
GG

(a) (b)

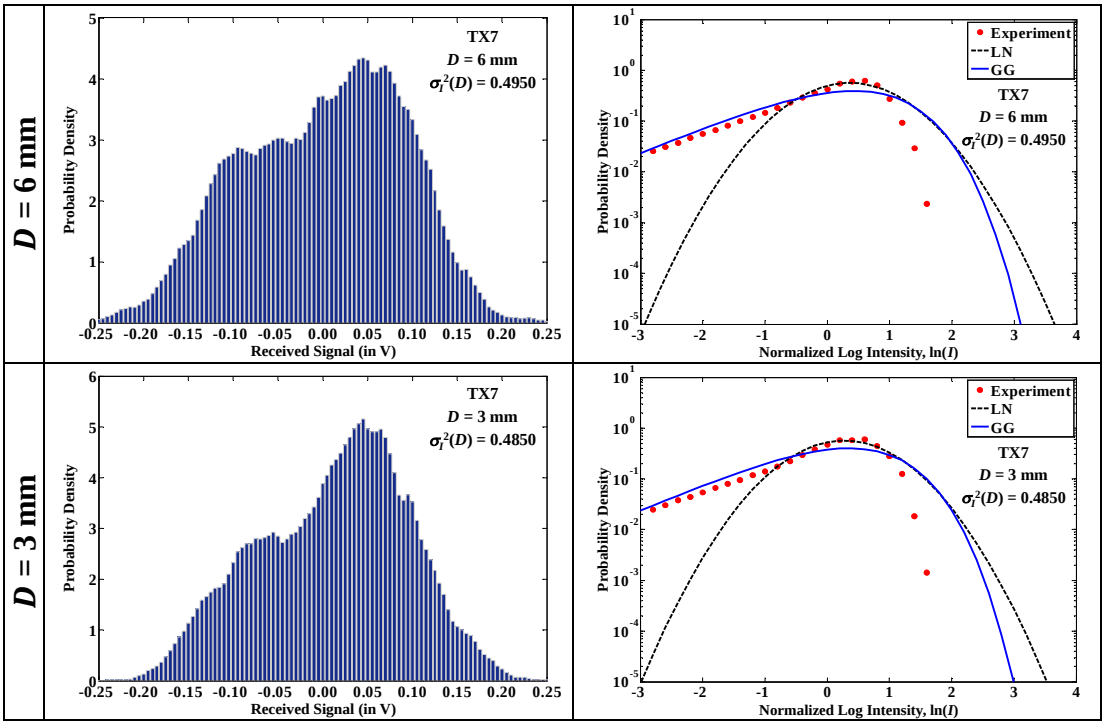

(a) (b)

Figure A.8: (a) Received signal distribution for different receiver aperture diameters of $D = \{40, 30, 20, 15, 10, 6, 3\}$ mm and beam width setting of $w_0 = 4.5174$ mm, with turbulence at $\sigma_R^2 = 2.5616$ ($C_n^2 = 2.2505 \times 10^{-10}$ m$^{-2/3}$); and (b) comparisons of the normalized log irradiance PDF between the experimental data and the theoretical models.

Table A.8: The corresponding statistical test results depicting the GOF between the experimental data and the lognormal and gamma-gamma models, for a variety of receiver aperture diameter $D = \{40, 30, 20, 15, 10, 6, 3\}$ mm and beam width $w_0 = 4.5174$ mm, at $\sigma_R^2 = 2.5616$.

D (mm)	Model	MBE	$RMSE$	Student t-Test (95% Confidence Level)			R
				DF	t_c	t_s	
40	LN	-3.2472E-03	0.2293	48	2.0106	0.0694	0.9956
30	LN	-3.6124E-03	0.2248	44	2.0154	0.0754	0.9967
20	LN	-9.3201E-04	0.4015	56	2.0032	0.0127	0.9236
	GG	-6.4912E-04	0.3922	55	2.0040	0.0091	0.9304
15	LN	-1.9811E-03	0.3574	41	2.0195	0.0260	0.9522
	GG	-1.5029E-03	0.3732	41	2.0195	0.0189	0.9460
10	LN	4.3829E-04	0.0885	95	1.9853	0.0343	0.9741
	GG	4.4849E-04	0.0975	95	1.9853	0.0319	0.9700
6	LN	-2.0129E-03	0.0504	96	1.9850	0.2770	0.9582
	GG	-1.8140E-03	0.0671	90	1.9867	0.1874	0.9351
3	LN	-2.0136E-03	0.0423	96	1.9850	0.3302	0.9711
	GG	-1.8181E-03	0.0617	91	1.9864	0.2042	0.9461

Appendix B

Student's t-Distribution Critical Values

cum. prob	$t_{.50}$	$t_{.75}$	$t_{.80}$	$t_{.85}$	$t_{.90}$	$t_{.95}$	$t_{.975}$	$t_{.99}$	$t_{.995}$	$t_{.999}$	$t_{.9995}$
one-tail	**0.50**	**0.25**	**0.20**	**0.15**	**0.10**	**0.05**	**0.025**	**0.01**	**0.005**	**0.001**	**0.0005**
two-tail	**1.00**	**0.50**	**0.40**	**0.30**	**0.20**	**0.10**	**0.05**	**0.02**	**0.01**	**0.002**	**0.001**
DF											
1	0.000	1.000	1.376	1.963	3.078	6.314	12.71	31.82	63.66	318.31	636.62
2	0.000	0.816	1.061	1.386	1.886	2.920	4.303	6.965	9.925	22.327	31.599
3	0.000	0.765	0.978	1.250	1.638	2.353	3.182	4.541	5.841	10.215	12.924
4	0.000	0.741	0.941	1.190	1.533	2.132	2.776	3.747	4.604	7.173	8.610
5	0.000	0.727	0.920	1.156	1.476	2.015	2.571	3.365	4.032	5.893	6.869
6	0.000	0.718	0.906	1.134	1.440	1.943	2.447	3.143	3.707	5.208	5.959
7	0.000	0.711	0.896	1.119	1.415	1.895	2.365	2.998	3.499	4.785	5.408
8	0.000	0.706	0.889	1.108	1.397	1.860	2.306	2.896	3.355	4.501	5.041
9	0.000	0.703	0.883	1.100	1.383	1.833	2.262	2.821	3.250	4.297	4.781
10	0.000	0.700	0.879	1.093	1.372	1.812	2.228	2.764	3.169	4.144	4.587
11	0.000	0.697	0.876	1.088	1.363	1.796	2.201	2.718	3.106	4.025	4.437
12	0.000	0.695	0.873	1.083	1.356	1.782	2.179	2.681	3.055	3.930	4.318
13	0.000	0.694	0.870	1.079	1.350	1.771	2.160	2.650	3.012	3.852	4.221
14	0.000	0.692	0.868	1.076	1.345	1.761	2.145	2.624	2.977	3.787	4.140
15	0.000	0.691	0.866	1.074	1.341	1.753	2.131	2.602	2.947	3.733	4.073
16	0.000	0.690	0.865	1.071	1.337	1.746	2.120	2.583	2.921	3.686	4.015
17	0.000	0.689	0.863	1.069	1.333	1.740	2.110	2.567	2.898	3.646	3.965
18	0.000	0.688	0.862	1.067	1.330	1.734	2.101	2.552	2.878	3.610	3.922
19	0.000	0.688	0.861	1.066	1.328	1.729	2.093	2.539	2.861	3.579	3.883
20	0.000	0.687	0.860	1.064	1.325	1.725	2.086	2.528	2.845	3.552	3.850
21	0.000	0.686	0.859	1.063	1.323	1.721	2.080	2.518	2.831	3.527	3.819
22	0.000	0.686	0.858	1.061	1.321	1.717	2.074	2.508	2.819	3.505	3.792
23	0.000	0.685	0.858	1.060	1.319	1.714	2.069	2.500	2.807	3.485	3.768
24	0.000	0.685	0.857	1.059	1.318	1.711	2.064	2.492	2.797	3.467	3.745
25	0.000	0.684	0.856	1.058	1.316	1.708	2.060	2.485	2.787	3.450	3.725
26	0.000	0.684	0.856	1.058	1.315	1.706	2.056	2.479	2.779	3.435	3.707
27	0.000	0.684	0.855	1.057	1.314	1.703	2.052	2.473	2.771	3.421	3.690
28	0.000	0.683	0.855	1.056	1.313	1.701	2.048	2.467	2.763	3.408	3.674
29	0.000	0.683	0.854	1.055	1.311	1.699	2.045	2.462	2.756	3.396	3.659
30	0.000	0.683	0.854	1.055	1.310	1.697	2.042	2.457	2.750	3.385	3.646
40	0.000	0.681	0.851	1.050	1.303	1.684	2.021	2.423	2.704	3.307	3.551
50	0.000	0.679	0.849	1.047	1.299	1.676	2.009	2.403	2.678	3.261	3.496
60	0.000	0.679	0.848	1.045	1.296	1.671	2.000	2.390	2.660	3.232	3.460
80	0.000	0.678	0.846	1.043	1.292	1.664	1.990	2.374	2.639	3.195	3.416
100	0.000	0.677	0.845	1.042	1.290	1.660	1.984	2.364	2.626	3.174	3.390
1000	0.000	0.675	0.842	1.037	1.282	1.646	1.962	2.330	2.581	3.098	3.300
Z	0.000	0.674	0.842	1.036	1.282	1.645	1.960	2.326	2.576	3.090	3.291
	0%	**50%**	**60%**	**70%**	**80%**	**90%**	**95%**	**98%**	**99%**	**99.8%**	**99.9%**
	Confidence Level										

References

[1] R. Baldemair, E. Dahlman, G. Fodor, G. Mildh, S. Parkvall, Y. Selen, *et al.*, "Evolving wireless communications: addressing the challenges and expectations of the future," *IEEE Veh. Technol. Mag.*, vol. 8, pp. 24-30, Mar. 2013.

[2] L. Hanzo, H. Haas, S. Imre, D. O'Brien, M. Rupp, and L. Gyongyosi, "Wireless myths, realities, and futures: from 3G/4G to optical and quantum wireless," *Proc. IEEE,* vol. 100, pp. 1853-1888, May 2012.

[3] Ericsson. (2013). Ericsson mobility report: On the pulse of the networked society. [Online]. Available: http://www.ericsson.com/mobility-report (accessed January 4, 2014)

[4] G. Fettweis and E. Zimmermann, "ICT energy consumption - trends and challenges," in *Proc. 11th International Symposium on Wireless Personal Multimedia Communications (WPMC 2008)*, 2008, pp. 1-4.

[5] A. Fehske, G. Fettweis, J. Malmodin, and G. Biczok, "The global footprint of mobile communications: The ecological and economic perspective," *IEEE Commun. Mag.*, vol. 49, pp. 55-62, 2011.

[6] A. K. Majumder, "Free-space laser communication performance in the atmospheric channel," in *Free-Space Laser Communications: Principles and Advances* A. K. Majumder and J. C. Ricklin, Eds., ed New York, NY: Springer-Verlag, 2008, pp. 57-108.

[7] H. Willebrand and B. Ghuman, *Free-space optics: enabling optical connectivity in today's networks*. Indianapolis, IN: Sams Publishing, 2002.

[8] T. H. Carbonneau and D. R. Wisely, "Opportunities and challenges for optical wireless: the competitive advantage of free space telecommunications links in today's crowded marketplace," in *Proc. SPIE, Wireless Technologies and Systems: Millimeter-Wave and Optical*, 1997, pp. 119-128.

[9] K. Tsukamoto, A. Hashimoto, Y. Aburakawa, and M. Matsumoto, "The case for free space," *IEEE Microw. Mag.*, vol. 10, pp. 84-92, Aug. 2009.

[10] A. Mahdy and J. S. Deogun, "Wireless optical communications: a survey," in *Proc. IEEE Wireless Communications and Networking Conference (WCNC)*, 2004, pp. 2399-2404.

[11] L. C. Andrews and R. L. Philips, *Laser Beam Propagation through Random Media*. Bellingham, WA: SPIE Optical Engineering Press, 2005.

[12] K. Kazaura, K. Wakamori, M. Matsumoto, T. Higashino, K. Tsukamoto, and S. Komaki, "RoFSO: A universal platform for convergence of fiber and free-space optical communication networks," *IEEE Commun. Mag.*, vol. 48, pp. 130-137, Feb. 2010.

[13] D. Kedar and S. Arnon, "Urban optical wireless communication networks: the main challenges and possible solutions," *IEEE Commun. Mag.*, vol. 42, pp. S2-S7, May 2004.

[14] Lightpointe (2013). http://www.lightpointe.com/support/casestudies.html [Online] (December 18, 2013).

[15] D.-Y. Song, Y.-S. Hurh, J.-w. Cho, J.-H. Lim, D.-W. Lee, J.-S. Lee, *et al.*, "4 x 10 Gb/s terrestrial optical free space transmission over 1.2 km using an EDFA preamplifier with 100 GHz channel spacing," *Opt. Express*, vol. 7, pp. 280-284, Oct. 2000.

[16] M.-C. Jeong, J.-S. Lee, S.-Y. Kim, S.-W. Namgung, J.-H. Lee, M.-Y. Cho, *et al.*, "8 x 10-Gb/s terrestrial optical free-space transmission over 3.4 km using an optical repeater," *IEEE Photon. Technol. Lett.*, vol. 15, pp. 171-173, Jan. 2003.

[17] Y. Arimoto, M. Presi, V. Guarino, A. D'Errico, G. Contestabile, M. Matsumoto, et al., "320 Gbit/s (8x40 Gbit/s) double-pass terrestrial free-space optical link transparently connected to optical fibre lines," in *Proc. 34th European Conference on Optical Communication (ECOC 2008)*, 2008, pp. 1-2.

[18] E. Ciaramella, Y. Arimoto, G. Contestabile, M. Presi, A. D'Errico, V. Guarino, *et al.*, "1.28 terabit/s (32x40 Gbit/s) WDM transmission system for free space optical communications," *IEEE J. Sel. Areas Commun.*, vol. 27, pp. 1639-1645, Dec. 2009.

[19] P.-L. Chen, S.-T. Chang, S.-T. Ji, S.-C. Lin, H.-H. Lin, H.-L. Tsay, *et al.*, "Demonstration of 16 channels 10 Gb/s WDM free space transmission over 2.16 km," in *Proc. 2008 Digest of the IEEE/LEOS Summer Topical Meetings*, 2008, pp. 235-236.

[20] A. Bekkali, C. Ben Naila, K. Kazaura, K. Wakamori, and M. Matsumoto, "Transmission analysis of OFDM-based wireless services over turbulent radio-on-FSO links modeled by gamma-gamma distribution," *IEEE Photonics J.*, vol. 2, pp. 510-520, Jun. 2010.

[21] Y. Arimoto, "Compact free-space optical terminal for multi-gigabit signal transmissions with a single-mode fiber," in *Proc. SPIE, Free-Space Laser Communication Technologies XXI*, 2009, pp. 719908(1)-(9).

[22] C. B. Naila, K. Wakamori, M. Matsumoto, A. Bekkali, and K. Tsukamoto, "Transmission analysis of digital TV signals over a Radio-on-FSO channel," *IEEE Commun. Mag.*, vol. 50, pp. 137-144, Aug. 2012.

[23] Z. Ghassemlooy, W. Popoola, and S. Rajbhandari, *Optical Wireless Communications: System and Channel Modelling with MATLAB*. Boca Raton, FL: Taylor & Francis Group, 2012.

[24] A. A. Farid and S. Hranilovic, "Outage capacity optimization for free-space optical links with pointing errors," *J. Lightwave Technol.*, vol. 25, pp. 1702-1710, Jul. 2007.

[25] D. K. Borah and D. G. Voelz, "Pointing error effects on free-space optical communication links in the presence of atmospheric turbulence," *J. Lightw. Technol.*, vol. 27, pp. 3965-3973, Sep. 2009.

[26] I. I. Kim, B. McArthur, and E. Korevaar, "Comparison of laser beam propagation at 785 nm and 1550 nm in fog and haze for optical wireless communications," in *Proc. SPIE, Optical Wireless Communications III*, 2001, pp. 26-37.

[27] I. I. Kim and E. Korevaar, "Availability of free space optics (FSO) and hybrid FSO/RF systems," in *Proc. SPIE, Optical Wireless Communications IV*, 2001, pp. 84-95.

[28] E. J. Lee and V. W. S. Chan, "Part 1: optical communication over the clear turbulent atmospheric channel using diversity," *IEEE J. Sel. Areas Commun.*, vol. 22, pp. 1896-1906, Nov. 2004.

[29] X. M. Zhu and J. M. Kahn, "Free-space optical communication through atmospheric turbulence channels," *IEEE Trans. Commun.*, vol. 50, pp. 1293-1300, Aug. 2002.

[30] S. Arnon, "Effects of atmospheric turbulence and building sway on optical wireless-communication systems," *Opt. Lett.*, vol. 28, pp. 129-131, Jan. 2003.

[31] S. Arnon, "Optimization of urban optical wireless communication systems," *IEEE Trans. Wireless Commun.*, vol. 2, pp. 626-629, Jul 2003.

[32] H. E. Nistazakis, T. A. Tsiftsis, and G. S. Tombras, "Performance analysis of free-space optical communication systems over atmospheric turbulence channels," *IET Commun.*, vol. 3, pp. 1402-1409, Aug. 2009.

[33] H. E. Nistazakis, E. A. Karagianni, A. D. Tsigopoulos, M. E. Fafalios, and G. S. Tombras, "Average capacity of optical wireless communication systems over atmospheric turbulence channels," *J. Lightw. Technol.*, vol. 27, pp. 974-979, Apr. 2009.

[34] A. Garcia-Zambrana, C. Castillo-Vazquez, and B. Castillo-Vazquez, "On the capacity of FSO links over gamma-gamma atmospheric turbulence channels using OOK signaling," *EURASIP Journal on Wireless Communications and Networking*, vol. 2010, pp. 127657(1)-(9), May 2010.

[35] J. Anguita, I. Djordjevic, M. A. Neifeld, and B. Vasic, "Shannon capacities and error-correction codes for the optical atmospheric channel," *OSA J. Opt. Networking*, vol. 4, pp. 586-601, Sep. 2005.

[36] D. L. Fried, "Anisoplanatism in adaptive optics," *J. Opt. Soc. Am.*, vol. 72, pp. 52-61, Jan. 1982.

[37] R. R. Butts and C. B. Hogge, "Phase conjugate adaptive optics using perimeter phase measurement," *J. Opt. Soc. Am.*, vol. 67, pp. 278-281, Mar. 1977.

[38] N. Cvijetic, S. G. Wilson, and M. Brandt-Pearce, "Receiver optimization in turbulent free-space optical MIMO channels with APDs and Q-ary PPM," *IEEE Photon. Technol. Lett.*, vol. 19, pp. 103-105, Jan. 2007.

[39] A. Jurado-Navas and A. Puerta-Notario, "Generation of correlated scintillations on atmospheric optical communications," *IEEE/OSA J. Opt. Commun. Netw.*, vol. 1, pp. 452-462, Oct. 2009.

[40] M. A. Khalighi, N. Schwartz, N. Aitamer, and S. Bourennane, "Fading reduction by aperture averaging and spatial diversity in optical wireless systems," *IEEE/OSA J. Opt. Commun. Netw.*, vol. 1, pp. 580-593, Nov. 2009.

[41] N. Letzepis, I. Holland, and W. Cowley, "The Gaussian free space optical MIMO channel with Q-ary pulse position modulation," *IEEE Trans. Wireless Commun.*, vol. 7, pp. 1744-1753, May 2008.

[42] S. M. Navidpour, M. Uysal, and M. Kavehrad, "BER performance of free-space optical transmission with spatial diversity," *IEEE Trans. Wireless Commun.*, vol. 6, pp. 2813-2819, Aug. 2007.

[43] M. Razavi and J. H. Shapiro, "Wireless optical communications via diversity reception and optical preamplification," *IEEE Trans. Wireless Commun.*, vol. 4, pp. 975-983, May 2005.

[44] M. Safari and M. Uysal, "Do we really need OSTBCs for free-space optical communication with direct detection?," *IEEE Trans. Wireless Commun.*, vol. 7, pp. 4445-4448, Nov. 2008.

[45] M. K. Simon and V. A. Vilnrotter, "Alamouti-type space-time coding for free-space optical communication with direct detection," *IEEE Trans. Wireless Commun.*, vol. 4, pp. 35-39, Jan. 2005.

[46] T. A. Tsiftsis, H. G. Sandalidis, G. K. Karagiannidis, and M. Uysal, "Optical wireless links with spatial diversity over strong atmospheric turbulence channels," *IEEE Trans. Wireless Commun.*, vol. 8, pp. 951-957, Feb. 2009.

[47] S. G. Wilson, M. Brandt-Pearce, Q. Cao, and J. H. Leveque, "Free-space optical MIMO transmission with Q-ary PPM," *IEEE Trans. Commun.*, vol. 53, pp. 1402-1412, Aug. 2005.

[48] S. G. Wilson, M. Brandt-Pearce, C. Qianling, and M. Baedke, "Optical repetition MIMO transmission with multipulse PPM," *IEEE J. Sel. Areas Commun.*, vol. 23, pp. 1901-1910, Sep. 2005.

[49] C. H. Kwok, R. V. Penty, and I. H. White, "Link reliability improvement for optical wireless communication systems with temporal-domain diversity reception," *IEEE Photon. Technol. Lett.*, vol. 20, pp. 700-702, May 2008.

[50] F. Xu, A. Khalighi, P. Caussé, and S. Bourennane, "Channel coding and time-diversity for optical wireless links," *Opt. Express*, vol. 17, pp. 872-887, Jan. 2009.

[51] X. Liu, "Free-space optics optimization models for building sway and atmospheric interference using variable wavelength," *IEEE Trans. Commun.*, vol. 57, pp. 492-498, Feb. 2009.

[52] A. Abdulhussein, A. Oka, T. T. Nguyen, and L. Lampe, "Rateless coding for hybrid free-space optical and radio-frequency communication," *IEEE Trans. Wireless Commun.*, vol. 9, pp. 907-913, Mar. 2010.

[53] S. Bloom and W. Hartley, The last-mile solution: hybrid FSO radio, in Whitepaper, AirFiber Inc., 2002.

[54] B. He and R. Schober, "Bit-interleaved coded modulation for hybrid RF/FSO systems," *IEEE Trans. Commun.*, vol. 57, pp. 3753-3763, Dec. 2009.

[55] H. Tapse and D. Borah, "Hybrid optical/RF channels: characterization and performance study using low density parity check codes," *IEEE Trans. Commun.*, vol. 57, pp. 3288-3297, Nov. 2009.

[56] S. Vangala and H. Pishro-Nik, "A highly reliable FSO/RF communication system using efficient codes," in *Proc. 2007 IEEE Global Telecommunications Conference (GLOBECOM 2007)*, 2007, pp. 2232-2236.

[57] W. Zhang, S. Hranilovic, and C. Shi, "Soft-switching hybrid FSO/RF links using short-length raptor codes: design and implementation," *IEEE J. Sel. Areas Commun.*, vol. 27, pp. 1698-1708, Dec. 2009.

[58] K. Kiasaleh, "Performance of APD-based, PPM free-space optical communication systems in atmospheric turbulence," *IEEE Trans. Commun.*, vol. 53, pp. 1455-1461, Sep. 2005.

[59] J. Li, J. Q. Liu, and D. P. Taylor, "Optical communication using subcarrier PSK intensity modulation through atmospheric turbulence channels," *IEEE Trans. Commun.*, vol. 55, pp. 1598-1606, Aug. 2007.

[60] W. O. Popoola and Z. Ghassemlooy, "BPSK subcarrier intensity modulated free-space optical communications in atmospheric turbulence," *J. Lightw. Technol.,* vol. 27, pp. 967-973, Apr. 2009.

[61] Z. Wang, W. Zhong, S. Fu, and C. Lin, "Performance comparison of different modulation formats over free-space optical (FSO) turbulence links with space diversity reception technique," *IEEE Photonics J.,* vol. 1, pp. 277-285, Dec. 2009.

[62] Z. Wang, W. Zhong, and C. Lin, "Performance improvement of OOK free-space optical communication systems by coherent detection and dynamic decision threshold in atmospheric turbulence conditions," *IEEE Photon. Technol. Lett.,* vol. 24, pp. 2035-2037, Nov. 2012.

[63] V. W. S. Chan, "Coding for the Turbulent Atmospheric Optical Channel," *IEEE Trans. Commun.*, vol. 30, pp. 269-275, Jan. 1982.

[64] Y. T. Koh and F. Davidson, "Interleaved concatenated coding for the turbulent atmospheric direct detection optical communication channel," *IEEE Trans. Commun.*, vol. 37, pp. 648-651, Jun. 1989.

[65] H. G. Sandalidis, "Coded free-space optical links over strong turbulence and misalignment fading channels," IEEE Trans. Commun., vol. 59, pp. 669-674, Mar. 2011.

[66] P. Park and J. R. Barry, "Trellis-coded multiple-pulse-position modulation for wireless infrared communications," *IEEE Trans. Commun.,* vol. 52, pp. 643-651, Apr. 2004.

[67] X. M. Zhu and J. M. Kahn, "Performance bounds for coded free-space optical communications through atmospheric turbulence channels," *IEEE Trans. Commun.*, vol. 51, pp. 1233-1239, Aug. 2003.

[68] M. Uysal, J. Li, and M. Yu, "Error rate performance analysis of coded free-space optical links over gamma-gamma atmospheric turbulence channels," *IEEE Trans. Wireless Commun.,* vol. 5, pp. 1229-1233, Jun. 2006.

[69] I. B. Djordjevic, S. Denic, J. Anguita, B. Vasic, and M. A. Neifeld, "LDPC-coded MIMO optical communication over the atmospheric turbulence channel," *J. Lightw. Technol.,* vol. 26, pp. 478-486, Mar. 2008.

[70] I. B. Djordjevic, B. Vasic, and M. A. Neifeld, "Multilevel coding in free-space optical MIMO transmission with Q-ary PPM over the atmospheric turbulence channel," *IEEE Photon. Technol. Lett.,* vol. 18, pp. 1491-1493, Jul. 2006.

[71] J. H. Churnside, "Aperture averaging of optical scintillations in the turbulent atmosphere," *Appl. Opt.,* vol. 30, pp. 1982-1994, May 1991.

[72] T. J. Schulz, "Optimal beams for propagation through random media," *Opt. Lett.*, vol. 30, pp. 1093-1095, May 2005.

[73] C. Chen, H. Yang, X. Feng, and H. Wang, "Optimization criterion for initial coherence degree of lasers in free-space optical links through atmospheric turbulence," *Opt. Lett.*, vol. 34, pp. 419-421, Feb. 2009.

[74] D. K. Borah and D. G. Voelz, "Spatially partially coherent beam parameter optimization for free space optical communications," *Opt. Express*, vol. 18, pp. 20746-20758, Sep. 2010.

[75] C. Liu, Y. Yao, Y. X. Sun, J. J. Xiao, and X. H. Zhao, "Average capacity optimization in free-space optical communication system over atmospheric turbulence channels with pointing errors," *Opt. Lett.*, vol. 35, pp. 3171-3173, Oct. 2010.

[76] J. Cang and X. Liu, "Average capacity of free-space optical systems for a partially coherent beam propagating through non-Kolmogorov turbulence," *Opt. Lett.*, vol. 36, pp. 3335-3337, Sep. 2011.

[77] L. B. Pedireddi and B. Srinivasan, "Characterization of atmospheric turbulence effects and their mitigation using wavelet-based signal processing," *IEEE Trans. Commun.*, vol. 58, pp. 1795-1802, Jun. 2010.

[78] L. B. Stotts, P. Kolodzy, A. Pike, B. Graves, D. Dougherty, and J. Douglass, "Free-space optical communications link budget estimation," *Appl. Opt.*, vol. 49, pp. 5333-5343, Oct. 2010.

[79] A. A. Farid and S. Hranilovic, "Outage capacity for MISO intensity-modulated free-space optical links with misalignment," *IEEE/OSA J. Opt. Commun. Netw.*, vol. 3, pp. 780-789, Oct. 2011.

[80] A. García-Zambrana, C. Castillo-Vázquez, and B. Castillo-Vázquez, "Outage performance of MIMO FSO links over strong turbulence and misalignment fading channels," *Opt. Express*, vol. 19, pp. 13480-13496, Jul. 2011.

[81] D. Borah, A. Boucouvalas, C. Davis, S. Hranilovic, and K. Yiannopoulos, "A review of communication-oriented optical wireless systems," *EURASIP Journal on Wireless Communications and Networking*, vol. 2012:91, pp. 1-28, 2012.

[82] L. B. Stotts, L. C. Andrews, P. C. Cherry, J. J. Foshee, P. J. Kolodzy, W. K. McIntire, *et al.*, "Hybrid optical RF airborne communications," *Proc. IEEE*, vol. 97, pp. 1109-1127, Jun. 2009.

[83] H. Izadpanah, T. ElBatt, V. Kukshya, F. Dolezal, and B. K. Ryu, "High-availability free space optical and RF hybrid wireless networks," *IEEE Wireless Commun.*, vol. 10, pp. 45-53, Apr. 2003.

[84] H. Moradi, M. Falahpour, H. H. Reafi, P. G. LoPresti, and M. Atiquzzaman, "Availability modeling of FSO/RF mesh networks through turbulence-induced fading channels," in *Proc. IEEE Conference on Computer Communications Workshops (INFOCOM 2010)*, 2010, pp. 1-5.

[85] H. Moradi, M. Falahpour, H. H. Refai, P. G. LoPresti, and M. Atiquzzaman, "Reconfiguration modeling of reconfigurable hybrid FSO/RF links," in *Proc. IEEE International Conference on Communications (ICC 2010)*, 2010, pp. 1-5.

[86] F. E. Goodwin, "A review of operational laser communication systems," *Proc. IEEE*, vol. 58, pp. 1746-1752, Oct. 1970.

[87] Z. Ghassemlooy and W. O. Popoola. (2010). "Terrestrial free-space optical communications," in *Mobile and Wireless Communications Network Layer and Circuit Level Design*, S. A. Fares and F. Adachi, Eds. Available: http://www.intechopen.com/books/mobile-and-wireless-communications-network-layer-and-circuit-level-design/terrestrial-free-space-optical-communications

[88] A. Ishimaru, *Wave Propagation and Scattering in Random Media*. New York, NY: Academic, 1978.

[89] A. Ishimaru, "The beam wave case in remote sensing," in *Laser Beam Propagation in the Atmosphere*, J. W. Strohbehn, Ed., ed New York, NY: Springer, 1978.

[90] J. C. Ricklin and F. M. Davidson, "Atmospheric turbulence effects on a partially coherent Gaussian beam: implications for free-space laser communication," *J. Opt. Soc. Am. A*, vol. 19, pp. 1794-1802, Sep. 2002.

[91] O. Korotkova, L. C. Andrews, and R. L. Phillips, "Model for a partially coherent Gaussian beam in atmospheric turbulence with application in Lasercom," *Opt. Eng.*, vol. 43, pp. 330-341, Feb. 2004.

[92] J. C. Ricklin and F. M. Davidson, "Atmospheric optical communication with a Gaussian Schell beam," *J. Opt. Soc. Am. A*, vol. 20, pp. 856-866, May 2003.

[93] H. G. Sandalidis, "Optimization models for misalignment fading mitigation in optical wireless links," *IEEE Commun. Lett.*, vol. 12, pp. 395-397, May 2008.

[94] H. G. Sandalidis, T. A. Tsiftsis, and G. K. Karagiannidis, "Optical wireless communications with heterodyne detection over turbulence channels with pointing errors," *J. Lightw. Technol.*, vol. 27, pp. 4440-4445, Oct. 2009.

[95] H. G. Sandalidis, T. A. Tsiftsis, G. K. Karagiannidis, and M. Uysal, "BER performance of FSO links over strong atmospheric turbulence channels with pointing errors," *IEEE Commun. Lett.*, vol. 12, pp. 44-46, Jan. 2008.

[96] G. P. Agarwal, *Fiber-Optic Communication Systems*, 3rd ed. New York, NY: John-Wiley & Sons, Inc., 2002.

[97] J. Gowar, *Optical Communication Systems*, 2nd ed. Hemel Hempstead, Hertfordshire: Prentice Hall, 1993.

[98] W. van Etten and J. van der Plaats, *Fundamentals of Optical Fiber Communications*. Hemel Hempstead, Hertfordshire: Prentice Hall, 1991.

[99] H. Kressel, M. Ettenberg, J. P. Wittke, and I. Ladany, "Laser diodes and LEDs for fiber optical communication," in *Semiconductor Devices for Optical Communication*, H. Kressel, Ed., Berlin: Springer-Verlag, 1980, pp. 9-62.

[100] D. R. Goff, *Fiber Optic Reference Guide - A Practical Guide to the Technology*. Boston, MA: Focal Press, 1996.

[101] D. Hassin and R. Vahldieck, "Feedforward linearization of analog modulated laser diodes-theoretical analysis and experimental verification," *IEEE Trans. Microw. Theory Tech.,* vol. 41, pp. 2376-2382, Dec. 1993.

[102] M. Fukuda, *Reliability and Degradation of Semiconductor Lasers and LEDs*. Boston, MA: Artech House, 1991.

[103] S. Hranilovic, *Wireless Optical Communication Systems*. Boston: Springer, 2005.

[104] G. Keiser, *Optical Fiber Communications*. Singapore: McGraw-Hill, 2000.

[105] W. B. Leigh, *Devices for Optoelectronics*. New York, NY: Marcel Dekker, Inc., 1996.

[106] J. M. Kahn and J. R. Barry, "Wireless infrared communications," *Proc. IEEE,* vol. 85, pp. 265-298, Feb. 1997.

[107] R. Ramirez-Iniguez, S. M. Idrus, and Z. Sun, *Optical Wireless Communications: IR for Wireless Connectivity*. Boca Raton, FL: Taylor & Francis, 2008.

[108] D. J. T. Heatley, D. R. Wisely, I. Neild, and P. Cochrane, "Optical wireless: the story so far," *IEEE Commun. Mag.*, vol. 36, pp. 72-74, 79-82, Dec. 1998.

[109] S. Bloom, E. Korevaar, J. Schuster, and H. Willebrand, "Understanding the performance of free-space optics [Invited]," *J. Opt. Netw.*, vol. 2, pp. 178-200, Jun. 2003.

[110] L. Matthews and G. Garcia, *Laser and Eye Safety in the Laboratory*. Piscataway, NJ: IEEE Press, 1995.

[111] A. Ishimaru, "Wave propagation and scattering in random media and rough surfaces," *Proc. IEEE,* vol. 79, pp. 1359-1366, Oct. 1997.

[112] W. B. Miller, J. C. Ricklin, and L. C. Andrews, "Log-amplitude variance and wave structure function: a new perspective for Gaussian beams," *J. Opt. Soc. Am. A,* vol. 10, pp. 661-672, Apr. 1993.

[113] L. C. Andrews, W. B. Miller, and J. C. Ricklin, "Geometrical representation of Gaussian beams propagating through complex paraxial optical systems," *Appl. Opt.,* vol. 32, pp. 5918-5929, Oct. 1993.

[114] B. E. A. Saleh and M. C. Teich, *Fundamentals of Photonics*, 2nd ed. Hoboken, New Jersey: John Wiley & Sons, 2007.

[115] J. C. Ricklin, S. M. Hammel, F. D. Eaton, and S. L. Lachinova, "Atmospheric channel effects on free-space laser communication," in *Free-Space Laser Communications: Principles and Advances* A. K. Majumder and J. C. Ricklin, Eds., ed New York, NY: Springer-Verlag, 2008, pp. 9-56.

[116] R. M. Gagliardi and S. Karp, *Optical Communications*, 2nd ed. Danvers, MA: John Wiley & Sons, Inc., 1995.

[117] J. M. Wallace and P. V. Hobbs, *Atmospheric Science: An Introductory Survey*, 2nd ed. Burlington, MA: Academic Press, 2006.

[118] H. Weichel, *Laser Beam Propagation in the Atmosphere*. Bellingham, WA: SPIE Optical Engineering Press, 1990.

[119] R. S. Lawrence and J. W. Strohbehn, "A survey of clear-air propagation effects relevant to optical communications," *Proc. IEEE,* vol. 58, pp. 1523-1545, Oct. 1970.

[120] R. F. Lutomirski and H. T. Yura, "Propagation of a finite optical beam in an inhomogeneous medium," *Appl. Opt.,* vol. 10, pp. 1652-1658, Jul. 1971.

[121] A. M. Prokhorov, F. V. Bunkin, K. S. Gochelashvily, and V. I. Shishov, "Laser irradiance propagation in turbulent media," *Proc. IEEE,* vol. 63, pp. 790-811, May 1975.

[122] R. L. Fante, "Electromagnetic beam propagation in turbulent media," *Proc. IEEE,* vol. 63, pp. 1669-1692, Dec. 1975.

[123] R. L. Fante, "Electromagnetic beam propagation in turbulent media: an update," *Proc. IEEE,* vol. 68, pp. 1424-1443, Nov. 1980.

[124] A. Ishimaru, *Wave Propagation and Scattering in Random Media*. Piscataway, NJ: IEEE Press, 1997.

[125] J. H. Churnside and R. J. Lataitis, "Wander of an optical beam in the turbulent atmosphere," *Appl. Opt.,* vol. 29, pp. 926-930, Mar. 1990.

[126] R. Esposito, "Power scintillations due to the wandering of the laser beam," *Proc. IEEE,* vol. 55, pp. 1533-1534, Aug. 1967.

[127] T. Chiba, "Spot dancing of the laser beam propagated through the turbulent atmosphere," *Appl. Opt.,* vol. 10, pp. 2456-2461, Nov. 1971.

[128] D. L. Fried, "Statistics of laser beam fade induced by pointing jitter," *Appl. Opt.*, vol. 12, pp. 422-423, Feb. 1973.

[129] P. J. Titterton, "Power reduction and fluctuations caused by narrow laser beam motion in the far field," *Appl. Opt.*, vol. 12, pp. 423-425, Feb. 1973.

[130] D. L. Fried and H. T. Yura, "Telescope-performance reciprocity for propagation in a turbulent medium," *J. Opt. Soc. Am.*, vol. 62, pp. 600-602, Jan. 1972.

[131] R. J. Hill and S. F. Clifford, "Modified spectrum of atmospheric temperature fluctuations and its application to optical propagation," *J. Opt. Soc. Am.*, vol. 68, pp. 892-899, Jul. 1978.

[132] J. C. Owens, "Optical refractive index of air: dependence on pressure, temperature and composition," *Appl. Opt.*, vol. 6, pp. 51-59, Jan. 1967.

[133] G. C. Valley, "Isoplanatic degradation of tilt correction and short-term imaging systems," *Appl. Opt.*, vol. 19, pp. 574-577, Feb. 1980.

[134] I. E. Lee, Z. Ghassemlooy, W. P. Ng, and S. Rajbhandari, "Fundamental analysis of hybrid free space optical and radio frequency communication systems," in *Proc. 12th Annual Post Graduate Symposium on the Convergence of Telecommunications, Networking and Broadcasting (PGNet 2011)*, 2011.

[135] M. A. Al-Habash, R. L. Phillips, and L. C. Andrews, "Mathematical model for the irradiance probability density function of a laser beam propagating through turbulent media," *Opt. Eng.*, vol. 40, pp. 1554-1562, Aug. 2001.

[136] M. Abramowitz and I. A. Stegun, *Handbook of Mathematical Functions with Formulas, Graphs, and Mathematical Tables*. New York, NY: Dover Publications, 1965.

[137] S. R. Forrest, "Optical detectors: three contenders," *IEEE Spectr.* , vol. 23, pp. 76-85, May 1986.

[138] H. Melchior, M. B. Fisher, and F. R. Arams, "Photodetectors for optical communication systems," *Proc. IEEE*, vol. 58, pp. 1466-1486, Oct. 1970.

[139] S. B. Alexander, *Optical Communication Receiver Design*. Bellingham, DC: SPIE Optical Engineering Press, 1997.

[140] J. C. Palais, *Fiber Optic Communications*, 5th ed. Upper Saddle River, NJ: Prentice-Hall, 2005.

[141] D. P. Schinke, R. G. Smith, and A. R. Hartman, "Photodetectors," in *Semiconductor Devices for Optical Communication*, H. Kressel, Ed., ed Berlin: Springer-Verlag, 1980, pp. 61-87.

[142] R. R. Hayes and D. L. Persechini, "Nonlinearity of p-i-n photodetectors," *IEEE Photon. Technol. Lett.*, vol. 5, pp. 70-72, Jan. 1993.

[143] H. Melchior, "Detectors for lightwave communication," *Phys. Today,* vol. 30, pp. 32-39, Nov. 1977.

[144] B. L. Kasper and J. C. Campbell, "Multigigabit-per-second avalanche photodiode lightwave receivers," *J. Lightwave Tech.,* vol. 5, pp. 1351-1364, Oct. 1987.

[145] F. Osaka, T. Mikawa, T. Kaneda, and F. Osaka, "Impact ionization coefficients of electrons and holes in (100)-oriented GaInAsP," *IEEE J. Quantum Electron.,* vol. 21, pp. 1326-1338, Sep. 1985.

[146] L. R. Tomasetta, H. Law, R. C. Eden, I. Deyhimy, and K. Nakano, "High sensitivity optical receivers for 1.0-1.4 um fiber-optic systems," *IEEE J. Quantum Electron.* , vol. 14, pp. 800-804, Nov. 1978.

[147] B. F. Levine, "Optimization of 10-20 GHz avalanche photodiodes," *IEEE Photon. Technol. Lett.* , vol. 8, pp. 1528-1530, Nov. 1996.

[148] M. C. Brain and T.-P. Lee, "Optical receivers for lightwave communication systems," *J. Lightwave Tech.,* vol. 3, pp. 1281-1300, Dec. 1985.

[149] W. Wu, A. R. Hawkins, and J. E. Bowers, "Design of silicon hetero-interface photodetectors," *J. Lightwave Tech.,* vol. 15, pp. 1608-1615, Aug. 1997.

[150] B. M. Oliver, "Thermal and quantum noise," *Proc. IEEE,* vol. 53, pp. 436-454, May 1965.

[151] S. Karp, E. L. O'Neill, and R. M. Gagliardi, "Communication theory for the free-space optical channel," *Proc. IEEE,* vol. 58, pp. 1611-1626, Oct. 1970.

[152] A. H. Mikesell, A. A. Hoag, and J. S. Hall, "The scintillation of starlight," *J. Opt. Soc. Am.,* vol. 41, pp. 689-691, Oct. 1951.

[153] S. H. Reiger, "Starlight scintillation and atmospheric turbulence," *Astron. J.*, vol. 68, pp. 395-406, Aug. 1963.

[154] A. T. Friberg and R. J. Sudol, "Propagation parameters of gaussian Schell-model beams," *Opt. Commun.*, vol. 41, pp. 383-387, May 1982.

[155] L. Mandel and E. Wolf, *Optical Coherence and Quantum Optics*. Cambridge, UK: Cambridge University Press, 1995.

[156] Y. Ren, A. Dang, B. Luo, and H. Guo, "Capacities for Long-Distance Free-Space Optical Links Under Beam Wander Effects," *IEEE Photon. Technol. Lett.*, vol. 22, pp. 1069-1071, Jul. 2010.

[157] V. W. S. Chan, "Free-space optical communications," *J. Lightw. Technol.,* vol. 24, pp. 4750-4762, Dec. 2006.

[158] L. Jing and M. Uysal, "Achievable information rate for outdoor free space optical communication with intensity modulation and direct detection," in *Proc. IEEE Global Telecommunications Conference (GLOBECOM 2003)*, 2003, pp. 2654-2658.

[159] E. Biglieri, J. Proakis, and S. Shamai, "Fading channels: information-theoretic and communications aspects," *IEEE Trans. Inf. Theory,* vol. 44, pp. 2619-2692, Oct. 1998.

[160] J.-B. Wang, M. Sheng, X. Song, Y. Jiao, and M. Chen, "Comments on `BER performance of FSO links over strong atmospheric turbulence channels with pointing errors," *IEEE Commun. Lett.,* vol. 16, pp. 22-23, Jan. 2012.

[161] T. M. Cover and J. A. Thomas, *Elements of Information Theory*, Second ed.: Wiley-Interscience, 2006.

[162] D. G. Voelz and X. Xiao, "Metric for optimizing spatially partially coherent beams for propagation through turbulence," *Optical Engineering,* vol. 48, pp. 036001-036001, 2009.

[163] N. Perlot and D. Fritzsche, "Aperture averaging: theory and measurements," in *Proc. SPIE, Free-Space Laser Communication Technologies XVI*, 2004, pp. 233-242.

[164] F. S. Vetelino, C. Young, L. Andrews, and J. Recolons, "Aperture averaging effects on the probability density of irradiance fluctuations in moderate-to-strong turbulence," *Appl. Opt.,* vol. 46, pp. 2099-2108, Apr. 2007.

[165] R. Barrios and F. Dios, "Exponentiated Weibull distribution family under aperture averaging for Gaussian beam waves," *Opt. Express,* vol. 20, pp. 13055-13064, Jun. 2012.

[166] Z. Ghassemlooy, H. Le Minh, S. Rajbhandari, J. Perez, and M. Ijaz, "Performance analysis of ethernet/fast-ethernet free space optical communications in a controlled weak turbulence condition," *J. Lightwave Technol.,* vol. 30, pp. 2188-2194, Jul. 2012.

[167] S. Rajbhandari, J. Perez, H. Le-Minh, and Z. Ghassemlooy, "A fast ethernet FSO link performance under the fog controlled environment," in *Proc. 37th European Conference and Exhibition on Optical Communication (ECOC)*, 2011, pp. 1-3.

[168] M. Ijaz, Z. Ghassemlooy, J. Pesek, O. Fiser, H. Le Minh, and E. Bentley, "Modeling of fog and smoke attenuation in free space optical communications link under controlled laboratory conditions," *J. Lightw. Technol.,* vol. 31, pp. 1720-1726, Jun. 2013.

[169] M. Ijaz, Z. Ghassemlooy, J. Perez, V. Brazda, and O. Fiser, "Enhancing the atmospheric visibility and fog attenuation using a controlled FSO channel," *IEEE Photon. Technol. Lett.*, vol. 25, pp. 1262-1265, Jul. 2013.

[170] J. Perez, Z. Ghassemlooy, S. Rajbhandari, M. Ijaz, and H. L. Minh, "Ethernet FSO communications link performance study under a controlled fog environment," *IEEE Commun. Lett.*, vol. 16, pp. 408-410, Mar. 2012.

[171] Z. Ghassemlooy, X. Tang, and S. Rajbhandari, "Experimental investigation of polarisation modulated free space optical communication with direct detection in a turbulence channel," *IET Commun.*, vol. 6, pp. 1489-1494, Jul. 2012.

[172] W. O. Popoola, Z. Ghassemlooy, C. G. Lee, and A. C. Boucouvalas, "Scintillation effect on intensity modulated laser communication systems - a laboratory demonstration," *Optics & Laser Technology*, vol. 42, pp. 682-692, Dec. 2010.

[173] Thorlabs (2013). http://www.thorlabs.de/thorProduct.cfm?partNumber=PDA10A-EC [Online] (accessed January 5, 2014).

[174] A. P. Oliveira, J. F. Escobedo, A. J. Machado, and J. Soares, "Correlation models of diffuse solar-radiation applied to the city of Sao Paulo, Brazil," *Applied Energy*, vol. 71, pp. 59-73, Jan. 2002.

[175] R. J. Stone, "Improved statistical procedure for the evaluation of solar radiation estimation models," *Solar Energy*, vol. 51, pp. 289-291, Oct. 1993.

[176] J. D. Petrucelli, B. Nandram, and M. Chen, *Applied Statistics for Engineers and Scientists*. Upper Saddle River, NJ: Prentice Hall, 1999.

[177] L. L. Lapin, *Modern Engineering Statistics*. Belmont, CA: Duxbury Press, 1997.

[178] L. Ott and M. T. Longnecker, *An Introduction to Statistical Methods and Data Analysis*, 6th ed. Belmont, CA: Cengage Learning, 2008.

[179] W. Shieh and I. Djordjevic, *Orthogonal Frequency Division Multiplexing for Optical Communications*. Burlington, MA: Academic Press/Elsevier, 2010.

[180] R. Luna, D. K. Borah, R. Jonnalagadda, and D. G. Voelz, "Experimental demonstration of a hybrid link for mitigating atmospheric turbulence effects in free-space optical communication," *IEEE Photon. Technol. Lett.*, vol. 21, pp. 1196-1198, Sep. 2009.

[181] J. N. Laneman, E. Martinian, G. W. Wornell, and J. G. Apostolopoulos, "Source-channel diversity for parallel channels," *IEEE Trans. Inf. Theory*, vol. 51, pp. 3518-3539, Oct. 2005.

[182] N. Letzepis, K. D. Nguyen, A. Guillen i Fabregas, and W. G. Cowley, "Outage analysis of the hybrid free-space optical and radio-frequency channel," *IEEE J. Sel. Areas Commun.*, vol. 27, pp. 1709-1719, Dec. 2009.

[183] F. Giannetti, M. Luise, and R. Reggiannini, "Mobile and personal communications in the 60 GHz band: a survey," *Wireless Personal Communications*, vol. 10, pp. 207-243, Jul. 1999.

[184] R. C. Daniels and R. W. Heath, "60 GHz wireless communications: emerging requirements and design recommendations," *IEEE Veh. Technol. Mag.*, vol. 2, pp. 41-50, Sep. 2007.

[185] R. C. Daniels, J. N. Murdock, T. S. Rappaport, and R. W. Heath, "60 GHz wireless: up close and personal," *IEEE Microw. Mag.*, vol. 11, pp. 44-50, Dec. 2010.

[186] N. Guo, R. C. Qiu, S. S. Mo, and K. Takahashi, "60-GHz millimeter-wave radio: principle, technology, and new results," *EURASIP Journal on Wireless Communications and Networking*, vol. 2007, pp. 68253(1)-68253(8), Dec. 2006.

[187] J. Schönthier, The 60 GHz channel and its modelling, *WP3-Study, BROADWAY IST-2001-32686*, version V1.0, May 2003.

[188] C. Tepedelenlioglu, A. Abdi, and G. B. Giannakis, "The Ricean K factor: estimation and performance analysis," *IEEE Trans. Wireless Commun.*, vol. 2, pp. 799-810, Jul. 2003.

[189] United Nations Environment Programme (2011). Towards a green economy: pathways to sustainable development and poverty eradication. [Online]. Available: http://www.unep.org/greeneconomy/greeneconomyreport/tabid/29846/default.aspx (accessed January 17, 2013).

[190] United Nations Framework Convention on Climate Change (2012). http://unfccc.int [Online] (accessed January 17, 2013).

[191] EARTH Consortium (2012). https://www.ict-earth.eu [Online] (accessed July 30, 2012).

[192] Stichting GreenTouch (2012). http://www.greentouch.org [Online] (accessed July 30, 2012).

[193] S. Vadgama, "Trends in green wireless access," *Fujitsu Sci. Tech. J.*, vol. 45, pp. 404-408, 2009.

[194] W. Vereecken, W. Van Heddeghem, M. Deruyck, B. Puype, B. Lannoo, W. Joseph, *et al.*, "Power consumption in telecommunication networks: Overview and reduction strategies," *IEEE Commun. Mag.*, vol. 49, pp. 62-69, Jun. 2011.

[195] Global e-Sustainability Initiative (2008). SMART 2020: Enabling the low carbon economy in the information age. [Online]. Available: http://gesi.org/ReportsPublications/Smart2020/tabid/192/Default.aspx (accessed July 30, 2012).

[196] Mobile VCE (2012). http://www.mobilevce.com [Online] (accessed January 17, 2013).

[197] Huawei Technologies (2011). Corporate sustainability report: Enriching life through communication. [Online]. Available: http://www.huawei.com/en/about-huawei/corporate-citizenship/csr-report/index.htm (accessed January 17, 2013).

[198] C. Forster, I. Dickie, G. Maile, H. Smith, and M. Crisp, (2009). Understanding the environmental impact of communication systems. [Online]. Available: http://stakeholders.ofcom.org.uk/market-data-research/other/technology-research/research/sector-studies/environment/ (accessed January 17, 2013).

[199] R. Prasad and F. J. Velez, *WiMAX networks: techno-economic vision and challenges.* New York, NY: Springer, 2010.

[200] W. Webb, *Wireless communications: the future*. West Sussex: John Wiley & Sons, 2007.

[201] The future of infrastructure: compact base stations, in Whitepaper, In-Stat, 2010.

[202] J. Mitola and Z. Zvonar, *Software radio technologies: selected readings*. Piscataway, NJ: Wiley-IEEE Press, 2001.

[203] T. Ulversoy, "Software defined radio: challenges and opportunities," *IEEE Commun. Surveys Tuts.*, vol. 12, pp. 531-550, Fourth Quarter 2010.

[204] S. Bellofiore, C. A. Balanis, J. Foutz, and A. S. Spanias, "Smart-antenna systems for mobile communication networks. Part 1: overview and antenna design," *IEEE Antennas Propag. Mag.*, vol. 44, pp. 145-154, Jun. 2002.

[205] S. Bellofiore, J. Foutz, C. A. Balanis, and A. S. Spanias, "Smart-antenna system for mobile communication networks. Part 2: beamforming and network throughput," *IEEE Antennas Propag. Mag.*, vol. 44, pp. 106-114, Aug. 2002.

[206] A. Alexiou and M. Haardt, "Smart antenna technologies for future wireless systems: trends and challenges," *IEEE Commun. Mag.*, vol. 42, pp. 90-97, Sep. 2004.

[207] N. Nandiraju, D. Nandiraju, L. Santhanam, H. Bing, W. Junfang, and D. P. Agrawal, "Wireless mesh networks: current challenges and future directions of web-in-the-sky," *IEEE Wireless Commun.*, vol. 14, pp. 79-89, Aug. 2007.

[208] I. F. Akyildiz, X. Wang, and W. Wang, "Wireless mesh networks: a survey," *Computer Networks*, vol. 47, pp. 445-487, Mar. 2005.

[209] C. Wei, K. B. Letaief, and C. Zhigang, "Network interference cancellation," *IEEE Trans. Wireless Commun.*, vol. 8, pp. 5982-5999, Dec. 2009.

[210] L. Jungwon, D. Toumpakaris, and Y. Wei, "Interference mitigation via joint detection," *IEEE J. Sel. Areas Commun.*, vol. 29, pp. 1172-1184, Jun. 2011.

[211] Nokia Siemens Networks good green business sense, in Whitepaper, Nokia Siemens Networks, 2008.

[212] Compact base stations: a new step in the evolution of base station design, in Whitepaper, Senza Fili Consulting, 2010.

[213] The emergence of compact base stations in the new RAN architecture paradigm, in Whitepaper, ABI Research, 2010.

[214] Metro zone wi-fi for cellular data offloading, in Whitepaper, Wavion Wireless Networks, 2010.

[215] O. Tipmongkolsilp, S. Zaghloul, and A. Jukan, "The evolution of cellular backhaul technologies: current issues and future trends," *IEEE Commun. Surveys Tuts.*, vol. 13, pp. 97-113, First Quarter 2011.

[216] SoC-based mobile broadband evolution, in Whitepaper, DesignArt Networks, 2011.

[217] Self organizing network: NEC's proposals for next-generation radio network management, in Whitepaper, NEC Corp., 2009.

[218] Self-organizing network (SON): introducing the Nokia Siemens Networks SON suite – an efficient, future-proof platform for SON, in Whitepaper, Nokia Siemens Networks, 2009.

[219] WiMAX.com (2012). Backhaul for WiMAX: top 8 technical considerations. [Online]. Available: http://www.wimax.com/microwave-backhaul/backhaul-for-wimax-top-8-technical-considerations (accessed January 18, 2013).

[220] D. Jones (2008). 4G: can't stand the rain. [Online]. Available: http://www.heavyreading.com/document.asp?doc_id=154434 (accessed January 18, 2013).

[221] K. Piamrat, A. Ksentini, J.-M. Bonnin, and C. Viho, "Radio resource management in emerging heterogeneous wireless networks," *Computer Communications*, vol. 34, pp. 1066-1076, Jun. 2011.

[222] M. F. Hossain, K. S. Munasinghe, and A. Jamalipour, "A protocooperation-based sleep-wake architecture for next generation green cellular access networks," in *Proc. 4th International Conference on Signal Processing and Communication Systems (ICSPCS 2010)*, 2010, pp. 1-8.

[223] L. M. Correia, D. Zeller, O. Blume, D. Ferling, Y. Jading, Go, et al., "Challenges and enabling technologies for energy aware mobile radio networks," *IEEE Commun. Mag.*, vol. 48, pp. 66-72, Nov. 2011.

[224] P. E. Heegaard, "Evolution of traffic patterns in telecommunication systems," in *Proc. 2nd International Conference on Communications and Networking in China (CHINACOM 2007)*, 2007, pp. 28-32.

[225] H. W. Kuhn, "The Hungarian method for the assignment problem," in *50 Years of Integer Programming 1958-2008*, M. Junger, T. M. Liebling, D. Naddef, G. L.

Nemhauser, W. R. Pulleyblank, G. Reinelt, *et al.*, Eds., ed Berlin: Springer-Verlag, pp. 29-47, 2010.

[226] N. Bonello, R. Zhang, S. Chen, and L. Hanzo, "Reconfigurable rateless codes," *IEEE Trans. Wireless Commun.*, vol. 8, pp. 5592-5600, Nov. 2009.

[227] N. Bonello, S. Chen, and L. Hanzo, "Low-density parity-check codes and their rateless relatives," *IEEE Commun. Surveys Tuts.*, vol. 13, pp. 3-26, First Quarter 2011.